Modelling and simulation of phase-transformations in elasto-plastic polycrystals

von der Fakultät Maschinenbau
der Technischen Universität Dortmund
zur Erlangung des akademischen Grades

Doktor-Ingenieur (Dr.-Ing.)

genehmigte Dissertation

von

Richard Ostwald

aus Herten

Referent:	Prof. Dr.-Ing. A. Menzel
Korreferenten:	Prof. Dr. A. S. J. Suiker
	Jun.-Prof. B. Kiefer, Ph.D.
Tag der Einreichung:	13.02.2015
Tag der mündlichen Prüfung:	13.05.2015

“We should take care not to make the intellect our god;
it has, of course, powerful muscles, but no personality.”

Albert Einstein (1879–1955)

Acknowledgements

This work has been carried out from 2009 to 2015 during my time as a research assistant at the Institute of Mechanics at TU Dortmund University.

First of all, I want to thank Professor Andreas Menzel for his continuous support and the friendly working atmosphere that I enjoyed over the past years. His extensive knowledge, inspiring ideas, and remarkable attention to detail that he shared in many stimulating discussions had a great impact on this work. I also thank Professor Akke Suiker for kindly agreeing to act as the co-referee of this thesis and Professor Björn Kiefer for serving as the third referee.

Moreover, I want to express my gratitude to Dr. Thorsten Bartel for the fruitful discussions and nice teamwork over the past years. Special thanks go to Professor Jörn Mosler for contributing to the friendly working atmosphere at the institute and to my colleagues Alexander Bartels, Rolf Berthelsen, Karsten Buckmann, Dinesh Kumar Dusthakar, Dr. Krishnendu Haldar, Tim Heitbreder, Raphael Holtermann, Dr. Guillermo Díaz Ortíz, César Polindara, Christian Sievers and Maniprakash Subramanian as well as to my former colleagues Till Clausmeyer, Dr. Ralf Denzer, Dr. Christian Hortig, Dr. Tobias Kayser, Dr. Vadim Palnau and Dr. Tobias Waffenschmidt for enjoyable discussions and friendship. Special thanks also go to Professor Bob Svendsen and Professor Jaan Unger for introducing me to the field of mechanics in the first place and for guiding me during my undergraduate studies. Last but not least I thank Kerstin Walter and Tina McDonagh for their kind helpfulness I enjoyed at the Institute of Mechanics at any time.

Most of all, however, I want to thank my family—my parents, my siblings, my grandfather Ferdinand† and especially Nadine—for their invaluable support and enrichment of my life.

Dortmund, May 2015 Richard Ostwald

Zusammenfassung

Die vorliegende Arbeit behandelt einen neuartigen Modellierungsrahmen zur Simulation von austenitisch-martensitischen Phasentransformationen in Formgedächtnislegierungen (SMA) und TRIP-Stählen. Das Ziel der Arbeit ist die Entwicklung und Ausarbeitung eines generalisierten Modells, welches das charakteristische makroskopische Verhalten sowohl von SMA als auch von TRIP-Stahl abbildet. Als Basis für die Formulierung dient ein skalarwertiges, thermodynamisch konsistentes, auf statistischer Physik basierendes Modell für die Simulation von SMA. Im Verlauf dieser Arbeit wird das Modell in affine und nicht-affine Microsphere-Formulierungen eingebettet um das polykristalline Materialverhalten abzubilden und um die Simulation dreidimensionaler Randwertprobleme zu ermöglichen. Darüberhinaus wird eine Kopplung an Plastizität vorgestellt, welche zusätzlich die Abbildung des Verhaltens von TRIP-Stahl ermöglicht. Abschließend wird die Implementierung eines dreidimensionalen Phasentransformationsmodells für finite Deformationen mit dem Fokus auf repräsentative Transformationsrichtungen in einem thermo-elastoplastischen Framework gezeigt.

Abstract

In this work, a new framework for the simulation of shape memory alloys (SMA) and TRIP steels undergoing martensite-austenite phase-transformations is introduced. The goal is the derivation and elaboration of a generalised model which facilitates the reflection of the characteristic macroscopic behaviour of SMA as well as of TRIP steels. The foundation of the overall formulation is a scalar-valued, thermodynamically consistent, statistical physics based model for the simulation of SMA. As this work proceeds, the model is implemented in affine and non-affine micro-sphere formulations in order to capture polycrystalline behaviour and to simulate three-dimensional boundary value problems. Moreover, a coupling to plasticity is introduced, additionally enabling the capturing of the macroscopic behaviour of TRIP steels. Finally, the implementation of a three-dimensional finite-deformation phase-transformation model that focuses on representative transformation directions is elaborated in a thermo-elastoplastic framework.

Publications

Key parts of this thesis are based on peer-reviewed journal articles, which were published during the progress of this thesis.

1. R. Ostwald, T. Bartel, A. Menzel: *A computational micro-sphere model applied to the simulation of phase-transformations*, Journal of Applied Mathematics and Mechanics, 90(7–8):605–622, 2010 [101].
2. R. Ostwald, T. Bartel, A. Menzel: *A Gibbs-energy-barrier-based computational micro-sphere model for the simulation of martensitic phase-transformations*, International Journal for Numerical Methods in Engineering, 97:851–877, 2014 [104].
3. R. Ostwald, T. Bartel, A. Menzel: *A one-dimensional computational model for the interaction of phase-transformations and plasticity*, International Journal of Structural Changes in Solids, 3(1):63–82, 2011 [102].
4. R. Ostwald, T. Bartel, A. Menzel: *Phase-transformations interacting with plasticity – a micro-sphere model applied to TRIP steel*, Computational Materials Science, 64:12–16, 2012 [103].
5. R. Ostwald, T. Bartel, A. Menzel: *An energy-barrier-based computational micro-sphere model for phase-transformations interacting with plasticity*, Computer Methods in Applied Mechanics and Engineering, 293:232–265, 2015 [105].

For the above named journal articles, the author of this thesis contributed essential aspects with regard to the outline of the theory, carried out all of the numerical implementations and simulations, and also prepared the articles themselves.

Contents

Notation xi

1 Introduction 1

1.1 Motivation and state of the art . . . 1

1.1.1 Microstructure and mechanical properties of shape memory alloys 1

1.1.2 Microstructure and mechanical properties of TRIP steels . . . 5

1.1.3 Modelling and simulation of phase-transformations . . . 8

1.2 Objective of this work . . . 12

2 An affine micro-sphere model for phase-transformations 15

2.1 One-dimensional, probabilistic phase-transformation model . . . 16

2.1.1 Kinematics of phase transitions . . . 17

2.1.2 Integration of the system of evolution equations . . . 18

2.2 Application of the micro-sphere model . . . 19

2.2.1 Kinematics . . . 22

2.2.2 Micro-macro-relations . . . 22

2.2.3 Numerical evaluation . . . 23

2.3 Numerical examples . . . 24

2.3.1 Non-deviatoric tension-compression . . . 25

2.3.2 Deviatoric tension-compression . . . 26

2.3.3 Rod under tension-compression . . . 27

2.4 Summary . . . 33

2.5 Appendix . . . 34

2.5.1 Numerical integration of the evolution equation . . . 34

2.5.2 On general properties of the affine micro-sphere approach . . . 36

2.5.3 Transformation strains of the martensite compression variant . . . 37

3 A non-affine micro-sphere model for phase-transformations 39

3.1 Scalar-valued phase-transformation model with volumetric-deviatoric split 40

3.1.1 Phase potentials . . . 40

3.1.2 Evolution of volume fractions . . . 42

3.1.3 Gibbs energy barriers of elliptic-paraboloidal potentials . . . 42

3.1.4 Algorithmic computation of Gibbs energy barriers . . . 44

3.1.5 Scalar-valued model – computational examples at the micro-level 48

3.2 Micro-sphere formulation . . . 51

3.2.1 Three-dimensional extension of the model 53
3.2.2 Micro-sphere application – computational examples at the meso-level 57
3.3 Finite element implementation 61
3.4 Summary 66
3.5 Appendix 68
3.5.1 Material parameters 68
3.5.2 Analytical solution for the minimum of the Gibbs potential of a single phase 68
3.5.3 Numerical scheme - computation of Gibbs energy barriers 70
3.5.4 Overall constitutive algorithm 71

4 Phase-transformations interacting with plasticity 73
4.1 A model for the interaction of phase-transformations and plasticity . . . 74
4.1.1 Evolution of volume fractions 75
4.1.2 Evolution of plastic strains 76
4.1.3 Plasticity inheritance law for two phases 78
4.2 Numerical integration of evolution equations 82
4.3 Numerical Examples 84
4.3.1 SMA – phase-transformations without plasticity 84
4.3.2 SMA – phase-transformations with plasticity 85
4.3.3 TRIP steel – phase-transformations with plasticity 88
4.4 Summary 90
4.5 Appendix 91
4.5.1 Material parameters 91
4.5.2 Algorithmic flowchart 93

5 An affine micro-sphere model for phase-transformations interacting with plasticity 95
5.1 One-dimensional model for phase-transformations interacting with plasticity 96
5.2 Micro-sphere application 99
5.3 Finite element implementation 102
5.4 Summary 108

6 A non-affine micro-sphere model for phase-transformations interacting with plasticity 109
6.1 Scalar-valued phase-transformation model with volumetric-deviatoric split and plasticity 110
6.1.1 Helmholtz and Gibbs energy potentials of the individual phases . 110
6.1.2 Evolution of volume fractions 113
6.1.3 Incorporation of plasticity 114
6.2 Consistent plasticity inheritance law for three phases 116

6.2.1 Derivation of inheritance rules in the case of one increasing and two decreasing phases . . . 117
6.2.2 Derivation of inheritance rules in the case of one decreasing and two increasing phases . . . 119
6.2.3 Remarks on the inheritance rules . . . 120
6.3 Micro-sphere application . . . 121
6.3.1 Kinematics . . . 122
6.3.2 Micro-macro-relations . . . 122
6.3.3 Anisotropic elasticity tensor and tangent operator . . . 125
6.3.4 Micro-sphere application – numerical examples . . . 126
6.3.5 Sensitivity of the macroscopic constitutive response with respect to the underlying micro-sphere integration scheme . . . 134
6.4 Finite element implementation . . . 138
6.4.1 Plate with hole under tension – SMA . . . 141
6.4.2 Plate with hole under tension – TRIP steel . . . 142
6.4.3 Plate with hole under shear deformation – SMA . . . 143
6.4.4 Plate with hole under shear deformation – TRIP steel . . . 144
6.5 Summary and conclusions . . . 145
6.6 Appendix . . . 146
6.6.1 Material parameters . . . 146
6.6.2 Computation of Gibbs energy barriers . . . 149
6.6.3 Algorithmic scheme for the numerical constitutive update . . . 150

7 A finite strain model for phase-transformations interacting with plasticity based on representative transformation directions 153
7.1 Crystallographic considerations . . . 153
7.2 Basics of the constitutive model . . . 155
7.2.1 Inelastic material behaviour . . . 158
7.3 Numerical solution of the constitutive equations . . . 161
7.3.1 Algorithmic solution scheme . . . 161
7.3.2 Numerical results for states under homogeneous deformation . . . 164
7.4 Enforcement of inequality constraints – convergence study . . . 171
7.4.1 Tensile load – upper constraint boundary . . . 173
7.4.2 Tensile load – lower constraint boundary . . . 174
7.4.3 Shear load – upper constraint boundary . . . 175
7.4.4 Shear load – lower constraint boundary . . . 176
7.5 Finite element implementation . . . 177
7.6 Appendix – material parameters . . . 181

8 Concluding remarks 183

Bibliography 187

Notation

The notation used in this work becomes obvious from its context. However, the following essential relations are collectively provided for the sake of the reader's convenience.

Tensors In a three-dimensional Euclidean space spanned by the Cartesian basis vectors $\{\boldsymbol{e}_i\}, i = 1, 2, 3$, tensors of first, second and fourth order are expressed in terms of their coefficients $(\bullet)_i$ following Einstein's summation convention, namely

$$
\begin{aligned}
&\boldsymbol{u} = u_i \, \boldsymbol{e}_i \quad , && \text{(first-order tensor, i.e. vector)} \\
&\boldsymbol{S} = S_{ij} \, \boldsymbol{e}_i \otimes \boldsymbol{e}_j \quad , && \text{(second-order tensor)} \\
&\boldsymbol{\mathsf{T}} = \mathsf{T}_{ijkl} \, \boldsymbol{e}_i \otimes \boldsymbol{e}_j \otimes \boldsymbol{e}_k \otimes \boldsymbol{e}_l \quad . && \text{(fourth-order tensor)}
\end{aligned}
$$

Here and in the following, we use non-bold letters for scalars, bold-face lower-case italic letters for vectors, bold-face upper-case italic letters for second-order tensors and bold-face upper-case sans-serif letters for fourth-order tensors.

Inner tensor products Inner tensor products are denoted by dots where the number of dots characterises the number of contractions, i.e.

$$
\begin{aligned}
\boldsymbol{u} \cdot \boldsymbol{v} &= u_i \, v_i \quad , \\
\boldsymbol{S} \cdot \boldsymbol{u} &= S_{ij} \, u_j \, \boldsymbol{e}_i \quad , \\
\boldsymbol{S} \cdot \boldsymbol{T} &= S_{ij} \, T_{jk} \, \boldsymbol{e}_i \otimes \boldsymbol{e}_k \quad , \\
\boldsymbol{S} : \boldsymbol{T} &= S_{ij} \, T_{ij} \quad , \\
\boldsymbol{\mathsf{S}} : \boldsymbol{T} &= \mathsf{S}_{ijkl} \, T_{kl} \, \boldsymbol{e}_i \otimes \boldsymbol{e}_j \quad .
\end{aligned}
$$

An n-fold contraction of two nth-order tensors always results in a scalar.

Outer tensor products Outer tensor products—also referred to as dyadic products—are represented by the classical symbol $\otimes$ as well as by the non-standard symbols $\overline{\otimes}$ and $\underline{\otimes}$ using the definitions

$$\begin{aligned}
\boldsymbol{u} \otimes \boldsymbol{v} &= u_i \, v_j \, \boldsymbol{e}_i \otimes \boldsymbol{e}_j \quad , \\
\boldsymbol{S} \otimes \boldsymbol{T} &= S_{ij} \, T_{kl} \, \boldsymbol{e}_i \otimes \boldsymbol{e}_j \otimes \boldsymbol{e}_k \otimes \boldsymbol{e}_l \quad , \\
\boldsymbol{S} \,\overline{\otimes}\, \boldsymbol{T} &= S_{ik} \, T_{jl} \, \boldsymbol{e}_i \otimes \boldsymbol{e}_j \otimes \boldsymbol{e}_k \otimes \boldsymbol{e}_l \quad , \\
\boldsymbol{S} \,\underline{\otimes}\, \boldsymbol{T} &= S_{il} \, T_{jk} \, \boldsymbol{e}_i \otimes \boldsymbol{e}_j \otimes \boldsymbol{e}_k \otimes \boldsymbol{e}_l \quad ,
\end{aligned}$$

The dyadic product of two first-order tensors, i.e. vectors, results in second-order tensors, whereas the dyadic products of two second-order tensors result in fourth-order tensors.

Identity tensors The second-order identity tensor $\boldsymbol{I}$ and the fourth-order symmetric, volumetric and deviatoric identity tensors, $\mathsf{I}^{\mathrm{sym}}$, $\mathsf{I}^{\mathrm{vol}}$ and $\mathsf{I}^{\mathrm{dev}}$, respectively, are defined as

$$\begin{aligned}
\boldsymbol{I} &= \delta_{ij} \, \boldsymbol{e}_i \otimes \boldsymbol{e}_j \quad , \\
\mathsf{I}^{\mathrm{sym}} &= \frac{1}{2} \left[\boldsymbol{I} \,\overline{\otimes}\, \boldsymbol{I} + \boldsymbol{I} \,\underline{\otimes}\, \boldsymbol{I} \right] \quad , \\
\mathsf{I}^{\mathrm{vol}} &= \frac{1}{3} \left[\boldsymbol{I} \otimes \boldsymbol{I} \right] \quad , \\
\mathsf{I}^{\mathrm{dev}} &= \mathsf{I}^{\mathrm{sym}} - \mathsf{I}^{\mathrm{vol}} \quad ,
\end{aligned}$$

with the Kronecker delta symbol $\delta_{ij} = \boldsymbol{e}_i \cdot \boldsymbol{e}_j$.

1 Introduction

1.1 Motivation and state of the art

Functional materials like TRIP steels and shape memory alloys (SMA) offer a great potential for the industrial manufacturing of sophisticated components benefitting from the advantages that these materials can provide, such as locally varying hardness and stiffness. The need for reliable manufacturing and application of such components leads to the demand for accurate constitutive models not only to predict the material's response by means of simulations, but also in view of material and structural design purposes. However, the coupling of phase-transformations and plasticity involves the interaction of multiple complex physical mechanisms, which have not yet been fully elaborated.

1.1.1 Microstructure and mechanical properties of shape memory alloys

Shape memory alloys (SMA) do not only show fascinating phenomena, effects and properties in an academic sense, but also exhibit a large potential for industrial applications. These include medical devices [96], aerospace applications [57] and oil industry needs among other industrial fields [90, 106].

Stress-induced and thermally induced martensitic transformations in NiTi-based SMA have been studied extensively since the 1980s. One focal point of experimental investigations has been the twinning structure of martensite that is observed at the micro-scale, see Fig. 1.1. Martensite twins appear as parallel bands that each contain one martensitic variant, where both variants are related to each other by a simple shear deformation. Martensite twins of different types are documented in the literature, where the twin type refers to the crystallographic orientation of the corresponding twinned martensite variants. The actual twin type is determined with the help of selected area diffraction (SAD) patterns. Commonly occurring twins are, e.g., the so-called $(11\bar{1})$ type I twins or the $\langle 011 \rangle$ type II twins [144]. The martensitic transformation state is furthermore characterised by the so-called habit plane, which defines the interface between the crystal

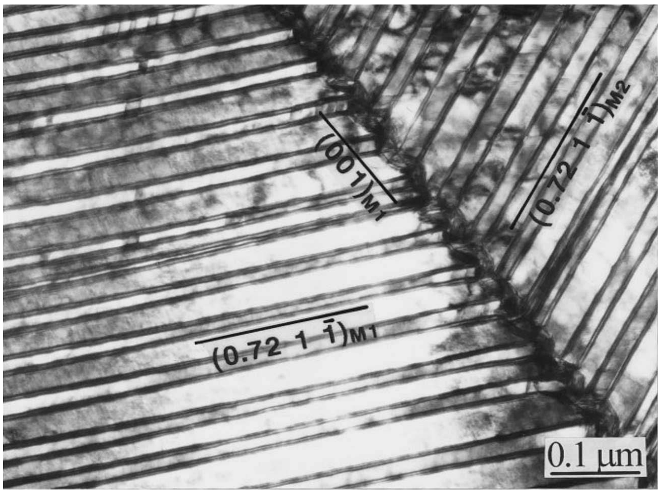

Figure 1.1: Bright-field (BF) micrograph of NiTi-based SMA showing ⟨011⟩ type II twins, taken from [144] with kind permission. The martensite twins appear in a parallel band-like structure, where each band contains one specific martensitic variant. The width of the individual bands is about 10-50 nm.

lattices of initial and final phases [22]. Moreover, the interface between two twins—or rather the plane separating two twinned martensite regions—is referred to as midrib plane or midrib region, as elaborated in, e.g., [117].

The microstructure evolution of polycrystalline NiTi under mechanical loading can be observed with electron microscopy. For example, in situ observation of stress-induced martensitic transformations accompanied by plastic deformations is carried out in [70] with the help of transmission electron microscopy (TEM). Moreover, macroscopic material anisotropy regarding the stress-strain response of SMA as a result of texture effects in cold-drawn NiTi sheets is investigated in [81]. The TEM observations provided therein show that the ⟨011⟩ type II twins evolve predominantly during deformation. Crystallographic analysis furthermore shows that the shear direction of the different martensite twin variants relative to the macroscopic loading direction differs, i.e. martensite twins of different types show different deformation behaviour.

A more macro-scale investigation of the transformation behaviour of SMA is carried out in [116], where the inhomogeneous deformation of SMA strips under uniaxial tension is studied. The initially austenitic material shows nucleation of martensite in sharp bands that can be observed by optical microscopy. As a result of mechanical loads, the evolution of a martensitic criss-cross pattern—comparable to Lüders bands in steels—is observed. These results are supported by the use of a thermal camera that captures the latent heat release during transformation at the same time.

In line with [116], the correlation between the grain microstructure—associated to martensitic variants—and the mechanical material response on the macro-scale has been studied in [25] for polycrystalline NiTi specimens. Macroscopic photographs of the transformation surface in combination with optical microscopes for the detection of meso-scale surface structure changes are used and the results are related to the macroscopic strain

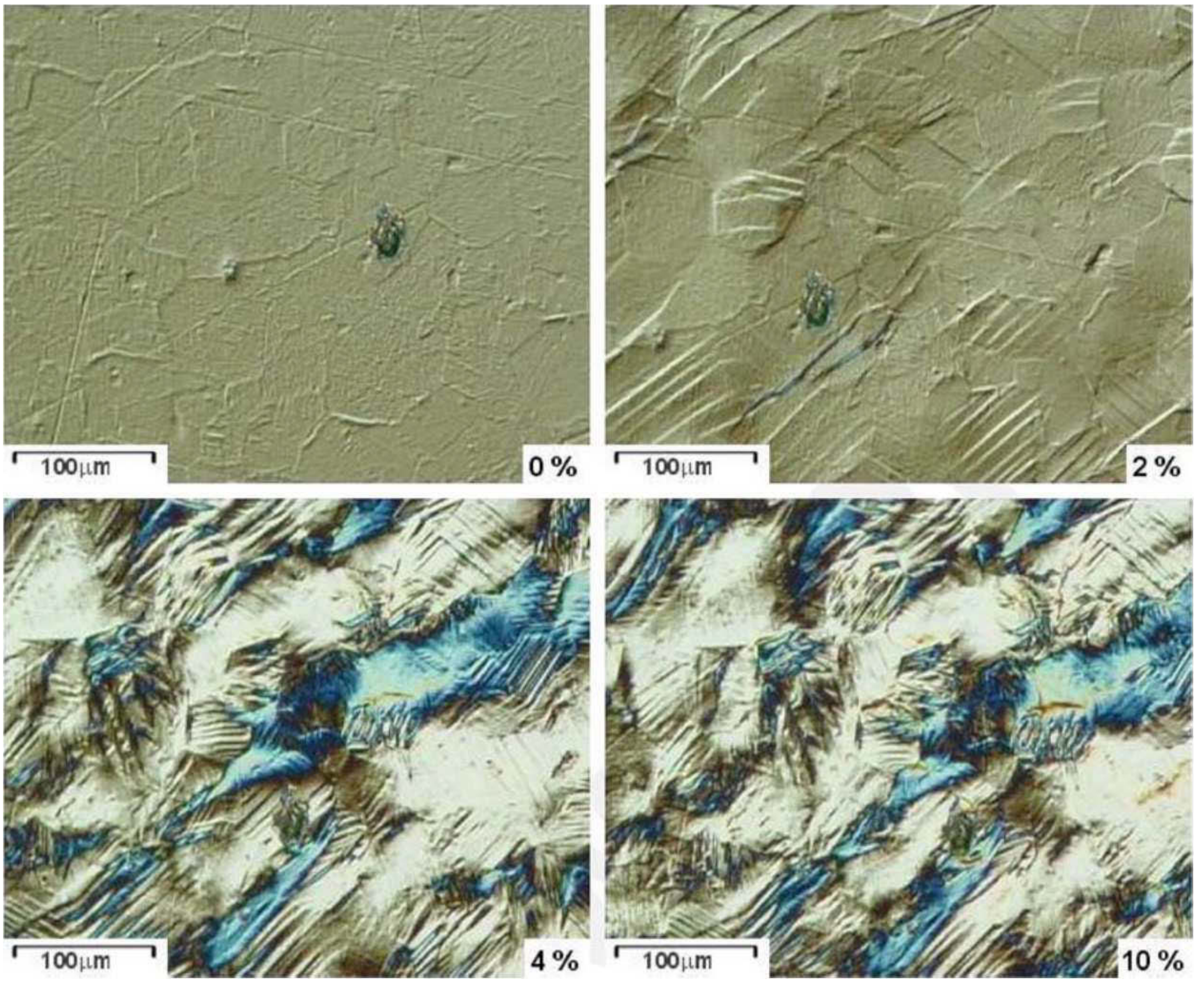

Figure 1.2: Microscopic images of a uniaxially stretched polycrystalline NiTi-based SMA specimen at strain levels of 0%, 2%, 4%, and 10%, respectively, taken from [25] with kind permission. In the last image, the full transformation point is already reached, whereas the microstructure indicates that the martensitic volume fraction is at most 60% as a result of so-called variant locking induced by sequential grain transformation. The variant locking that avoids 100 % martensite transformation in polycrystals is a critical effect that has to be captured by the micro-mechanical modeling of phase-tranformations in polycrystals.

of the tensile test specimen. It is shown that the martensite transformation concentrates in the macroscopically visible transformation bands on the specimen surface. However, at the same time it is shown that martensitic transformations occurs throughout the material at all strain levels. Thus, the observed macroscopic bands are regions of intense martensite transformation, but the areas outside these bands can by no means be considered as martensite-free.

Several different mechanisms exist for the growth and deformation of martensite even in the case of simple monotonic tension. In fact, the growth and deformation of martensite within the stress plateau of the stress-strain diagram can either result from stress-induced growth of favourably oriented martensite variants, from stress-induced reorientation of martensite, or from stress-induced twin boundary motion. It is important to note that NiTi-based SMA transforms from cubic austenite to monoclinic martensite either directly or via an intermediate rhombohedral phase, the so-called R-phase. The intermediate R-phase is not discussed in this work—for details, the reader is referred to, e.g., [119] and the references cited therein.

As for all metals, the alloy composition by means of alloy components and mass percentages as well as the annealing process highly influences the resulting microstructure and thus the behaviour of the material. Note that the alloy component concentration is connected to the phase equilibrium temperatures in a non-linear manner as shown in [46]. Moreover—depending on annealing temperature, annealing time and cooling method—the austenite start and finish and martensite start and finish temperatures can be modified, enabling the production of SMA that is either stable in an austenitic, a martensitic or a mixture phase at room temperature.

Regarding the mechanical response during tensile deformation, a sharp rise in the macroscopic specimen stress indicates that the end of transformation has been reached. However, it is important to note that a polycrystalline, initially purely austenitic specimen does generally not transform to 100 % martensite. On the one hand, unfavourably oriented grains might not transform at all, and on the other hand even favourably oriented grains usually only transform partially—as reported in [25], the sequencial transformation behaviour of individual grains can lead to so-called variant or grain locking. Precisely speaking, the onset of transformation in one grain changes the stress state in the local surrounding area, which thus affects the stress state within a neighboured grain. If the stress state in the neighboured grain was a favourable one and the grain therefore transformed, the sudden change into an unfavourable stress state can then start to hinder further transformation, cf. Fig. 1.2.

For multiple mechanical load cycles, experimental results show that lattice defects develop as for example shown in [83, 144]. Here, the accumulation of dislocations inside twin plates and at the junction plane area is investigated with the help of bright-field micrographs in connection with SAD pattern analyses. The effects of cycling on the stress-strain response of NiTi-based SMA can also be observed on the macro-scale, as the starting stress for transformation as well as the cycle hysteresis decreases, whereas the slope of the transformation plateau simultaneously increases [25].

One macroscopic key feature of SMA is the temperature-dependent pseudo-elastic or pseudo-plastic material response, respectively [50]. For elevated temperatures, SMA behaves pseudo-elastically as shown in Fig. 1.3. For low temperatures, a pseudo-plastic stress-strain behaviour—i.e. a non-zero remaining strain at zero stress—is observed. Moreover, the macroscopic stress-strain behaviour of SMA shows an asymmetry under tension and compression as elaborated in [82].

Regarding the macroscopic elastic properties, it can be shown that the Young's modulus of the austenitic phase in NiTi-based SMA takes a value of around 70 GPa, whereas the martensitic phase has a Young's modulus of around 25 GPa as discussed in detail

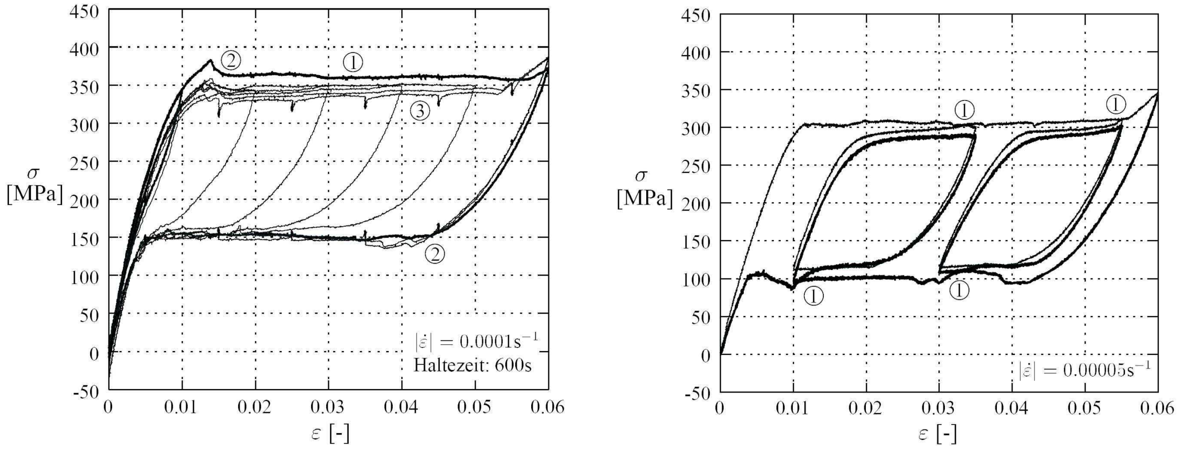

(a) Tension-compression step test resulting in a distinct stress-strain envelope [59].

(b) Stress-strain minor loops within an envelope obtained in a single-step experiment [59].

Figure 1.3: Experimental step tests on a NiTi shape memory alloy taken from [59] with kind permission. The experimental results show that the stress-strain response of the SMA material possesses a distinct envelope when tension-compression step tests are carried out in the pseudo-elastic range of the material, see (a) and also [60]. Moreover, experiments show that stress-strain minor loops are also enveloped by the stress-strain curve obtained from a single-step experiment (b). The micromechanically motivated material model presented in Chapter 3 captures these effects amongst others.

in [120]. As a result—in contrast to TRIP steels, where martensite is considered as the hard phase—in NiTi-based SMA the martensitic phase is generally considered as the softer phase.

1.1.2 Microstructure and mechanical properties of TRIP steels

Transformation Induced Plasticity (TRIP) steel is a steel alloy that shows excellent mechanical properties in terms of strength and ductility [71, 125, 126]. The "TRIP" effect describes the transformation from austenite to martensite accompanied by plastic deformation [148]. Since austenite is the high-temperature phase in steel that—under normal conditions—only exists in thermo-mechanical equilibrium at temperatures of more than 720°C, a special annealing process is required for the production of TRIP steel so that retained austenite is contained within the steel even at room temperature [36, 69].

For the production of a TRIP steel, the heated eutectoid steel is isothermally cooled to a temperature of about 400°C, where parts of the austenite form a bainitic ferrite phase, because the so-called intercritical annealing process [113, 114, 150] that takes place favours the formation of ferrite [26, 44]. In a normal steel, the excess carbon resulting from this annealing process starts to form a cementite phase with high carbon content. To prevent this, a TRIP steel has small amounts of added silicon, aluminium and manganese [147] alloy components that prevent the formation of cementite, leading to a diffusion of the excess carbon atoms into the remaining austenite phase. After a

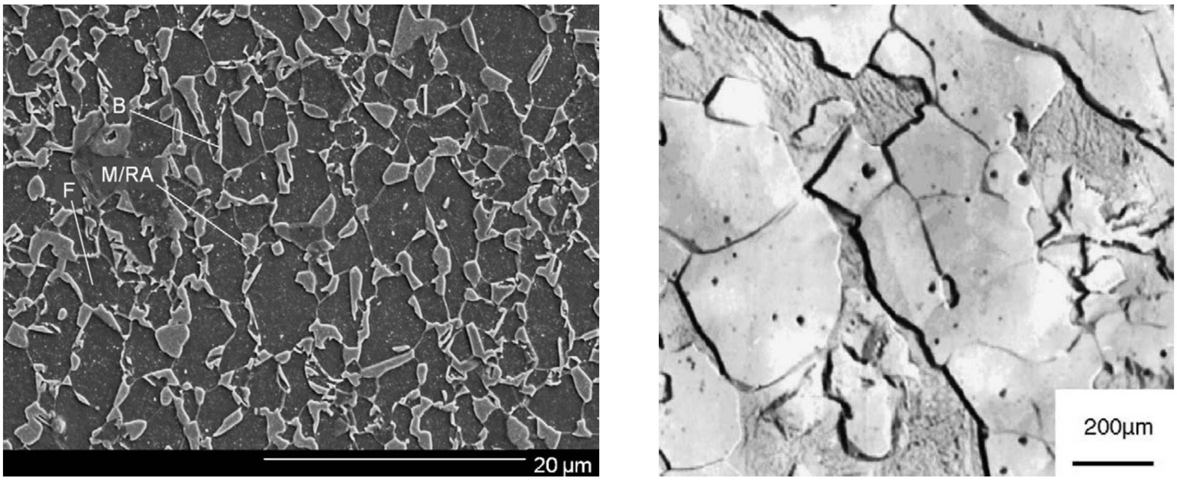

(a) Micrograph of TRIP steel with an equiaxed ferrite matrix microstructure. Highlighted is ferrite (F), bainite (B), and martensite/retained austenite (M/RA). Taken from [33] with kind permission.

(b) Homogeneously distributed retained austenite occurring as isolated particles in the ferrite matrix or in connection with bainite regions. Taken from [121] with kind permission.

Figure 1.4: TRIP steel micrographs obtained using scanning electron microscopy (SEM) (a) and transmission electron microscopy (TEM) (b), respectively.

sufficiently high carbon content within austenite is reached, the austenitic phase becomes stable even at room temperature [80]. As a result of this production process, the obtained TRIP steel is mainly composed of ferrite, bainite and retained austenite with high carbon content [67].

The high strength and ductility of TRIP steel results from the fact that the retained austenite is finely dispersed in the ferrite and bainite phases, see Fig. 1.4(b). Therefore, the high-carbon—and thus brittle—martensite that forms during phase-transformation is embedded in the matrix material consisting of a ductile ferrite and a harder bainite phase. This arrangement and combination of phases is the basis for the high ductility and strength observed for TRIP steels. Another characteristic property of TRIP steels is their very stable and continuous work hardening that is observed in experiments as demonstrated in Fig. 1.5.

A detailed characterisation of the microstructures in TRIP steel by means of optical microscopy, scanning electron microscopy and transmission electron microscopy is given in, e.g., [143], where electrical resistance measurement and tensile tests lead to the conclusion that the retained austenite exhibits good thermodynamical stability. Moreover—in view of the technical application of TRIP steels—it is shown that TRIP steel shows a transition temperature from stress-induced martensitic transformation to strain-induced martensitic transformation at about $-5\,^{\circ}\mathrm{C}$, i.e. at room temperature the strain-induced martensite transformation is predominant.

The particular effects of added manganese, silicon and niobium alloy components on the transformation behavior of TRIP steel are investigated and discussed in [9] based on mechanical tensile and dilatation tests. One important conclusion is the fact that manganese acts as a stabilising element in the austenitic phase, where a certain optimum value of manganese content within the steel was identified. If the manganese content exceeds this value, the ferrite transformation taking place during the cooling process is delayed, thus leading to a decrease of soluble carbon which induces a destabilisation of the retained austenite.

The influence of different thermo-mechanical processing conditions of low-alloy TRIP steel on subsequent phase-transformation behaviour is investigated in [121]. To this end, high temperature deformation is applied, followed by isothermal holding in the bainite region and a subsequent cooling to room temperature. The resulting microstructure is characterised with the help of optical and electron microscopy, and changes in the volume fraction of retained austenite are documented using X-ray diffractometers. The ferritic-bainitic fine-grained microstructure is investigated for different test specimen, facilitating the determination of the optimal thermo-mechanical processing scheme in view of the sought microstructural material properties, cf. Fig. 1.4(b).

Two distinct TRIP steel microstructures are common, namely equiaxed and lamellar structures. A TRIP steel microstructure with an equiaxed ferrite matrix refers to ferrite crystals that show approximately the same axes length. In contrast, a lamellar microstructure is composed of alternating crystallographic layers as introduced for NiTi-based SMA in Section 1.1.1. An investigation on the influence of equiaxed and lamellar TRIP steel microstructures on the transformation of austenite during uniaxial tension was carried out in [33]. To this end, both microstructures were produced by means of appropriate heat treatment conditions. In particular, the bainite hold time during annealing was varied in order to manipulate the volume fraction of retained austenite.

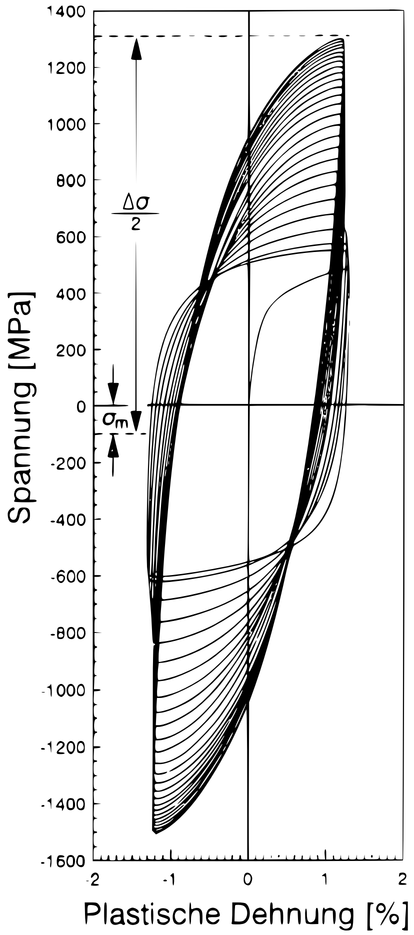

Figure 1.5: Cyclic stress response showing the characteristic work hardening of a metastable TRIP steel. Taken from [87] with kind permission.

Another characteristic property of a TRIP steel is the stability of the retained austenite phase, referring to its resistance to transformation with stress, strain, and temperature. In [33] it is noted that carbon is the most important stabilising element in view of strain resistance. For austenite grains with low levels of carbon—less than 0.6 wt.% C—the transformation is induced already at low levels of strain. In contrast, high levels of carbon—more than 1.8 wt.% C—prevent the austenite grains from transforming at all. However, there are further parameters that affect the austenite stability, such as the austenitic grain size and morphology and the elastic properties of the surrounding matrix material. For example, smaller grains of retained austenite are more stable under deformation due to their smaller number of martensitic nucleation sites.

Depending on the heat treatment, different morphologies of retained austenite can be obtained within TRIP steel. Usually, a two-stage heat treatment is applied, resulting in retained austenite that forms discrete particles between equiaxed ferrite grains, cf. Fig. 1.4. However, other heat treatment methods can either lead to thin layers of austenite or to a thicker lamellar-type morphology. The most important morphology of the retained austenite is given in terms of the isolated particles that are finely dispersed in the ferritic-bainitic matrix, cf. Fig. 1.4(b). Only this type of austenite morphology transforms to martensite during plastic deformation and therefore improves the mechanical material properties, whereas even for large plastic deformation no martensitic transformation is observed for austenite with a film-type morphology [121].

1.1.3 Modelling and simulation of phase-transformations

The reliability of phase-transformation simulations highly depends on the underlying material model. Due to the complex behaviour of materials undergoing phase-transformations—for example characterised by specific microstructure arrangements and twin formation—micromechanically motivated material models as developed by, e.g., [13, 35, 53, 55] can be regarded as most reliable.

Micromechanically motivated material models usually capture the behaviour of individual single-crystalline material domains—or rather individual grains of a polycrystal—which are commonly referred to as the micro-level. In consequence, micromechanically motivated material models are characterised by considering the microstructure of a material and its stress- or temperature-driven evolution. As shown in [10] and [24], in particular the kinematics of martensitic, i.e. diffusionless, solid-solid phase-transformations are characterised by homogeneous deformations of the crystal lattice. Thus, the transformation kinematics can be captured by so-called Bain-strains represented for example by the right stretch tensor $\boldsymbol{U}^{\text{tr}}$ in a continuum mechanical context, see [20, 68]. Apart from that, the material's microstructure can be approximately accounted for by matrix-inclusion homogenisation schemes as suggested in [32, 130, 131]. By means of appropriate homogenisation schemes, the computational results obtained at the micro-level can be transferred to the meso- and macro-level, where the material body and the acting loads are modelled in terms of a two or three-dimensional boundary value problem.

These matrix-inclusion homogenisation schemes approximate effective material properties for the phase mixture which are bounded by the Voigt and Reuss limits, respectively. In this regard, a promising method for the determination of a suitable effective material response is referred to as energy relaxation. The concept of energy relaxation is dedicated to the computation of the so-called quasiconvex energy hull of an underlying multi-well potential. It also offers the possibility to predict the energetically favorable arrangement of the underlying microstructure. For a comprehensive treatise on quasiconvex analysis the reader is referred to the works presented in [11, 37, 38, 97, 141] among others. Since the exact determination of this desired energy hull is only possible in rare cases, as shown in [41, 42, 72, 122], the quasiconvexification is mostly approximated by upper and lower bounds, see for example [30, 52, 53, 100, 107]. Similar approaches have also been introduced in [54–56, 124]. Recently, an extension of this concept has been presented in [13], where the deformations within each phase are directly derived from a superimposed displacement fluctuation field. Moreover, a distinction between elastic and dissipative internal variables is introduced therein in order to determine a well-suited energy hull as well as to take into account the hysteretic behaviour of shape memory alloys. In this context, the evolution of dissipative variables can be established by ordinary differential equations derived from inelastic potentials according to, e.g., [94, 95]. This model has also been extended to include plastic deformations in [15, 16].

The change of the crystalline structure from, e.g., austenite into martensite is always accompanied by a reduction of the crystallographic symmetry. Thus, several martensite variants have to be taken into account at the microscopic material scale. The coexistence of these phases is restricted to certain kinematical compatibility conditions which are reflected in rank-one connections between the deformations of each phase, cf. Fig. 1.1. Fundamental studies on this suject are provided in [12]. One major conclusion to be drawn from these investigations is the occurence of martensite twins in order to form compatible or, in other words, coherent interfaces between austenite and martensite as introduced in Section 1.1.1. This is exemplified in the so-called twinning equation from which exact solutions for the geometry of the microstructure and the respective volume fractions can be derived. This concept is frequently used for the modelling of martensitic phase transformations as for example shown in [21, 47, 65, 108].

The aforementioned micromechanically motivated models have in common that the optimum composition of the material is achieved by the minimisation of total energy and total power, respectively. In contrast, the models presented in [1–3, 18, 88] are based upon the derivation of driving forces directly acting on the phase front which propagates with a finite velocity depending upon the driving traction and the temperature.

A finite-strain multiscale model that considers the crystal lattice transformation from the austenitic cubic lattice to the martensitic tetragonal lattice is developed in [140], facilitating the simulation of the thermomechanical response of single-crystal grains of austenite. The formulation captures the interface between martensite and austenite by means of a surface energy term. Microstructural effects on subgrain length scales are incorporated and a pre-homogenisation is established by the computation of an anisotropic effective stiffness tensor at the grain level. A fully implicit time-integration scheme of the aforementioned model is elaborated in [128]. However, as introduced in Sections 1.1.1 and 1.1.2, for the multi-cyclic simulation of SMA and for the simulation of TRIP steels in general, coupling between phase-transformation and plasticity effects has to be considered.

For the simulation of austenitic-martensitic phase-transformations in steel, not only the plastic deformation of the matrix phase but also the damage growth in the evolving martensite phase is simulated in [129] in a three-dimensional finite-strain framework. The model is extended to a crystallography-based formulation in [134], where it is shown that the consideration of plasticity in the austenite phase is important for a realistic prediction of the overall response of the multi-phase material. Similar results are reported in [16, 45].

The influence of grain size on the macroscopic stress-strain response of a multi-phase steel is investigated in [139], where RVE-type finite element simulations of austenitic grains of different size within a ferritic matrix have been carried out. In line with experimental observations discussed in 1.1.2, it is observed that a smaller grain size of austenite leads to a higher transformation resistance. The relation between the relative orientation of the lattice of the austenitic inclusion with respect to the loading direction is investigated in [138], where it is shown that this relative orientation can indeed significantly influence the observed material response.

A crystal-plasticity model in the context of an RVE-type simulation approach is applied in [135]. Here, an elasto-plastic single-crystalline BCC ferrite matrix is considered, whereas austenitic inclusions are captured by a crystal-plasticity ansatz for FCC crystals coupled to a phase-transformation model. In line with experimental observations, cf. Fig. 1.5, the obtained numerical results capture—amongst other effects—a continuous work hardening of the effective stress-strain response. A crystal-plasticity based model formulation with particular focus on the release of latent heat during transformation and on its effect on the mechanical material response is provided in [145]. Here, a full thermo-mechanical coupling is considered, where the heat generation associated with martensitic phase-transformations and plasticity is accounted for in the energy balance relation. Moreover, the governing equations are solved monolithically in a fully implicit integration scheme.

The behaviour of larger RVEs—in terms of a larger amount of considered grains—is simulated in [146], where periodic boundary conditions applied to the RVE account for a consistent macroscopic material response. One important outcome of this work is the comparison between a ferritic RVE with randomly dispersed austenitic grains and an RVE that contains a film-type morphology of austenite. In line with the experimental findings reported in [121]—cf. Section 1.1.2—the micromechanically motivated simulations show that the film-type morphology of austenite diminishes the strengthening effect usually accompanied by martensitic phase-transformation in TRIP steel as a result of substantial plastic localisation in the ferrite matrix.

On an even smaller scale, molecular dynamics (MD) studies facilitate the analysis of nucleation behaviour and transformation kinetics in the context of thermally induced displacive phase-transformations. On this scale, the transformation behaviour is influenced by free surfaces, grain boundaries, crystal lattice defects, and of course the Brownian motion governed by the thermal initial conditions amongst other effects. In recent MD simulations provided in [127], the named factors are taken into account and analysed with respect to their influence on the transformation behaviour for different choices of the interatomic potential.

However, increased accuracy and physical plausiblity of such micromechanical models is commonly accompanied by an increase in computational effort. Although the use of micromechanically motivated models may, in particular, apply in view of light-weight structures and the modelling of the interaction between phase transformations and different micromechanical processes such as damage effects or plasticity phenomena, a comprehensive framework including all material scales from micro to macro is rather cumbersome and may lead to computationally inefficient simulation approaches when applied to the simulation of macroscopic workpieces.

Phenomenological approaches on the other hand are suitable for the computation of large macroscopic problems—for example in the context of finite element simulations. These approaches, as for example introduced in [8, 61, 111], are mainly based on thermodynamics-based frameworks. In addition to the first and second law of thermodynamics, the concept of generalised irreversible forces and fluxes, as established in [137] amongst others, is used in order to derive evolution equations for the internal variables. An extension of the model proposed in [111] has been presented in [98] in terms of finite strains and a self-consistent Eulerian theory accounting for heat generation during phase-transformations.

As a result, phenomenological models can be used for efficient simulations of macroscopic workpieces. In general, such models include specific modelling parameters which need to be fitted to the experimentally observed response of the bulk material for particular loading paths; see Fig. 1.3 and, e.g., [58–60]. In the context of phase-transformations, phenomenological models are usually based on a classic plasticity-type approach. Early phenomenological models for SMA were formulated in a one-dimensional setting and restricted to simple tensile load cases [132]. Meanwhile, sophisticated phenomenological models have been established, as for example in [8, 61, 112]. In particular, approaches for the constitutive modelling of phase-transformations in single crystals can be found in, e.g., [52, 123] and [109]. Approaches for the modelling of SMA polycrystals are, e.g., elaborated in [78].

Statistical considerations resulting in transformation probabilities characterise another class of thermodynamical models—one of which is presented in this thesis. As for example elaborated in [2, 4, 5, 66, 99, 115], these models are based on multi-well

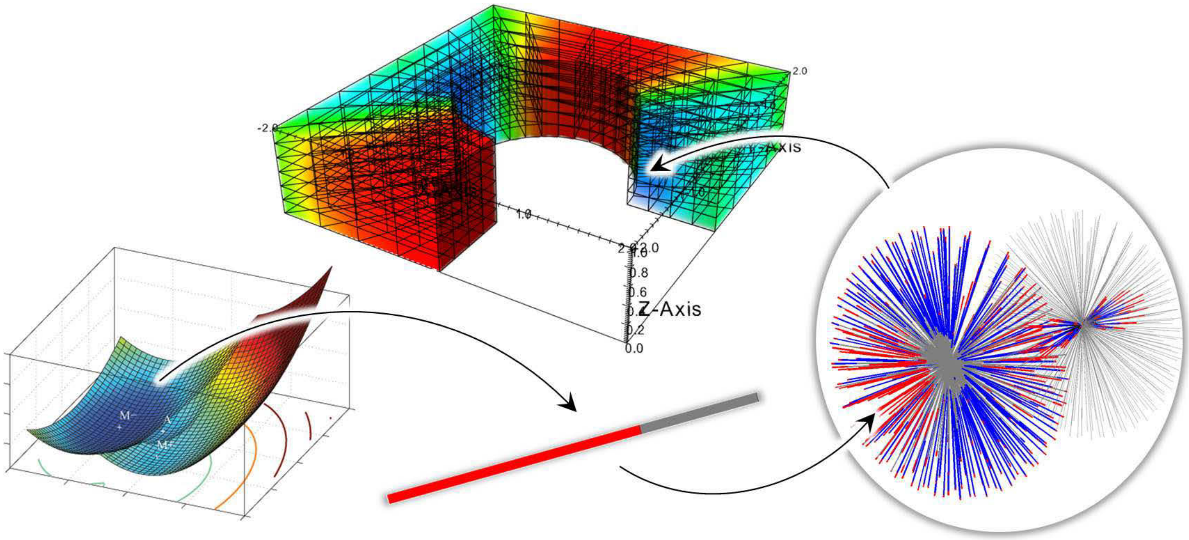

Figure 1.6: Overall multiscale scheme developed in the course of Chapters 2-6. A non-affine micro-sphere formulation for the simulation of the polycrystalline response is considered in each integration point of each finite element. Moreover, in each micro-sphere integration direction we derive individual evolution equations for the microscopic volume fractions and their corresponding, individual plastic strains. The evolution of volume fractions in each micro-sphere direction is based on the actual Gibbs energy barriers of the mixture which are obtained by numerical minimisation of implicit intersection curves of the unique, state-dependent elliptical Gibbs energy paraboloids assigned to each phase considered.

Helmholtz free energy potentials. The nucleation criteria are formulated in terms of energy barriers, which lead to statistically derived transformation probabilities governing—together with Boltzmann-based transition attempt frequencies, see e.g. [51]—the evolution of material phases.

1.2 Objective of this work

One objective of this work is to achieve a compromise between physical integrity and numerical efficiency. To this end, a scalar-valued phase transformation model is used at the lowest scale considered, adopting concepts from the works of [5, 51]. The underlying scalar-valued model is motivated by single-crystal considerations, where scalar transformation strains—related to Bain strains—and a tension-compression transformation-asymmetry are considered in Chapter 2. As an extension to Chapter 2, the scalar-valued strain of the micro-model is decomposed into deviatoric and volumetric parts in Chapter 3 in view of the subsequent implementation into a micro-sphere formulation according to [74] and [49, 91, 92]. This extension particularly affects the algorithmic determination of energy barriers which govern the evolution of phase fractions.

We use the micro-sphere formalism to approximate the material behaviour of a polycrystal consisting of a sufficiently large amount of single-crystals with a statistically homogeneous spatial distribution. In view of anisotropic elastic micro-sphere formula-

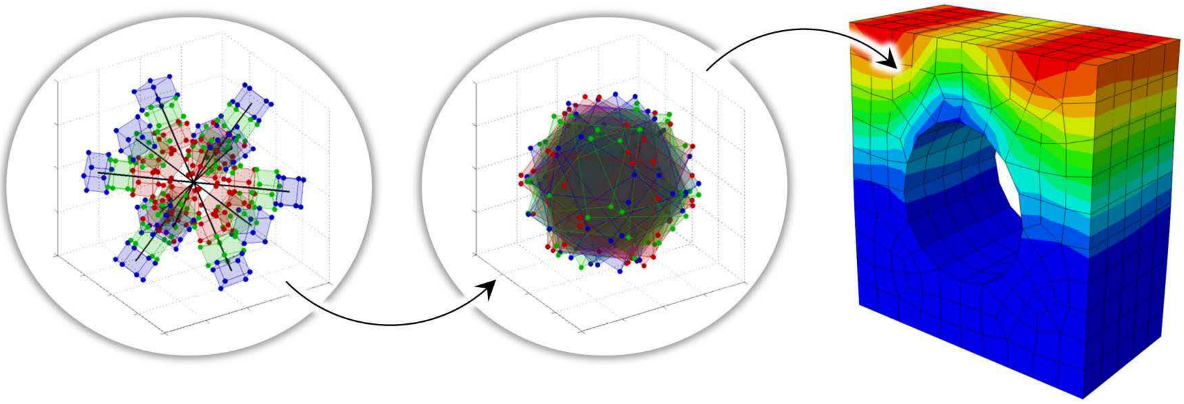

Figure 1.7: Overall multiscale scheme presented in Chapter 7. We implement the thermodynamically consistent model elaborated in [14], where phase-transformations between spatially arranged martensitic unit cells in an austenitic matrix are considered in a thermo-elastoplastic finite-strain framework. The individually evolving spatially oriented martensitic variants are pre-homogenised using the Voigt assumption, facilitating a subsequent convexification of the energy density of the martensitic-austenitic conglomerate in the logarithmic strain space.

tions, the reader is referred to [7] and [6]. Moreover, a coupled micro-sphere formulation is proposed in [133]. One advantage of the micro-sphere framework is its ability to derive texture-type structural tensors of different order, thus facilitating, e.g., the assessment of the anisotropy evolution within the material, see, e.g., [142]. Regarding the micro-sphere integration scheme, Chapter 6 shows that the use of 21 integration directions per hemisphere allows for an efficient yet sufficiently accurate computation of the material response at a meso-scale-type level, cf. [17, 74, 92].

To extend the micromechanically motivated material model for the simulation of phase-transformations in SMA presented in Chapters 2 and 3 to include the capture of TRIP steels, the interactions between simultaneously evolving plastic strains and phase transitions must be incorporated into the model. To this end, the underlying statistics-based model for the simulation of phase-transformations is coupled to plasticity in Chapter 4. The three-dimensional extension of the coupled model by means of a micro-sphere implementation is provided in Chapter 5. Finally, an extension to include a non-affine micro-sphere implementation of the coupled phase-transformation and plasticity model is presented in Chapter 6, showing that the coupled non-affine micro-sphere formulation developed in this work allows for a physically sound, micro-mechanically motivated simulation of shape memory alloys as well as TRIP steels, cf. Fig. 1.6. Throughout this work, for the TRIP models the focus is placed on the interactions between phase-transformations and plasticity in a polycrystalline aggregate consisting of austenite and martensite. For conceptual simplicity, these frameworks are referred to as “TRIP models”, even though the isotropic elasto-plastic ferrite matrix is neglected in this work.

In view of large deformation simulations of TRIP steels, an alternative modelling approach, taken from [14], is provided in Chapter 7. The approach follows a similar idea as do the previously considered micro-sphere formulations—however, we introduce tensor-valued quantities that are considered in each spatial crystal direction, and we restrict the formulation to *representative transformation directions* with the goal of providing a physically sound, thermodynamically consistent large-deformation thermo-elastoplastic framework for the simulation of phase-transformations in TRIP steel, cf. Fig. 1.7.

2 An affine micro-sphere model for phase-transformations

In this chapter, an efficient model for the simulation of polycrystalline materials undergoing solid to solid phase transformations is presented. As a basis, a one-dimensional, thermodynamically consistent phase-transformation model is used. This model is embedded into a micro-sphere formulation in order to simulate three-dimensional boundary value problems. To solve the underlying evolution equations, a newly developed explicit integration scheme which could be proved to be unconditionally A-stable is presented. Besides the investigation of homogeneous deformation states, representative finite element examples are discussed. It is shown that the model reflects the overall behaviour of shape memory alloys.

The contribution presented in this chapter aims at the formulation of a thermodynamically consistent model based upon transformation probabilities which is embedded into a numerically efficient global algorithm. Note that the micro-sphere model presented in this chapter is—for the linear elastic case—restricted to a macroscopic Poisson's ratio of $\nu_{\mathrm{P}} = 1/4$, see Section 2.5.2 for a detailed discussion. An extension of the model to the common range of reasonable values for Poisson's ratio is presented in Chapter 3. The outline of the current chapter is as follows: In Section 2.1, an overview on the adapted one-dimensional material model presented in [51] is given. This model is based on a multi-well Helmholtz free energy density which is transformed into Gibbs functionals in order to determine load dependent energy barriers for the transformation from one phase to another. The energy barriers affect transformation probabilities according to [5]. Eventually, the evolution of phases is characterised by a vector-valued ordinary differential equation (ODE). One focal point of this contribution is the implementation of a newly derived numerical scheme called 'Modified Newmark Method' for the solution of the underlying ODE. In order to maintain the efficiency of the overall model, this method is chosen to be explicit. However, it can be shown to be unconditionally A-stable and hence is superior to other explicit schemes like the Forward Euler method. Another extension of the original model is reflected by the implementation of tension-compression asymmetry in terms of the stress-strain behaviour, which is captured by crystallography-based transformation strains. Finally, we elaborate on the response of the one-dimensional model subjected to prescribed scalar strains. Section 2.2 deals with the extension of the one-dimensional model to three dimensions. In order to avoid complex enhancements of the model described in Section 2.1, the three-dimensional behaviour of a polycrystalline aggregate is carried out by the so-called micro-sphere approach. This technique is well-established in the context of computational inelasticity at small strains [28, 75, 76] as well as for the modeling of polymers, see [92, 93], and anisotropic biological tissues, see [6, 7, 89]. In Section 2.3, several numerical examples are elaborated. Firstly, the material behaviour of the micro-sphere under homogeneous deformations is discussed in detail. Secondly, we focus on the implementation of the micro-sphere model in the context of the finite element method and the results of a geometrically inhomogeneous macroscopic body under cyclic loading in terms of stresses and phase distributions, respectively. The chapter will be concluded by a short summary in Section 2.4.

2.1 One-dimensional, probabilistic phase-transformation model

The one-dimensional phase transformation model implemented in this work can handle an arbitrary amount of material phases. To be specific, we adopt the computational model for shape memory alloys provided in [51]. Here, the material is assumed to consist of ν phases, where the volume fraction

$$\xi^\alpha := \lim_{v \to 0} \left(\frac{v^\alpha}{v} \right) \tag{2.1}$$

of each phase $\alpha \in \{1, \dots, \nu\} \subset \mathbb{N}$ must fulfill the restrictions

$$\xi^\alpha \in \ [0,1] \subset \mathbb{R} \quad , \quad \sum_{\alpha=1}^{\nu} \xi^\alpha = \ 1 \quad , \quad \sum_{\alpha=1}^{\nu} \dot{\xi}^\alpha = \ 0 \quad , \tag{2.2}$$

wherein $\dot{\bullet}$ denotes the material time derivative. The validity of (2.2a) is evident, while (2.2b) and (2.2c) follow from the conservation of mass, as all phases are assumed to possess identical time-independent referential mass densities, i.e. $\rho^\alpha = \rho_0 = \text{const}$.

Each material phase is presumed to behave thermo-elastically, thus, according to [4], a Helmholtz free energy function $\psi^\alpha = \widehat{\psi}^\alpha(\varepsilon, \theta)$ of the form

$$\psi^\alpha = \frac{1}{2} \mathsf{E}^\alpha [\varepsilon - \varepsilon^\alpha_{\text{tr}}]^2 - \zeta^\alpha \mathsf{E}^\alpha [\varepsilon - \varepsilon^\alpha_{\text{tr}}][\theta - \theta_0] + \rho_0 c^\alpha_p \theta \left[1 - \log \left(\frac{\theta}{\theta_0} \right) \right] - \rho_0 \lambda^\alpha_T \left[1 - \frac{\theta}{\theta_0} \right] \tag{2.3}$$

can be assigned to each phase α, with E the Young's modulus, $\varepsilon = \nabla_x u$ the total strains, ε_{tr} the transformation strains, ζ the coefficient of thermal expansion, θ the current absolute temperature, θ_0 the reference temperature, c_p the heat capacity, and λ_T the latent heat of the respective material phase. The overall free energy $\varPsi = \widehat{\varPsi}(\varepsilon, \theta, \boldsymbol{\xi}) = \sum_\alpha \xi^\alpha \psi^\alpha$, with $\boldsymbol{\xi} = [\xi^1, \ldots, \xi^\nu]$, of the mixture is given by the free energy contributions of the respective constituents, whereby the distortional energy of the phase boundaries is neglected. Based on this, a Legendre-transformation can be carried out in order to obtain a Gibbs potential $G = \widehat{G}(\partial\varPsi/\partial\varepsilon, \theta)$, namely,

$$G = \varPsi - \left.\frac{\partial \varPsi}{\partial \varepsilon}\right|_\theta \varepsilon = \sum_{\alpha=1}^{\nu} \xi^\alpha \left[\psi^\alpha - \sigma\, \varepsilon\right] = \sum_{\alpha=1}^{\nu} \xi^\alpha g^\alpha \quad , \tag{2.4}$$

with $\sigma = \partial\varPsi/\partial\varepsilon|_\theta = \widehat{\sigma}(\varepsilon, \boldsymbol{\xi})$ being the stress acting in the one-dimensional continuum considered and $g^\alpha = \widehat{g}^\alpha(\sigma, \varepsilon, \theta) := \psi^\alpha - \sigma\, \varepsilon$ the contribution of phase α to the Gibbs potential G.

2.1.1 Kinematics of phase transitions

The approach of calculating the evolution of the volume fractions is based on statistical physics. Therefore a transformation probability matrix $\boldsymbol{Q} = \widehat{\boldsymbol{Q}}(\boldsymbol{\xi}) \in \mathbb{R}^{\nu\times\nu}$ can be introduced as shown in [51], facilitating the expression of the evolution of volume fractions as

$$\dot{\boldsymbol{\xi}} = \widehat{\boldsymbol{Q}}(\boldsymbol{\xi}) \cdot \boldsymbol{\xi} \quad . \tag{2.5}$$

Here, the transformation probability matrix takes the form

$$\boldsymbol{Q} = \omega \begin{bmatrix} -\sum\limits_{\alpha}^{\alpha\neq 1} P_{1\to\alpha} & P_{2\to 1} & \cdots & P_{\nu\to 1} \\ P_{1\to 2} & -\sum\limits_{\alpha}^{\alpha\neq 2} P_{2\to\alpha} & \ddots & \vdots \\ \vdots & \ddots & \ddots & P_{\nu\to\nu-1} \\ P_{1\to\nu} & \cdots & P_{\nu-1\to\nu} & -\sum\limits_{\alpha}^{\alpha\neq\nu} P_{\nu\to\alpha} \end{bmatrix} \neq \boldsymbol{Q}^{\mathrm{t}} \tag{2.6}$$

with ω the transition attempt frequency and $P_{\alpha\to\beta} = \widehat{P}_{\alpha\to\beta}(\theta, b_{\alpha\to\beta})$ the probability of a transformation of an arbitrary phase α to another phase β, where $(\alpha, \beta) \in [1, \ldots, \nu]^2$. Note that $\sum_i Q_{ij} = 0 \ \forall\ j$ guarantees that (2.2c) is fulfilled.

In particular, according to [5], the transformation probabilities can be obtained from

$$P_{\alpha\to\beta} = \exp\left(\frac{-\Delta v\, b_{\alpha\to\beta}}{k\,\theta}\right) \quad , \tag{2.7}$$

with k the Boltzmann's constant, Δv the (constant) transformation region's volume, θ the given temperature and $b_{\alpha\to\beta}$ the energy barrier for the transformation from phase α to phase β. Note that, in general, $b_{\alpha\to\beta} \neq b_{\beta\to\alpha}$ and thus $P_{\alpha\to\beta} \neq P_{\beta\to\alpha}$. The energy barriers are given by

$$b_{\alpha\to\beta} = \widehat{g}^{\alpha}(\sigma, \varepsilon^{\star}_{\alpha,\beta}, \theta) - \widehat{g}^{\alpha}(\sigma, \varepsilon^{\min}_{\alpha}, \theta) \tag{2.8}$$

with

$$\varepsilon^{\star}_{\alpha,\beta} = \inf_{g^{\alpha}, g^{\beta}} \left\{ \varepsilon \mid \widehat{g}^{\alpha}(\sigma, \epsilon, \theta)|_{\sigma,\theta} = \widehat{g}^{\beta}(\sigma, \varepsilon, \theta)|_{\sigma,\theta} \right\} \tag{2.9}$$

and

$$\varepsilon^{\min}_{\alpha} = \left\{ \varepsilon \mid \left. \frac{\partial \widehat{g}^{\alpha}(\sigma, \varepsilon, \theta)}{\partial \varepsilon} \right|_{\sigma,\theta} = 0 \right\} \quad . \tag{2.10}$$

Here, $\widehat{g}^{\alpha}(\sigma, \varepsilon^{\star}_{\alpha,\beta}, \theta) = \widehat{g}^{\beta}(\sigma, \varepsilon^{\star}_{\alpha,\beta}, \theta)$ represents the value of the energy potential at the intersection of the parabolic phase potential functions for two arbitrary material phases (α, β) in strain space, while $\widehat{g}^{\alpha}(\sigma, \varepsilon^{\min}_{\alpha}, \theta)$ represents the minimum energy potential of a particular phase α for fixed stresses and temperature.

The behaviour of the one-dimensional material model by means of the stress-strain-relation and the evolution of phase fractions for the material parameters provided in Table 2.1 is shown in Fig. 2.1. Here, a three-phase material with an austenitic parent phase is chosen. Furthermore, two martensite variants, in particular, one tensile variant and one compression variant, are assumed; see also Appendix 2.5.3. To illustrate the previously described relations, two different states of the energy potential parabolas depending on the acting stresses σ are illustrated in Fig. 2.2 for the investigated three-phase material.

2.1.2 Integration of the system of evolution equations

The solution of the strongly non-linear system of evolution equations (2.5), required to obtain an update of the internal variables, is traditionally carried out using classical implicit integration schemes in combination with Newton-type iterations. In contrast to that, in the current work a newly developed explicit integration scheme based on a modification of the Newmark integration method is applied. This method is based on the assumption, that the transformation rates of volume fractions $\dot{\boldsymbol{\xi}}$ proceed linearly within a time step $\Delta t = t_{n+1} - t_n > 0$, i.e. from state n to $n + 1$. This results in

$$\dot{\boldsymbol{\xi}}(\tau) = \frac{1}{\Delta t} \left[\dot{\boldsymbol{\xi}}_{n+1} - \dot{\boldsymbol{\xi}}_{n} \right] \tau + \dot{\boldsymbol{\xi}}_{n} \tag{2.11}$$

and accordingly

$$\boldsymbol{\xi}(\tau) = \frac{1}{2\,\Delta t}\left[\dot{\boldsymbol{\xi}}_{n+1} - \dot{\boldsymbol{\xi}}_n\right]\tau^2 + \dot{\boldsymbol{\xi}}_n\,\tau + \boldsymbol{\xi}_n \quad , \tag{2.12}$$

where the time coordinate $\tau = t - t_n > 0$ has been introduced. Inserting these relations into (2.5) without considering any Newmark parameters and setting $\tau = \Delta t$ yields

$$\dot{\boldsymbol{\xi}}_{n+1} = \left[\boldsymbol{I} - \frac{1}{2}\Delta t\,\widehat{\boldsymbol{Q}}(\boldsymbol{\xi}_n)\right]^{-1} \cdot \widehat{\boldsymbol{Q}}(\boldsymbol{\xi}_n) \cdot \left[\frac{1}{2}\Delta t\,\dot{\boldsymbol{\xi}}_n + \boldsymbol{\xi}_n\right] \tag{2.13}$$

as well as

$$\boldsymbol{\xi}_{n+1} = \frac{1}{2}\,\Delta t\left[\dot{\boldsymbol{\xi}}_{n+1} + \dot{\boldsymbol{\xi}}_n\right] + \boldsymbol{\xi}_n \tag{2.14}$$

where $\boldsymbol{Q}$ is assumed to be constant here and thus is evaluated invariably at time t_n. Here, $\boldsymbol{I} \in \mathbb{N}^{\nu\times\nu}$ denotes the second-order identity tensor. The transformation rates $\dot{\boldsymbol{\xi}}_n$ in the equations above are now consistently substituted by $\widehat{\boldsymbol{Q}}(\boldsymbol{\xi}_n) \cdot \boldsymbol{\xi}_n$, which eventually leads to

$$\boldsymbol{\xi}_{n+1} = \boldsymbol{\xi}_n + \frac{1}{2}\Delta t\left[\dot{\boldsymbol{\xi}}_{n+1} + \widehat{\boldsymbol{Q}}(\boldsymbol{\xi}_n) \cdot \boldsymbol{\xi}_n\right] \tag{2.15}$$

with

$$\dot{\boldsymbol{\xi}}_{n+1} := \left[\boldsymbol{I} - \frac{1}{2}\Delta t\,\widehat{\boldsymbol{Q}}(\boldsymbol{\xi}_n)\right]^{-1} \cdot \widehat{\boldsymbol{Q}}(\boldsymbol{\xi}_n) \cdot \left[\frac{1}{2}\Delta t\,\widehat{\boldsymbol{Q}}(\boldsymbol{\xi}_n) \cdot \boldsymbol{\xi}_n + \boldsymbol{\xi}_n\right] \quad . \tag{2.16}$$

Using this approach facilitates the solution of the presented system with high efficiency and at the same time high numerical stability—see Section 2.5.1 for detailed background information.

2.2 Application of the micro-sphere model

In this section, we show how the one-dimensional model is extended to three dimensions by embedding it into an affine micro-sphere framework. To this end, Section 2.2.1 provides a brief overview of the affine micro-sphere kinematics, i.e. we show how the scalar-valued micro-strains that serve as input value for the one-dimensional phase-transformation model are obtained from projections of the macroscopic strain tensor onto spatial directions $\boldsymbol{r}$. Subsequently, Section 2.2.2 summarises the micro-macro relations for the macroscopic stress tensor, macroscopic volume fractions and the macroscopic free energy of the material. Section 2.2.3 deals with the numerical evaluation of the aforementioned continuum relations.

Table 2.1: Material parameters used—compare, e.g., [20, 51]. The different transformation strains of the martensitic tensile and compression phase, $\varepsilon_{\mathrm{tr}}^{\mathrm{M_t}}$ and $\varepsilon_{\mathrm{tr}}^{\mathrm{M_c}}$ respectively, lead to an asymmetric behaviour in tension and compression as provided in Fig. 2.1(a).

SMA phase	material parameter	symbol	value
austenite A	Young's modulus	E^{A}	67 GPa
	transformation strain	$\varepsilon_{\mathrm{tr}}^{\mathrm{A}}$	0
	latent heat	λ_T^{A}	0
martensite $\mathrm{M_t}$ (tensile phase)	Young's modulus	$\mathsf{E}^{\mathrm{M_t}}$	26.3 GPa
	transformation strain	$\varepsilon_{\mathrm{tr}}^{\mathrm{M_t}}$	0.025
	latent heat	$\lambda_T^{\mathrm{M_t}}$	14500 J/kg
martensite $\mathrm{M_c}$ (compression phase)	Young's modulus	$\mathsf{E}^{\mathrm{M_c}}$	26.3 GPa
	transformation strain	$\varepsilon_{\mathrm{tr}}^{\mathrm{M_c}}$	-0.0675
	latent heat	$\lambda_T^{\mathrm{M_c}}$	14500 J/kg
common parameters	coefficient of thermal expansion	ζ	$12 \cdot 10^{-7}$ K^{-1}
	current temperature	θ	303 K
	reference temperature	θ_0	273 K
	heat capacity	c_p	400 J/kgK
	transformation region's volume	Δv	$2.71 \cdot 10^{-18}$ mm^3
	Boltzmann's constant	k	$1.381 \cdot 10^{-23}$ J/K

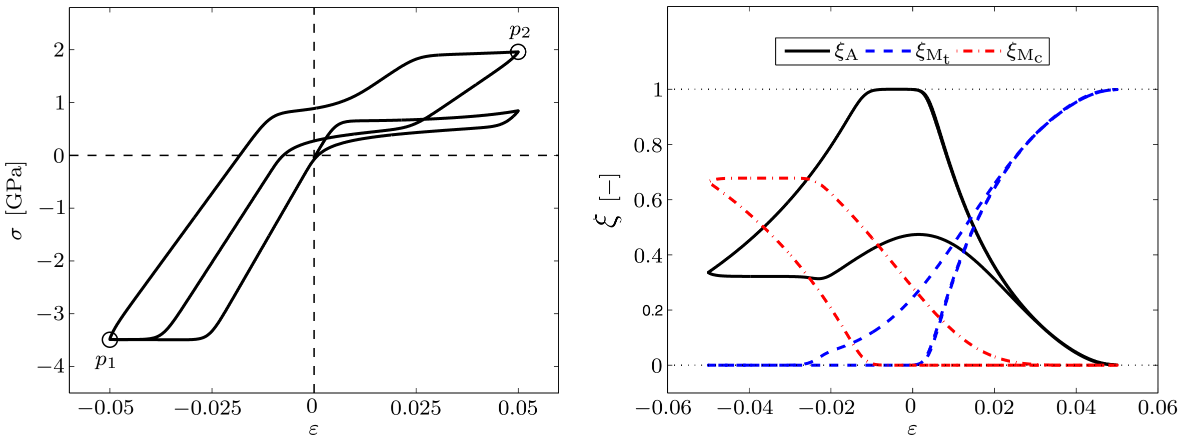

(a) Stress-strain diagram of the one-dimensional material model.

(b) Evolution of volume fractions.

Figure 2.1: Behaviour of the one-dimensional material model at a temperature of $\theta = 303\,\mathrm{K}$. Here, three different material phases, namely austenite A, a tension martensite variant $\mathrm{M_t}$, and a compression martensite variant $\mathrm{M_c}$, are considered, whereby the material was assumed to initially consist of pure austenite, i.e. $\xi_\mathrm{A}|_{t_0} = 1, \xi_{\mathrm{M_t}}|_{t_0} = \xi_{\mathrm{M_c}}|_{t_0} = 0$. The material parameters used are given in Table 2.1.

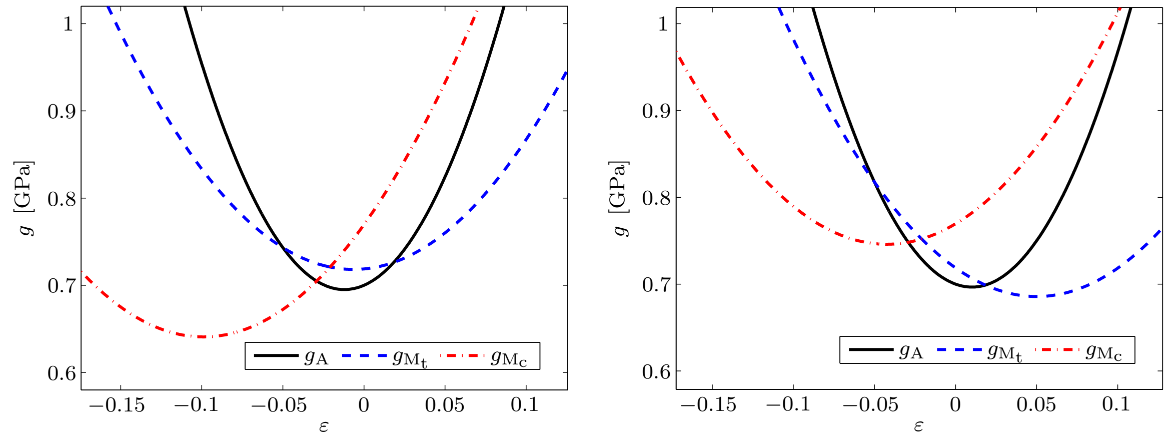

(a) Gibbs phase potentials at $\sigma \approx -3.5$ GPa, cf. state p_1 in Fig. 2.1(a).

(b) Gibbs phase potentials at $\sigma \approx 2$ GPa, cf. state p_2 in Fig. 2.1(a).

Figure 2.2: Evolution of the history-dependent Gibbs phase potentials g due to applied external strains. Depending on the stress acting within the one-dimensional continuum considered, the minima of the Gibbs potentials do not only take different values, but also different positions in strain space. At negative stresses and strains, the martensitic compression phase becomes energetically favorable, while at positive stresses and strains first the austenitic phase, and then the martensitic tensile phase evolves.

2.2.1 Kinematics

In order to generalise the one-dimensional phase-transformation model, a kinematically constrained micro-sphere approach is applied. In the context of kinematically constrained micro-sphere models, the one-dimensional micro-scale strains ε^{mic} are obtained using projections of the macro-scale strain tensor $\boldsymbol{\varepsilon}^{\text{mac}}$ with respect to the underlying integration directions, say $\boldsymbol{r} \in \mathbb{U}^2$. In particular, the vector $\boldsymbol{\varepsilon}^{\text{mac}} \cdot \boldsymbol{r}$ can be decomposed into two contributions, $\boldsymbol{\varepsilon}^{\text{mac}} \cdot \boldsymbol{r} = \boldsymbol{\varepsilon}^{\text{mac}}_r + \boldsymbol{\varepsilon}^{\text{mac}}_t$, where $\boldsymbol{\varepsilon}^{\text{mac}}_r = [\boldsymbol{r} \cdot \boldsymbol{\varepsilon}^{\text{mac}} \cdot \boldsymbol{r}]\boldsymbol{r}$ represents the strain in radial direction, while $\boldsymbol{\varepsilon}^{\text{mac}}_t = [\boldsymbol{I} - \boldsymbol{r} \otimes \boldsymbol{r}] \cdot \boldsymbol{\varepsilon}^{\text{mac}} \cdot \boldsymbol{r}$ yields the strain in the tangent plane of the considered surface point. Thus, the scalar-valued micro-strain ε^{mic}, which serves as an input parameter for the one-dimensional phase transformation model, can be computed with the help of

$$\varepsilon^{\text{mic}} = \widehat{\varepsilon}^{\,\text{mic}}(\boldsymbol{\varepsilon}^{\text{mac}}, \boldsymbol{r}) = \|\boldsymbol{\varepsilon}^{\text{mac}}_r\| = \boldsymbol{r} \cdot \boldsymbol{\varepsilon}^{\text{mac}} \cdot \boldsymbol{r} = \widehat{\varepsilon}^{\,\text{mic}}(\boldsymbol{\varepsilon}^{\text{mac}}, -\boldsymbol{r}) \quad . \tag{2.17}$$

The integration of quantities related to the micro-sphere can be surface- or volume-based. In general, the surface integral over the unit sphere yields

$$\int_{\mathbb{U}^2} \mathrm{d}a = 4\pi \quad , \tag{2.18}$$

while the volume integral results in

$$\int_{\mathbb{U}^2} \mathrm{d}v = \frac{4}{3}\pi \quad . \tag{2.19}$$

For symmetry reasons of the integration scheme adopted later on, it is sufficient to restrict the integration procedure to one unit hemisphere in the following.

2.2.2 Micro-macro-relations

The micro-macro-relations represent the scale bridging equations facilitating to establish connections between micro and macro quantities. Conceptually speaking, the macroscopic state of deformation is transferred to the micro-level by means of projecting $\boldsymbol{\varepsilon}^{\text{mac}}$ on ε^{mic}, while the macroscopic stresses $\boldsymbol{\sigma}^{\text{mac}}$—or rather the flux term of the macroscopic balance of linear momentum representation—is determined based on ε^{mic} and the related history, respectively microscopic volume fractions, $\boldsymbol{\xi}$. In view of the finite element simulations discussed later on, the macroscopic algorithmic tangent operator is additionally computed, namely $\mathrm{d}\boldsymbol{\sigma}^{\text{mac}}/\mathrm{d}\boldsymbol{\varepsilon}^{\text{mac}}$. The macroscopic stress tensor $\boldsymbol{\sigma}^{\text{mac}} = \widehat{\boldsymbol{\sigma}}^{\,\text{mac}}(\sigma^{\text{mic}})$ can be assembled from the scalar-valued stress responses $\sigma^{\text{mic}} = \widehat{\sigma}^{\,\text{mic}}(\varepsilon^{\text{mac}}, \boldsymbol{r}, \boldsymbol{\xi})$ of the underlying one-dimensional phase transformation model by means of

$$\boldsymbol{\sigma}^{\text{mac}} = \widehat{\boldsymbol{\sigma}}^{\,\text{mac}}(\sigma^{\text{mic}}) = \frac{1}{4\pi} \int_{\mathbb{U}^2} \sigma^{\text{mic}} \boldsymbol{r} \otimes \boldsymbol{r} \, \mathrm{d}a \quad , \tag{2.20}$$

which reflects the polycrystalline response at the macro level. Similarly, the fourth-order algorithmic tangent operator can be assembled based on the scalar-valued microscopic tangent moduli, $\partial\sigma^{\text{mic}}/\partial\varepsilon^{\text{mic}}$, according to

$$\frac{\mathrm{d}\boldsymbol{\sigma}^{\text{mac}}}{\mathrm{d}\boldsymbol{\varepsilon}^{\text{mac}}} = \frac{1}{4\pi}\int_{\mathbb{U}^2} \frac{\mathrm{d}\sigma^{\text{mic}}}{\mathrm{d}\varepsilon^{\text{mic}}}\,\boldsymbol{r}\otimes\boldsymbol{r}\otimes\boldsymbol{r}\otimes\boldsymbol{r}\,\mathrm{d}a \quad . \tag{2.21}$$

Moreover, the macroscopic volume fractions $\boldsymbol{\Xi} = \widehat{\boldsymbol{\Xi}}(\boldsymbol{\xi})$ as well as the macroscopic free energy density $\widehat{\Psi}^{\text{mac}}(\Psi^{\text{mic}})$ can be normalised with respect to the surface of the unit sphere and thus follow as

$$\boldsymbol{\Xi} = \frac{1}{4\pi}\int_{\mathbb{U}^2}\boldsymbol{\xi}\,\mathrm{d}a \quad \text{and} \quad \Psi^{\text{mac}} = \frac{1}{4\pi}\int_{\mathbb{U}^2}\Psi^{\text{mic}}\,\mathrm{d}a \quad , \tag{2.22}$$

respectively.

2.2.3 Numerical evaluation

Based on the known strain state following from the kinematically constrained—or rather affine—model, the micro-sphere integration procedure is carried out. The projection of the strain tensor $\boldsymbol{\varepsilon}^{\text{mac}}$ onto the integration directions $\boldsymbol{r}$ is computed using $\varepsilon^{\text{mic}} = [\boldsymbol{r}\otimes\boldsymbol{r}] : \boldsymbol{\varepsilon}^{\text{mac}}$. In particular, the integral relation for the macroscopic stress response $\boldsymbol{\sigma}^{\text{mac}}$, (2.20), can be approximated numerically via

$$\boldsymbol{\sigma}^{\text{mac}} \approx \frac{1}{4\pi}\sum_{i=1}^{n_r}\sigma_i^{\text{mic}} w_i^{\text{surf}}\,\boldsymbol{r}_i\otimes\boldsymbol{r}_i \tag{2.23}$$

with 4π the surface of the unit sphere and $w_i^{\text{surf}} = \widehat{w}_i^{\text{surf}}(n_r,\boldsymbol{r}_i)$ the surface elements of the unit sphere, i.e.

$$\lim_{n_r\to\infty}\widehat{w}_i^{\text{surf}}(n_r,\boldsymbol{r}_i) = \mathrm{d}a \quad , \tag{2.24}$$

and $\sum_i w_i^{\text{surf}} = 4\pi$. Note that the surface elements w_i^{surf} serve as weighting factors in (2.23) so that normalised weighting factors $\bar{w}_i$ can be introduced, i.e.

$$\boldsymbol{\sigma}^{\text{mac}} \approx \sum_{i=1}^{n_r}\sigma_i^{\text{mic}}\,\bar{w}_i\,\boldsymbol{r}_i\otimes\boldsymbol{r}_i \quad \text{with} \quad \bar{w}_i := \frac{1}{4\pi}w_i^{\text{surf}} \quad . \tag{2.25}$$

The algorithmic tangent operator $\mathsf{E}^{\mathrm{alg}} = \mathrm{d}\boldsymbol{\sigma}^{\mathrm{mac}}/\mathrm{d}\boldsymbol{\varepsilon}^{\mathrm{mac}}$ is based on the numerical approximation of (2.21), i.e.

$$\mathsf{E}^{\mathrm{alg}} = \sum_{i=1}^{n_r} \mathsf{E}_i^{\mathrm{alg}}\, \bar{w}_i\, \boldsymbol{r}_i \otimes \boldsymbol{r}_i \otimes \boldsymbol{r}_i \otimes \boldsymbol{r}_i \quad , \tag{2.26}$$

with $\mathsf{E}_i^{\mathrm{alg}} = \mathrm{d}\sigma_i^{\mathrm{mic}}/\mathrm{d}\varepsilon_i^{\mathrm{mic}}$.

Apart from the computation of the stress tensor and algorithmic tangent operator, the macroscopic free energy density $\varPsi^{\mathrm{mac}}$ can be calculated based on the microscopic free energy densities $\varPsi_i^{\mathrm{mic}} = \widehat{\varPsi}_i^{\mathrm{mic}}(\varepsilon_i^{\mathrm{mic}}, \theta, \boldsymbol{\xi}_i)$ of the underlying one-dimensional phase transformation model for each integration direction. Thus,

$$\widehat{\varPsi}^{\mathrm{mac}}(\varPsi^{\mathrm{mic}}) = \frac{1}{4\pi}\int_{\mathbb{U}^2} \varPsi^{\mathrm{mic}}\,\mathrm{d}a \approx \sum_{i=1}^{n_r} \varPsi_i^{\mathrm{mic}}\, \bar{w}_i \tag{2.27}$$

follows for the macroscopic free energy, and the numerical evaluation of (2.27) is facilitated using

$$\varPsi_i^{\mathrm{mic}} = \sum_{\alpha=1}^{\nu} \widehat{\psi}_i^{\alpha}(\varepsilon_i^{\mathrm{mic}}, \theta)\, \xi_i^{\alpha} \quad . \tag{2.28}$$

Accordingly, $\varPsi^{\mathrm{mac}}$ can finally be computed via

$$\varPsi^{\mathrm{mac}} = \sum_{i=1}^{n_r} \left[\sum_{\alpha=1}^{\nu} \widehat{\psi}_i^{\alpha}(\varepsilon_i^{\mathrm{mic}}, \theta)\, \xi_i^{\alpha} \right] \bar{w}_i \quad . \tag{2.29}$$

Analogously, the macroscopic volume fractions $\varXi^{\alpha} = \widehat{\varXi}^{\alpha}(\xi^{\alpha})$ can be obtained using

$$\varXi^{\alpha} = \sum_{i=1}^{n_r} \xi_i^{\alpha}\, \bar{w}_i \tag{2.30}$$

with ξ_i^{α} the volume fraction of phase α situated in the ith integration direction $\boldsymbol{r}_i$.

2.3 Numerical examples

In this section, the constitutive response under homogeneous deformations as well as finite element simulations are presented for the previously described model. In Sections 2.3.1 and 2.3.2, cyclic tension and compression is discussed for the non-deviatoric and deviatoric case. Finally, in Section 2.3.3 the results of a finite element implementation in terms of displacements, stresses and the distribution of phase fractions for two different load states are shown. Here and in the following, the microscopic Young's

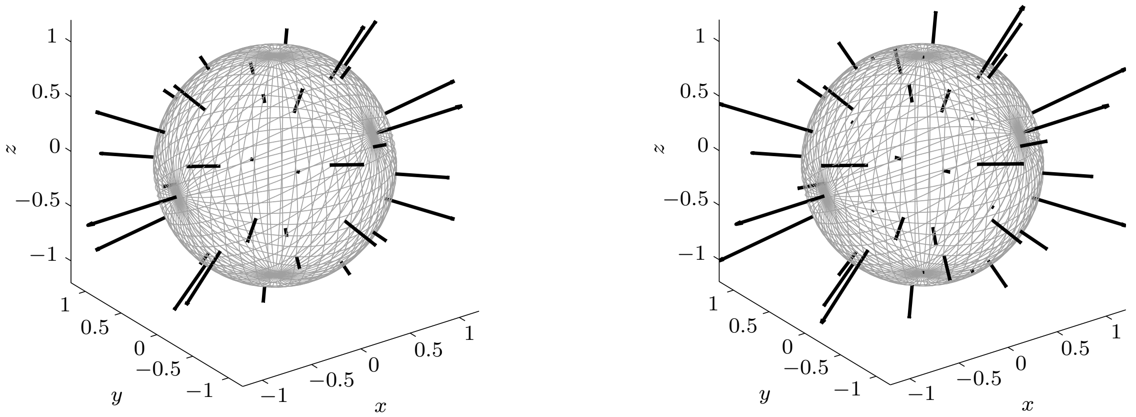

(a) Strain projections.

(b) Obtained micro-stresses.

Figure 2.3: Non-deviatoric tension-compression: micro-strains and according stresses obtained at maximum macroscopic strain, i.e. $\boldsymbol{\varepsilon}^{\text{mac}} = \varepsilon_0 \, \boldsymbol{e}_1 \otimes \boldsymbol{e}_1$. Note that the arrows are scaled linearly to obtain a maximum arrow length of 1.

moduli are adapted to obtain a mechanical response macroscopically identical for the case of isotropic linear elasticity with a Poisson's ratio of $\nu_{\text{P}} = 1/4$. In particular, the micro-moduli are multiplied by the factor 6, which is derived in Appendix 2.5.2. Furthermore, in the following the $\boldsymbol{e}_1$-direction is identified with the x-axis, while $\boldsymbol{e}_2$- and $\boldsymbol{e}_3$-directions are referred to the y- and z-axis, respectively. In view of the numerical integration scheme applied to the micro-sphere, a standard algorithm is adopted based on 42, respectively 21, integration directions; compare [17, 75, 92].

2.3.1 Non-deviatoric tension-compression

To investigate the behaviour of the material under homogeneous deformation, two characteristic tension-compression load cycles are studied in the following using identical material parameters as shown in Table 2.1. As initial conditions, a stress- and strain-free configuration of pure austenite, i.e. $\xi_{\text{A}}|_{t_0} = 1$, $\xi_{\text{M}_\text{t}}|_{t_0} = \xi_{\text{M}_\text{c}}|_{t_0} = 0$, is assumed. In the first case, the applied strain, prescribed by means of the macroscopic strain tensor $\boldsymbol{\varepsilon}^{\text{mac}} = \widehat{\boldsymbol{\varepsilon}}^{\text{mac}}(t)$, is set to

$$\widehat{\boldsymbol{\varepsilon}}^{\text{mac}}(t) = \widehat{\kappa}(t) \, \varepsilon_0 \, \boldsymbol{e}_1 \otimes \boldsymbol{e}_1 \tag{2.31}$$

with a linearly varying scaling factor $\kappa = \widehat{\kappa}(t) \in [-1, 1]$ and a maximum strain of $\varepsilon_0 = 0.05$. The resulting projections of the macroscopic strain onto each integration direction, $\varepsilon_i^{\text{mic}} \boldsymbol{r}_i$, as well as the obtained one-dimensional stresses, $\sigma_i^{\text{mic}} \boldsymbol{r}_i$, are shown in Fig. 2.3. As expected, the maximum strain is obtained in $\boldsymbol{e}_1$-direction, i.e. in x-direction. The projected strains decrease as the integration direction diverges from the x-direction.

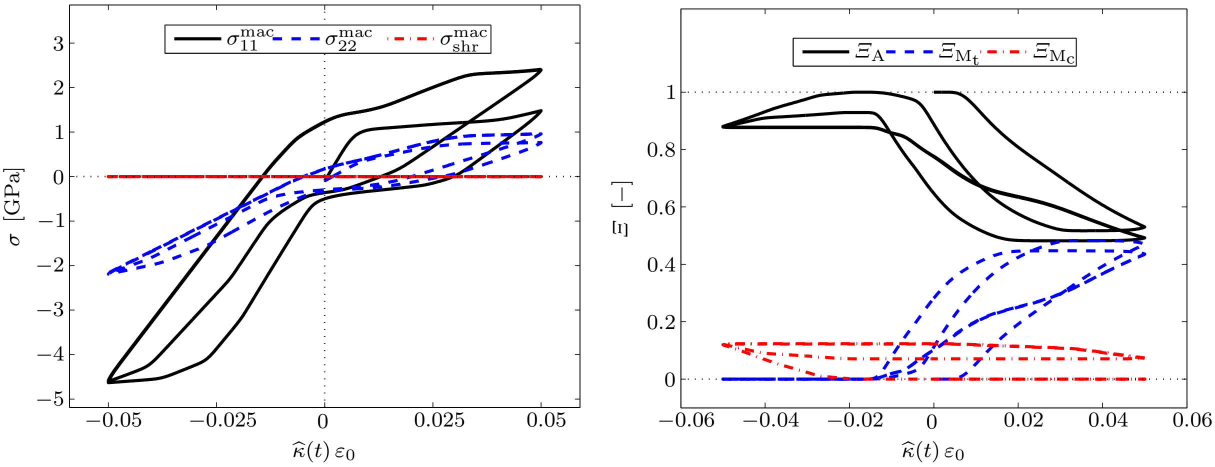

(a) Stress-strain diagram.

(b) Evolution of macroscopic volume fractions.

Figure 2.4: Non-deviatoric tension-compression: evolution of the macroscopic stress components as well as macroscopic volume fractions. Note that $\sigma_{22}^{\mathrm{mac}} = \sigma_{33}^{\mathrm{mac}}$ and $\sigma_{\mathrm{shr}}^{\mathrm{mac}} = \sigma_{12}^{\mathrm{mac}} = \sigma_{13}^{\mathrm{mac}} = \sigma_{23}^{\mathrm{mac}} = 0$ holds due to $\widehat{\boldsymbol{\varepsilon}}^{\mathrm{mac}}(t) = \widehat{\kappa}(t)\,\varepsilon_0\,\boldsymbol{e}_1 \otimes \boldsymbol{e}_1$ and the fact, that one integration direction $\boldsymbol{r}_i$ coincides with $\boldsymbol{e}_1$.

For all integration directions orientated perpendicular to the x-axis, i.e. situated in the y-z-plane, the strain projections are zero for all time steps.

The obtained macroscopic material response in terms of macroscopic stress components and macroscopic volume fractions are provided in Figs. 2.4(a) and 2.4(b), respectively. The stress-strain diagram shows that the macroscopic material point is subjected to an asymmetric tension and compression behaviour resulting from different martensitic transformation strains. The stress plateau obtained in the first tensile cycle results from the initiation of phase transformations. As the load reverses, hysteresis effects become obvious. The evolution of volume fractions taking place are given in Fig. 2.4(b), which shows that during the tensile cycle the martensitic tensile phase $\mathrm{M_t}$ evolves. As the load reaches the compression state, the martensitic compression phase $\mathrm{M_c}$ evolves and remains for all following tensile and compression cycles.

Finally, the different transformation intensities by means of directionally dependent phase fractions are displayed in Fig. 2.5. As expected, the maximum phase transformations are obtained in x-direction, while in the orthogonal y-z-plane no transformations are observed.

2.3.2 Deviatoric tension-compression

To investigate a different state of tension-compression, a homogeneous macroscopic strain tensor $\boldsymbol{\varepsilon}^{\mathrm{mac}} = \widehat{\boldsymbol{\varepsilon}}^{\mathrm{mac}}(t)$ with

$$\widehat{\boldsymbol{\varepsilon}}^{\mathrm{mac}}(t) = \widehat{\kappa}(t)\,\varepsilon_0\left[\boldsymbol{e}_1 \otimes \boldsymbol{e}_1 - \frac{1}{2}[\boldsymbol{e}_2 \otimes \boldsymbol{e}_2 + \boldsymbol{e}_3 \otimes \boldsymbol{e}_3]\right] \tag{2.32}$$

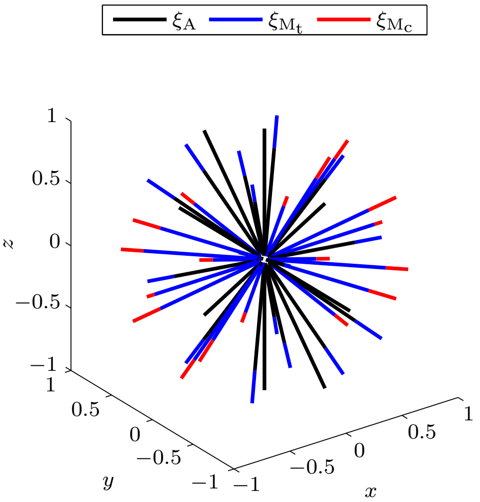

Figure 2.5: Non-deviatoric tension-compression: visualisation of the volume fractions of the underlying one-dimensional phase transformation model for the evaluated integration directions at $\widehat{\kappa}(t)\,\varepsilon_0 = 0.05$ after several load cycles. The material fractions in the orthogonal y-z-plane do not transform at all, i.e. $\xi_{\mathrm{A}}|_t = 1 \;\forall\, t$, since the projected one-dimensional strains are always zero in case of $\widehat{\boldsymbol{\varepsilon}}^{\mathrm{mac}} = \widehat{\kappa}(t)\,\varepsilon_0\,\boldsymbol{e}_1 \otimes \boldsymbol{e}_1$.

is prescribed. Once more, a linearly varying scaling factor $\kappa = \widehat{\kappa}(t) \in [-1, 1]$ and a maximum strain of $\varepsilon_0 = 0.05$ is chosen. The resulting projections of the macroscopic strain onto each integration direction as well as the obtained one-dimensional stresses are shown in Fig. 2.6. In contrast to the non-deviatoric case evaluated in Section 2.3.1, the strain projections in the orthogonal y-z plane are now negative.

The resulting macroscopic material response in terms of macroscopic stress components and macroscopic volume fractions is provided in Figs. 2.7(a) and 2.7(b), respectively. The stress drop of the normal stress $\sigma_{11}^{\mathrm{mac}}$, as observed at $\widehat{\kappa}(t)\,\varepsilon_0 \geq 0.025$, results from the evolution of the martensitic compression phase in the orthogonal y-z-plane; see Fig. 2.7(b).

As in the non-deviatoric case, the different one-dimensional transformation intensities at maximum tensile strains, i.e. at $\widehat{\kappa}(t)\,\varepsilon_0 = 0.05$, are shown in Fig. 2.8, whereby the particular state of deformation considered refers to a deformation path after several load cycles.

2.3.3 Rod under tension-compression

To investigate the behaviour of the material under inhomogeneous deformations, the constitutive model is embedded into a finite element formulation. The particular example studied consists of an axisymmetric specimen loaded under tension-compression. The geometry of the axisymmetric rod and the used finite element mesh are shown in Fig. 2.9. As depicted there, the bottom of the rod is constrained in axial direction, while on the top an axial displacement is imposed. Note that the displacements applied in the

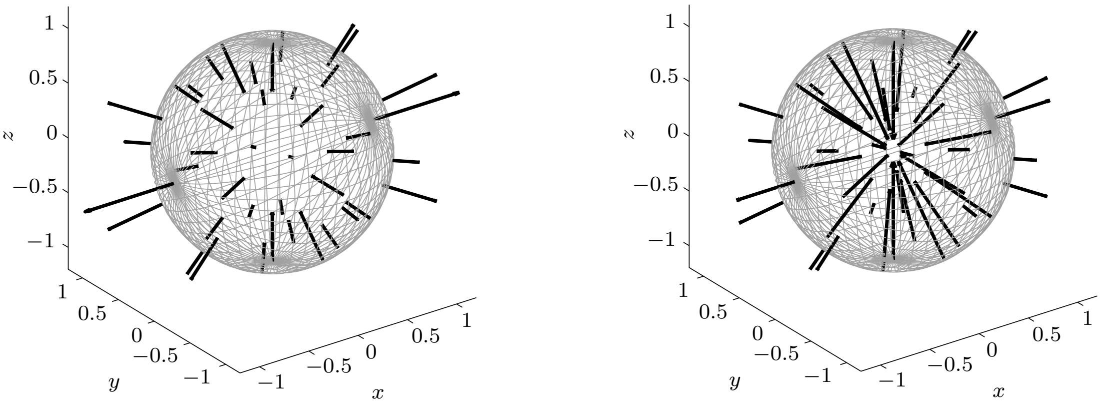

(a) Strain projections (b) Obtained micro-stresses

Figure 2.6: Deviatoric tension-compression: micro-strains and according stresses obtained for maximum macroscopic strain, i.e. for $\boldsymbol{\varepsilon}^{\text{mac}} = \varepsilon_0\,[\boldsymbol{e}_1 \otimes \boldsymbol{e}_1 - 1/2\,[\boldsymbol{e}_2 \otimes \boldsymbol{e}_2 + \boldsymbol{e}_3 \otimes \boldsymbol{e}_3]]$. As above, the arrows are scaled linearly to ensure a maximum arrow length of 1.

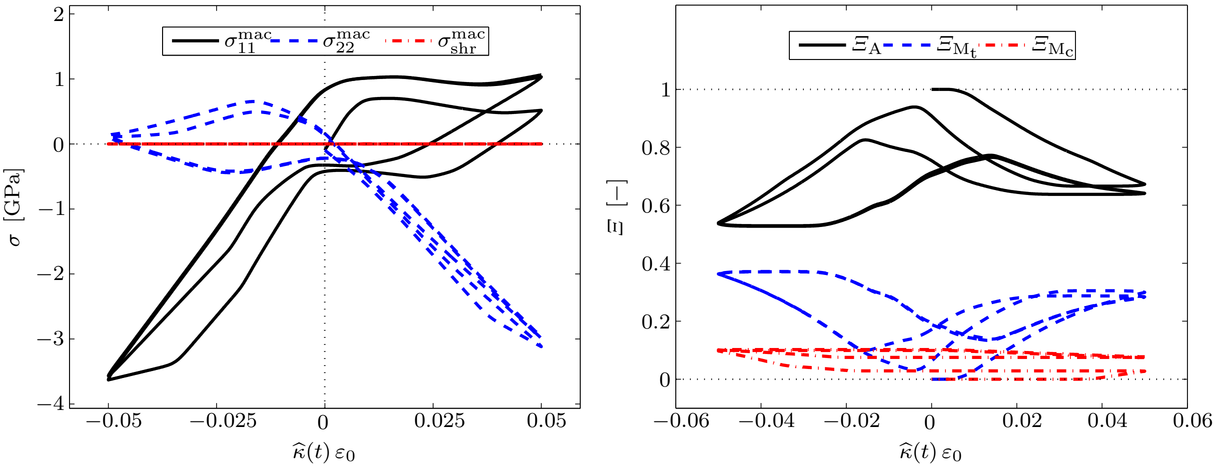

(a) Stress-strain diagram (b) Evolution of macroscopic volume fractions

Figure 2.7: Deviatoric tension-compression: evolution of the macroscopic stress components as well as macroscopic volume fractions. Note that $\sigma_{22}^{\text{mac}} = \sigma_{33}^{\text{mac}}$ and $\sigma_{\text{shr}}^{\text{mac}} = \sigma_{12}^{\text{mac}} = \sigma_{13}^{\text{mac}} = \sigma_{23}^{\text{mac}} = 0$ holds due to $\widehat{\boldsymbol{\varepsilon}}^{\text{mac}}(t) = \widehat{\kappa}(t)\,\varepsilon_0\,[\boldsymbol{e}_1 \otimes \boldsymbol{e}_1 - 1/2\,[\boldsymbol{e}_2 \otimes \boldsymbol{e}_2 + \boldsymbol{e}_3 \otimes \boldsymbol{e}_3]]$ and the fact, that one integration direction $\boldsymbol{r}_i$ coincides with $\boldsymbol{e}_1$.

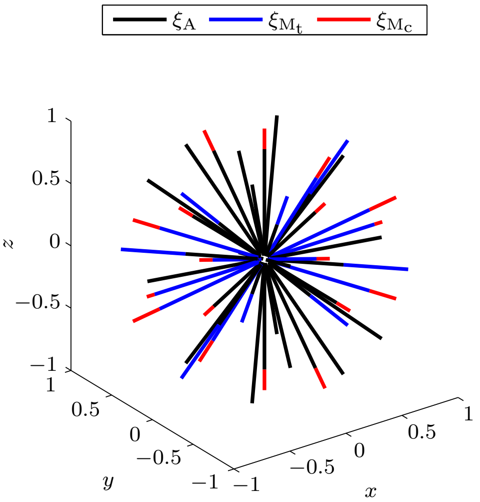

Figure 2.8: Deviatoric tension-compression: visualisation of the volume fractions of the underlying one-dimensional phase transformation model for the evaluated integration directions. In specific integration directions a complete transformation of the initially purely austenitic phase takes place, while in other directions no transformation occurs at all.

following refer to the center of the rod, as for symmetry resons, it is sufficient to take into account only one quarter of the cross-section of the double-symmetric rod. The overall height of the specimen is 100 mm while the center cross section has a diameter of 10 mm. Furthermore, the rod initially consists of pure austenite. It is then subjected to cyclic tension and compression as shown in the force-displacement diagram given in Fig. 2.10. Finally, for two characteristic load states, i.e. maximum tensile displacement and maximum compression displacement, the current material state by means of stresses and distribution of phase fractions is provided in Figs. 2.11-2.14.

First, Figs. 2.11 and 2.12 show the state of the specimen after the first tension cycle was applied, cf. point p_1 in Fig. 2.10. Fig. 2.11(a) provides a visualisation of the resulting vertical displacement field. As the figure shows, the maximum displacement is present at the center of the rod and decreases linearly within the cylindrical inner region of the specimen. As expected, the stress σ_{zz} in tensile direction coincides with the largest principal stresses, see Figs. 2.11(b) and 2.11(c). Due to the strains resulting from tensioning the specimen, the initially purely austenitic rod shows a martensitic tensile phase mainly evolving at the cylindrical inner region as provided in Figs. 2.12(a) and 2.12(b).

Next, the compression state of the rod—corresponding to the load state depicted by point p_2 in Fig. 2.10—is visualised in Figs. 2.13 and 2.14. Fig. 2.13(a) shows the resulting axial compression displacement field. Due to the previously applied tension cycle and the according material inhomogeneities caused by initiated phase transformations, the field of largest principal stresses displayed in Fig. 2.13(c) is now strongly inhomogeneous and shows a distinct deviation from the field of axial compression stresses presented in

Fig. 2.13(b). Fig. 2.14 shows that a martensitic compression phase evolved, while parts of the martensitic tensile phase remain within the material, cf. Figs. 2.14(c) and 2.14(b), respectively.

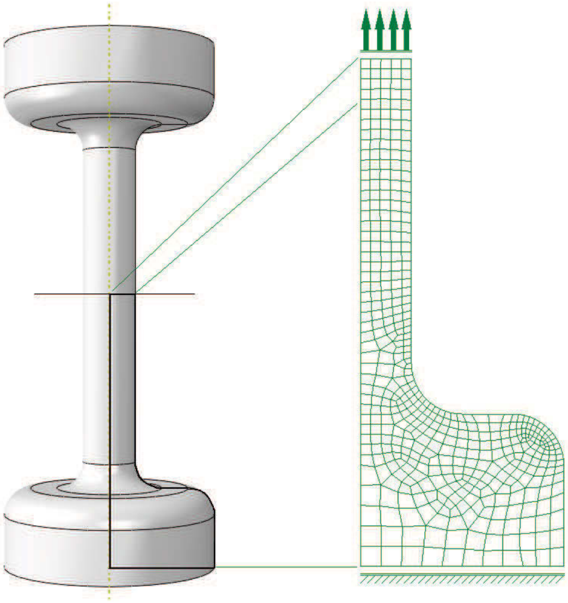

Figure 2.9: Rod under tension-compression: geometry of the investigated axisymmetric rod. For symmetry reasons, it is sufficient to take into account only one quarter of the cross-section. The bottom of the rod is constrained in axial direction, while on the top an axial displacement is imposed. For symmetry reasons, it is sufficient to prescribe axial displacements at the center of the rod.

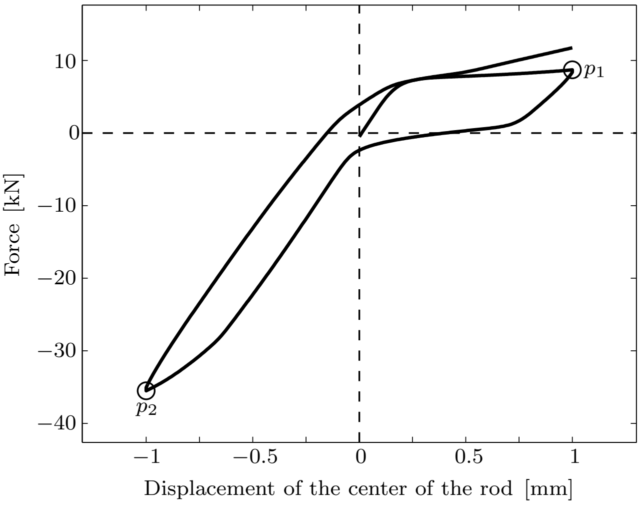

Figure 2.10: Rod under tension-compression: force-displacement relation obtained during the simulation of the tensile specimen. The macroscopic material response shows a distinct asymmetry regarding tension and compression behaviour. Note that the displacements refer to the center of the rod for symmetry reasons as described in Section 2.3.3.

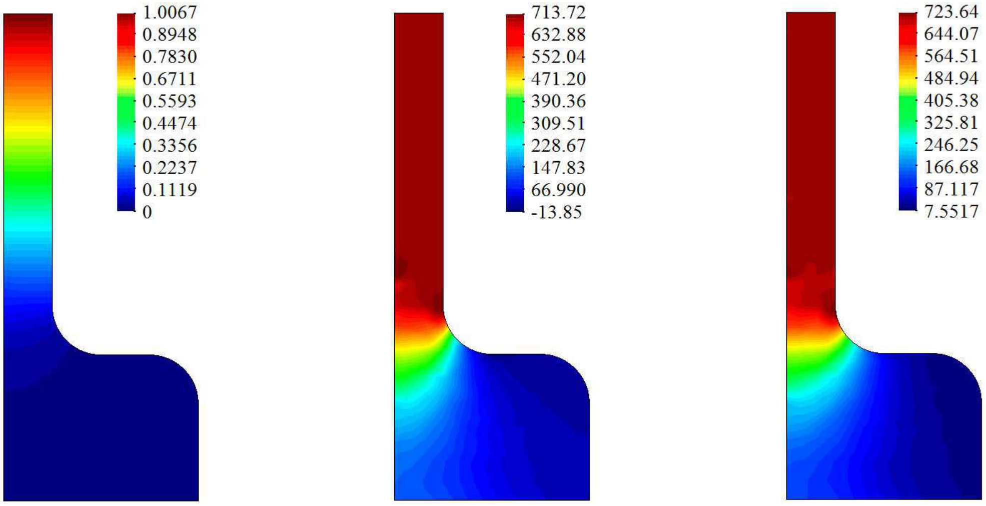
1.0067
0.8948
0.7830
0.6711
0.5593
0.4474
0.3356
0.2237
0.1119
0
713.72
632.88
552.04
471.20
390.36
309.51
228.67
147.83
66.990
-13.85
723.64
644.07
564.51
484.94
405.38
325.81
246.25
166.68
87.117
7.5517

(a) Axial, i.e. vertical, tensile displacement u_z [mm].

(b) Stress σ_{zz} [MPa] in tensile direction.

(c) Maximum principal stresses σ_I [MPa].

Figure 2.11: Rod under tension-compression: finite element displacements and stresses obtained for the rod at state p_1 in Fig. 2.10. Note that the rod was initially homogeneous and consisted of pure austenite. The obtained tensile stresses as well as the largest principal stresses, cf. (b) and (c), respectively, are distributed homogeneously within the rod after the first tensile load cycle.

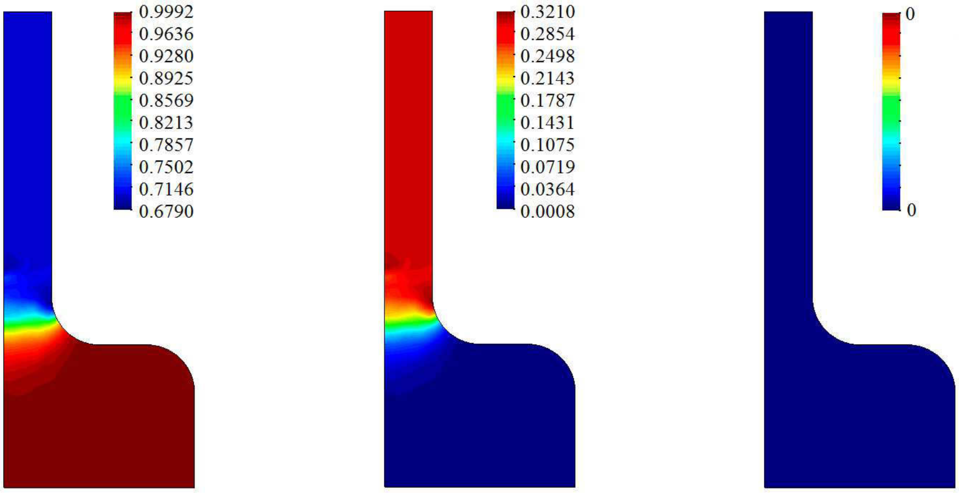
0.9992
0.9636
0.9280
0.8925
0.8569
0.8213
0.7857
0.7502
0.7146
0.6790
0.3210
0.2854
0.2498
0.2143
0.1787
0.1431
0.1075
0.0719
0.0364
0.0008
0
0

(a) Distribution of austenitic phase $\varXi_{\mathrm{A}}$ [−].

(b) Martensitic tensile phase $\varXi_{\mathrm{M_t}}$ [−].

(c) Martensitic compression phase $\varXi_{\mathrm{M_c}}$ [−].

Figure 2.12: Rod under tension-compression: volume fractions $\varXi$ present within the rod at state p_1 in Fig. 2.10. Due to the tension loading of the initially purely austenitic rod, the martensitic tensile phase $\mathrm{M_t}$ starts to evolve (b). As expected, the volume fractions $\varXi_{\mathrm{M_c}}$ of the martensitic compression phase remain zero (c).

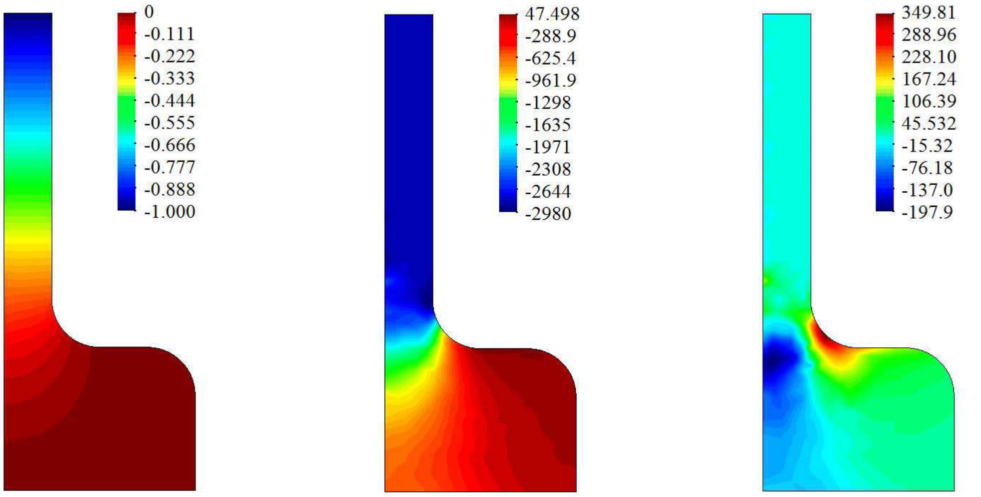

(a) Axial, i.e. vertical, compression displacement u_z [mm].

(b) Stress σ_{zz} [MPa] in compression direction.

(c) Maximum principal stresses σ_I [MPa].

Figure 2.13: Rod under tension-compression: finite element displacements (a) and stresses, (b) and (c), obtained for the rod at state p_2 in Fig. 2.10. As shown in Fig. 2.12, inhomogeneities evolved within the rod during tension as highlighted for the martensitic tensile phase at state p_1. As a result, the compression load at state p_2 leads to a strongly inhomogeneous distribution of largest principal stresses (c).

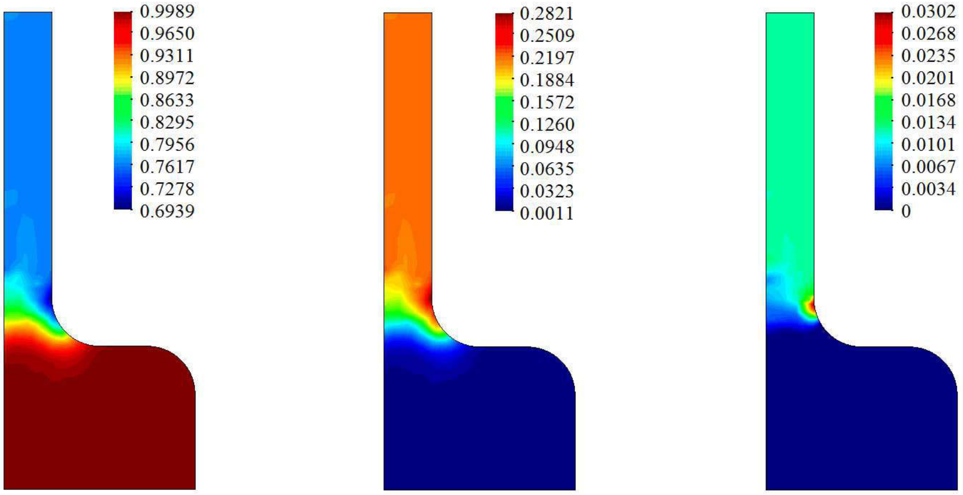

(a) Distribution of austenitic phase Ξ_A [−].

(b) Martensitic tensile phase $\Xi_{\mathrm{M_t}}$ [−].

(c) Martensitic compression phase $\Xi_{\mathrm{M_c}}$ [−].

Figure 2.14: Rod under tension-compression: volume fractions Ξ present within the rod at state p_2 in Fig. 2.10. Based on the phase fractions obtained at state p_1, see Fig. 2.12(b), the martensitic tensile phase fraction decreases (b). Instead, the martensitic compression phase starts to evolve (c).

2.4 Summary

The main goal of this chapter was to develop an efficient model for the micro-mechanical simulation of phase transformations in polycrystalline materials. Thus, a one-dimensional, thermodynamically consistent, micro-mechanically based constitutive law was chosen to model the basic phase transformation behaviour. In this model, an asymmetric tension-compression behaviour was incorporated by means of unique transformation strain values used for tension and compression, respectively. The transformation strains adopted are based on physically well-motivated Bain strains. The one-dimensional material model was then implemented into a micro-sphere ansatz, facilitating to prescribe three-dimensional strain states. To be specific, the macroscopic strain tensor was projected onto the different integration directions as referred to the micro-sphere. With the strain projections inserted into the underlying one-dimensional material model, the resulting one-dimensional stresses were assembled to a macroscopic stress tensor. Furthermore, the implementation into a finite element environment was carried out in order to study the constitutive model at inhomogeneous deformations. In this regard, the algorithmic tangent operator of fourth order was reviewed, as based on the micro-tangent operators obtained from the phase-transformation model.

The high numerical efficiency of the overall model was mainly achieved by introducing a newly developed explicit integration scheme which could be proved to possess the same numerical stability as the classical mid-point rule. With this integration scheme at hand, the strongly non-linear phase transformation problems present within the one-dimensional material model was solved in a single step for each macroscopic load increment applied. Thus, the exemplary finite element model presented in Section 2.3.3 consisting of 256 axisymmetric elements could be solved even for 1800 incremental displacement steps in 4 hours on a standard laptop computer. The presented integration scheme also provides good stability properties facilitating to solve the mentioned boundary value problem within, for instance, 100 time steps.

In summary, the results obtained show the capability of the present model for the efficient simulation of phase transformations. For simplicity, the model was restricted to a specific Poisson's ratio in the current chapter. As shown in Appendix 2.5.2, due to the nature of the strain projections, the mechanical response of the micro-sphere possesses a geometrically inherent Poisson's ratio of $\nu_{\mathrm{P}} = 1/4$. Furthermore, it could be shown that the micro-moduli have to be multiplied by a factor of 6 in order to obtain a desired macroscopic Hooke-equivalent material response. It is also important to note that the constitutive response depends on the chosen integration scheme over the micro-sphere as well as on the reference frame to which the particular orientations of the integration directions are referred to. In fact, this might also induce material anisotropy as a numerical artifact. However, as inherent to integration schemes in general, this effect tends towards negligible values upon refinement of the integration algorithm applied or, in other words, upon the use of higher-order integration schemes.

In particular, the extension of the one-dimensional model, for example in terms of additional phases, plasticity, damage and the thermomechanical coupling, respectively, reflect promising objectives. Moreover, the micro-sphere ansatz provides the possibility to account for texture and its evolution, respectively. This can be achieved by a non uniform distribution of integration directions which are allowed to change subjected to evolution equations or an additional weighting by an evolving orientation distribution function. The discrepancy of the micro-sphere ansatz exemplified by the fact, that computations are restricted to a fixed value for Poisson's ratio, needs to be compensated by a non-affine model as presented in Chapter 3.

2.5 Appendix

2.5.1 Numerical integration of the evolution equation

The evolution of different phases is, in this work, characterised by the vector-valued ordinary differential equation $\dot{\boldsymbol{\xi}} = \boldsymbol{f}\,(\boldsymbol{\xi}(t))$ with $\boldsymbol{f}\,(\boldsymbol{\xi}(t)) = \widehat{\boldsymbol{Q}}\,(\boldsymbol{\xi}(t)) \cdot \boldsymbol{\xi}(t)$. For the purpose of illustration of the numerical integration scheme proposed, in the following we—without loss of generality—refer to the case of a scalar-valued ordinary differential equation.

A typical ansatz for updating such ordinary differential equations from step t_n to t_{n+1} is given by

$$\xi_{n+1} = \xi_n + \Delta t\, f\,(\xi_n + \beta\,\Delta\xi) = \xi_n + \Delta t\, f\,(\xi_n + \beta\,\Delta t\,\kappa) \quad , \tag{2.33}$$

wherein $\beta \in [0,1] \subset \mathbb{R}$ reflects a general step size und use of the definition $\kappa := f\,(\xi_n + \beta\Delta\xi) = \Delta\xi/\Delta t$ has been made.

In order to assess stability properties of a numerical time integration scheme, the linear test function $\dot{\xi} = \lambda\,\xi$, for $\lambda < 0$, is consulted. In this case we observe

$$\kappa = \lambda\,[\xi_n + \beta\,\Delta t\,\kappa] \quad \text{so that} \quad \kappa = \frac{\lambda\,\xi_n}{1 - \beta\,\lambda\,\Delta t} \quad . \tag{2.34}$$

Together with the definition of κ, one obtains

$$\xi_{n+1} = \xi_n \left[1 + \frac{\lambda\,\Delta t}{1 - \beta\,\lambda\,\Delta t}\right] = \xi_n\, R(\lambda\,\Delta t) \quad , \tag{2.35}$$

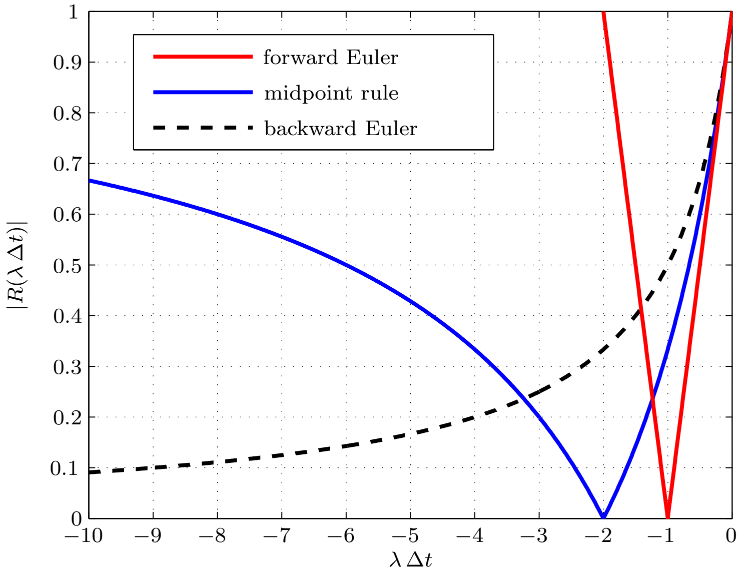

Figure 2.15: Absolute values of stability functions for the forward Euler method, midpoint rule and backward Euler method. The forward Euler scheme is only conditionally stable, both midpoint rule and backward Euler schemes turn out to be A-stable where only the latter is also L-stable.

wherein $R(\lambda\,\Delta t)$ denotes the so-called stability function. With this quantity at hand, conditions in terms of so-called A- and L-stability, respectively, can be stated as

$$|R(\lambda\,\Delta t)| \leq 1 \;\forall\; \lambda\,\Delta t \in [-\infty, 0[\qquad \rightarrow \quad \text{A-stability} \quad , \tag{2.36}$$

$$\lim_{\lambda\,\Delta t \rightarrow -\infty} R(\lambda\,\Delta t) = 0 \qquad \rightarrow \quad \text{L-stability} \quad . \tag{2.37}$$

For three standard time discretisation methods, namely forward Euler (‘FE’, $\beta = 0$), midpoint rule (‘MP’, $\beta = 0.5$) and backward Euler (‘BE’, $\beta = 1$), the stability functions are given by

$$R^{\mathrm{FE}} = 1 + \lambda\,\Delta t \quad , \qquad R^{\mathrm{MP}} = \frac{2 + \lambda\,\Delta t}{2 - \lambda\,\Delta t} \quad , \qquad R^{\mathrm{BE}} = \frac{1}{1 - \lambda\,\Delta t} \quad , \tag{2.38}$$

which are also depicted in Fig. 2.15.

As elaborated in section 2.1.2, the explicit update of volume fractions is given by

$$\boldsymbol{\xi}_{n+1} = \boldsymbol{\xi}_n + \frac{1}{2}\,\Delta t\,\left[\dot{\boldsymbol{\xi}}_{n+1} + \widehat{\boldsymbol{Q}}(\boldsymbol{\xi}_n)\cdot\boldsymbol{\xi}_n\right] \quad , \tag{2.39}$$

with

$$\dot{\boldsymbol{\xi}}_{n+1} := \left[\boldsymbol{I} - \frac{1}{2}\,\widehat{\boldsymbol{Q}}(\boldsymbol{\xi}_n)\,\Delta t\right]^{-1}\cdot\widehat{\boldsymbol{Q}}(\boldsymbol{\xi}_n)\cdot\left[\frac{1}{2}\,\widehat{\boldsymbol{Q}}(\boldsymbol{\xi}_n)\cdot\boldsymbol{\xi}_n\,\Delta t + \boldsymbol{\xi}_n\right] \quad . \tag{2.40}$$

By reducing (2.39) and (2.40) to the scalar case and setting $\lambda := Q(\xi_n)$—as the components of $\boldsymbol{Q}(\boldsymbol{\xi}_n)$ are constant during the iteration process to find $\boldsymbol{\xi}_{n+1}$—the incremental update can be rewritten as

$$\xi_{n+1} = \xi_n + \frac{1}{2}\,\Delta t \left[\left[1 - \frac{1}{2}\,\lambda\,\Delta t \right]^{-1} \lambda \left[\frac{1}{2}\,\lambda\,\xi_n\,\Delta t + \xi_n \right] + \lambda\,\xi_n \right] = \frac{2 + \lambda\,\Delta t}{2 - \lambda\,\Delta t}\,\xi_n \quad . \tag{2.41}$$

In fact, the stability function of the 'modified Newmark method' turns out to be identical to the one of the Mid-Point rule. Accordingly, this newly developed explicit intergation scheme is unconditionally A-stable.

2.5.2 On general properties of the affine micro-sphere approach

In this appendix, we elaborate on the general properties of the micro-sphere approach in the framework of three-dimensional linear isotropic elasticity. Provided that the underlying one-dimensional constitutive relation for each direction of the microsphere is given by $\sigma^{\text{mic}} = \mathsf{E}^{\text{mic}}\,\varepsilon^{\text{mic}}$, the effective response of the micro-sphere is transferred to the macro-level via

$$\boldsymbol{\sigma}^{\text{mac}} = \frac{1}{4\,\pi} \int\limits_{\mathbb{U}^2} \sigma^{\text{mic}}\,\boldsymbol{r} \otimes \boldsymbol{r}\;\mathrm{d}a = \frac{\mathsf{E}^{\text{mic}}}{4\,\pi}\,\boldsymbol{\varepsilon}^{\text{mac}} : \int\limits_{\mathbb{U}^2} \boldsymbol{r} \otimes \boldsymbol{r} \otimes \boldsymbol{r} \otimes \boldsymbol{r}\;\mathrm{d}a \quad , \tag{2.42}$$

with $\boldsymbol{r} \in \mathbb{U}^2$. The latter integral can be calculated analytically, which results in

$$\int\limits_{\mathbb{U}^2} \boldsymbol{r} \otimes \boldsymbol{r} \otimes \boldsymbol{r} \otimes \boldsymbol{r}\;\mathrm{d}a = \frac{4\,\pi}{15}\;[\boldsymbol{I} \otimes \boldsymbol{I} + 2\,\mathsf{I}^{\text{sym}}] \quad , \tag{2.43}$$

wherein $\boldsymbol{I}$ denotes the second-order identity tensor and I^{sym} characterises the fourth-order symmetric identity tensor. As a consequence, the substitution of (2.43) into (2.42) yields

$$\boldsymbol{\sigma}^{\text{mac}} = \frac{\mathsf{E}^{\text{mic}}}{15}\,[\text{tr}\,(\boldsymbol{\varepsilon}^{\text{mac}})\;\boldsymbol{I} + 2\,\boldsymbol{\varepsilon}^{\text{mac}}] \quad . \tag{2.44}$$

One possibility to pre-calibrate the micro-sphere model consists in its correlation to the case of linear isotropic elasticity—denoted by the superscript 'lie'—where the stresses are given as functions of strains by

$$\boldsymbol{\sigma}^{\text{lie}} = \frac{\mathsf{E}^{\text{lie}}}{[1 - 2\,\nu_{\text{P}}][1 + \nu_{\text{P}}]}\,[\nu_{\text{P}}\,\text{tr}(\boldsymbol{\varepsilon}^{\text{mac}})\,\boldsymbol{I} + [1 - 2\,\nu_{\text{P}}]\,\boldsymbol{\varepsilon}^{\text{mac}}] \tag{2.45}$$

with the macroscopic Poisson's ratio ν_P. By arguments of comparison—(2.44) and (2.45)—one obtains the relations

$$\nu_\mathrm{P} = \frac{15\,\mathsf{E}^\mathrm{lie} - 2\,\mathsf{E}^\mathrm{mic}}{2\,\mathsf{E}^\mathrm{mic}} \quad \text{and} \quad \frac{\nu_\mathrm{P}\,\mathsf{E}^\mathrm{lie}}{[1-2\,\nu_\mathrm{P}]\,[1+\nu_\mathrm{P}]} = \frac{\mathsf{E}^\mathrm{mic}}{15} \quad , \tag{2.46}$$

the solution of which is identified as

$$\mathsf{E}^\mathrm{mic} = 6\,\mathsf{E}^\mathrm{lie} \quad \text{and} \quad \nu_\mathrm{P} = \frac{1}{4} \quad . \tag{2.47}$$

2.5.3 Transformation strains of the martensite compression variant

In this work, two martensite variants, namely one tensile variant and one compression variant, are assumed. These are often chosen to be symmetric with respect to the initial state ($\sigma = 0, \varepsilon = 0$) and referred to as '+' and '−' phase. This ansatz may be motivated by the invariance of the lattice shear direction with respect to the so-called habit plane.

Here, we enhance the adapted model in terms of transformation strains motivated by crystallographic considerations. In three dimensions, so-called Bain strains can be derived due to the locally homogeneous deformations of the underlying crystal lattice following, e.g., [10]. These deformations allow representation in terms of a right Cauchy-Green stretch tensor $\boldsymbol{U}^\mathrm{tr}$, which we transfer to the geometrically linear case via $\boldsymbol{\varepsilon}^\mathrm{tr} = \boldsymbol{U}^\mathrm{tr} - \boldsymbol{I}$.

Next, let the one-dimensional transformation strain in tension be given by $\varepsilon_\mathrm{tr}^{\mathrm{M_t}}$. Suppose further, that the underlying crystal is subjected to uniaxial stresses, so that $\varepsilon_\mathrm{tr}^{\mathrm{M_t}} = \mathsf{C}_{1111}\,\sigma_{11}^\mathrm{t}$ holds. Here, C_{1111} denotes the respective component of the compliance tensor and $\sigma_{11}^\mathrm{t} > 0$ are the applied stresses. Now, the question arises which compression state, $\sigma_{11}^\mathrm{c} < 0$, must be established in order to fulfill $\varepsilon_{22}^* = \varepsilon_\mathrm{tr}^{\mathrm{M_t}}$. As $\varepsilon_{22}^* = \mathsf{C}_{2211}\,\sigma_{11}^\mathrm{c}$, one obtains $\varepsilon_\mathrm{tr}^{\mathrm{M_c}} = \mathsf{C}_{1111}\,\sigma_{11}^\mathrm{c} = [\mathsf{C}_{1111}/\mathsf{C}_{2211}]\,\varepsilon_\mathrm{tr}^{\mathrm{M_t}}$. Adopting elastic parameters for materials undergoing cubic–tetragonal martensitic transformations from [138, 140], we obtain $\varepsilon_\mathrm{tr}^{\mathrm{M_c}} = -2.7\,\varepsilon_\mathrm{tr}^{\mathrm{M_t}}$.

3 A non-affine micro-sphere model for phase-transformations

In this chapter, we introduce a material model for the simulation of polycrystalline materials undergoing solid to solid phase-transformations. As a basis, we present a scalar-valued phase-transformation model where a Helmholtz free energy function depending on volumetric and deviatoric strain measures is assigned to each phase. The analysis of the related overall Gibbs energy density allows for the calculation of energy barriers. With these quantities at hand, we use a statistical-physics-based approach to determine the resulting evolution of volume fractions. Though the model allows to take into account an arbitrary number of solid phases of the underlying material, we restrict this chapter to the simulation of phase-transformations between an austenitic parent phase and a martensitic tension and compression phase. The scalar model is embedded into a non-affine computational micro-sphere formulation in view of the simulation of three-dimensional boundary value problems. The final modelling approach necessary for macroscopic simulations is accomplished by a finite element formulation, where the local material behaviour at each integration point is governed by the response of the micro-sphere model.

The chapter is organised as follows: In Section 3.1 we introduce the scalar-valued phase-transformation model with a volumetric-deviatoric kinematic split. We start with a Helmholtz free energy potential which is transformed to a Gibbs potential, see Section 3.1.1, allowing for the computation of Gibbs energy barriers that facilitate the computation of transformation probabilities between the phases considered as shown in Section 3.1.3. We derive mathematical expressions for the energy barriers, where intersection curves of elliptic-paraboloidal Gibbs potentials are considered. The algorithmic minimisation of these intersection curves is elaborated in Section 3.1.4. Numerical results obtained for three representative load cases are presented in Section 3.1.5, where we show the capability of the scalar-valued model to capture stress-strain-temperature responses as well as experimentally observed material behaviour for tensile step tests. In Section 3.2 we introduce the micro-sphere extension of the previously introduced scalar-valued model. The 3D-extension shown in Section 3.2.1 briefly discusses micro-meso-relations between free energy, strains, stresses, the elasticity measures, and volume fractions. The computational micro-sphere examples provided in Section 3.2.2 are computed for two representative load cases, namely a purely deviatoric one and a mixed volumetric-deviatoric one. In Section 3.3 we provide the results of a finite element analysis considering combined torsion and tension of a material block. For the chosen load history in terms of top surface axial displacements and top surface torsional angles we compute the according tensile reaction force and the torsional reaction moment in order to investigate necking-type behaviour of the material resulting from deformation-induced phase-transformations. Moreover, we provide contour plots of the tensile stresses and macroscopic austenitic volume fractions for selected representative deformation states. The chapter is closed by a summary and conclusions in Section 3.4.

3.1 Scalar-valued phase-transformation model with volumetric-deviatoric split

The scalar-valued phase-transformation model is based on a mixture theory, where we make use of the Voigt assumption, i.e. the total strain is distributed homogeneously among the phases, cf. Section 2.1. The implemented phase-transformation model is capable of handling an arbitrary number of material phases, where the non-negative volume fraction

$$\xi^\alpha := \lim_{v \to 0} \left(\frac{v^\alpha}{v} \right) \tag{3.1}$$

of each phase $\alpha \in \{1, \dots, \nu\} \subset \mathbb{N}$ is subject to the usual physical restrictions. From conservation of mass—for the referential mass densities remaining constant and identical for all phases—it follows that

$$\xi^\alpha \in \; [0,1] \subset \mathbb{R} \quad \text{and} \quad \sum_{\alpha=1}^{\nu} \xi^\alpha = \; 1 \quad \text{so that} \quad \sum_{\alpha=1}^{\nu} \dot{\xi}^\alpha = \; 0 \quad . \tag{3.2}$$

3.1.1 Phase potentials

We start by assigning a Helmholtz free energy potential $\psi^\alpha = \widehat{\psi}^\alpha(\varepsilon_{\text{dev}}, \varepsilon_{\text{vol}}, \theta)$ of the form

$$\psi^\alpha = \frac{1}{2}\,\mathsf{E}^\alpha_{\text{dev}} \left[\varepsilon_{\text{dev}} - \varepsilon^\alpha_{\text{tr,dev}}\right]^2 + \frac{1}{2}\,\mathsf{E}^\alpha_{\text{vol}} \left[\varepsilon_{\text{vol}} - \varepsilon^\alpha_{\text{tr,vol}}\right]^2 - \zeta^\alpha\,\mathsf{E}^\alpha \left[\varepsilon - \varepsilon^\alpha_{\text{tr}}\right]\left[\theta - \theta_0\right] + \widehat{C}^\alpha(\theta) \tag{3.3}$$

to each phase α, where we consider a volumetric-deviatoric-type split of total strains $\varepsilon = \varepsilon_{\text{dev}} + \varepsilon_{\text{vol}}$ and transformation strains $\varepsilon^\alpha_{\text{tr}} = \varepsilon^\alpha_{\text{tr,dev}} + \varepsilon^\alpha_{\text{tr,vol}}$. The considered strain measures ε_{dev} and ε_{vol} are derived from projections of the macroscopic three-dimensional strain tensor $\boldsymbol{\varepsilon}$ onto a spatial direction $\boldsymbol{r}$ in the context of a micro-sphere approach, specifically $\varepsilon_{\text{dev}} = \boldsymbol{r} \cdot \boldsymbol{\varepsilon} \cdot \boldsymbol{r} - 1/3\,\text{tr}(\boldsymbol{\varepsilon})$ and $\varepsilon_{\text{vol}} = 1/3\,\text{tr}(\boldsymbol{\varepsilon})$. Further details on the micro-sphere kinematics are provided in Section 3.2.1.1.

For the Helmholtz potential given in (3.3), we consider $\mathsf{E}^{\alpha}_{\text{dev}} = \widehat{\mathsf{E}}^{\alpha}_{\text{dev}}(\mathsf{E}, \nu_{\text{P}})$ and $\mathsf{E}^{\alpha}_{\text{vol}} = \widehat{\mathsf{E}}^{\alpha}_{\text{vol}}(\mathsf{E}, \nu_{\text{P}})$ as deviatoric and volumetric elasticity coefficients on the micro-level, where we choose $\widehat{\mathsf{E}}^{\alpha}_{\text{dev}}(\mathsf{E}, \nu_{\text{P}}) = 5\,\mathsf{E}/[2 + 2\,\nu_{\text{P}}]$ and $\widehat{\mathsf{E}}^{\alpha}_{\text{vol}}(\mathsf{E}, \nu_{\text{P}}) = \mathsf{E}/[1 - 2\,\nu_{\text{P}}]$ in order to match a macroscopic Young's modulus E and Poisson's ratio ν_{P} in the later micro-sphere application. Further details on the relation between micro-level elasticity coefficients and macroscopic elastic quantities in the context of the micro-sphere framework are elaborated in [27]. Moreover, we denote ζ^{α} as the coefficient of thermal expansion, θ as the current absolute temperature and θ_0 as a reference temperature. The temperature-dependent chemical energy $\widehat{C}^{\alpha}(\theta)$ is given as

$$\widehat{C}^{\alpha}(\theta) = \rho_0\, c^{\alpha}_{p}\, \theta \left[1 - \log\left(\frac{\theta}{\theta_0}\right)\right] - \rho_0\, \lambda^{\alpha}_{T} \left[1 - \frac{\theta}{\theta_0}\right] \quad , \tag{3.4}$$

with c^{α}_{p} being the heat capacity and λ^{α}_{T} the latent heat of the respective material phase α, cf. [51]. The overall phase potential $\Psi = \widehat{\Psi}(\varepsilon_{\text{dev}}, \varepsilon_{\text{vol}}, \boldsymbol{\xi}, \theta)$ is obtained from the contributions of the constituents and can be expressed as

$$\Psi = \sum_{\alpha=1}^{\nu} \xi^{\alpha} \psi^{\alpha} \quad , \tag{3.5}$$

where $\boldsymbol{\xi} = [\xi^1, \ldots, \xi^{\nu}]^{\text{t}} \in \mathbb{R}^{\nu \times 1}$ is the collection of the volume fractions.

In view of the energy barriers utilised for the evolution of volume fractions, we compute the Gibbs energy contributions of the individual phases. Carrying out a Legendre-transformation of the Helmholtz free energy of the mixture (3.5) yields the overall Gibbs potential

$$\begin{aligned}
\widehat{G}(\partial_{\varepsilon_{\text{dev}}}\Psi, \partial_{\varepsilon_{\text{vol}}}\Psi) &= \Psi - \left.\frac{\partial \Psi}{\partial \varepsilon_{\text{dev}}}\right|_{\varepsilon_{\text{dev}},\theta} \varepsilon_{\text{dev}} - \left.\frac{\partial \Psi}{\partial \varepsilon_{\text{vol}}}\right|_{\varepsilon_{\text{vol}},\theta} \varepsilon_{\text{vol}} && (3.6)\\
&= \sum_{\alpha=1}^{\nu} \xi^{\alpha}\psi^{\alpha} - \sum_{\alpha=1}^{\nu} \xi^{\alpha} \left.\frac{\partial \psi^{\alpha}}{\partial \varepsilon_{\text{dev}}}\right|_{\varepsilon_{\text{dev}},\theta} \varepsilon_{\text{dev}} \\
&\qquad - \sum_{\alpha=1}^{\nu} \xi^{\alpha} \left.\frac{\partial \psi^{\alpha}}{\partial \varepsilon_{\text{vol}}}\right|_{\varepsilon_{\text{vol}},\theta} \varepsilon_{\text{vol}} && (3.7)\\
&= \sum_{\alpha=1}^{\nu} \xi^{\alpha} g^{\alpha} \quad , && (3.8)
\end{aligned}$$

where use has been made of (3.5). Here,

$$\widehat{g}^{\alpha}(\partial_{\varepsilon_{\text{dev}}}\psi^{\alpha}, \partial_{\varepsilon_{\text{vol}}}\psi^{\alpha}) = \psi^{\alpha} - \left.\frac{\partial\psi^{\alpha}}{\partial\varepsilon_{\text{dev}}}\right|_{\varepsilon_{\text{dev}},\theta} \varepsilon_{\text{dev}} - \left.\frac{\partial\psi^{\alpha}}{\partial\varepsilon_{\text{vol}}}\right|_{\varepsilon_{\text{vol}},\theta} \varepsilon_{\text{vol}} \tag{3.9}$$

is the contribution of phase α to the overall Gibbs potential G.

Note that the Gibbs potential g^{α} of every individual phase α has the form of an elliptic paraboloid with ε_{dev} and ε_{vol} as functional parameters, see Fig. 3.1(a). The overall Gibbs energy G of the material, which is obtained from the contributions of the constituents according to (3.8), in consequence has three local minima for a three-phase material, see Fig. 3.1(b).

3.1.2 Evolution of volume fractions

The evolution of volume fractions ξ^{α} is based on the approach introduced in Section 2.1.1, i.e. we make use of the transformation probability matrix $\boldsymbol{Q} \in \mathbb{R}^{\nu\times\nu}$ (2.6), which drives the evolution of volume fractions in terms of $\dot{\boldsymbol{\xi}} = \boldsymbol{Q}\cdot\boldsymbol{\xi}$. However, the computation of the Gibbs energy barriers $b_{\alpha\to\beta}$ that determine the transformation probabilites $P_{\alpha\to\beta}$ (2.7) and thereby govern the components of $\boldsymbol{Q}$ take a significantly more complex form in the context of non-affine kinematics as elaborated in Section 3.1.3.

3.1.3 Gibbs energy barriers of elliptic-paraboloidal potentials

For the computation of an energy barrier $b_{\alpha\to\beta}$, the intersection of two elliptic paraboloids—namely the Gibbs potentials g^{α} and g^{β} of the two involved phases α and β—must be evaluated in volumetric and deviatoric strain space. We assume that an intersection of the two paraboloids exists and that the paraboloids are not identical. The intersection of two elliptic paraboloids can then be expressed by means of a parametric curve. To be specific, equating the Gibbs potentials of the two phases α and β,

$$\widehat{g}^{\alpha}(\varepsilon_{\text{dev}}, \varepsilon_{\text{vol}}, \theta) = \widehat{g}^{\beta}(\varepsilon_{\text{dev}}, \varepsilon_{\text{vol}}, \theta) \quad , \tag{3.10}$$

represents one equation with two unknowns ε_{dev} and ε_{vol} for given temperature θ in the current material state. Rearranging terms, one obtains an implicit relation between the two unknowns, facilitating to express e.g. the deviatoric strains $\varepsilon_{\text{dev}}^{\text{isc}}$, at which g^{α} and g^{β} intersect, in terms of the volumetric strains, i.e.

$$\varepsilon_{\text{dev}}^{\text{isc}} = \widehat{\varepsilon}_{\text{dev}}^{\text{isc}}(\varepsilon_{\text{vol}}) \quad , \tag{3.11}$$

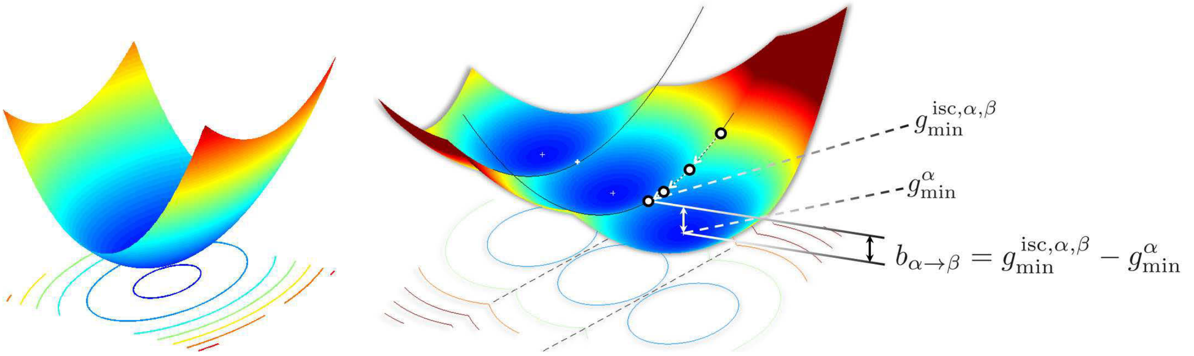
$g_{\text{min}}^{\text{isc},\alpha,\beta}$
g_{min}^{α}
$b_{\alpha\to\beta} = g_{\text{min}}^{\text{isc},\alpha,\beta} - g_{\text{min}}^{\alpha}$

(a) Gibbs potential g^α of one phase α plotted above the ε_{dev}-ε_{vol}-plane.

(b) Gibbs potential contributions g of a 3-phase material plotted above the ε_{dev}-ε_{vol}-plane and graphical representation of one exemplary Gibbs energy barrier $b_{\alpha\to\beta}$ as introduced in Section 3.1.3.

Figure 3.1: Illustration of Gibbs free energy potentials. The Gibbs potential g^α of every single phase α, (a), is an elliptic paraboloid. The Gibbs potential contributions g of a 3-phase material, (b), have one local minimum assigned to each individual phase—yielding three local minima for the considered phase mixture. The intersection curves of two neighbouring elliptic paraboloids are minimised iteratively, facilitating the computation of the actual energy barriers that have to be overcome for transformations from one phase to another. Note that this idea is an extension of the basic energy-barrier-based model introduced in [51], where no volumetric-deviatoric split of kinematic quantities is considered. In the latter case, the problem of determining energy barriers reduces to the trivial task of computing intersection points of simple parabolas [101].

where the superscript isc refers to the intersection curve. The actual value of the potentials along the intersection curve in terms of the variable ε_{vol} is then given by

$$\widehat{g}^{\,\text{isc},\alpha,\beta}(\varepsilon_{\text{vol}})\big|_\theta \;:=\; \widehat{g}^{\,\alpha}(\widehat{\varepsilon}^{\,\text{isc}}_{\text{dev}}(\varepsilon_{\text{vol}}),\varepsilon_{\text{vol}},\theta) \tag{3.12}$$

$$\equiv\; \widehat{g}^{\,\beta}(\widehat{\varepsilon}^{\,\text{isc}}_{\text{dev}}(\varepsilon_{\text{vol}}),\varepsilon_{\text{vol}},\theta) \quad . \tag{3.13}$$

To obtain the energy barrier required for the evolution of volume fractions, the minimum of the Gibbs energy along this parametric curve is calculated, i.e.

$$g_{\text{min}}^{\text{isc},\alpha,\beta} := \min_{\varepsilon_{\text{vol}}}\left(\widehat{g}^{\,\text{isc},\alpha,\beta}(\varepsilon_{\text{vol}})\big|_\theta\right) \tag{3.14}$$

must be computed. In Fig. 3.1(b), the minimum of the exemplary intersection curves is denoted accordingly. In general, due to the implicit nature of the equations, it is not possible to obtain an analytical solution for this problem. Hence, the minimisation of (3.13) must be carried out numerically using e.g. a Newton scheme as shown in Section 3.1.4. With the minimum $g_{\text{min}}^{\text{isc},\alpha,\beta}$ of the intersection curve of the Gibbs potentials of two phases α and β at hand, the energy barriers are computed according to

$$b_{\alpha\to\beta} = g_{\text{min}}^{\text{isc},\alpha,\beta} - g_{\text{min}}^{\alpha} \tag{3.15}$$

and

$$b_{\beta\to\alpha} = g_{\min}^{\mathrm{isc},\alpha,\beta} - g_{\min}^{\beta} \quad , \tag{3.16}$$

where $g_{\min}^{\alpha}$ and $g_{\min}^{\beta}$ denote the absolute minima of the Gibbs potentials g^{α} and g^{β}, respectively, as exemplified in Fig. 3.1(b). The absolute minimum of the Gibbs potential g^{α} of a single phase, say α, can be computed analytically by solving for the unique point $(\varepsilon_{\mathrm{dev}}^{g^{\alpha}\mathrm{min}}, \varepsilon_{\mathrm{vol}}^{g^{\alpha}\mathrm{min}})$ in deviatoric-volumetric strain space, where the gradient of g^{α} vanishes, i.e.

$$\nabla \widehat{g}^{\alpha}(\varepsilon_{\mathrm{dev}}^{g^{\alpha}\mathrm{min}}, \varepsilon_{\mathrm{vol}}^{g^{\alpha}\mathrm{min}})\Big|_{\theta} = \mathbf{0} \quad , \tag{3.17}$$

inducing

$$g_{\min}^{\alpha} = \widehat{g}^{\alpha}(\varepsilon_{\mathrm{dev}}^{g^{\alpha}\mathrm{min}}, \varepsilon_{\mathrm{vol}}^{g^{\alpha}\mathrm{min}})\Big|_{\theta} \quad , \tag{3.18}$$

see Section 3.5.2 for details on the analytical derivation of the minimum of an elliptic Gibbs energy paraboloid.

3.1.4 Algorithmic computation of Gibbs energy barriers

In this section the computation of the Gibbs energy barriers that drive the evolution of volume fractions is discussed. We will first derive a compact representation of the Gibbs energy where we introduce simplified Gibbs energy coefficients, denoted as $\{a, b, c, d, e\}$, cf. (3.19) and (3.20). Next, these coefficients are specified in terms of the material parameters introduced in (3.3), see (3.30)-(3.34). With the well-defined simplified Gibbs coefficients $\{a, b, c, d, e\}$ at hand, we can then carry out the computation of Gibbs energy barriers in a compact notation. To this end, we equate two Gibbs potentials in (3.35), enabling us to express the intersection curve of both potentials in terms of just one parameter, see (3.38). Finally, we compute the minimum value of the parametric intersection curve as defined in (3.40) via a Newton-Raphson scheme, which requires the calculation of the first and second derivative of the intersection curve. The latter derivatives are specified in (3.41) and (3.42), respectively.

For the computation of the Gibbs energy barriers $b_{\alpha\to\beta}$ and $b_{\beta\to\alpha}$ between two phases α and β—here, $\alpha, \beta \in \{\mathrm{A}, \mathrm{M_t}, \mathrm{M_c}\}$—we make use of the compact representations

$$\widehat{g}^{\alpha}(\varepsilon_{\mathrm{dev}}, \varepsilon_{\mathrm{vol}}) = a^{\alpha}{\varepsilon_{\mathrm{dev}}}^2 + b^{\alpha}\varepsilon_{\mathrm{dev}} + c^{\alpha}{\varepsilon_{\mathrm{vol}}}^2 + d^{\alpha}\varepsilon_{\mathrm{vol}} + e^{\alpha} \tag{3.19}$$

and

$$\widehat{g}^{\beta}(\varepsilon_{\mathrm{dev}}, \varepsilon_{\mathrm{vol}}) = a^{\beta}{\varepsilon_{\mathrm{dev}}}^2 + b^{\beta}\varepsilon_{\mathrm{dev}} + c^{\beta}{\varepsilon_{\mathrm{vol}}}^2 + d^{\beta}\varepsilon_{\mathrm{vol}} + e^{\beta} \tag{3.20}$$

of the Gibbs potentials for both phases α and β which reflect that (3.9) is quadratic in ε_{dev} and ε_{vol}. The Gibbs-energy-related coefficients $a^{\alpha}, ..., e^{\alpha}$ and $a^{\beta}, ..., e^{\beta}$ depend on the current loading state as well as on the material parameters of the phases considered and hence are dissimilar and not constant in general.

To derive the simplified Gibbs energy coefficients, we take the following steps:

1. Rearrange the given terms of the Helmholtz free energy (3.3) in order to obtain simplified Helmholtz free energy coefficients $a^{\alpha}_{\psi}, ..., e^{\alpha}_{\psi}$ for each phase α at fixed temperature. As a result, (3.3) can be written as

$$\widehat{\psi}^{\bullet}(\varepsilon_{\text{dev}}, \varepsilon_{\text{vol}})\big|_{\varepsilon^{\bullet}_{\text{pl}},\theta} = a^{\bullet}_{\psi}\,{\varepsilon_{\text{dev}}}^2 + b^{\bullet}_{\psi}\,\varepsilon_{\text{dev}} + c^{\bullet}_{\psi}\,{\varepsilon_{\text{vol}}}^2 + d^{\bullet}_{\psi}\,\varepsilon_{\text{vol}} + e^{\bullet}_{\psi} \quad , \tag{3.21}$$

with

$$\begin{aligned}
a^{\bullet}_{\psi} &= 0.5\,\mathsf{E}^{\bullet}_{\text{dev}} && (3.22)\\
b^{\bullet}_{\psi} &= -\,\mathsf{E}^{\bullet}_{\text{dev}}\,\varepsilon^{\bullet}_{\text{tr,dev}} - \zeta^{\bullet}\,\mathsf{E}^{\bullet}\,[\theta-\theta_0] && (3.23)\\
c^{\bullet}_{\psi} &= 0.5\,\mathsf{E}^{\bullet}_{\text{vol}} && (3.24)\\
d^{\bullet}_{\psi} &= -\,\mathsf{E}^{\bullet}_{\text{vol}}\,\varepsilon^{\bullet}_{\text{tr,vol}} - \zeta^{\bullet}\,\mathsf{E}^{\bullet}\,[\theta-\theta_0] && (3.25)\\
e^{\bullet}_{\psi} &= 0.5\,\mathsf{E}^{\bullet}_{\text{dev}}\,\left[\varepsilon^{\bullet}_{\text{tr,dev}}\right]^2 + 0.5\,\mathsf{E}^{\bullet}_{\text{vol}}\,\varepsilon^{2}_{\text{tr,vol}} && (3.26)\\
&\quad + \zeta^{\bullet}\,\mathsf{E}^{\bullet}\,[\theta-\theta_0]\left[\varepsilon^{\bullet}_{\text{tr,dev}} + \varepsilon^{\bullet}_{\text{tr,vol}}\right] + \widehat{C}^{\bullet}(\theta) && (3.27)
\end{aligned}$$

and $\widehat{C}^{\bullet}(\theta)$ the chemical energy of the respective material phase as defined in (3.4).

2. Carry out the Legendre transformation of (3.21) in order to obtain the Gibbs free energy in a compact notation. This yields

$$\begin{aligned}
\widehat{g}^{\bullet}(\varepsilon_{\text{dev}}, \varepsilon_{\text{vol}}) &= \psi^{\bullet} - \left.\frac{\partial\psi^{\bullet}}{\partial\varepsilon_{\text{dev}}}\right|_{\varepsilon_{\text{dev}}|_t,\theta}\varepsilon_{\text{dev}} - \left.\frac{\partial\psi^{\bullet}}{\partial\varepsilon_{\text{vol}}}\right|_{\varepsilon_{\text{vol}}|_t,\theta}\varepsilon_{\text{vol}} && (3.28)\\
&= a^{\bullet}_{\psi}\,{\varepsilon_{\text{dev}}}^2\\
&\quad + \left[b^{\bullet}_{\psi} - \xi^{\bullet}\left[\mathsf{E}^{\bullet}_{\text{dev}}\,\varepsilon_{\text{dev}}|_t - \mathsf{E}^{\bullet}_{\text{dev}}\left[\varepsilon^{\bullet}_{\text{tr,dev}}\right] - \zeta^{\bullet}\,\mathsf{E}^{\bullet}\,[\theta-\theta_0]\right]\right]\varepsilon_{\text{dev}}\\
&\quad + c^{\bullet}_{\psi}\,{\varepsilon_{\text{vol}}}^2\\
&\quad + \left[d^{\bullet}_{\psi} - \xi^{\bullet}\left[\mathsf{E}^{\bullet}_{\text{vol}}\,\varepsilon_{\text{vol}}|_t - \mathsf{E}^{\bullet}_{\text{vol}}\,\varepsilon^{\bullet}_{\text{tr,vol}} - \zeta^{\bullet}\,\mathsf{E}^{\bullet}\,[\theta-\theta_0]\right]\right]\varepsilon_{\text{vol}}\\
&\quad + e^{\bullet}_{\psi} \quad , && (3.29)
\end{aligned}$$

where $\varepsilon_{\text{dev}}|_t$ and $\varepsilon_{\text{vol}}|_t$ denote the currently applied deviatoric and volumetric strains, i.e. the given strain values characterising the current load state at time t. Note that we here express $g^{\bullet}$ in terms of ε_{dev} and ε_{vol}, in contrast to the usual Legendre notation introduced in, e.g., (3.9). To be specific, we make use of a re-parametrisation of the Gibbs energy, i.e. we express the Gibbs energy arguments

$\partial_{\varepsilon_{\text{dev}}}\psi^\alpha$ and $\partial_{\varepsilon_{\text{vol}}}\psi^\alpha$ in terms of ε_{dev} and ε_{vol}, respectively, in order to compute the Gibbs energy barriers in volumetric-deviatoric strain space.

3. Finally, the simplified Gibbs potential coefficients can be expressed as

$$
\begin{aligned}
a^\bullet &= a^\bullet_\psi && (3.30)\\
b^\bullet &= b^\bullet_\psi - \xi^\bullet \left[\mathsf{E}^\bullet_{\text{dev}}\, \varepsilon_{\text{dev}}|_t - \mathsf{E}^\bullet_{\text{dev}}\, \varepsilon^\bullet_{\text{tr,dev}} - \zeta^\bullet\, \mathsf{E}^\bullet\, [\theta - \theta_0]\right] \\
&= -\left[1 - \xi^\bullet\right] \mathsf{E}^\bullet_{\text{dev}}\, \varepsilon^\bullet_{\text{tr,dev}} - \xi^\bullet \mathsf{E}^\bullet_{\text{dev}}\, \varepsilon_{\text{dev}}|_t - \zeta^\bullet\, \mathsf{E}^\bullet\, [\theta - \theta_0] && (3.31)\\
c^\bullet &= c^\bullet_\psi && (3.32)\\
d^\bullet &= d^\bullet_\psi - \xi^\bullet \left[\mathsf{E}^\bullet_{\text{vol}}\, \varepsilon_{\text{vol}}|_t - \mathsf{E}^\bullet_{\text{vol}}\, \varepsilon^\bullet_{\text{tr,vol}} - \zeta^\bullet\, \mathsf{E}^\bullet\, [\theta - \theta_0]\right] \\
&= -\left[1 - \xi^\bullet\right] \mathsf{E}^\bullet_{\text{vol}}\, \varepsilon^\bullet_{\text{tr,vol}} - \xi^\bullet \mathsf{E}^\bullet_{\text{vol}}\, \varepsilon_{\text{vol}}|_t - \zeta^\bullet\, \mathsf{E}^\bullet\, [\theta - \theta_0] && (3.33)\\
e^\bullet &= e^\bullet_\psi && (3.34)
\end{aligned}
$$

by evaluation and simplification of terms in (3.29).

With the well-defined Gibbs potential coefficients at hand, (3.30)-(3.34), we can equate (3.19) and (3.20) and solve for $\varepsilon^{\text{isc}}_{\text{dev}} = \widehat{\varepsilon}^{\text{isc}}_{\text{dev}}(\varepsilon_{\text{vol}})$ in order to obtain the subdomain of g which is mapped to the intersection curve of g^α and g^β. The parametric subdomain of g mapped to the intersection curve of g^α and g^β is obtained by equating

$$
\begin{aligned}
&& \widehat{g}^\alpha(\varepsilon_{\text{dev}}, \varepsilon_{\text{vol}}) &= \widehat{g}^\beta(\varepsilon_{\text{dev}}, \varepsilon_{\text{vol}}) \\
\Rightarrow && \widehat{\varepsilon}^{\text{isc}}_{\text{dev}}(\varepsilon_{\text{vol}}) &= \frac{-\Delta b \pm T_{\text{sqrt}}}{2\,\Delta a} && (3.35)
\end{aligned}
$$

with T_{sqrt} abbreviating the square-root term

$$
T_{\text{sqrt}} := \sqrt{[\Delta b]^2 - 4\,\Delta a\,[\Delta e + \varepsilon_{\text{vol}}\,[\Delta d + \Delta c\,\varepsilon_{\text{vol}}]]} \quad . \tag{3.36}
$$

Here, $\Delta\bullet := \bullet^\alpha - \bullet^\beta$ represents the difference of two corresponding Gibbs phase coefficients of phase α and β, e.g. $\Delta a := a^\alpha - a^\beta$. The intersection curve $\widehat{g}^{\text{isc},\alpha,\beta}(\varepsilon_{\text{vol}})$ of both elliptic paraboloids g^α and g^β in volumetric-deviatoric strain space can now be expressed in terms of the variable ε_{vol} by evaluation of

$$
\begin{aligned}
\widehat{g}^{\text{isc},\alpha,\beta}(\varepsilon_{\text{vol}}) &:= \widehat{g}^\alpha(\widehat{\varepsilon}^{\text{isc}}_{\text{dev}}(\varepsilon_{\text{vol}}), \varepsilon_{\text{vol}}) \equiv \widehat{g}^\beta(\widehat{\varepsilon}^{\text{isc}}_{\text{dev}}(\varepsilon_{\text{vol}}), \varepsilon_{\text{vol}}) && (3.37)\\
&= c^\alpha\, {\varepsilon_{\text{vol}}}^2 + d^\alpha\, \varepsilon_{\text{vol}} + e^\alpha \\
&\quad - f_s\, \frac{b^\alpha\,[\Delta b + T_{\text{sqrt}}]}{2\Delta a} \\
&\quad + \frac{a^\alpha\,[f_s \Delta b + T_{\text{sqrt}}]}{4[\Delta a]^2} \quad . && (3.38)
\end{aligned}
$$

Note that two solutions are obtained as induced by the two solutions already given in (3.35). To simplify notation, the switching factor $f_s \in \{-1, 1\}$ is introduced in order to switch the algebraic signs that differ in both solutions. In other words, the intersection curve $\widehat{g}^{\,\mathrm{isc},\alpha,\beta}(\varepsilon_{\mathrm{vol}})$ in terms of the variable $\varepsilon_{\mathrm{vol}}$ is given as the conjunction of two line sections $\widehat{g}^{\,\mathrm{isc},\alpha,\beta}(\varepsilon_{\mathrm{vol}}) = \widehat{g}^{\,\mathrm{isc},\alpha,\beta}(\varepsilon_{\mathrm{vol}})|_{f_s=-1} \bigcup \widehat{g}^{\,\mathrm{isc},\alpha,\beta}(\varepsilon_{\mathrm{vol}})|_{f_s=1}$.

In the next step, the minimum value

$$\begin{aligned} g_{\min}^{\mathrm{isc},\alpha,\beta} &= \min_{\varepsilon_{\mathrm{vol}},\,\varepsilon_{\mathrm{dev}}} \big(\widehat{g}^{\,\alpha}(\varepsilon_{\mathrm{dev}}, \varepsilon_{\mathrm{vol}}) \mid \widehat{g}^{\,\alpha}(\varepsilon_{\mathrm{dev}}, \varepsilon_{\mathrm{vol}}) = \widehat{g}^{\,\beta}(\varepsilon_{\mathrm{dev}}, \varepsilon_{\mathrm{vol}}) \big) && (3.39) \\ &= \min_{\varepsilon_{\mathrm{vol}}} \big(\widehat{g}^{\,\mathrm{isc},\alpha,\beta}(\varepsilon_{\mathrm{vol}}) \big) && (3.40) \end{aligned}$$

of the intersection curve is to be computed. Recall that the minimum of this intersection curve is the specific Gibbs energy value that is needed for the computation of the Gibbs energy barriers that must be overcome for the transformation from one phase α to another phase β and vice versa, cf. (3.15) and (3.16). To evaluate (3.40), we calculate the derivative of (3.38) with respect to $\varepsilon_{\mathrm{vol}}$ and find the zero-value of the obtained expression. This yields the condition

$$\begin{aligned} \mathrm{D}g^{\,\mathrm{isc},\alpha,\beta} = \frac{\partial\, \widehat{g}^{\,\mathrm{isc},\alpha,\beta}(\varepsilon_{\mathrm{vol}})}{\partial \varepsilon_{\mathrm{vol}}} &= d^\alpha + 2c^\alpha \varepsilon_{\mathrm{vol}} + f_s \frac{b^\alpha \left[\Delta d + 2\Delta c\, \varepsilon_{\mathrm{vol}}\right]}{T_{\mathrm{sqrt}}} \\ &\quad - \frac{\left[a^\alpha \left[\Delta d + 2\Delta c\, \varepsilon_{\mathrm{vol}}\right] \left[f_s \Delta b + T_{\mathrm{sqrt}}\right]\right]}{\Delta a\, T_{\mathrm{sqrt}}} \\ &\doteq 0 \quad . && (3.41) \end{aligned}$$

It is not possible to rearrange terms in (3.41) in order to obtain an explicit analytical solution for $\varepsilon_{\mathrm{vol}}$. We apply a Newton-Raphson iteration scheme to solve (3.41). The specific value of $\varepsilon_{\mathrm{vol}}$ that satisfies (3.41) and therefore minimises the intersection curve, say $\varepsilon_{\mathrm{vol}}^{\mathrm{isc,min}}$, can then be used to compute the Gibbs energy value associated with the minimum of the intersection curve of the elliptic Gibbs energy paraboloids of two phases α and β. For the application of the Newton-Raphson scheme, we need the derivative of the residual function to be solved, i.e. the derivative of (3.41) with respect to $\varepsilon_{\mathrm{vol}}$. We end up with

$$\begin{aligned} \mathrm{D}^2 g^{\,\mathrm{isc},\alpha,\beta} = \frac{\partial^2\, \widehat{g}^{\,\mathrm{isc},\alpha,\beta}(\varepsilon_{\mathrm{vol}})}{\partial {\varepsilon_{\mathrm{vol}}}^2} &= 2c^\alpha + f_s \frac{2\Delta a\, b^\alpha \left[\Delta d + 2\Delta c^\alpha\, \varepsilon_{\mathrm{vol}}\right]^2}{\left[T_{\mathrm{sqrt}}\right]^3} \\ &\quad + \frac{2a^\alpha \left[\Delta d + 2\Delta c\, \varepsilon_{\mathrm{vol}}\right]^2}{\left[T_{\mathrm{sqrt}}\right]^2} + f_s \frac{2b^\alpha \Delta c}{T_{\mathrm{sqrt}}} \\ &\quad - \frac{\left[2a^\alpha \left[\Delta d + 2\Delta c\, \varepsilon_{\mathrm{vol}}\right]^2 \left[f_s \Delta b + T_{\mathrm{sqrt}}\right]\right]}{\left[T_{\mathrm{sqrt}}\right]^3} \\ &\quad - \frac{2a^\alpha\, \Delta c \left[f_s \Delta b + T_{\mathrm{sqrt}}\right]}{\Delta a\, T_{\mathrm{sqrt}}} \quad , && (3.42) \end{aligned}$$

with T_{sqrt} defined in (3.36) and $f_s \in \{-1, 1\}$ the sign switching factor as introduced in (3.38). The algorithm of the overall minimisation problem is summarised in Section 3.5.3.

3.1.5 Scalar-valued model – computational examples at the micro-level

To investigate the behaviour of the proposed model at the micro-level, several representative load cases and different boundary conditions are studied. For the numerical examples, we consider SMA-type materials which have negligible volumetric transformation strains, i.e. $\varepsilon_{\mathrm{tr,vol}} = 0$. In the following computations, the strains are applied in terms of

$$\widehat{\varepsilon}(t) = \varepsilon_0 \, \widehat{\kappa}(t) \quad , \tag{3.43}$$

with ε_0 the maximum strain and a piecewise linear time-scaling function $\kappa \in [0, 1] \subset \mathbb{R}$. The absolute value of the strain rate is set to $|\dot{\varepsilon}| = 10^{-4}\,\mathrm{s}^{-1}$. For the computation of examples solely on the micro-level, the volumetric-deviatoric split ratio is not obtained from macroscopic strain tensor projections, cf. Section 3.2.1.1, but rather must be defined and prescribed manually in terms of

$$\widehat{\varepsilon}_{\mathrm{dev}}(t) = \widehat{\chi}_{\mathrm{dev}}(t)\, \widehat{\varepsilon}(t) \quad \text{and} \quad \widehat{\varepsilon}_{\mathrm{vol}}(t) = \widehat{\chi}_{\mathrm{vol}}(t)\, \widehat{\varepsilon}(t) \tag{3.44}$$

with $\widehat{\chi}_{\mathrm{dev}}(t)$ and $\widehat{\chi}_{\mathrm{vol}}(t)$ defining the volumetric-deviatoric split ratio of the scalar-valued overall strain $\widehat{\varepsilon}(t)$, where $\widehat{\chi}_{\mathrm{dev}}(t) + \widehat{\chi}_{\mathrm{vol}}(t) = 1 \;\forall\; t$.

Note that the scalar-valued stress response is derived from

$$\sigma := \frac{\partial \Psi}{\partial \varepsilon} = \frac{\partial \Psi}{\partial \varepsilon_{\mathrm{dev}}} \frac{\partial \varepsilon_{\mathrm{dev}}}{\partial \varepsilon} + \frac{\partial \Psi}{\partial \varepsilon_{\mathrm{vol}}} \frac{\partial \varepsilon_{\mathrm{vol}}}{\partial \varepsilon} \tag{3.45}$$

$$= \widehat{\chi}_{\mathrm{dev}}(t) \frac{\partial \Psi}{\partial \varepsilon_{\mathrm{dev}}} + \widehat{\chi}_{\mathrm{vol}}(t) \frac{\partial \Psi}{\partial \varepsilon_{\mathrm{vol}}} \quad . \tag{3.46}$$

Moreover, the elastic tangent modulus E_{el} of the scalar-valued micro-scale model takes the form

$$\mathsf{E}_{\mathrm{el}} = \frac{\mathrm{d}\sigma}{\mathrm{d}\varepsilon} = \frac{\mathrm{d}}{\mathrm{d}\varepsilon}\left[\widehat{\chi}_{\mathrm{dev}}(t) \frac{\partial \Psi}{\partial \varepsilon_{\mathrm{dev}}} + \widehat{\chi}_{\mathrm{vol}}(t) \frac{\partial \Psi}{\partial \varepsilon_{\mathrm{vol}}}\right] \tag{3.47}$$

$$= \widehat{\chi}_{\mathrm{dev}}(t) \frac{\partial^2 \Psi}{\partial \varepsilon_{\mathrm{dev}}\, \partial \varepsilon_{\mathrm{dev}}} \frac{\partial \varepsilon_{\mathrm{dev}}}{\partial \varepsilon} + \widehat{\chi}_{\mathrm{vol}}(t) \frac{\partial^2 \Psi}{\partial \left[\varepsilon_{\mathrm{vol}}\right]^2} \frac{\partial \varepsilon_{\mathrm{vol}}}{\partial \varepsilon} \tag{3.48}$$

$$= \left[\widehat{\chi}_{\mathrm{dev}}(t)\right]^2 \frac{\partial^2 \Psi}{\partial \varepsilon_{\mathrm{dev}}\, \partial \varepsilon_{\mathrm{dev}}} + \left[\widehat{\chi}_{\mathrm{vol}}(t)\right]^2 \frac{\partial^2 \Psi}{\partial \varepsilon_{\mathrm{vol}}\, \partial \varepsilon_{\mathrm{vol}}} \tag{3.49}$$

$$= \left[\widehat{\chi}_{\mathrm{dev}}(t)\right]^2 \sum_{\alpha=1}^{\nu} \xi^\alpha\, \mathsf{E}^\alpha_{\mathrm{dev}} + \left[\widehat{\chi}_{\mathrm{vol}}(t)\right]^2 \sum_{\alpha=1}^{\nu} \xi^\alpha\, \mathsf{E}^\alpha_{\mathrm{vol}} \quad , \tag{3.50}$$

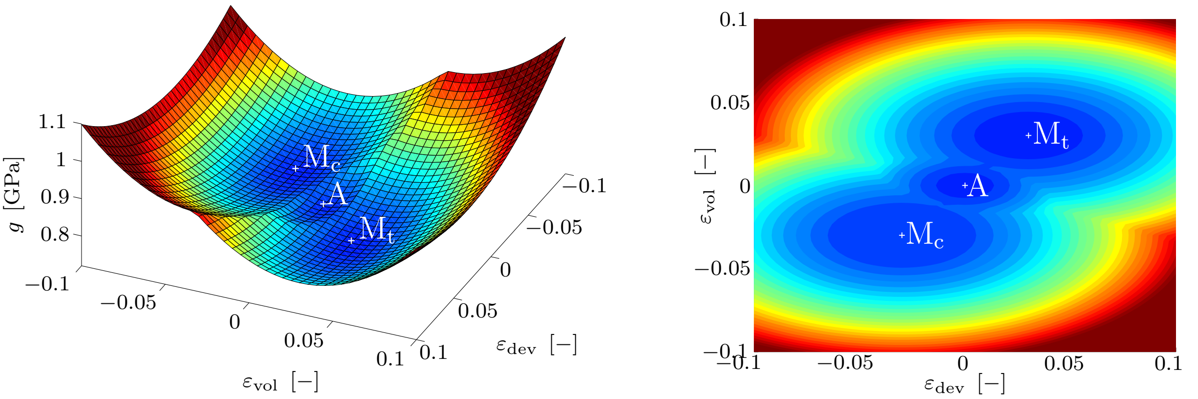

(a) Initial configuration: Gibbs energy landscape.

(b) Initial configuration: Gibbs energy contour plot.

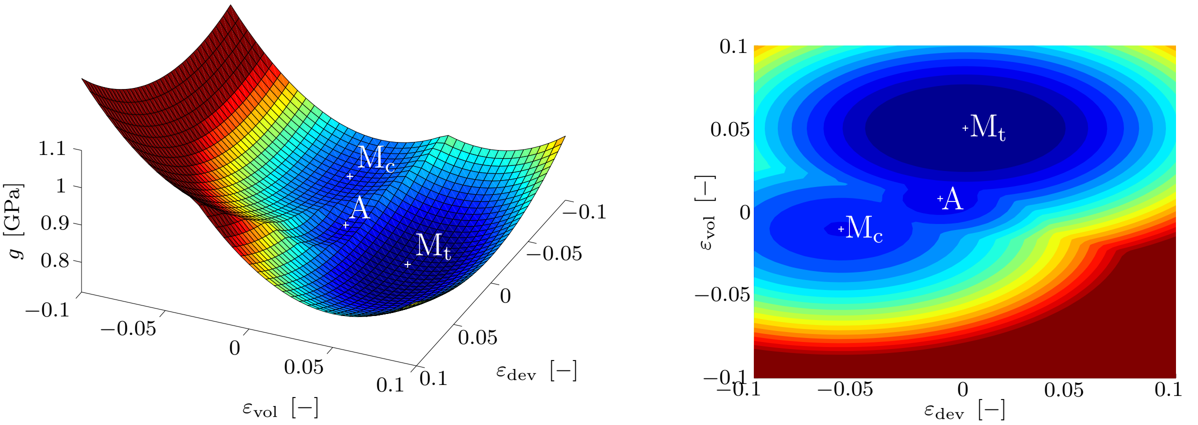

(c) Stretched configuration: Gibbs energy landscape.

(d) Stretched configuration: Gibbs energy contour plot.

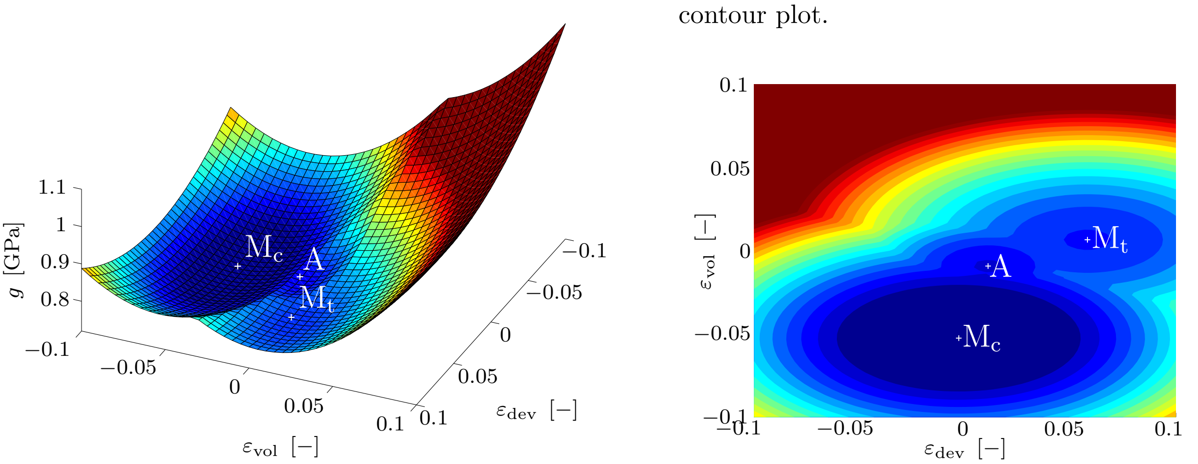

(e) Compressed configuration: Gibbs energy landscape.

(f) Compressed configuration: Gibbs energy contour plot.

Figure 3.2: Visualisation of the contributions to the overall Gibbs free energy potential G of the considered three-phase material mixture at $\theta = 30\,°\mathrm{C}$. In the initial state, the material is in equilibrium, see (a) and (b). After applying a mixed deviatoric-volumetric tensile load, the martensitic tensile phase $\mathrm{M_t}$ becomes energetically favourable and therefore evolves, cf. (c) and (d). As the load reverses and the compression regime is reached, the martensitic compression phase $\mathrm{M_c}$ is energetically favourable as shown in (e) and (f).

as an explicit integration scheme for the volume fractions ξ is applied. For simplicity, for the micro-scale computations provided, we assume a constant volumetric-deviatoric split ratio with $\widehat{\chi}_{\text{dev}}(t) = \widehat{\chi}_{\text{vol}}(t) = \text{const} = 0.5$, which yields $\widehat{\varepsilon}_{\text{vol}}(t) = \widehat{\varepsilon}_{\text{dev}}(t) = 0.5\,\widehat{\varepsilon}(t)$.

Since the evolution of volume fractions is mainly determined from the values of the Gibbs energy barriers between the considered phases, we investigate the Gibbs energy landscape for different load states in order to assess the physical plausibility of the model. Fig. 3.2 shows the computed actual Gibbs energy landscape of the three-phase material that we consider in this chapter, see Section 3.5.1 for the material parameters used. The load-dependent transformations of the energy potentials of the individual phases show that the model behaves as intended, i.e. for homogeneous initial conditions, the energy landscape of the material is symmetric and no phase evolution takes place. As tensile deformation is applied, the martensitic tensile phase M_t becomes energetically favourable. The analogous behaviour is observed for the compression regime, where the martensitic compression phase M_c is energetically favourable and thus evolving.

Fig. 3.3 shows the capability of the proposed model to capture the stress-strain-temperature response usually observed for SMA-type materials. Here, we consider the material to be initially martensitic with two equally distributed martensitic variants, i.e. $\xi^{\text{M}_\text{t}}(t=0) = \xi^{\text{M}_\text{c}}(t=0) = 0.5$, see Fig. 3.3(b). Due to the low initial temperature of $\theta = -30°\text{C}$, cf. Fig. 3.3(a), the martensitic phases are stable and the evolution of austenite during loading is prevented. As the applied strains increase, the martensitic tensile variant ξ^{M_t} evolves at the cost of the compression variant ξ^{M_c}. At a maximum strain of $\varepsilon = 0.03$, the load is reversed until the material reaches a stress-free configuration with remaining strains of $\varepsilon \approx 0.01$, see Fig. 3.3(a). Note that, due to the low temperature of $\theta = -30°\text{C}$, a pseudo-plastic response is obtained for the considered material. When increasing the temperature of the material while retaining its stress-free configuration, we observe that the remaining strains decrease, showing that the model proposed is capable of reflecting the experimentally observed characteristic stress-strain-temperature response of SMA as elaborated in, e.g., [77].

Apart from stress-strain-temperature load cycles, we simulate tensile step tests at different temperatures θ, where we here restrict the investigations to $\theta = 30\,°\text{C}$ and $\theta = 100\,°\text{C}$. In the first example, see Figs. 3.4(a), 3.4(c), 3.4(e), we choose a temperature of $\theta = 30°\text{C}$. Here, we incrementally increase the maximum applied strain and then release the strains to zero, which results in the load path provided in Fig. 3.4(a). The obtained stress-strain response, Fig. 3.4(c), shows that each load cycle with higher maximum strains represents an envelope to the stress-strain responses obtained for lower maximum strains, which coincides with experimental observations presented in, e.g., [59].

In the second example, see Figs. 3.4(b), 3.4(d), 3.4(f), a higher temperature of $\theta = 100°\text{C}$ is chosen. In this computation, we incrementally increase the applied strain and release it only to a certain amount, as illustrated in the load path provided in Fig. 3.4(b). The obtained stress-strain response, Fig. 3.4(d), shows a clearly pseudo-elastic reponse resulting from the elevated temperature level. Moreover, the minor loops obtained in

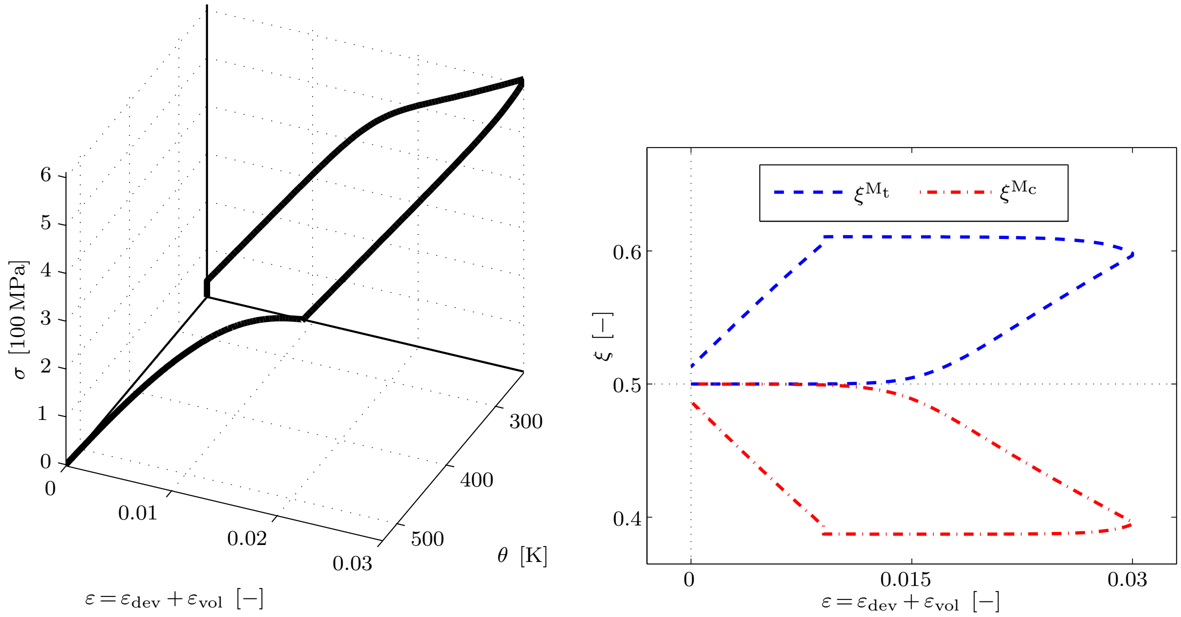

(a) Stress-strain-temperature response. (b) Strain-dependent evolution of volume fractions.

Figure 3.3: Results obtained for a stress-strain-temperature load cycle at the micro-level. Due to the low initial temperature considered, the material shows a pseudo-plastic stress-strain response. After reaching the stress-free configuration at $\varepsilon \approx 0.01$, the temperature is increased until the remaining total strains $\varepsilon = \varepsilon_{\text{dev}} + \varepsilon_{\text{vol}}$ reach zero, see (a). The evolution of the two martensitic variants is provided in (b). Note that the low temperature prevents the evolution of austenite in this simulation. During heating, the material transforms back to its initial state with equally distributed martensitic variants, i.e. $\xi^{\text{M}_\text{t}} = \xi^{\text{M}_\text{c}} \approx 0.5$.

the stress-strain response coincide with observations made in [59] for the same loading path.

The results presented show that the proposed model captures the stress-strain-temperature response of SMA, see Fig. 3.3. It also captures the pseudo-plastic response of SMA observed for low temperatures, as well as the pseudo-elastic response observed for high temperatures, cf. Figs. 3.3(a) and 3.4(d). Moreover, the model also captures experimentally observed behaviour of SMA in the context of tensile step tests. In particular, it reproduces stress-strain envelopes and appropriate stress-strain minor loops as investigated in [59].

3.2 Micro-sphere formulation

The presented scalar-valued model for the simulation of phase-transformations is embedded into a micro-sphere formulation in order to simulate three-dimensional boundary value problems. The local deformation state at small strains, $\boldsymbol{\varepsilon} := \nabla_{\boldsymbol{x}}^{\text{sym}} \boldsymbol{u}$, is split into volumetric and deviatoric contributions, $\boldsymbol{\varepsilon} = \boldsymbol{\varepsilon}_{\text{vol}} + \boldsymbol{\varepsilon}_{\text{dev}}$ with $\boldsymbol{\varepsilon}_{\text{vol}} = 1/3\,\text{tr}(\boldsymbol{\varepsilon})\boldsymbol{I}$ and

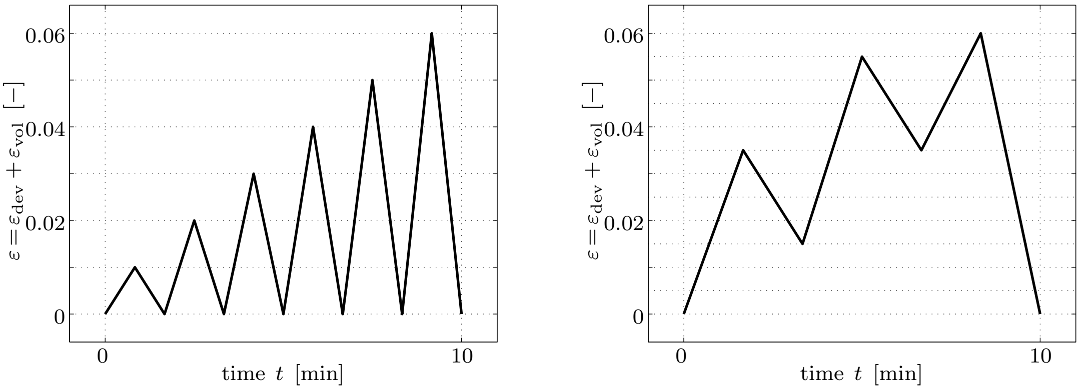

(a) Loading path applied – note that $\widehat{\varepsilon}_{\mathrm{dev}}(t) = \widehat{\varepsilon}_{\mathrm{vol}}(t)$.

(b) Loading path applied – note that $\widehat{\varepsilon}_{\mathrm{dev}}(t) = \widehat{\varepsilon}_{\mathrm{vol}}(t)$.

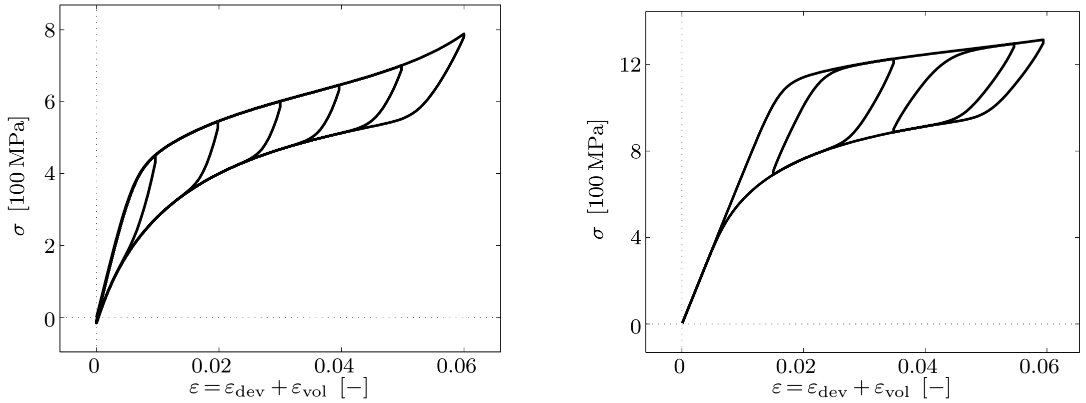

(c) Stress-strain response obtained at $\theta = 30\,^\circ\mathrm{C}$, loading path given in (a).

(d) Stress-strain response obtained at $\theta = 100\,^\circ\mathrm{C}$, loading path given in (b).

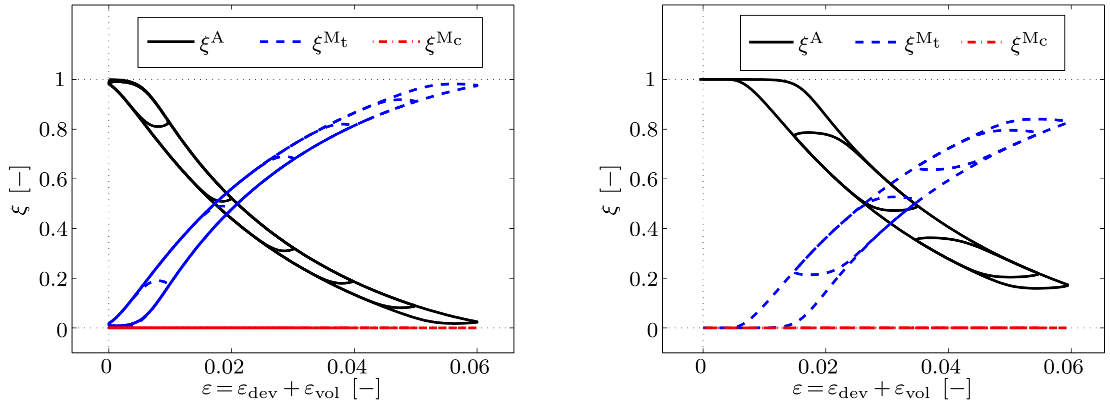

(e) Volume fractions obtained at $\theta = 30\,^\circ\mathrm{C}$, loading path given in (a).

(f) Volume fractions obtained at $\theta = 100\,^\circ\mathrm{C}$, loading path given in (b).

Figure 3.4: Scalar-valued model: responses obtained for step tests at $\theta = 30\,^\circ\mathrm{C}$, see (a), (c), (e), and $\theta = 100\,^\circ\mathrm{C}$, see (b), (d), (f). For both step tests a distinct envelope of the stress-strain response is predicted, which matches experimental observations as presented in, e.g., [59]—cf. Fig. 1.3 for a qualitative comparison to experimentally obtained curves of a similar NiTi shape memory alloy.

$\boldsymbol{\varepsilon}_{\text{dev}} = \boldsymbol{\varepsilon} - 1/3\,\text{tr}(\boldsymbol{\varepsilon})\boldsymbol{I}$, which are further projected onto each integration direction of the micro-sphere, see Section 3.2.1.1. Due to the considered volumetric-deviatoric split, the kinematic framework of the micro-sphere formulation used here becomes non-affine in the sense that the strain measure considered for a specific direction of interest does not only depend on the total strains projected onto this particular direction. In other words, the material responses obtained later on for the individual integration directions of the micro-sphere are not treated as independent one-dimensional responses—instead, for each integration direction $\boldsymbol{r}_i \in \mathbb{U}^2$ the macro-stress contribution $\boldsymbol{\sigma}_i$ will be given in terms of a second order tensorial quantity consisting of volumetric and deviatoric terms, see Section 3.2.1.2.

3.2.1 Three-dimensional extension of the model

The micro-sphere relations represent the scale-bridging equations between the micro-scale, where the scalar-valued phase-transformation model is applied, and the meso-scale, where the micro-sphere formulation is used. Due to the projections of the macroscropic strain tensor onto each integration direction, see Section 3.2.1.1, the volumetric and deviatoric strain contributions are transferred to the micro-level. Based on these strains and the history variables, the material response is evaluated. In the next step, the obtained micro-stresses have to be transferred back to the macro-level as shown in Section 3.2.1.2. Other micro-quantities, such as free energy expressions and spatial distributions of volume fractions can be transferred to the macro-level for post-processing purpose as shown in Sections 3.2.1.3 and 3.2.1.4.

3.2.1.1 Strains

In general, different kinematic constraints can be assumed within the so-called micro-sphere framework. In this chapter, we use a kinematically constrained non-affine micro-sphere model in small strain form, where the vector norm of the normal part $\boldsymbol{\varepsilon}_{r_i} = [\boldsymbol{r}_i \cdot \boldsymbol{\varepsilon} \cdot \boldsymbol{r}_i]\,\boldsymbol{r}_i$ of the projection of the strain tensor $\boldsymbol{\varepsilon}$ onto each integration direction $\boldsymbol{r}_i$ is split into the volumetric and deviatoric contributions ε_{dev} and ε_{vol}, namely

$$\boldsymbol{\varepsilon}_{r_i} = [\varepsilon_{\text{dev},i} + \varepsilon_{\text{vol}}]\,\boldsymbol{r}_i \quad \text{with} \quad \varepsilon_{\text{dev},i} = \boldsymbol{r}_i \cdot \boldsymbol{\varepsilon} \cdot \boldsymbol{r}_i - 1/3\,\text{tr}(\boldsymbol{\varepsilon}) \quad \text{and} \quad \varepsilon_{\text{vol}} = 1/3\,\text{tr}(\boldsymbol{\varepsilon}) \quad . \tag{3.51}$$

Using this approach in combination with volumetric and deviatoric elasticity coefficients on the micro-level, $\mathsf{E}_{\text{vol}} = \mathsf{E}/[1 - 2\,\nu_{\text{P}}]$ and $\mathsf{E}_{\text{dev}} = 5\,\mathsf{E}/[2 + 2\,\nu_{\text{P}}]$, facilitates the capturing of different Young's moduli E and Poisson's ratios $\nu_{\text{P}} \in [-1, 0.5]$ on the macro-level, cf. [27]. Further kinematic approaches are discussed in, e.g., [29, 74, 92].

3.2.1.2 Stresses

Using the micro-sphere approach, the macroscopic stress tensor $\boldsymbol{\sigma}$ is obtained by integration over the unit sphere, i.e.

$$\boldsymbol{\sigma} = \frac{1}{4\pi} \int_{\mathbb{U}^2} \frac{\partial \Psi}{\partial \boldsymbol{\varepsilon}} \, \mathrm{d}a \quad , \tag{3.52}$$

cf. [74, 92, 101] among others. To approximate this equation numerically, a finite number of integration directions is considered. The constitutive relation is evaluated in every such direction, where the respective strain- and history-dependent material response related to each integration direction $\boldsymbol{r}_i$ contributes to the macroscopic stress tensor $\boldsymbol{\sigma}$ in terms of

$$\boldsymbol{\sigma} \approx \sum_{i=1}^{n_r} \frac{\partial \Psi_i}{\partial \boldsymbol{\varepsilon}} \, \bar{w}_i \tag{3.53}$$

with $\partial \Psi_i / \partial \boldsymbol{\varepsilon}$ the contribution of the ith integration direction weighted by the normalised weighting factor $\bar{w}_i$. Here and in the following, $\Psi_i = \widehat{\Psi}_i(\varepsilon_{\mathrm{dev},i}, \varepsilon_{\mathrm{vol}}, \boldsymbol{\xi}_i)$ is the overall potential of the phase mixture, where $\boldsymbol{\xi}_i = [\xi_i^1, \ldots, \xi_i^\nu]^{\mathrm{t}} \in \mathbb{R}^{\nu \times 1}$ is the collection of the volume fractions present in the integration direction $\boldsymbol{r}_i$. Applying the chain rule to the partial derivative of the overall phase potential Ψ_i with respect to the strain tensor $\boldsymbol{\varepsilon}$ yields

$$\begin{aligned} \frac{\partial \Psi_i}{\partial \boldsymbol{\varepsilon}} &= \frac{\partial \Psi_i}{\partial \varepsilon_{\mathrm{vol}}} \frac{\partial \varepsilon_{\mathrm{vol}}}{\partial \boldsymbol{\varepsilon}} + \frac{\partial \Psi_i}{\partial \varepsilon_{\mathrm{dev},i}} \frac{\partial \varepsilon_{\mathrm{dev},i}}{\partial \boldsymbol{\varepsilon}} && (3.54) \\ &= \frac{\partial \Psi_i}{\partial \varepsilon_{\mathrm{vol}}} \frac{1}{3} \boldsymbol{I} + \frac{\partial \Psi_i}{\partial \varepsilon_{\mathrm{dev},i}} \left[\boldsymbol{r}_i \otimes \boldsymbol{r}_i - \frac{1}{3} \boldsymbol{I} \right] && (3.55) \end{aligned}$$

for every integration direction $\boldsymbol{r}_i$ of the micro-sphere. Considering (3.5) together with (3.3), the remaining terms $\partial \Psi_i / \partial \varepsilon_{\mathrm{vol}}$ and $\partial \Psi_i / \partial \varepsilon_{\mathrm{dev}}$ in (3.55) can be evaluated as

$$\begin{aligned} \frac{\partial \Psi_i}{\partial \varepsilon_{\mathrm{vol}}} &= \frac{\partial}{\partial \varepsilon_{\mathrm{vol}}} \sum_{\alpha=1}^{\nu} \xi_i^\alpha \widehat{\psi}_i^\alpha(\varepsilon_{\mathrm{dev},i}, \varepsilon_{\mathrm{vol}}, \theta) && (3.56) \\ &= \sum_{\alpha=1}^{\nu} \xi_i^\alpha \left[\mathsf{E}_{\mathrm{vol}}^\alpha \left[\varepsilon_{\mathrm{vol}} - \varepsilon_{\mathrm{tr,vol}}^\alpha \right] - \zeta^\alpha \mathsf{E}^\alpha \left[\theta - \theta_0 \right] \right] && (3.57) \end{aligned}$$

and

$$\begin{aligned} \frac{\partial \Psi_i}{\partial \varepsilon_{\mathrm{dev},i}} &= \frac{\partial}{\partial \varepsilon_{\mathrm{dev},i}} \sum_{\alpha=1}^{\nu} \xi_i^\alpha \widehat{\psi}_i^\alpha(\varepsilon_{\mathrm{dev},i}, \varepsilon_{\mathrm{vol}}, \theta) && (3.58) \\ &= \sum_{\alpha=1}^{\nu} \xi_i^\alpha \left[\mathsf{E}_{\mathrm{dev}}^\alpha \left[\varepsilon_{\mathrm{dev},i} - \varepsilon_{\mathrm{tr,dev}}^\alpha \right] - \zeta^\alpha \mathsf{E}^\alpha \left[\theta - \theta_0 \right] \right] \quad , && (3.59) \end{aligned}$$

with the volumetric strain projection $\varepsilon_{\mathrm{vol}}$ being identical for all integration directions. In contrast to that, for every integration direction $\boldsymbol{r}_i$ of the micro-sphere the deviatoric strain projections $\varepsilon_{\mathrm{dev},i}$ and the volume fractions of all phases ξ_i^α need to be considered and evaluated individually. The stress response at the, say, macro-level, i.e. the stress response of the micro-sphere (3.53), is finally obtained from

$$\begin{aligned}\boldsymbol{\sigma} \approx \sum_{i=1}^{n_r}\sum_{\alpha=1}^{\nu} \xi_i^\alpha \bigg[\frac{1}{3}\left[\mathsf{E}_{\mathrm{vol}}^\alpha\left[\varepsilon_{\mathrm{vol}} - \varepsilon_{\mathrm{tr,vol}}^\alpha\right] - \zeta^\alpha\,\mathsf{E}^\alpha\left[\theta-\theta_0\right]\right]\boldsymbol{I} \\ + \left[\mathsf{E}_{\mathrm{dev}}^\alpha\left[\varepsilon_{\mathrm{dev},i} - \varepsilon_{\mathrm{tr,dev}}^\alpha\right] - \zeta^\alpha\,\mathsf{E}^\alpha\left[\theta-\theta_0\right]\right]\left[\boldsymbol{r}_i\otimes\boldsymbol{r}_i - \frac{1}{3}\boldsymbol{I}\right]\bigg]\bar{w}_i \end{aligned} \tag{3.60}$$

3.2.1.3 Meso-scale free energy

The meso-scale free energy density $\varPsi^{\mathrm{ms}}$ is obtained by averaging the microscopic free energy densities $\varPsi = \widehat{\varPsi}(\varepsilon_{\mathrm{dev}}, \varepsilon_{\mathrm{vol}}, \boldsymbol{\xi}, \theta)$ via

$$\widehat{\varPsi}^{\mathrm{ms}}(\varPsi_1, ..., \varPsi_{n_r}) = \frac{1}{4\pi}\int_{\mathbb{U}^2} \varPsi\,\mathrm{d}a \approx \sum_{i=1}^{n_r} \varPsi_i\,\bar{w}_i \quad , \tag{3.61}$$

With $\bar{w}_i$ denoting the respective integration factors. The numerical evaluation of (3.61) is facilitated by consideration of the free energy contributions ψ_i^α in the given integration direction $\boldsymbol{r}_i$, i.e.

$$\varPsi_i = \sum_{\alpha=1}^{\nu} \xi_i^\alpha\,\widehat{\psi}_i^\alpha(\varepsilon_{\mathrm{dev},i}, \varepsilon_{\mathrm{vol}}, \theta) \quad , \tag{3.62}$$

inducing

$$\varPsi^{\mathrm{ms}} = \sum_{i=1}^{n_r}\left[\sum_{\alpha=1}^{\nu} \xi_i^\alpha\,\widehat{\psi}_i^\alpha(\varepsilon_{\mathrm{dev},i}, \varepsilon_{\mathrm{vol}}, \theta)\right]\bar{w}_i \tag{3.63}$$

for the computation of $\varPsi^{\mathrm{ms}}$.

3.2.1.4 Meso-scale volume fractions

One advantage of the micro-sphere approach is the possibility to derive texture-type structural tensors of different order. For example, the micro-sphere volume fractions $\varXi^\alpha = \widehat{\varXi}^\alpha(\xi^\alpha)$, which represent a moment of zeroth order, can be obtained by integration over the unit sphere, i.e.

$$\varXi^\alpha = \sum_{i=1}^{n_r} \xi_i^\alpha\,\bar{w}_i \tag{3.64}$$

with ξ_i^α the volume fraction of phase α situated in the i th integration direction $\boldsymbol{r}_i$. From a macroscopic point of view, a more detailed insight in the anisotropy of the material is obtained by computing, e.g., a second-order structural tensor that gives additional information about the spatial distribution of volume fractions. By analogy with the elasticity tensor E_{el} higher-order moments can be introduced but are not applied as this chapter proceeds.

3.2.1.5 Elasticity tensor

The anisotropic approximated elasticity tensor can be evaluated as

$$\mathsf{E}_{\text{el}} = \frac{\partial}{\partial \boldsymbol{\varepsilon}} \sum_{i=1}^{n_r} \frac{\partial \varPsi_i}{\partial \boldsymbol{\varepsilon}} \bar{w}_i \tag{3.65}$$

with the help of (3.53). Considering (3.55) in addition yields

$$\begin{aligned}
\mathsf{E}_{\text{el}} &= \frac{\partial}{\partial \boldsymbol{\varepsilon}} \sum_{i=1}^{n_r} \left[\frac{\partial \varPsi_i}{\partial \varepsilon_{\text{vol}}} \frac{1}{3} \boldsymbol{I} + \frac{\partial \varPsi_i}{\partial \varepsilon_{\text{dev},i}} \left[\boldsymbol{r}_i \otimes \boldsymbol{r}_i - \frac{1}{3} \boldsymbol{I} \right] \right] \bar{w}_i && (3.66)\\
&= \sum_{i=1}^{n_r} \left[\frac{\partial^2 \varPsi_i}{\partial \varepsilon_{\text{vol}}\, \partial \varepsilon_{\text{vol}}} \frac{1}{3} \boldsymbol{I} \otimes \frac{\partial \varepsilon_{\text{vol}}}{\partial \boldsymbol{\varepsilon}} \right. && (3.67)\\
&\qquad \left. + \frac{\partial^2 \varPsi_i}{\partial \varepsilon_{\text{dev},i}\, \partial \varepsilon_{\text{dev},i}} \left[\boldsymbol{r}_i \otimes \boldsymbol{r}_i - \frac{1}{3} \boldsymbol{I} \right] \otimes \frac{\partial \varepsilon_{\text{dev},i}}{\partial \boldsymbol{\varepsilon}} \right] \bar{w}_i && (3.68)\\
&= \sum_{i=1}^{n_r} \left[\frac{\partial^2 \varPsi_i}{\partial \varepsilon_{\text{vol}}\, \partial \varepsilon_{\text{vol}}} \mathsf{I}^{\text{vol}} + \frac{\partial^2 \varPsi_i}{\partial \varepsilon_{\text{dev},i}\, \partial \varepsilon_{\text{dev},i}} \mathsf{D}_i \right] \bar{w}_i && (3.69)
\end{aligned}$$

with the fourth-order tensors $\mathsf{I}^{\text{vol}} = 1/3\, \boldsymbol{I} \otimes \boldsymbol{I}$ and $\mathsf{D}_i = [\boldsymbol{r}_i \otimes \boldsymbol{r}_i - 1/3\, \boldsymbol{I}] \otimes [\boldsymbol{r}_i \otimes \boldsymbol{r}_i - 1/3\, \boldsymbol{I}]$. Evaluating the derivatives of (3.57) and (3.59) with respect to ε_{vol} and $\varepsilon_{\text{dev},i}$, respectively, allows to express the elasticity tensor as

$$\mathsf{E}_{\text{el}} = \sum_{i=1}^{n_r} \sum_{\alpha=1}^{\nu} \xi_i^\alpha \left[\mathsf{E}_{\text{vol}}^\alpha\, \mathsf{I}^{\text{vol}} + \mathsf{E}_{\text{dev}}^\alpha\, \mathsf{D}_i \right] \bar{w}_i \quad . \tag{3.70}$$

For the investigation of the anisotropic properties of the elasticity tensor, we generate Young's modulus surface plots as e.g. elaborated in [23, 31, 142]. In this context, we compute the fourth-order compliance tensor $\mathsf{C}_{\text{el}} := \mathsf{E}_{\text{el}}^{-1}$ and project this quantitiy onto directions $\boldsymbol{d}$, where the latter are unit vectors obtained from a parametrisation of the unit sphere $\mathbb{U}^2$ in terms of, e.g.,

$$\boldsymbol{d}(\vartheta, \varphi) = \sin(\vartheta) \cos(\varphi)\, \boldsymbol{e}_1 + \sin(\vartheta) \sin(\varphi)\, \boldsymbol{e}_2 + \cos(\vartheta)\, \boldsymbol{e}_3 \tag{3.71}$$

with $\vartheta \in [0, \pi]$, $\varphi \in [0, 2\,\pi]$ and $\boldsymbol{e}_i \cdot \boldsymbol{e}_j = \delta_{ij}$. The projection $\delta^{\mathsf{C}_{\text{el}}}(\mathsf{C}_{\text{el}}, \boldsymbol{d})$ of the fourth-order compliance tensor on each of the unit vectors $\boldsymbol{d}(\vartheta, \varphi)$ according to

$$\delta^{\mathsf{C}_{\text{el}}}(\mathsf{C}_{\text{el}}, \boldsymbol{d}) = [\boldsymbol{d} \otimes \boldsymbol{d}] : \mathsf{C}_{\text{el}} : [\boldsymbol{d} \otimes \boldsymbol{d}] \tag{3.72}$$

yields the inverse of the Young's modulus in direction $\boldsymbol{d}$, see [31]. To this end, for the computation of the macroscopic scalar-valued Young's modulus $\mathsf{E}(\boldsymbol{d})$ as a function of the spatial direction $\boldsymbol{d}$ we evaluate

$$\mathsf{E}(\boldsymbol{d}) = \delta^{-1\mathsf{C}_{\text{el}}}(\mathsf{C}_{\text{el}}, \boldsymbol{d}) = [\,[\boldsymbol{d} \otimes \boldsymbol{d}] : \mathsf{C}_{\text{el}} : [\boldsymbol{d} \otimes \boldsymbol{d}]\,]^{-1} \tag{3.73}$$

for each direction of interest. See Figs. 3.6 and 3.7 for a computational example including a graphical representations of $\mathsf{E}(\boldsymbol{d})$ for selected representative deformation states.

3.2.2 Micro-sphere application – computational examples at the meso-level

In this section, the constitutive response of the previously described model is presented for two characteristic homogeneous deformation states. We investigate a purely deviatoric tension-compression load cycle, see Fig. 3.6, and a mixed volumetric-deviatoric tension-compression load cycle, see Fig. 3.7. We assume quasi-static loading conditions with quasi-static strain-rates of $|\dot{\varepsilon}| = 10^{-4}$ and apply the material parameters provided in Section 3.5.1. For both load cases, the stress-strain response in terms of the $\sigma_{11} = \boldsymbol{e}_1 \cdot \boldsymbol{\sigma} \cdot \boldsymbol{e}_1$ stress component is computed. Moreover, the spatial distributions of volume fractions and Young's modulus surface plots—allowing for the assessment of the anisotropy evolution—are provided at the states of maximum tension and maximum compression.

For the investigation of the behaviour of the material model under purely deviatoric tension-compression, the applied macroscopic strain $\boldsymbol{\varepsilon} = \widehat{\boldsymbol{\varepsilon}}(t)$, is set to

$$\widehat{\boldsymbol{\varepsilon}}(t) = \widehat{\kappa}(t)\, \varepsilon_0\, [3/2\, \boldsymbol{e}_1 \otimes \boldsymbol{e}_1 - 1/2\, \boldsymbol{I}] \tag{3.74}$$

with a linearly varying scaling factor $\kappa = \widehat{\kappa}(t) \in [-1, 1]$ and a maximum strain magnitude of $\varepsilon_0 = 0.07$. Fig. 3.6(a) depicts the loading path obtained in $\boldsymbol{e}_1$-direction. Since the macroscopic strain tensor is purely deviatoric, the volumetric strains being transferred to the micro-level are zero for all integration directions of the micro-sphere. As initial conditions, we choose a stress- and strain-free configuration of pure austenite, i.e. $\xi^{\text{A}}|_{t_0} = 1, \xi^{\text{M}_\text{t}}|_{t_0} = \xi^{\text{M}_\text{c}}|_{t_0} = 0$. The material response is investigated for a fixed temperature of $\theta = 30\,^\circ\text{C}$. The transformation intensities by means of directionally dependent phase fractions are displayed in Figs. 3.6(c) and 3.6(d) for the states of maximum tension and compression, respectively. Furthermore, the spherical projections of Young's moduli $\mathsf{E}(\boldsymbol{d})$ are depicted in Figs. 3.5(a) and 3.5(b).

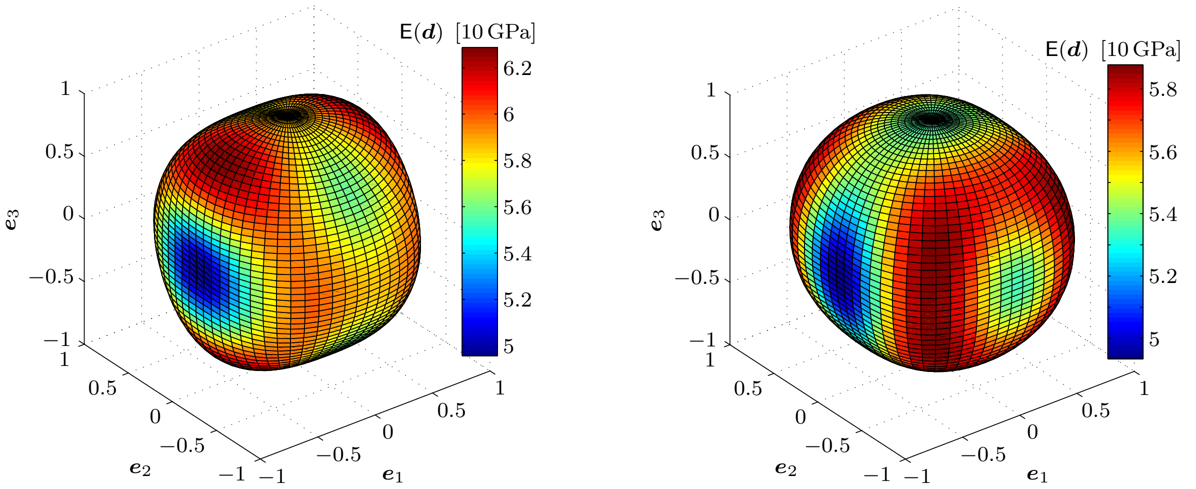

(a) Distribution of directional Young's moduli at maximum tension, i.e. at $\widehat{\kappa}(t)\,\varepsilon_0 = 0.07$, cf. Fig. 3.6(b).

(b) Distribution of directional Young's moduli at maximum compression, i.e. at $\widehat{\kappa}(t)\,\varepsilon_0 = -0.07$, cf. Fig. 3.6(b).

Figure 3.5: Distribution of directional Young's moduli corresponding to the anisotropic material states provided in Figs. 3.6(c) and 3.6(d), respectively.

The results obtained for mixed volumetric-deviatoric tension-compression are provided in Fig. 3.7. For this computation, the macroscopic strain tensor is set to

$$\widehat{\boldsymbol{\varepsilon}}(t) = \widehat{\kappa}(t)\,\varepsilon_0\,[\boldsymbol{e}_1 \otimes \boldsymbol{e}_1] \tag{3.75}$$

with a non-zero volumetric part, resulting in a loading path in $\boldsymbol{e}_1$-direction as depicted in Fig. 3.7(a). The volumetric strains ε_{vol} being transferred to the micro-level are identical for all integration directions. Due to the volumetric parts of the load, a higher maximum stress level is reached when compared to the purely deviatoric load case, cf. Fig. 3.7(b). As in the deviatoric case, the transformation intensities displayed in Figs. 3.7(c) and 3.7(d) and the spherical projections of Young's moduli $\mathsf{E}(\boldsymbol{d})$, Figs. 3.8(a) and 3.8(b), refer to the states of maximum tension and compression, respectively.

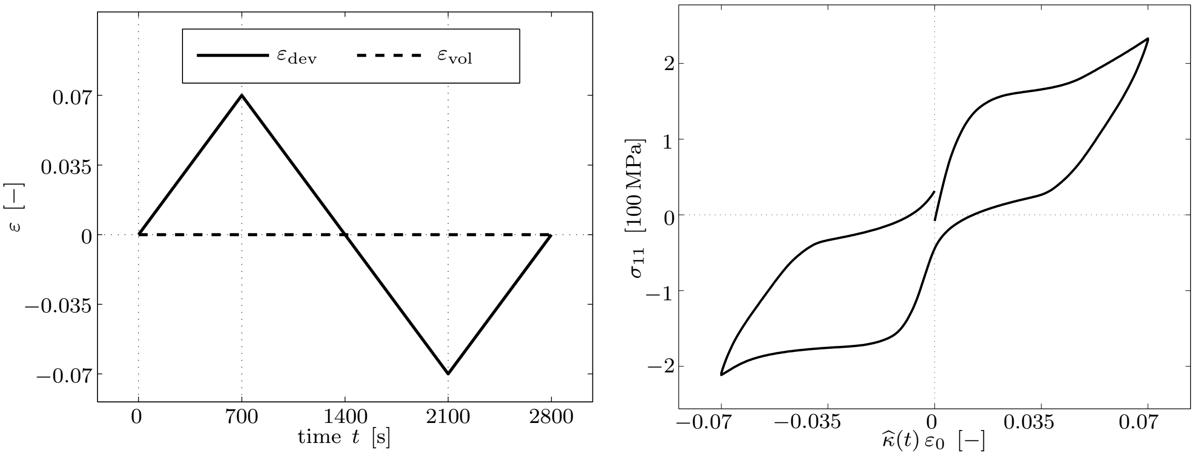

(a) Loading path obtained in $\boldsymbol{e}_1$-direction.

(b) Stress-strain response.

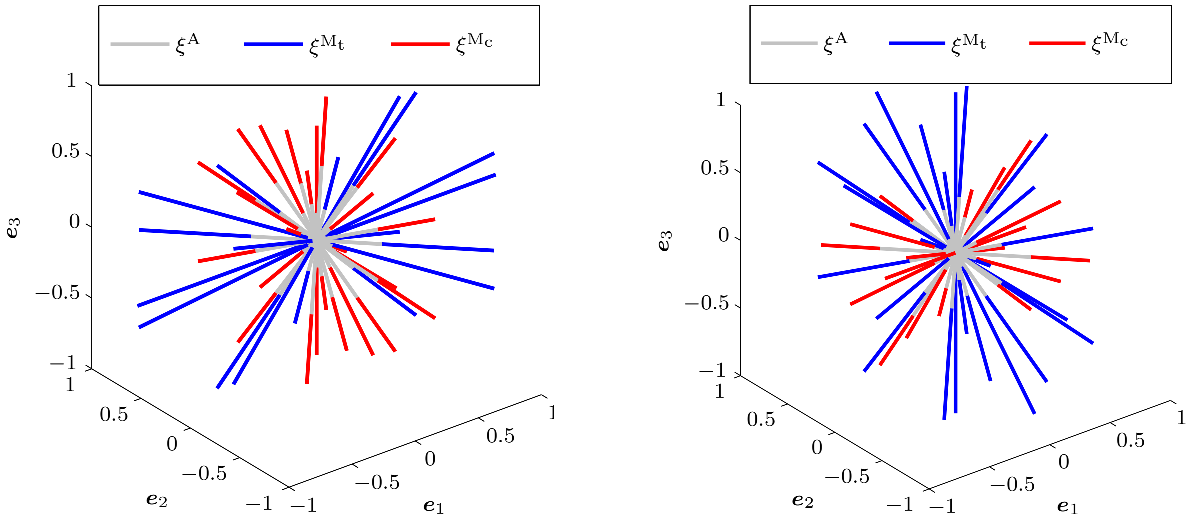

(c) Spatial distribution of volume fractions at maximum tension, i.e. at $\widehat{\kappa}(t)\,\varepsilon_0 = 0.07$, cf. (b).

(d) Spatial distribution of volume fractions at maximum compression, i.e. at $\widehat{\kappa}(t)\,\varepsilon_0 = -0.07$, cf. (b).

Figure 3.6: Meso-scale response obtained at $\theta = 30\,^\circ\text{C}$ for a purely deviatoric load of $\widehat{\boldsymbol{\varepsilon}}(t) = \widehat{\kappa}(t)\,\varepsilon_0\,[3/2\,\boldsymbol{e}_1 \otimes \boldsymbol{e}_1 - 1/2\,\boldsymbol{I}]$. Quasi-static loading conditions with a maximum strain rate of $|\dot{\varepsilon}| = 10^{-4}\,\text{s}^{-1}$ are applied.

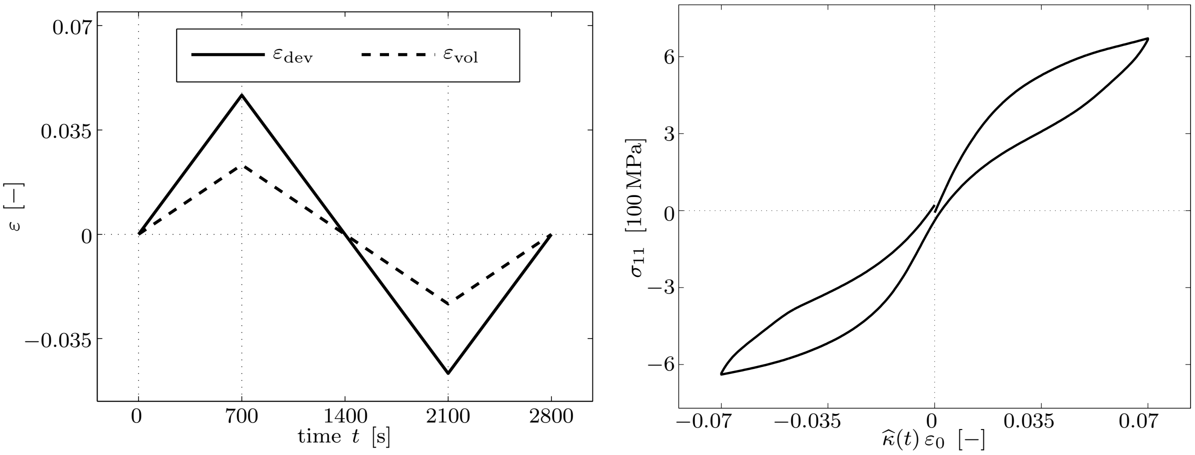

(a) Loading path obtained in $\boldsymbol{e}_1$-direction.

(b) Stress-strain response.

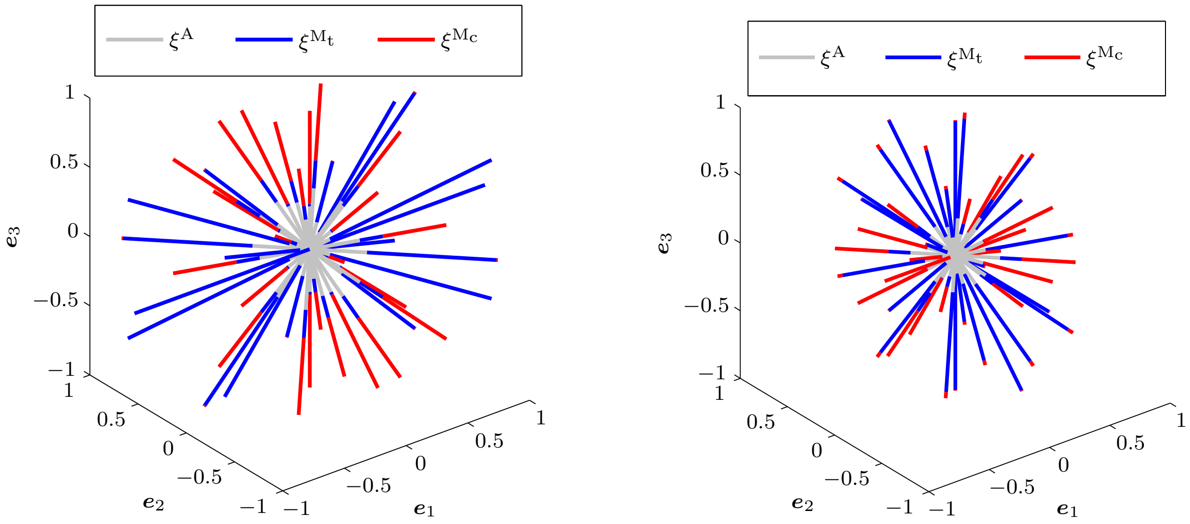

(c) Spatial distribution of volume fractions at maximum tension, i.e. at $\widehat{\kappa}(t)\,\varepsilon_0 = 0.07$, cf. (b).

(d) Spatial distribution of volume fractions at maximum compression, i.e. at $\widehat{\kappa}(t)\,\varepsilon_0 = -0.07$, cf. (b).

Figure 3.7: Meso-scale response obtained at $\theta = 30\,^\circ\text{C}$ for a mixed volumetric-deviatoric load of $\widehat{\boldsymbol{\varepsilon}}(t) = \widehat{\kappa}(t)\,\varepsilon_0\,[\boldsymbol{e}_1 \otimes \boldsymbol{e}_1]$. Quasi-static loading conditions with a maximum strain rate of $|\dot{\varepsilon}| = 10^{-4}\,\text{s}^{-1}$ are applied.

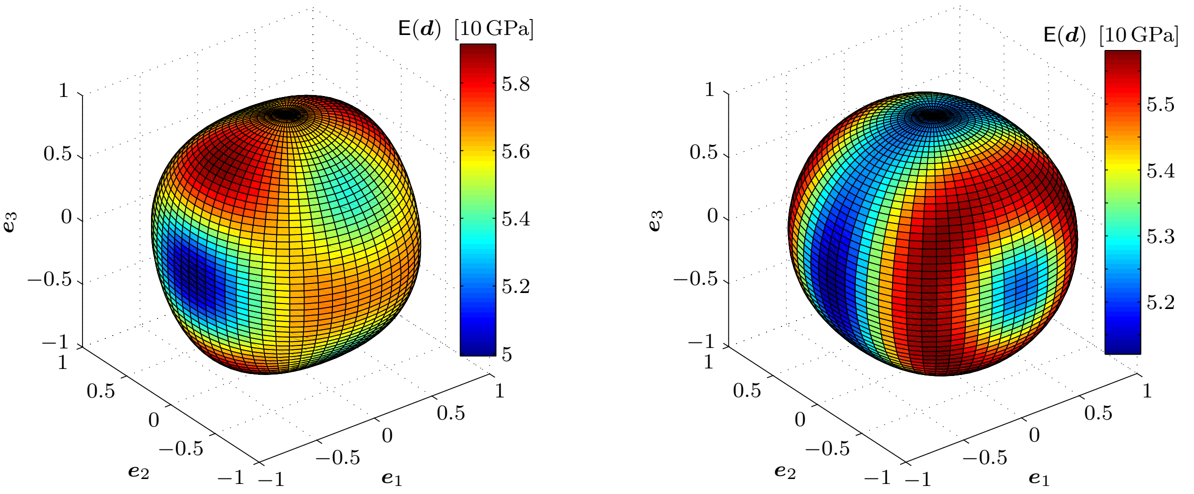

(a) Distribution of directional Young's moduli at maximum tension, i.e. at $\widehat{\kappa}(t)\,\varepsilon_0 = 0.07$, cf. Fig. 3.7(b).

(b) Distribution of directional Young's moduli at maximum compression, i.e. at $\widehat{\kappa}(t)\,\varepsilon_0 = -0.07$, cf. Fig. 3.7(b).

Figure 3.8: Distribution of directional Young's moduli corresponding to the anisotropic material states provided in Figs. 3.7(c) and 3.7(d), respectively.

3.3 Finite element implementation

In this section, we show the results of a finite element implementation of the model. As an example for a three-dimensional boundary value problem, we investigate a block-shaped body of the size 5 mm × 5 mm × 10 mm under combined torsion and tension load states. The results of the finite element computations are provided in terms of displacements, stresses, tensile forces, torsional reaction moment and distribution of volume fractions. To this end, the second-order stress tensor and the fourth-order elasticity tensor are computed according to (3.60) and (3.70), respectively. For the macroscopic volume fractions, we restrict this chapter to the computation of scalar-valued macroscopic quantities as derived in (3.64).

The loading path provided in Fig. 3.9(a) shows the four load steps applied. In the first step, at $0 < t < 1000\,\mathrm{s}$, the considered body is subjected to a linearly increasing torsional displacement up to an angle of $\varphi(t = 1000\,\mathrm{s}) = 15°$ on the top surface, while the vertical displacements of the top surface are constrained to zero. Next, at $1000\,\mathrm{s} < t < 2000\,\mathrm{s}$, the block is stretched by a linear increase of the displacement of its top surface at a constant torsional angle of $\varphi = 15°$. As the maximum tensile displacement of $u_{\max} = 1\,\mathrm{mm}$ is reached, the torsion angle is first reduced to zero and then the block is compressed back to its initial height of $h(t = 0) = h(t = 4000\,\mathrm{s}) = 10\,\mathrm{mm}$.

The linearly increasing torsional load applied during $0 < t < 1000\,\mathrm{s}$ leads to a reaction force and torsional reaction moment provided in Fig. 3.10. First, the reaction moment increases proportionally to time – while also being proportional to the applied torsional load. Due to the activation of phase-transformations, the graph of the reaction moment flattens since the martensitic phases with lower Young's modulus evolve in parts – finally reaching a maximum torsional reaction moment of $M = 25\,\mathrm{Nm}$. Fig. 3.11(a) shows the distribution of the remaining austenitic volume fraction at time $t = 1000\,\mathrm{s}$. The spatially inhomogeneous distribution of tensile stresses, i.e. $\sigma_{33} = \boldsymbol{e}_3 \cdot \boldsymbol{\sigma} \cdot \boldsymbol{e}_3$, is presented in Fig. 3.11(b). Note the existence of regimes of positive and negative tensile stress on the top surface, corresponding to a comparatively small total tensile force observed during the purely torsional load, cf. Fig. 3.10(a). The occurrence of a non-zero tensile force resulting from torsion is related to a swift-type effect.

During the time interval $1000\,\mathrm{s} < t < 2000\,\mathrm{s}$, the tensile load increases proportionally to time, cf. Fig. 3.9(a), and causes distinct transformations from the austenitic parent phase to the martensitic phases. Due to the ongoing transformation to the softer martensitic phases caused by the tensile load, the torsional reaction moment M shown in Fig. 3.10(b) decreases until transformations reach a saturation state and a slight increase of the reaction moment is observed as the tensile load increases further. At the end of the tensile load cycle, $t = 2000\,\mathrm{s}$, the remaining austenitic volume fraction reaches from $\varXi^{\mathrm{A}} \approx 0.16 \ldots 0.32$, see Fig. 3.12(a). The maximum tensile force $F \approx 11\,\mathrm{kN}$ obtained at $t = 2000\,\mathrm{s}$, see Fig. 3.10(a), corresponds to an average tensile stress of $\sigma_{33}^{\mathrm{avg}} \approx 450\,\mathrm{MPa}$ on the $5\,\mathrm{mm} \times 5\,\mathrm{mm}$ top surface area, cf. Fig. 3.12(b).

When reverting the torsional load, $2000\,\mathrm{s} < t < 3000\,\mathrm{s}$, the magnitude of both the tensile force and the torsional reaction moment decreases, see Figs. 3.10(a) and 3.10(b). For the given temperature level, a pseudo-plasticity-like effect is observed, where the torsional reaction moment changes sign during reversal of the load, ending up with a negative reaction moment of $M \approx -5\,\mathrm{Nm}$ at $t = 3000\,\mathrm{s}$. Corresponding to the decrease in the tensile force, the tensile stresses shown in Fig. 3.13(b) decreased as well when compared to Fig. 3.12(b). Note that the reversal of the torsional load leads to further transformations from austenite to martensite, cf. Fig. 3.13(a).

Finally, when the material block is deformed back to its initial shape at $t = 4000\,\mathrm{s}$, we end up with a slight pseudo-plasticity-like compression force of $F \approx -1\,\mathrm{kN}$, see Fig. 3.10(a). The corresponding inhomogeneous distribution of compressive stresses within the body is shown in Fig. 3.14(b). While tension is released, large parts of the material transform back to the initial austenitic phase as depicted in Fig. 3.14(a). At the same time, the torsional reaction moment provided in Fig. 3.10(b) tends towards its inital zero value.

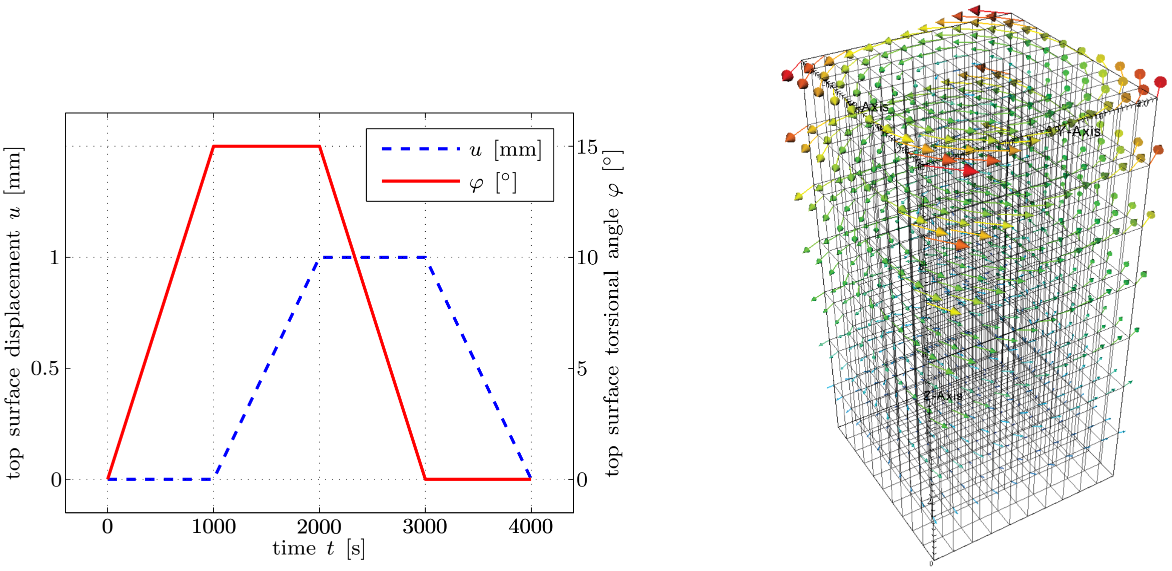

(a) Load path applied to the top surface.

(b) Finite element discretisation.

Figure 3.9: Finite element simulation: the loading path applied to the top surface is given in (a). The considered finite element discretisation using eight node hexahedron elements is provided in (b). Note that the arrows in (b) indicate the displacement increments obtained during the first torsional load step, i.e. during $0 < t < 1000\,\text{s}$. For the simulation we assume quasi-static loading conditions with an overall simulated time of $t_{\text{max}} = 4000\,\text{s}$, cf. (a).

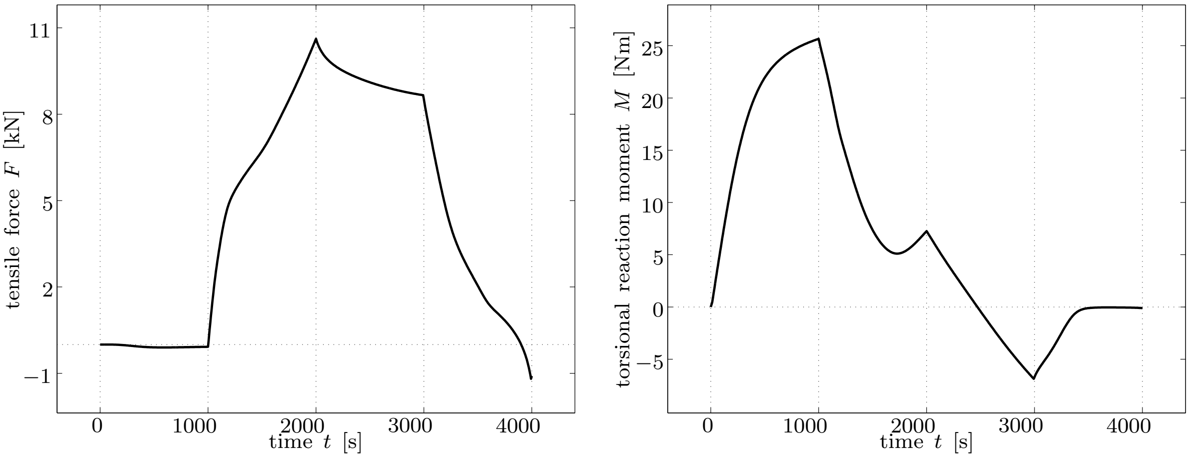

(a) Computed tensile reaction force.

(b) Computed torsional reaction moment.

Figure 3.10: Tensile force F and torsional reaction moment M obtained due to the applied loading history, see Fig. 3.9(a) for the loading path chosen. The overall load history is subdivided in four sections: $0 < t < 1000\,\text{s}$, time-proportional torsional load; $1000\,\text{s} < t < 2000\,\text{s}$, subsequent time-proportional tension; $2000\,\text{s} < t < 3000\,\text{s}$, time-proportional undoing of torsion; $3000\,\text{s} < t < 4000\,\text{s}$, time-proportional release of tension. At $t = 4000\,\text{s}$ the top and bottom surface of the material body have returned to their initial shapes.

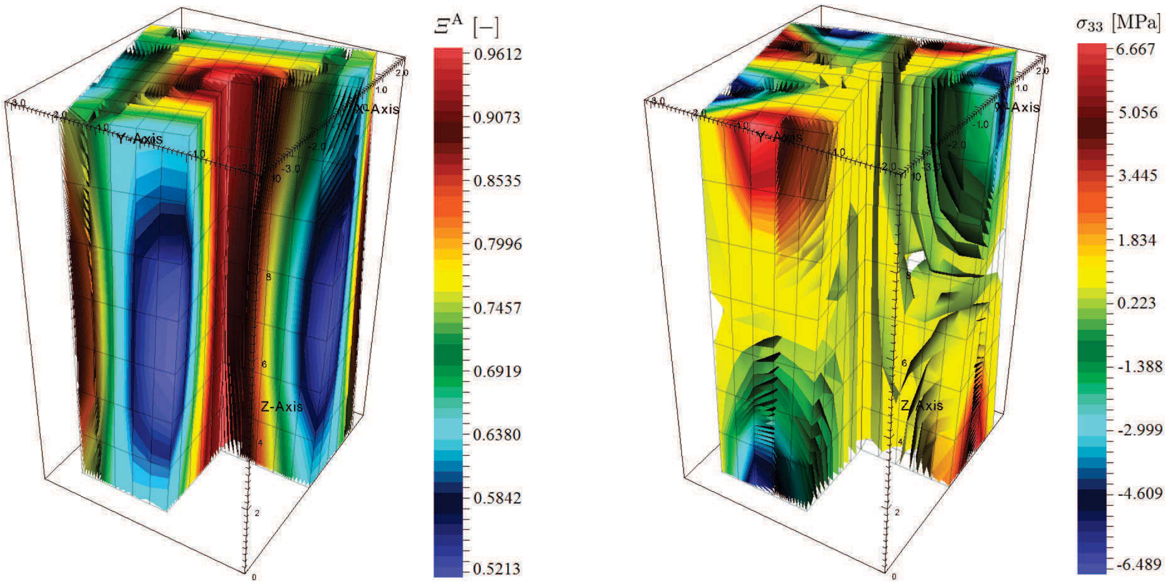

(a) Macroscopic austenite Ξ^{A}.

(b) Tensile stress resulting from anisotropy.

Figure 3.11: Test specimen after torsion – maximum torsion angle $\varphi = 15°$ at time $t = 1000\,\mathrm{s}$, cf. Fig. 3.9(a).

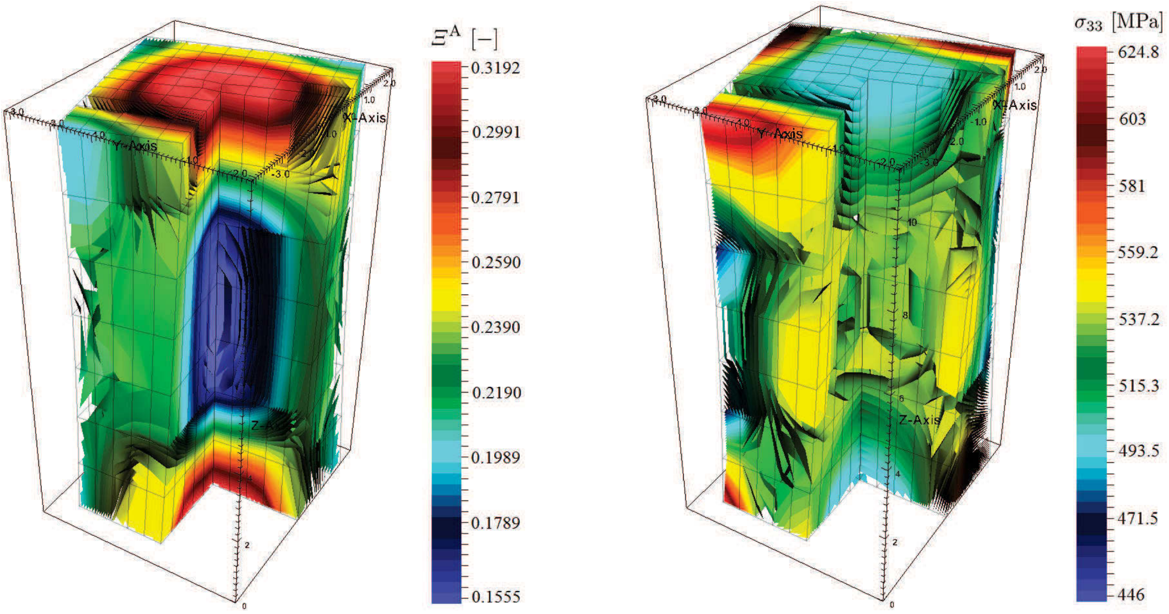

(a) Macroscopic austenite Ξ^{A}.

(b) Tensile stress.

Figure 3.12: Test specimen after torsion and tension – maximum torsion angle $\varphi = 15°$ and maximum tensile displacement $u = 1\,\mathrm{mm}$ at time $t = 2000\,\mathrm{s}$, cf. Fig. 3.9(a).

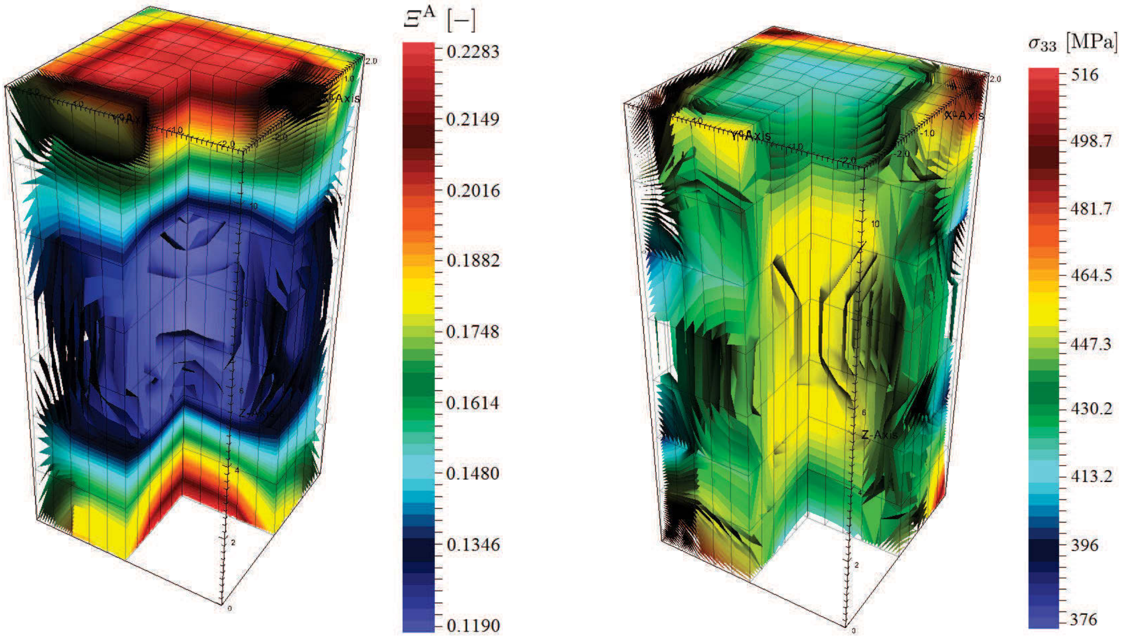

(a) Macroscopic austenite Ξ^A.

(b) Tensile stress.

Figure 3.13: Tensioned test specimen with $u = u_{\max} = 1\,\text{mm}$ and reversed torsion loading to $\varphi = 0$ at time $t = 3000\,\text{s}$, cf. Fig. 3.9(a).

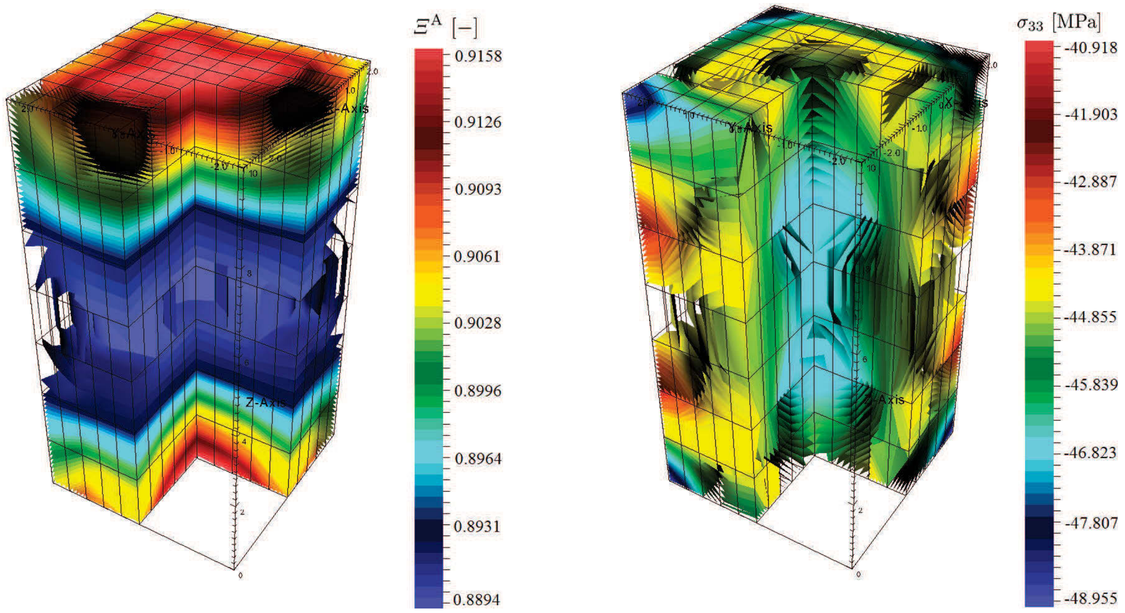

(a) Macroscopic austenite Ξ^A.

(b) Tensile stress.

Figure 3.14: Test specimen with reversed tension and torsion loading, i.e. with $u = 0\,\text{mm}$ and $\varphi = 0$ at time $t = 4000\,\text{s}$, cf. Fig. 3.9(a).

3.4 Summary

In this chapter, an enhanced approach for the modelling and simulation of solid-to-solid phase-transformations is introduced. The underlying phase-transformation scheme utilising micro-mechanically motivated material quantities and transformation probabilities based on statistical physics was introduced in [51] for a simple one-dimensional model. In Chapter 2, this model was extended to three dimensions using the simplified affine micro-sphere approach, see [101]. In order to capture varying Young's moduli and Poisson's ratios of the macro-scale, a non-affine micro-sphere framework including volumetric-deviatoric splits of the macroscopic strain tensor has been adopted as elaborated in, e.g., [27]. However, the introduction of a volumetric-deviatoric split in the micro-sphere kinematics has a significant impact on the underlying micro-scale model. To be specific, the introduction of independent volumetric and deviatoric micro-strains in the Helmholtz free energies of each considered phase leads to Gibbs phase potentials that are no longer simple parabolas, but now take the form of elliptical paraboloids in volumetric-deviatoric strain space. As a result, the computation of the actual Gibbs energy barriers which serve as threshold-type values for the transformation from one phase to another, turn into a computationally advanced problem. In this context, we make use of a numerical minimisation scheme for the highly non-linear problem to solve for the minimum of the parametric Gibbs energy intersection curves, see Section 3.1.4.

To underline the capabilities of the model established in this chapter, we discuss representative numerical examples not only on the micro-level, see Section 3.1.5, but also on the micro-sphere-level, Section 3.2.2, as well as on the finite element level, see Section 3.3. On the micro-scale, we show that the proposed model captures the experimentally observed stress-strain-temperature response—known as one of the main feature of SMA, see Fig. 3.3. We also highlight that the model captures the pseudo-plastic response of SMA observed at low temperatures, as well as the pseudo-elastic response observed for elevated temperatures, cf. Figs. 3.3(a) and 3.4(d). In addition, we investigate tensile step tests on the micro-level, showing that the model is able to capture another experimentally observed feature of SMA, which is the appearance of stress-strain envelopes and appropriate stress-strain minor loops in tensile step tests. Numerous experiments in this context were carried out in, e.g., [59], and the model features presented in this chapter nicely match these experimental investigations.

The results obtained at the micro-sphere level, see Section 3.2.2, show some of the advantages of the micro-sphere approach utilised in this work. To be specific, one advantage is that we may extract spatial distributions of volume fractions in the poly-crystal-like arrangement as shown in, e.g., Figs. 3.6(c) and 3.6(d). Moreover, the micro-sphere approach allows for a detailed assessment of the anisotropy evolution of the material. To this end, we include plots of the anisotropic directional Young's moduli at selected representative material states, see, Figs. 3.5 and 3.8.

Finally, we show that the model can be implemented into a finite element scheme, facilitating the computation of three-dimensional boundary value problems. In this regard, we show the subsequent torsion and tension of a block-shaped body, where we provide not only the tensile reaction forces and the torsional reaction moments for the chosen loading path, but also distributions of macroscropic volume fractions and the representative tensile stress component for several load states. The model introduced in this chapter provides physically sound results while maintaining a high computational efficiency. In the next chapters, we extend the model in order to capture the interactions of phase-transformations and plasticity. Note that the physically sound consideration of continuum plasticity requires a framework that provides a distinction between volumetric and deviatoric deformation states as established in this chapter.

3.5 Appendix

3.5.1 Material parameters

The material parameters used in this chapter are based on the ones already used in Chapter 2. However, additional variables were introduced in the current chapter as a result of the extension of the basic model that was carried out. To this end, an overview of the material parameters used in this chapter is provided in Table 3.1.

3.5.2 Analytical solution for the minimum of the Gibbs potential of a single phase

In order to simplify notation, we rearrange the terms in (3.3) and (3.9), respectively, such that the Gibbs potential g^α of one phase α can be expressed as

$$g^\alpha = a^\alpha {\varepsilon_\text{dev}}^2 + b^\alpha \varepsilon_\text{dev} + c^\alpha {\varepsilon_\text{vol}}^2 + d^\alpha \varepsilon_\text{vol} + e^\alpha \tag{3.76}$$

with coefficients a^α, b^α, c^α, d^α and e^α, see (3.30)–(3.34). The solution of (3.17) is then obtained from

$$\left.\frac{\partial g^\alpha}{\partial \varepsilon_\text{dev}}\right|_{\varepsilon_\text{dev}^{g^\alpha\text{min}}} = 2\,a^\alpha \varepsilon_\text{dev}^{g^\alpha\text{min}} + b^\alpha = 0 \tag{3.77}$$

$$\wedge \quad \left.\frac{\partial g^\alpha}{\partial \varepsilon_\text{vol}}\right|_{\varepsilon_\text{vol}^{g^\alpha\text{min}}} = 2\,c^\alpha \varepsilon_\text{vol}^{g^\alpha\text{min}} + d^\alpha = 0 \quad , \tag{3.78}$$

inducing

$$\varepsilon_\text{dev}^{g^\alpha\text{min}} = -\frac{b^\alpha}{2\,a^\alpha} \tag{3.79}$$

$$\wedge \quad \varepsilon_\text{vol}^{g^\alpha\text{min}} = -\frac{d^\alpha}{2\,c^\alpha} \quad . \tag{3.80}$$

Note that, due to the Legendre transformation carried out, the value of the global minimum g^α_min of the Gibbs potential of the phase considered, as well as its position in volumetric-deviatoric strain space $(\varepsilon_\text{dev}^{g^\alpha\text{min}}, \varepsilon_\text{vol}^{g^\alpha\text{min}})$ depends on the load or rather deformation applied, i.e. ε_dev and ε_vol, as well as on the volume fraction ξ^α of the respective material phase, cf. Fig. 3.2.

Table 3.1: SMA material parameters considered in the current chapter, compare, e.g., [20, 51].

	material parameter	symbol	value
austenite A (parent phase):	Young's modulus	E^{A}	67 GPa
	deviatoric transformation strains	$\varepsilon^{\mathrm{A}}_{\mathrm{tr,dev}}$	0
	volumetric transformation strains	$\varepsilon^{\mathrm{A}}_{\mathrm{tr,vol}}$	0
	latent heat	λ^{A}_{T}	0
tensile martensite $\mathrm{M_t}$:	Young's modulus	$\mathsf{E}^{\mathrm{M_t}}$	26.3 GPa
	deviatoric transformation strains	$\varepsilon^{\mathrm{M_t}}_{\mathrm{tr,dev}}$	0.025
	volumetric transformation strains	$\varepsilon^{\mathrm{M_t}}_{\mathrm{tr,vol}}$	0
	latent heat	$\lambda^{\mathrm{M_t}}_{T}$	14500 J/kg
compression martensite $\mathrm{M_c}$:	Young's modulus	$\mathsf{E}^{\mathrm{M_c}}$	26.3 GPa
	deviatoric transformation strains	$\varepsilon^{\mathrm{M_c}}_{\mathrm{tr,dev}}$	-0.04
	volumetric transformation strains	$\varepsilon^{\mathrm{M_c}}_{\mathrm{tr,vol}}$	0
	latent heat	$\lambda^{\mathrm{M_c}}_{T}$	14500 J/kg
common parameters:	coefficient of thermal expansion	ζ	12×10^{-7} K^{-1}
	reference temperature	θ_0	273 K
	heat capacity	c_p	400 J/kgK
	transition attempt frequency	ω	1.6 s^{-1}
	transformation region's volume	Δv	2.71×10^{-18} mm^3
	Poisson's ratio	ν_{P}	0.33
	Boltzmann's constant	k	1.381×10^{-23} J/K

3.5.3 Numerical scheme - computation of Gibbs energy barriers

```
get Gibbs coefficients $[a^\alpha, b^\alpha, c^\alpha, d^\alpha, e^\alpha]$ and $[a^\beta, b^\beta, c^\beta, d^\beta, e^\beta]$    ▷ see (3.30)–(3.34)
get minima positions $\left(\varepsilon_{\text{dev}}^{g^\alpha\text{min}}, \varepsilon_{\text{vol}}^{g^\alpha\text{min}}\right)$ and $\left(\varepsilon_{\text{dev}}^{g^\beta\text{min}}, \varepsilon_{\text{vol}}^{g^\beta\text{min}}\right)$    ▷ see (3.79) and (3.80)
set $j = 0$ and get starting value $\varepsilon_{\text{vol}}^{\text{isc,min}}\Big|_{j=0} = \left[\varepsilon_{\text{vol}}^{g^\alpha\text{min}} - \varepsilon_{\text{vol}}^{g^\beta\text{min}}\right]/2$
while abs$\left(\mathrm{D}g^{\,\text{isc},\alpha,\beta}\big|_j\right) > tol$ do
    get intersection curve gradient $\mathrm{D}g^{\,\text{isc},\alpha,\beta}\big|_j = \frac{\partial\,\widehat{g}^{\,\text{isc},\alpha,\beta}(\varepsilon_{\text{vol}})}{\partial\varepsilon_{\text{vol}}}\Big|_{\varepsilon_{\text{vol}}^{\text{isc,min}}|_j}$    ▷ see (3.41)
    get Newton gradient $\mathrm{D}^2 g^{\,\text{isc},\alpha,\beta}\big|_j = \frac{\partial^2\,\widehat{g}^{\,\text{isc},\alpha,\beta}(\varepsilon_{\text{vol}})}{\partial{\varepsilon_{\text{vol}}}^2}\Big|_{\varepsilon_{\text{vol}}^{\text{isc,min}}|_j}$    ▷ see (3.42)
    update $\varepsilon_{\text{vol}}^{\text{isc,min}}\Big|_{j+1} = \varepsilon_{\text{vol}}^{\text{isc,min}}\Big|_j - \mathrm{D}g^{\,\text{isc},\alpha,\beta}\big|_j \,/\, \mathrm{D}^2 g^{\,\text{isc},\alpha,\beta}\big|_j$
    increment $j \leftarrow j + 1$
end while
after convergence, set $\varepsilon_{\text{vol}}^{\text{isc,min}} = \varepsilon_{\text{vol}}^{\text{isc,min}}\Big|_j$
get position $\left(\widehat{\varepsilon}_{\text{dev}}^{\text{isc}}(\varepsilon_{\text{vol}}^{\text{isc,min}}), \varepsilon_{\text{vol}}^{\text{isc,min}}\right)$ of the intersection curve minimum    ▷ see (3.35)
get Gibbs energy value $g_{\text{min}}^{\text{isc},\alpha,\beta}$    ▷ see (3.39) and (3.40)
compute Gibbs energy potential minima $g_{\text{min}}^{\alpha}$ and $g_{\text{min}}^{\beta}$    ▷ see (3.18)
get $b_{\alpha\to\beta} = g_{\text{min}}^{\text{isc},\alpha,\beta} - g_{\text{min}}^{\alpha}$ and $b_{\beta\to\alpha} = g_{\text{min}}^{\text{isc},\alpha,\beta} - g_{\text{min}}^{\beta}$    ▷ see (3.15) and (3.16)
return $b_{\alpha\to\beta}$ and $b_{\beta\to\alpha}$
```

Algorithm 1: Minimisation of the intersection curve of two elliptic Gibbs energy paraboloids in deviatoric-volumetric strain space.

3.5.4 Overall constitutive algorithm

```
while $t < t_{\max}$ do
    set $t = {}^{n+1}t = {}^{n}t + \Delta t \in [\,0,\, t_{\max}\,]$
    given: ${}^{n+1}\boldsymbol{\varepsilon}$
    while $i < n_r$ do                                          ▷ for every micro-sphere direction...
        given: ${}^{n}\boldsymbol{\xi}_i = \left[{}^{n}\xi_i^{\mathrm{A}}, {}^{n}\xi_i^{\mathrm{M_t}}, {}^{n}\xi_i^{\mathrm{M_c}},\right]^{\mathrm{t}}$
        obtain $\varepsilon_{\mathrm{dev},i}$ and $\varepsilon_{\mathrm{vol}}$ from (3.51)
        for all combinations $(\alpha, \beta) \in [\mathrm{A}, \mathrm{M_t}, \mathrm{M_c}], \alpha \neq \beta$ do
            get energy barrier $b_{\alpha\to\beta,i}$           ▷ see Section 3.1.4 and Algorithm 1
            obtain transformation probabilities $P_{\alpha\to\beta,i}$   ▷ see (2.7)
        end for
        assemble $\boldsymbol{Q}_i$ and update ${}^{n+1}\boldsymbol{\xi}_i$ with time-integration scheme   ▷ see (2.6)
        update volume fractions ${}^{n}\boldsymbol{\xi}_i \leftarrow {}^{n+1}\boldsymbol{\xi}_i$
        add $i$th contribution to ${}^{n+1}\boldsymbol{\sigma}$ and ${}^{n+1}\mathbf{E}_{\mathrm{el}}$   ▷ see (3.60) and (3.70)
    end while
    return ${}^{n+1}\boldsymbol{\sigma}$, ${}^{n+1}\mathbf{E}_{\mathrm{el}}$, ${}^{n+1}\boldsymbol{\xi}_i$ $\forall\, i$ and set $n \leftarrow n + 1$
end while
```

Algorithm 2: Solution of the overall constitutive model based on a non-affine micro-sphere scheme.

4 Phase-transformations interacting with plasticity

In this chapter, we model the basic mechanisms of the interaction between phase-transformations and plasticity within a one-dimensional constitutive framework. Efficient algorithms are presented, facilitating to solve the underlying evolution equations with high numerical stability at low numerical costs. Furthermore, a family of functions covering physically reasonable classes for the inheritance of plasticity in the context of evolving phases is proposed and discussed by means of several representative numerical examples.

The goal of the work presented in this chapter is to enhance the statistics-based phase-transformation model described in Section 2.1 in order to take into account plasticity as well as the interaction between phase-transformation and plasticity effects by introducing a so-called plasticity inheritance law. The model is presented in Section 4.1, where extended Helmholtz free energy functions for each material phase are introduced, taking into account plastic strains as new variables for each individual phase. Based on the extended multi-well energy potentials, the probabilistic phase-transformation model is derived in Section 4.1.1. Moreover, the differential equations describing the evolution of plasticity as well as the potential-based derivation of the individual plastic driving forces are shown in Sections 4.1.2 and 4.1.2.1, respectively. The coupling of phase-transformation and plasticity effects is incorporated by means of a staggered algorithm. To this end, an inheritance algorithm for the inheritance of plastic strains resulting from a propagating phase front is introduced in Section 4.1.3. Moreover, two physically reasonable exponential-type inheritance probability functions are presented in Sections 4.1.3.1 and 4.1.3.2. Details on the numerical implementation of the model are provided in Section 4.2, followed by numerical examples shown in Section 4.3, where the model is applied not only to shape memory alloys, see Section 4.3.2, but also to TRIP steel as presented in Section 4.3.3. It is shown that the model reflects the physical behaviour of both types of materials.

4.1 A model for the interaction of phase-transformations and plasticity

As introduced in Section 2.1, the one-dimensional phase-transformation model is based on mixture theory, where we make use of the Voigt assumption, i.e. all material phases are subject to the same strain ε. As mentioned before, the utilised phase-transformation model is capable of handling an arbitrary amount of material phases, where the volume fraction

$$\xi^\alpha := \lim_{v\to 0}\left(\frac{v^\alpha}{v}\right) \tag{4.1}$$

of each phase $\alpha \in \{1,\dots,\nu\} \subset \mathbb{N}$ is subject to the restrictions

$$\xi^\alpha \in \; [0,1] \subset \mathbb{R} \quad , \quad \sum_{\alpha=1}^{\nu} \xi^\alpha = \; 1 \quad , \quad \sum_{\alpha=1}^{\nu} \dot{\xi}^\alpha = \; 0 \quad . \tag{4.2}$$

Each phase is presumed to behave thermo-elasto-plastically, thus a Helmholtz free energy function $\psi^\alpha = \widehat{\psi}^\alpha(\varepsilon, \varepsilon^\alpha_{\text{pl}}, \theta)$ of the form

$$\begin{aligned}\psi^\alpha \;&=\; \frac{1}{2}\mathsf{E}^\alpha[\varepsilon - \varepsilon^\alpha_{\text{tr}} - \varepsilon^\alpha_{\text{pl}}]^2 - \zeta^\alpha \mathsf{E}^\alpha[\varepsilon - \varepsilon^\alpha_{\text{tr}} - \varepsilon^\alpha_{\text{pl}}][\theta - \theta_0] \\ &+\; \rho_0 c^\alpha_p \theta \left[1 - \log\left(\frac{\theta}{\theta_0}\right)\right] - \rho_0 \lambda^\alpha_T \left[1 - \frac{\theta}{\theta_0}\right]\end{aligned} \tag{4.3}$$

is assigned to each phase α, with E the Young's modulus, $\varepsilon = \nabla_x u$ the total strains, ε_{tr} the transformation strains, ε_{pl} the plastic strains, ζ the coefficient of thermal expansion, θ the current absolute temperature, θ_0 the reference temperature, c_p the heat capacity, and λ_T the latent heat of the respective material phase. The overall free energy of the mixture $\varPsi = \widehat{\varPsi}(\varepsilon, \boldsymbol{\varepsilon}^{\text{1d}}_{\text{pl}}, \theta, \boldsymbol{\xi}) = \sum_\alpha \xi^\alpha \psi^\alpha$, with $\boldsymbol{\xi} = [\xi^1, \dots, \xi^\nu]$ and $\boldsymbol{\varepsilon}^{\text{1d}}_{\text{pl}} = [\varepsilon^1_{\text{pl}}, \dots, \varepsilon^\nu_{\text{pl}}]$, can directly be obtained from the free energy contributions of the respective constituents, since the distortional energy of the phase boundaries is neglected here.

Based on this, the Gibbs potential $G = \widehat{G}(\partial\varPsi/\partial\varepsilon, \boldsymbol{\xi}, \theta)$ can be obtained by carrying out a Legendre-transformation, i.e.

$$\begin{aligned} G \;&=\; \varPsi - \left.\frac{\partial\widehat{\varPsi}(\varepsilon, \boldsymbol{\varepsilon}^{\text{1d}}_{\text{pl}}, \theta, \boldsymbol{\xi})}{\partial\varepsilon}\right|_{\theta, \boldsymbol{\varepsilon}^{\text{1d}}_{\text{pl}}} \varepsilon && (4.4) \\ &=\; \sum_{\alpha=1}^{\nu} \xi^\alpha \left[\psi^\alpha - \sigma\,\varepsilon\right] && (4.5) \\ &=\; \sum_{\alpha=1}^{\nu} \xi^\alpha g^\alpha \quad , && (4.6)\end{aligned}$$

where $\sigma = \partial\Psi/\partial\varepsilon|_{\theta,\boldsymbol{\varepsilon}_{\text{pl}}^{\text{1d}}} = \widehat{\sigma}(\varepsilon, \boldsymbol{\varepsilon}_{\text{pl}}^{\text{1d}}, \boldsymbol{\xi}, \theta)$ is the stress acting in the one-dimensional continuum considered and $g^\alpha = \widehat{g}^\alpha(\sigma, \varepsilon, \varepsilon_{\text{pl}}^\alpha, \theta) := \psi^\alpha - \sigma\,\varepsilon$ represents the contribution of phase α to the overall Gibbs potential G.

4.1.1 Evolution of volume fractions

For the evolution of the volume fractions ξ^α we use an approach based on statistical physics as introduced in Section 2.1. To this end, the transformation probability matrix $\boldsymbol{Q} \in \mathbb{R}^{\nu\times\nu}$ (2.6) facilitates the derivation of the evolution equation for the volume fractions as $\dot{\boldsymbol{\xi}} = \boldsymbol{Q}\cdot\boldsymbol{\xi}$. For the sake of simplicity and conceptual clarity, we restrict ourselves to just two material phases in this chapter, namely austenite A and martensite M. The according transformation probability matrix $\boldsymbol{Q} \in \mathbb{R}^{2\times2}$ reduces to

$$\boldsymbol{Q} = \omega \begin{bmatrix} -P_{\text{A}\to\text{M}} & P_{\text{M}\to\text{A}} \\ P_{\text{A}\to\text{M}} & -P_{\text{M}\to\text{A}} \end{bmatrix} \neq \boldsymbol{Q}^{\text{t}} \tag{4.7}$$

with ω the transition attempt frequency and $P_{\alpha\to\beta} = \widehat{P}_{\alpha\to\beta}(\theta, b_{\alpha\to\beta})$ the probability of a transformation of one phase α to the other phase β. Note that (4.7) refers to $\boldsymbol{\xi} = [\xi^{\text{A}}, \xi^{\text{M}}]^{\text{t}} \in \mathbb{R}^2$.

In line with the previous chapters and [5], the transformation probabilities necessary to assemble $\boldsymbol{Q}$ are obtained from

$$P_{\alpha\to\beta} = \exp\left(\frac{-\Delta v\, b_{\alpha\to\beta}}{k\,\theta}\right) \quad , \tag{4.8}$$

with Δv the constant transformation region's volume, $b_{\alpha\to\beta}$ the energy barrier for the transformation from phase α to phase β, k the Boltzmann's constant, and θ the given temperature. Note that, in general, $b_{\alpha\to\beta} \neq b_{\beta\to\alpha}$ and thus $P_{\alpha\to\beta} \neq P_{\beta\to\alpha}$ holds. The energy barriers can be determined from

$$b_{\alpha\to\beta} = \widehat{g}^\alpha(\sigma, \varepsilon_{\alpha,\beta}^\star, \varepsilon_{\text{pl}}^\alpha, \theta) - \widehat{g}^\alpha(\sigma, \varepsilon_\alpha^{\min}, \varepsilon_{\text{pl}}^\alpha, \theta) \tag{4.9}$$

with

$$\varepsilon_{\alpha,\beta}^\star = \inf_{g^\alpha, g^\beta} \left\{ \varepsilon \mid \widehat{g}^\alpha(\sigma, \varepsilon, \varepsilon_{\text{pl}}^\alpha, \theta)|_{\sigma,\varepsilon_{\text{pl}}^\alpha,\theta} = \widehat{g}^\beta(\sigma, \varepsilon, \varepsilon_{\text{pl}}^\beta, \theta)|_{\sigma,\varepsilon_{\text{pl}}^\beta,\theta} \right\} \tag{4.10}$$

and

$$\varepsilon_\alpha^{\min} = \left\{ \varepsilon \mid \left. \frac{\partial\widehat{g}^\alpha(\sigma, \varepsilon, \varepsilon_{\text{pl}}^\alpha, \theta)}{\partial\varepsilon} \right|_{\sigma,\varepsilon_{\text{pl}}^\alpha,\theta} = 0 \right\} \quad , \tag{4.11}$$

where $\widehat{g}^\alpha(\sigma, \varepsilon_{\alpha,\beta}^\star, \varepsilon_{\text{pl}}^\alpha, \theta) = \widehat{g}^\beta(\sigma, \varepsilon_{\alpha,\beta}^\star, \varepsilon_{\text{pl}}^\beta, \theta)$ gives the value of the energy potentials at the intersection of the parabolic phase potential functions for two material phases α

and β in strain space, while $\widehat{g}^{\alpha}(\sigma, \varepsilon_{\alpha}^{\min}, \varepsilon_{\mathrm{pl}}^{\alpha}, \theta)$ denotes the minimum energy potential of a particular phase α for fixed stresses and temperature. Accordingly, the difference of both energy values (4.9) gives the energy barrier that has to be overcome for a transformation from phase α to phase β.

4.1.2 Evolution of plastic strains

To incorporate plasticity, we—for conceptual simplicity—assume von Mises-type plasticity with linear proportional hardening. Based on the overall free energy potential, the plastic driving force $q_{\mathrm{pl},\varPsi}^{\alpha}$ can be derived for each phase α, see Section 4.1.2.1 for details. With the driving force and the current yield stress Y^{α} at hand, the yield function $\varPhi^{\alpha} = \widehat{\varPhi}^{\alpha}(Y^{\alpha}, q_{\mathrm{pl},\varPsi}^{\alpha})$ determining the admissible elastic domain in phase α, is given as

$$\widehat{\varPhi}^{\alpha}(q_{\mathrm{pl},\varPsi}^{\alpha}, Y^{\alpha}) = |q_{\mathrm{pl},\varPsi}^{\alpha} - \xi^{\alpha} b^{\alpha}| - \xi^{\alpha}\, Y^{\alpha} \leq 0 \quad . \tag{4.12}$$

The current yield stress $Y^{\alpha} = \widehat{Y}^{\alpha}(\gamma^{\alpha}) = Y_0^{\alpha} + H^{\alpha}\, \gamma^{\alpha}$ is given by the initial yield stress Y_0^{α} being modified by $H^{\alpha}\, \gamma^{\alpha}$ due to accumulated plastic strains γ^{α} of the respective material phase, where H^{α} denotes the constant hardening modulus of phase α. The individual back stress $\xi^{\alpha} b^{\alpha}$ is additionally considered in order to prevent plastic flow occurring in the initial equilibrium state. To be specific, the underlying Voigt assumption leads to an initial stress of

$$\begin{aligned} b^{\alpha} &:= \widehat{\sigma}^{\alpha}(\varepsilon = 0, \varepsilon_{\mathrm{pl}}^{\alpha} = 0, \theta) \\ &= \left. \frac{\partial \widehat{\psi}^{\alpha}(\varepsilon, \varepsilon_{\mathrm{pl}}^{\alpha}, \theta)}{\partial \varepsilon} \right|_{\theta, \varepsilon_{\mathrm{pl}}^{\alpha}=0, \varepsilon=0} \\ &= -\,\mathsf{E}^{\alpha} \varepsilon_{\mathrm{tr}}^{\alpha} + \zeta^{\alpha} \mathsf{E}^{\alpha} \varepsilon_{\mathrm{tr}}^{\alpha} [\theta - \theta_0] \end{aligned} \tag{4.13}$$

that acts in each phase α and, in consequence, is considered as a back stress in the yield function. Based on the yield function presented, we make use of an associated flow rule, facilitating to derive the evolution law for the plastic strain in phase α by means of

$$\dot{\varepsilon}_{\mathrm{pl}}^{\alpha} = \dot{\lambda}^{\alpha} \frac{\partial \widehat{\varPhi}^{\alpha}(q_{\mathrm{pl},\varPsi}^{\alpha}, Y^{\alpha})}{\partial q_{\mathrm{pl},\varPsi}^{\alpha}} = \dot{\lambda}^{\alpha} \operatorname{sgn}\left(q_{\mathrm{pl},\varPsi}^{\alpha} - \xi^{\alpha} b^{\alpha}\right) \tag{4.14}$$

with an appropriate Lagrangian multiplier $\dot{\lambda}^{\alpha}$.

4.1.2.1 Remarks on the derivation of the plastic driving force

The stress-type force $q^{\alpha}_{\mathrm{pl},\Psi} = \widehat{q}^{\alpha}_{\mathrm{pl},\Psi}(\xi^{\alpha}, \varepsilon, \varepsilon^{\alpha}_{\mathrm{pl}}, \theta)$ driving the evolution of plasticity in phase α can be derived from the overall free energy Ψ according to

$$
\begin{aligned}
q^{\alpha}_{\mathrm{pl},\Psi} &= -\left.\frac{\partial\widehat{\Psi}(\varepsilon, \boldsymbol{\varepsilon}^{1\mathrm{d}}_{\mathrm{pl}}, \theta, \boldsymbol{\xi})}{\partial\varepsilon^{\alpha}_{\mathrm{pl}}}\right|_{\theta,\varepsilon,\boldsymbol{\xi}} && (4.15)\\
&= -\left.\frac{\partial}{\partial\varepsilon^{\alpha}_{\mathrm{pl}}}\right|_{\theta,\varepsilon} \sum_{\alpha=1}^{\nu} \xi^{\alpha}\widehat{\psi}^{\alpha}(\varepsilon, \varepsilon^{\alpha}_{\mathrm{pl}}, \theta) && (4.16)\\
&= -\xi^{\alpha}\left.\frac{\partial\widehat{\psi}^{\alpha}(\varepsilon, \varepsilon^{\alpha}_{\mathrm{pl}}, \theta)}{\partial\varepsilon^{\alpha}_{\mathrm{pl}}}\right|_{\theta,\varepsilon} \quad , && (4.17)
\end{aligned}
$$

finally resulting in

$$
q^{\alpha}_{\mathrm{pl},\Psi} = \xi^{\alpha}\left[\mathsf{E}^{\alpha}[\varepsilon - \varepsilon^{\alpha}_{\mathrm{tr}} - \varepsilon^{\alpha}_{\mathrm{pl}}] + \zeta^{\alpha}\mathsf{E}^{\alpha}[\theta - \theta_0]\right] \quad . \tag{4.18}
$$

Furthermore, the stress acting in the one-dimensional continuum is obtained from

$$
\begin{aligned}
\sigma &= \left.\frac{\partial\widehat{\Psi}(\varepsilon, \boldsymbol{\varepsilon}^{1\mathrm{d}}_{\mathrm{pl}}, \theta, \boldsymbol{\xi})}{\partial\varepsilon}\right|_{\theta,\boldsymbol{\varepsilon}^{1\mathrm{d}}_{\mathrm{pl}}} && (4.19)\\
&= \left.\frac{\partial}{\partial\varepsilon}\right|_{\theta,\boldsymbol{\varepsilon}^{1\mathrm{d}}_{\mathrm{pl}}} \left[\sum_{\alpha=1}^{\nu} \xi^{\alpha}\widehat{\psi}^{\alpha}(\varepsilon, \varepsilon^{\alpha}_{\mathrm{pl}}, \theta)\right] && (4.20)\\
&= \sum_{\alpha=1}^{\nu} \xi^{\alpha}\left.\frac{\partial\widehat{\psi}^{\alpha}(\varepsilon, \varepsilon^{\alpha}_{\mathrm{pl}}, \theta)}{\partial\varepsilon}\right|_{\theta,\varepsilon^{\alpha}_{\mathrm{pl}}} && (4.21)\\
&= \sum_{\alpha=1}^{\nu} \xi^{\alpha}\sigma^{\alpha} && (4.22)
\end{aligned}
$$

with $\sigma^{\alpha} = \widehat{\sigma}^{\alpha}(\varepsilon, \varepsilon^{\alpha}_{\mathrm{pl}}, \theta) = \mathsf{E}^{\alpha}[\varepsilon - \varepsilon^{\alpha}_{\mathrm{tr}} - \varepsilon^{\alpha}_{\mathrm{pl}}] + \zeta^{\alpha}\mathsf{E}^{\alpha}[\theta - \theta_0]$ the stress acting in phase α. Comparing this result to (4.18) shows that $q^{\alpha}_{\mathrm{pl},\Psi} = \xi^{\alpha}\sigma^{\alpha}$.

Alternatively, the plastic driving forces can be derived by considering each phase individually. Using this approach, the driving force $q^{\alpha}_{\mathrm{pl},\psi} = \widehat{q}^{\alpha}_{\mathrm{pl},\psi}(\varepsilon, \varepsilon^{\alpha}_{\mathrm{pl}}, \theta)$ yields

$$
\begin{aligned}
q^{\alpha}_{\mathrm{pl},\psi} &= -\left.\frac{\partial\widehat{\psi}^{\alpha}(\varepsilon, \varepsilon^{\alpha}_{\mathrm{pl}}, \theta)}{\partial\varepsilon^{\alpha}_{\mathrm{pl}}}\right|_{\theta,\varepsilon} && (4.23)\\
&= \mathsf{E}^{\alpha}[\varepsilon - \varepsilon^{\alpha}_{\mathrm{tr}} - \varepsilon^{\alpha}_{\mathrm{pl}}] + \zeta^{\alpha}\mathsf{E}^{\alpha}[\theta - \theta_0] && (4.24)\\
&= \sigma^{\alpha} \quad . && (4.25)
\end{aligned}
$$

In particular, this result leads to $q^{\alpha}_{\mathrm{pl},\mathit{\Psi}} = \xi^{\alpha} q^{\alpha}_{\mathrm{pl},\psi}$. Note that the consideration of the volume fraction ξ^{α} within the plastic driving force of each phase α guarantees that $\widehat{q}^{\alpha}_{\mathrm{pl},\mathit{\Psi}}(\xi^{\alpha} = 0, \varepsilon, \varepsilon^{\alpha}_{\mathrm{pl}}, \theta) = 0$, and thus $\dot{\varepsilon}^{\alpha}_{\mathrm{pl}} = 0$ as long as $\xi^{\alpha} = 0$, i.e. no evolution of plasticity can occur within a phase of zero volume fraction.

4.1.3 Plasticity inheritance law for two phases

When the phase front of a phase α evolves throughout a crystal from time step ${}^{n}t$ to ${}^{n+1}t$, the question arises, whether plastic strains present in the decreasing phase β are inherited by the phase front of the increasing phase or not, cf. Fig. 4.1. Conceptually speaking, one has to specify to which amount a positive volume fraction increment $\Delta\xi^{\alpha} = {}^{n+1}\xi^{\alpha} - {}^{n}\xi^{\alpha} > 0$ of phase α transfers plastic strains from phase β to phase α. In general, the updated plastic strains $\tilde{\varepsilon}^{\alpha}_{\mathrm{pl}} = \widehat{\tilde{\varepsilon}}^{\alpha}_{\mathrm{pl}}({}^{n}\xi^{\alpha}, \Delta\xi^{\alpha}, \varepsilon^{\alpha}_{\mathrm{pl}}, \varepsilon^{\beta}_{\mathrm{pl}}, \mathit{\Pi}^{\beta\rightarrow\alpha})$ in phase α can be determined via

$$\tilde{\varepsilon}^{\alpha}_{\mathrm{pl}} = \frac{1}{{}^{n+1}\xi^{\alpha}} \left[{}^{n}\xi^{\alpha}\, \varepsilon^{\alpha}_{\mathrm{pl}} + \mathit{\Pi}^{\beta\rightarrow\alpha}\, \Delta\xi^{\alpha}\, \varepsilon^{\beta}_{\mathrm{pl}} \right] \quad , \tag{4.26}$$

where $\mathit{\Pi}^{\beta\rightarrow\alpha}$ reflects the probability of phase α inheriting the dislocations present in phase β, see Fig. 4.1. If one further assumes, that the diffusionless lattice shearing taking place during the phase-transformations considered neither generates nor annihilates any dislocations, i.e. the overall amount of plastic deformations remains constant in terms of

$${}^{n+1}\xi^{\alpha}\, \tilde{\varepsilon}^{\alpha}_{\mathrm{pl}} + {}^{n+1}\xi^{\beta}\, \tilde{\varepsilon}^{\beta}_{\mathrm{pl}} = {}^{n}\xi^{\alpha}\, \varepsilon^{\alpha}_{\mathrm{pl}} + {}^{n}\xi^{\beta}\, \varepsilon^{\beta}_{\mathrm{pl}} \quad , \tag{4.27}$$

then the updated plastic deformations $\tilde{\varepsilon}^{\beta}_{\mathrm{pl}} = \widehat{\tilde{\varepsilon}}^{\beta}_{\mathrm{pl}}({}^{n}\xi^{\beta}, \Delta\xi^{\alpha}, \varepsilon^{\beta}_{\mathrm{pl}}, \mathit{\Pi}^{\beta\rightarrow\alpha})$ remaining in the decreased phase β are obtained from

$$\tilde{\varepsilon}^{\beta}_{\mathrm{pl}} = \frac{1}{{}^{n+1}\xi^{\beta}} \left[{}^{n}\xi^{\beta} - \mathit{\Pi}^{\beta\rightarrow\alpha}\, \Delta\xi^{\alpha} \right] \varepsilon^{\beta}_{\mathrm{pl}} \quad . \tag{4.28}$$

As we restrict ourselves, for the sake of simplicity, to two phases in the current chapter, it is obvious that the increase $\Delta\xi^{\alpha}$ of phase α is related to the decrease $\Delta\xi^{\beta}$ of phase β via

$$\Delta\xi^{\beta} = {}^{n+1}\xi^{\beta} - {}^{n}\xi^{\beta} = -\Delta\xi^{\alpha} \quad , \quad \Delta\xi^{\beta} < 0 \tag{4.29}$$

due to mass conservation, thus leading to

$${}^{n+1}\xi^{\beta} = {}^{n}\xi^{\beta} - \Delta\xi^{\alpha} \quad . \tag{4.30}$$

Comparing (4.28) and (4.30) then shows that, in case of $\mathit{\Pi}^{\beta\rightarrow\alpha} = 1$, the plastic deformations in the decreasing phase are not affected by the change of volume fractions, i.e.

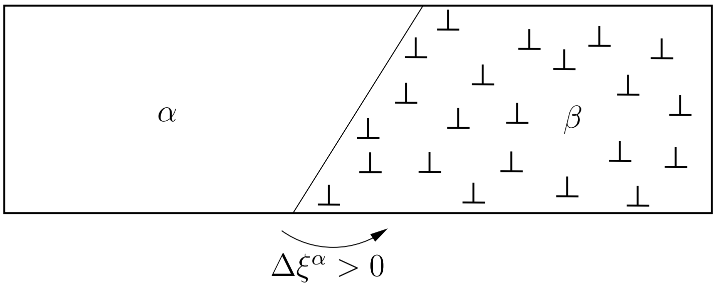

(a) Initial state: the phase front of α is about to move.

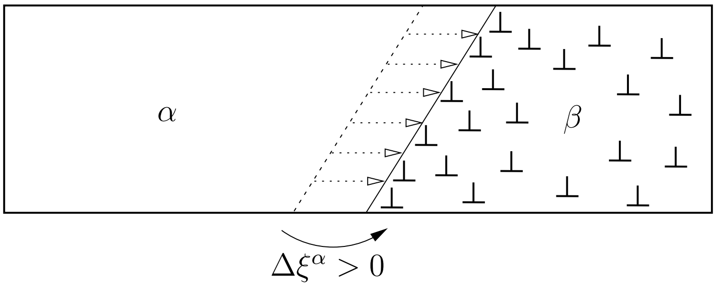

(b) $\Pi^{\beta\to\alpha} = 0$, i.e. all dislocations are pushed by the phase-front and remain within phase β.

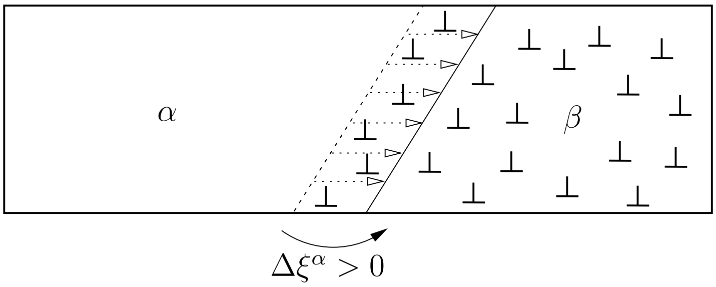

(c) $\Pi^{\beta\to\alpha} = 1$, i.e. all dislocations within the volume that undergoes a phase-change are inherited to the growing phase α.

Figure 4.1: Dislocations can either be inherited or pushed by the propagating phase front of an evolving phase α. Here, the two special cases, i.e. no inheritance (b) and full inheritance (c) of dislocations during phase front propagation are shown. However, the actual physical behaviour of a material regarding inheritance of dislocations—or rather plastic strains—can be expected to lie in between both extreme cases. Therefore an inheritance probability function $\Pi^{\beta\to\alpha} = \widehat{\Pi}^{\beta\to\alpha}(\xi^\beta, \varepsilon_{\mathrm{pl}}^\beta; ...) \in [0,1] \subset \mathbb{R}$, depending on the volume fraction ξ^β and plastic strain $\varepsilon_{\mathrm{pl}}^\beta$ of phase β as well as on material parameters, is introduced in this work (see Sections 4.1.3.1 and 4.1.3.2).

$\widehat{\widetilde{\varepsilon}}{}^{\beta}_{\text{pl}}({}^{n}\xi^{\beta}, \Delta\xi^{\alpha}, \varepsilon^{\beta}_{\text{pl}}, \mathit{\Pi}^{\beta\to\alpha} = 1) = \varepsilon^{\beta}_{\text{pl}}$. On the other hand, in case of $\mathit{\Pi}^{\beta\to\alpha} = 0$, i.e. if all dislocations are pushed rather than inherited by the propagating phase front of phase α, the plastic strains in phase β increase inversely proportional to the decrease of volume fraction.

However, it is physically reasonable to assume that the inheritance probability is not constant, but rather a function depending on the remaining volume fraction ξ^{β} and plastic strain $\varepsilon^{\beta}_{\text{pl}}$ of the decreasing phase β, as well as on further material parameters characterising the actual functional dependency. To this end, two reasonable approaches for introducing exponential-type inheritance probability functions, namely a convex and a concave one, $\mathit{\Pi}^{\beta\to\alpha}_{\text{cvx}} = \widehat{\mathit{\Pi}}{}^{\beta\to\alpha}_{\text{cvx}}(\xi^{\beta}, \varepsilon^{\beta}_{\text{pl}}; \kappa)$ and $\mathit{\Pi}^{\beta\to\alpha}_{\text{ccv}} = \widehat{\mathit{\Pi}}{}^{\beta\to\alpha}_{\text{ccv}}(\xi^{\beta}, \varepsilon^{\beta}_{\text{pl}}; \kappa, \varepsilon^{\beta}_{\text{pl,sat}})$, respectively, are presented in the following.

4.1.3.1 Convex inheritance probability function

The inheritance probability function considered is subjected to two physically reasonable restrictions. First, in case that the volume fraction of the decreasing phase β is very large, i.e. $\xi^{\beta} \approx 1$, a propagating phase front of phase α will most likely push dislocations present in phase β, since the dislocation density[1]—being inversely proportional to the volume fraction—in β is rather low in this case. In consequence and as the first condition, we require the inheritance probability function to match $\widehat{\mathit{\Pi}}{}^{\beta\to\alpha}_{\text{cvx}}(\xi^{\beta} = 1, \varepsilon^{\beta}_{\text{pl}}; \kappa) = 0$. On the other hand, if the remaining volume fraction ξ^{β} of the decreasing phase β tends to zero, the dislocation density takes high values so that the dislocations (or rather plastic strains) remaining in phase β are forced to be inherited by the evolving phase α, i.e. $\widehat{\mathit{\Pi}}{}^{\beta\to\alpha}_{\text{cvx}}(\xi^{\beta} = 0, \varepsilon^{\beta}_{\text{pl}}; \kappa) = 1$. One exponential-type ansatz for an inheritance probability function fulfilling these restrictions is

$$\widehat{\mathit{\Pi}}{}^{\beta\to\alpha}_{\text{cvx}}(\xi^{\beta}, \varepsilon^{\beta}_{\text{pl}}; \kappa) = [1 - \xi^{\beta}] \exp\left(\frac{-\kappa\,\xi^{\beta}}{|\varepsilon^{\beta}_{\text{pl}}|}\right) \quad . \tag{4.31}$$

For an exemplary material parameter $\kappa = 0.1$, the development of this inheritance function is visualised in Fig. 4.2. Besides that, the influence of the parameter κ for an exemplary fixed plastic strain of $\varepsilon^{\beta}_{\text{pl}} = 0.025$ is displayed. As the figure shows, the proposed family of parametric inheritance functions is convex in ξ for all parameters $\kappa \in \mathbb{R}^{+}$.

---

[1] The phrase *dislocation density* does not refer to curl($\boldsymbol{\varepsilon}_{\text{pl}}$), respectively $\partial_x \varepsilon_{\text{pl}}$ here. In the current context, we rather use this denomination as a synonym for the density of plastic strains.

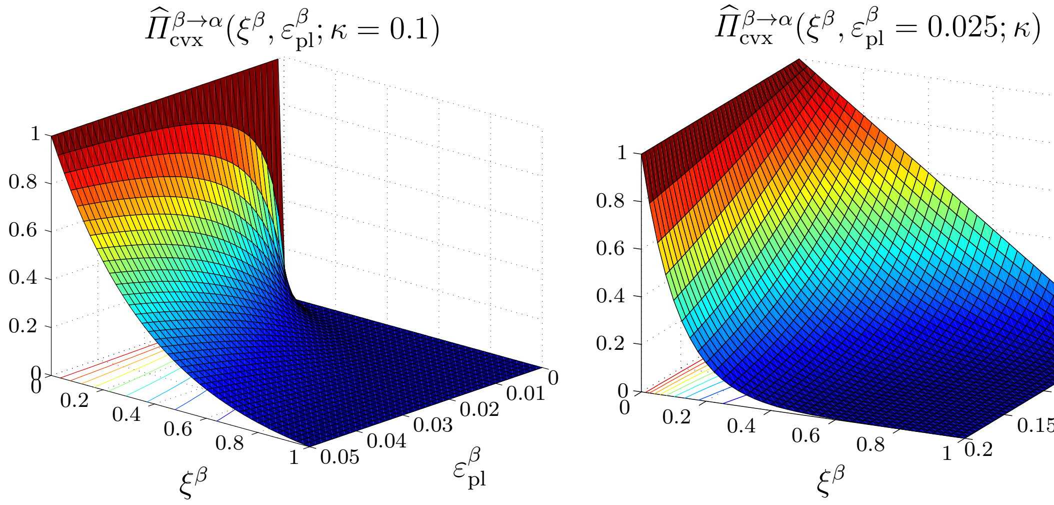

Figure 4.2: Convex inheritance probability function depending on volume fraction ξ^β and plastic strain $\varepsilon_{\text{pl}}^\beta$ for given parameter $\kappa = 0.1$ (left), and the function depending on ξ^β and κ for given plastic strain $\varepsilon_{\text{pl}}^\beta = 0.025$ (right).

4.1.3.2 Concave inheritance probability function

As an addition to the convex[2] inheritance probability function shown in Section 4.1.3.1, a concave[2] exponential-type inheritance function is presented in the following. As before, the physical restrictions, i.e. $\widehat{\Pi}_{\text{ccv}}^{\beta\to\alpha}(\xi^\beta = 1, \varepsilon_{\text{pl}}^\beta; \kappa) = 0$ and $\widehat{\Pi}_{\text{ccv}}^{\beta\to\alpha}(\xi^\beta = 0, \varepsilon_{\text{pl}}^\beta; \kappa) = 1$, are required to be fulfilled. To be specific, the function

$$\widehat{\Pi}_{\text{ccv}}^{\beta\to\alpha}(\xi^\beta, \varepsilon_{\text{pl}}^\beta; \kappa, \varepsilon_{\text{pl,sat}}^\beta) = \frac{1 - \exp\left(\dfrac{-\kappa\,[1-\xi^\beta]}{\varepsilon_{\text{pl,sat}}^\beta - |\varepsilon_{\text{pl}}^\beta|}\right)}{1 - \exp\left(\dfrac{-\kappa}{\varepsilon_{\text{pl,sat}}^\beta - |\varepsilon_{\text{pl}}^\beta|}\right)} \quad , \tag{4.32}$$

which again depends on a material parameter $\kappa \in \mathbb{R}^+$, is of exponential type, but provides a concave behaviour in ξ. As above, we require the inheritance probability to increase with increasing plastic strain. Accordingly, a plastic saturation strain $\varepsilon_{\text{pl,sat}}^\beta \in \mathbb{R}^+$, which can also be regarded as a material-dependent quantity, is introduced here. If the magnitude $|\varepsilon_{\text{pl}}^\beta|$ of the plastic strain present in phase β reaches the saturation strain $\varepsilon_{\text{pl,sat}}^\beta$, the inheritance probability tends towards 1, i.e. $\widehat{\Pi}_{\text{ccv}}^{\beta\to\alpha}(\xi^\beta, \varepsilon_{\text{pl}}^\beta \to \varepsilon_{\text{pl,sat}}^\beta; \kappa, \varepsilon_{\text{pl,sat}}^\beta) \to 1 \;\forall\; \xi^\beta < 1$. Figure 4.3 shows the development of the concave inheritance function for a given parameter of $\kappa = 0.1$ and an exemplary saturation strain

---

[2] Here and in the following, by *convex* or *concave* inheritance functions, we mean convex or concave with respect to the volume fraction ξ.

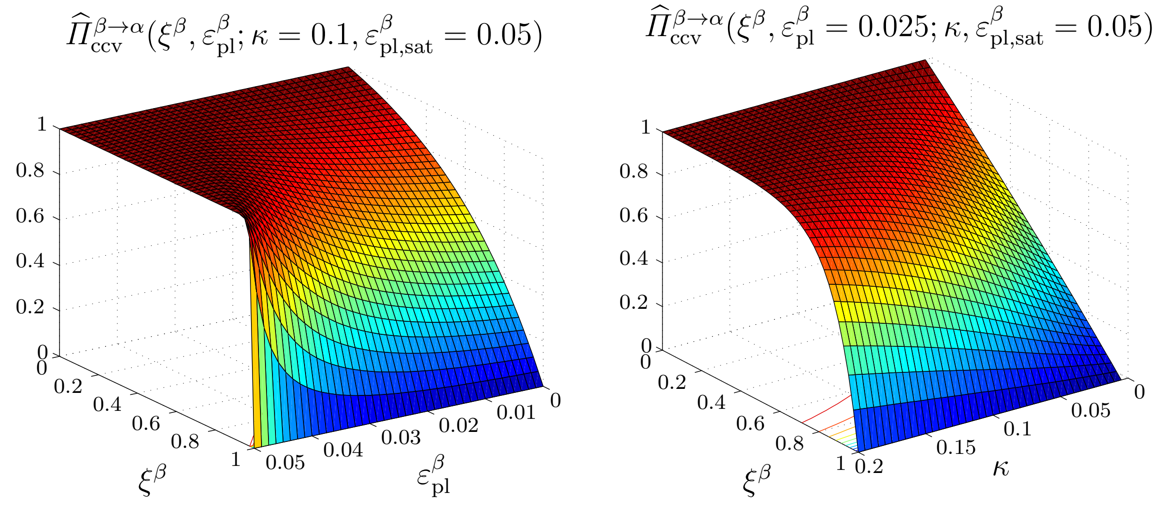
$\widehat{\Pi}^{\beta\to\alpha}_{\text{ccv}}(\xi^\beta, \varepsilon^\beta_{\text{pl}}; \kappa = 0.1, \varepsilon^\beta_{\text{pl,sat}} = 0.05)$

$\widehat{\Pi}^{\beta\to\alpha}_{\text{ccv}}(\xi^\beta, \varepsilon^\beta_{\text{pl}} = 0.025; \kappa, \varepsilon^\beta_{\text{pl,sat}} = 0.05)$

Figure 4.3: Concave inheritance probability function depending on volume fraction ξ^β and plastic strain $\varepsilon^\beta_{\text{pl}}$ for given parameters $\kappa = 0.1$ and $\varepsilon^\beta_{\text{pl,sat}} = 0.05$ (left), and the function depending on ξ^β and κ for given plastic strain $\varepsilon^\beta_{\text{pl}} = 0.025$ (right).

of $\varepsilon^\beta_{\text{pl,sat}} = 0.05$. Furthermore, the actual influence of κ on the inheritance probability function is presented for an exemplary plastic strain of $\varepsilon^\beta_{\text{pl}} = 0.025$.

4.2 Numerical integration of evolution equations

The solution of the strongly non-linear system of evolution equations required to obtain an update of the internal variables, i.e. volume fractions, is traditionally carried out using classical implicit integration schemes in combination with Newton-type iterations. In contrast to that, in the current chapter an explicit integration scheme, also discussed in [101] and Chapter 2, respectively, is applied. The integration scheme is based on the assumption that the transformation rates of volume fractions $\dot{\boldsymbol{\xi}}$ proceed linearly within a time step $\Delta t = {}^{n+1}t - {}^{n}t > 0$, i.e. from state n to $n+1$. As shown in Chapter 2, it is possible to obtain an explicit A-stable update using

$$ {}^{n+1}\boldsymbol{\xi} = {}^{n}\boldsymbol{\xi} + \frac{1}{2}\Delta t \left[{}^{n+1}\dot{\boldsymbol{\xi}} + {}^{n}\boldsymbol{Q} \cdot {}^{n}\boldsymbol{\xi} \right] \quad , \tag{4.33} $$

wherein

$$ {}^{n+1}\dot{\boldsymbol{\xi}} := \left[\boldsymbol{I} - \frac{1}{2}\Delta t\, {}^{n}\boldsymbol{Q} \right]^{-1} \cdot {}^{n}\boldsymbol{Q} \cdot \left[\frac{1}{2}\Delta t\, {}^{n}\boldsymbol{Q} \cdot {}^{n}\boldsymbol{\xi} + {}^{n}\boldsymbol{\xi} \right] \quad . \tag{4.34} $$

Using this approach facilitates the solution of the presented system with high efficiency, while the numerical stability is significantly improved compared to other explicit integration schemes such as forward-Euler. After the updated volume fractions are computed, the intermediate plastic strains ${}^{n}\tilde{\varepsilon}^{\alpha}_{\mathrm{pl}}$ and ${}^{n}\tilde{\varepsilon}^{\beta}_{\mathrm{pl}}$ solely resulting from the phase-transformation can be obtained from (4.26) and (4.28) as described in Section 4.1.3.

Besides that, the time-integration of the differential equations governing the evolution of plastic strain in each phase is carried out using a backward-Euler time integration scheme, compare, e.g., [118]. The discrete update of the plastic strains from timestep ${}^{n}t$ to ${}^{n+1}t$ according to (4.14) yields

$$
{}^{n+1}\varepsilon^{\alpha}_{\mathrm{pl}} = {}^{n}\tilde{\varepsilon}^{\alpha}_{\mathrm{pl}} + {}^{n+1}\lambda^{\alpha}\,\mathrm{sgn}\left({}^{n+1}q^{\alpha}_{\mathrm{pl},\mathit{\Psi}} - {}^{n+1}\xi^{\alpha} b^{\alpha}\right) \quad , \tag{4.35}
$$

with ${}^{n+1}\varepsilon^{\alpha}_{\mathrm{pl}} = \widehat{\varepsilon}^{\alpha}_{\mathrm{pl}}(t = {}^{n+1}t)$ the updated plastic strains, ${}^{n}\tilde{\varepsilon}^{\alpha}_{\mathrm{pl}}$ the current intermediate plastic strain resulting from phase-transformation, ${}^{n+1}\lambda^{\alpha} = \Delta t\,\dot{\lambda}^{\alpha} \in \mathbb{R}^{+}$ the current Langrangian multiplier, and $\mathrm{sgn}({}^{n+1}q^{\alpha}_{\mathrm{pl},\mathit{\Psi}} - {}^{n+1}\xi^{\alpha} b^{\alpha})$ the sign of the plastic driving force—being reduced by the back stress ${}^{n+1}\xi^{\alpha} b^{\alpha}$—assigned to phase α at time $t = {}^{n+1}t$.

In the current context, the Lagrangian multiplier can be expressed in terms of the trial value of the yield function $\mathit{\Phi}^{\alpha}_{\mathrm{tri}} = \widehat{\mathit{\Phi}}^{\alpha}(q^{\alpha}_{\mathrm{pl},\mathit{\Psi},\mathrm{tri}}, {}^{n}Y^{\alpha})$, with the trial plastic driving force $q^{\alpha}_{\mathrm{pl},\mathit{\Psi},\mathrm{tri}}$ and ${}^{n}Y^{\alpha} = \widehat{Y}^{\alpha}({}^{n}\gamma^{\alpha})$ the yield stress of phase α at time $t = {}^{n}t$. For the derivation of the trial plastic driving force, we make use of the intermediate state potential $\tilde{\mathit{\Psi}} := \widehat{\mathit{\Psi}}({}^{n+1}\varepsilon, {}^{n}\tilde{\boldsymbol{\varepsilon}}^{\mathrm{1d}}_{\mathrm{pl}}, \theta, {}^{n+1}\boldsymbol{\xi})$, where the updated volume fractions ${}^{n+1}\boldsymbol{\xi}$ obtained from the phase-transformation algorithm, (4.33) and (4.34), are considered. Thus, the trial plastic driving force for phase α results in

$$
\begin{aligned}
q^{\alpha}_{\mathrm{pl},\mathit{\Psi},\mathrm{tri}} &= -\left.\frac{\partial\widehat{\mathit{\Psi}}({}^{n+1}\varepsilon, {}^{n}\boldsymbol{\varepsilon}^{\mathrm{1d}}_{\mathrm{pl}}, \theta, {}^{n+1}\boldsymbol{\xi})}{\partial\,{}^{n}\varepsilon^{\alpha}_{\mathrm{pl}}}\right|_{\theta} \\
&= -\left.\frac{\partial}{\partial\,{}^{n}\varepsilon^{\alpha}_{\mathrm{pl}}}\right|_{\theta} \sum_{\alpha=1}^{\nu} {}^{n+1}\xi^{\alpha}\widehat{\psi}^{\alpha}({}^{n+1}\varepsilon, {}^{n}\varepsilon^{\alpha}_{\mathrm{pl}}, \theta) \\
&= -\,{}^{n+1}\xi^{\alpha}\left.\frac{\partial\widehat{\psi}^{\alpha}({}^{n+1}\varepsilon, {}^{n}\varepsilon^{\alpha}_{\mathrm{pl}}, \theta)}{\partial\,{}^{n}\varepsilon^{\alpha}_{\mathrm{pl}}}\right|_{\theta} \quad .
\end{aligned} \tag{4.36}
$$

Based on this, the trial value $\mathit{\Phi}^{\alpha}_{\mathrm{tri}}$ of the yield function can be evaluated, facilitating to express the Lagrangian multiplier as

$$
{}^{n+1}\lambda^{\alpha} = \frac{\mathit{\Phi}^{\alpha}_{\mathrm{tri}}}{{}^{n+1}\xi^{\alpha}\,\left[\mathsf{E}^{\alpha} + H^{\alpha}\right]} \quad . \tag{4.37}
$$

The plastic strains $\varepsilon^{\alpha}_{\mathrm{pl}}$ in each phase α can then be updated from time ${}^{n}t$ to ${}^{n+1}t$ in an explicit manner according to (4.35), while the accumulated plastic strains ${}^{n+1}\gamma^{\alpha}$ are obtained from

$$
{}^{n+1}\gamma^{\alpha} = {}^{n}\tilde{\gamma}^{\alpha} + {}^{n+1}\lambda^{\alpha} \quad . \tag{4.38}
$$

Here, the consistency of history variables is accounted for by considering the intermediate accumulated plastic strains

$$ {}^{n}\tilde{\gamma}^{\alpha} = \widehat{\tilde{\gamma}}^{\alpha}({}^{n}\gamma^{\alpha}, {}^{n}\tilde{\varepsilon}^{\alpha}_{\mathrm{pl}}, {}^{n}\varepsilon^{\alpha}_{\mathrm{pl}}) := {}^{n}\gamma^{\alpha} + |{}^{n}\tilde{\varepsilon}^{\alpha}_{\mathrm{pl}} - {}^{n}\varepsilon^{\alpha}_{\mathrm{pl}}| \quad . \tag{4.39} $$

Moreover, note that the change of plastic strains due to inheritance can be expressed in terms of

$$ \Delta\varepsilon^{\alpha}_{\mathrm{pl,inh}} := \tilde{\varepsilon}^{\alpha}_{\mathrm{pl}} - \varepsilon^{\alpha}_{\mathrm{pl}} \quad . \tag{4.40} $$

A flowchart visualising the actual algorithmical implementation is provided in Section 4.5.2.

4.3 Numerical Examples

This section provides several numerical examples for the model presented in Section 4.1, where we consider homogeneous deformation states at constant temperature using a quasi-static strain rate of $\dot{\varepsilon} = 10^{-4}\,s^{-1}$. In Section 4.3.1 we show the behaviour of the phase-transformation model without consideration of plasticity, illustrating that the implemented phase transformation model works correctly.

Then, in Section 4.3.2 the interactions between phase-transformations and plasticity are evaluated. In particular, two numerical examples are adressed, highlighting the influence of concave and convex plasticity inheritance functions. For these examples we restrict ourselves to the tensile regime in stress space, since we in this work only consider a martensitic tension phase for simplicity.

In Section 4.3.3 we investigate the behaviour of the phase-transformation-plasticity model when applied to material parameters corresponding to TRIP steel, see Table 4.2. Note that the TRIP steel material parameters chosen particularly involve higher martensitic transformation strains—however, the distinction between volumetric and deviatoric transformation strains is not possible at this point, as it is introduced in a further model extension provided in Chapter 3. For the presented TRIP steel results we once more focus on the tensile regime, where the results are restricted to non-negative stresses as in the case of SMA.

4.3.1 SMA – phase-transformations without plasticity

Figure 4.4 displays the stress-strain response of SMA at different temperatures. In order to show that the model properly describes the temperature-dependent pseudo-elastic response of SMA, we compute the stress-strain response at $\theta = 263\,\mathrm{K}$, Fig. 4.4(a), and $\theta = 323\,\mathrm{K}$, Fig. 4.4(a), using parameters as suggested in [51] and a maximum strain of $\varepsilon_{\max} = 0.08$.

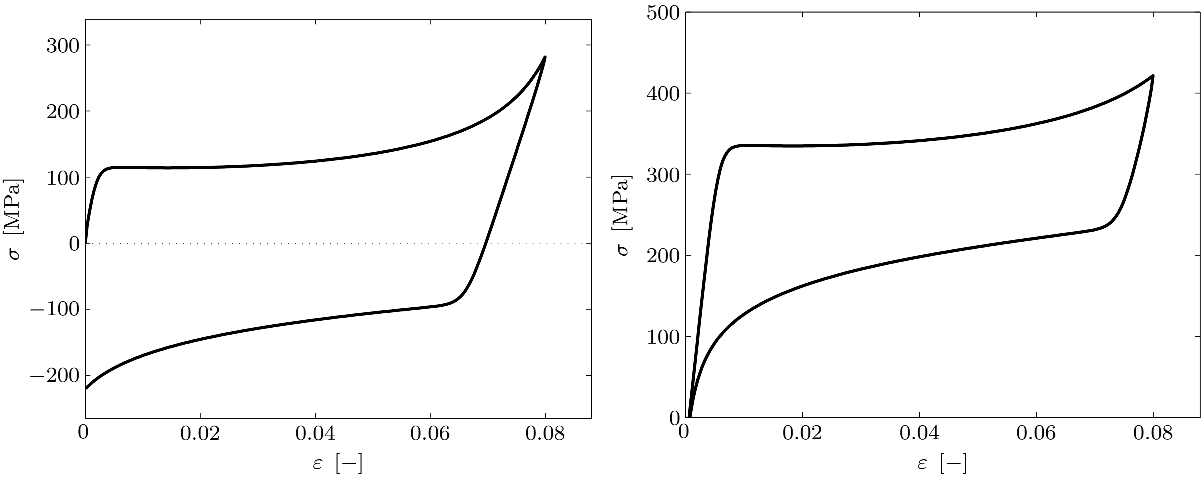

(a) Stress-strain diagram, $\theta = 263\,\mathrm{K}$.

(b) Stress-strain diagram, $\theta = 323\,\mathrm{K}$.

Figure 4.4: Phase-transformations without plasticity in SMA: pseudo-plastic response as observed at low temperatures, $\theta = 263\,\mathrm{K}$ (a) and pseudo-elastic response as observed at high temperatures, $\theta = 323\,\mathrm{K}$ (b), cf. [51].

4.3.2 SMA – phase-transformations with plasticity

In contrast to the non-plastic response provided in Section 4.3.1, we now make use of the material parameters provided in Table 4.1. In particular, we now investigate the behaviour of the model at a constant temperature of $\theta = 283\,\mathrm{K}$. As initial conditions, we assume the material to consist of pure austenite, i.e. ${}^0\boldsymbol{\xi} = [\,\xi^{\mathrm{A}}|_0,\, \xi^{\mathrm{M}}|_0\,]^{\mathrm{t}} = [\,1,\, 0\,]^{\mathrm{t}}$. The material is then loaded by applying a strain of $\widehat{\varepsilon}(t) = \widehat{\tau}(t)\,\varepsilon_{\max}$, where $\widehat{\tau}(t) \subset \mathbb{R}$ is a time-scaling function and $\varepsilon_{\max} = 0.05$ is the maximum applied strain.

Figure 4.5 shows the results obtained for a concave inheritance probability function, where we restrict ourselves to the tensile regime, i.e. $\sigma > 0$. As a tensile load is applied, martensite starts to evolve, see Fig. 4.5(b), while both material phases initially behave elastically in terms of $\varepsilon^{\mathrm{A}}_{\mathrm{pl}} = \varepsilon^{\mathrm{M}}_{\mathrm{pl}} = 0$ as $\varepsilon < 0.0175$, compare Fig. 4.5(c). At $\varepsilon \approx 0.0175$, plastic flow in the austenitic phase is initiated, and at $\varepsilon \approx 0.0225$ also martensite starts to deform plastically, such that $\varepsilon^{\mathrm{A}}_{\mathrm{pl}} > \varepsilon^{\mathrm{M}}_{\mathrm{pl}}$. The simultaneous plastic flow of both material phases can also be seen in the stress-strain diagram provided in Fig. 4.5(a) where a linear proportional hardening behaviour for $\varepsilon \in [\,0.0225,\, 0.05\,]$ is observed.

As austenite possesses a higher plastic strain than martensite during the first tensile load cycle since $\varepsilon^{\mathrm{A}}_{\mathrm{pl}} > \varepsilon^{\mathrm{M}}_{\mathrm{pl}}$ for $\varepsilon \in [\,0.0225,\, 0.05\,]$, compare Fig. 4.5(c), the evolving martensitic phase, Fig. 4.5(b), inherits additional plastic strains present in the austenitic phase. However, the change of plastic strains due to inheritance is rather small as long as the change of plastic strains is mainly governed by the plastic evolution law (4.14), see Fig. 4.5(d).

As the maximum strain of $\varepsilon = 0.05$ is reached, the load reverses. At this point also the phase-transformations start to revert. As shown in Fig. 4.5(b), the volume fraction of

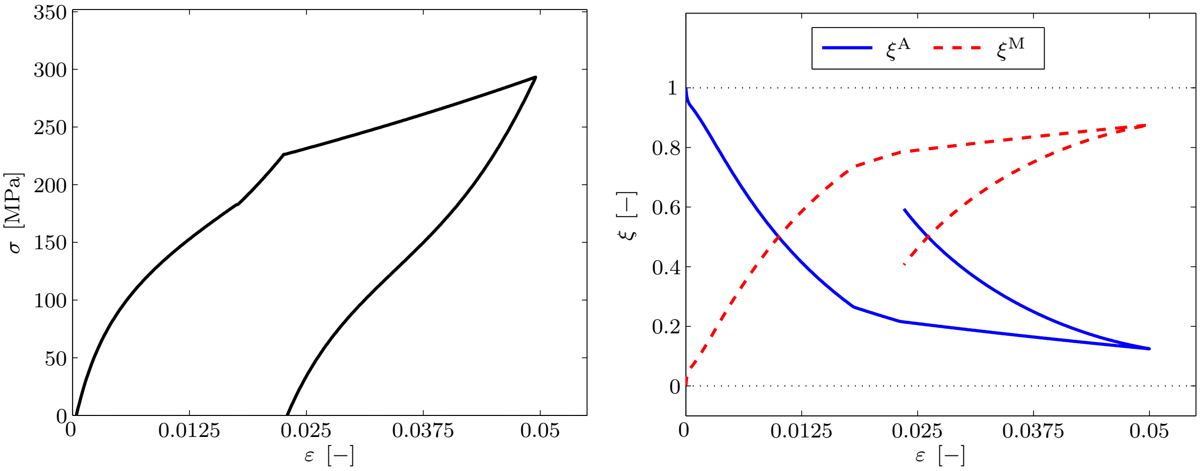

(a) Stress-strain diagram.

(b) Evolution of volume fractions.

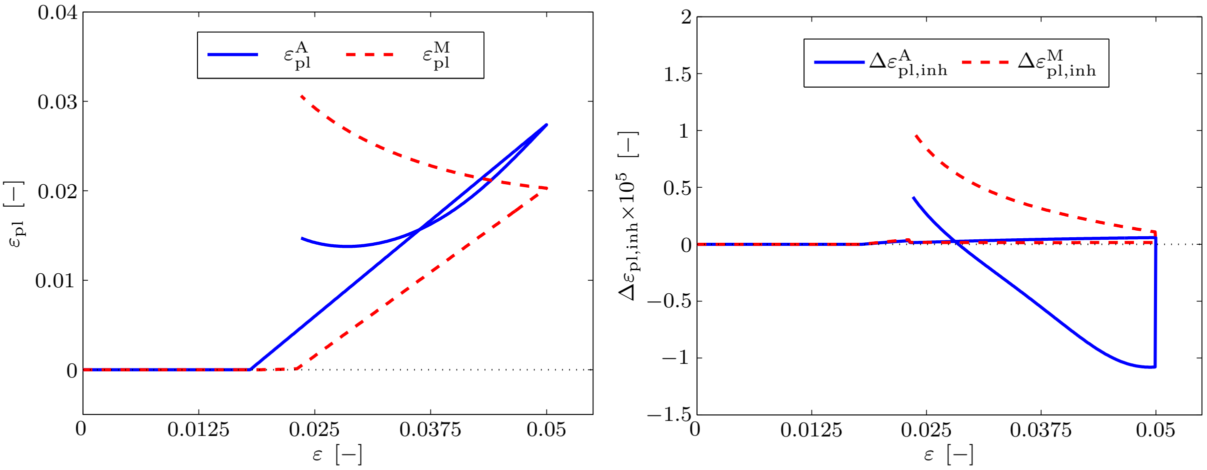

(c) Evolution of plastic strains.

(d) Change of plastic strains due to inheritance.

Figure 4.5: Phase-transformations in SMA: stress-strain diagram (a), evolution of volume fractions (b), evolution of plastic strains (c) and change of plastic strains due to inheritance (d) resulting from the evolution of phases obtained by applying a maximum tension of $\varepsilon_{\max} = 0.05$. Note that concave inheritance probability functions $\Pi^{\mathrm{A}\to\mathrm{M}} = \widehat{\Pi}^{\mathrm{A}\to\mathrm{M}}_{\mathrm{ccv}}(\xi^{\mathrm{A}}, \varepsilon^{\mathrm{A}}_{\mathrm{pl}}; \kappa = 0.05, \varepsilon^{\mathrm{A}}_{\mathrm{pl,sat}} = 0.1)$ and $\Pi^{\mathrm{M}\to\mathrm{A}} = \widehat{\Pi}^{\mathrm{M}\to\mathrm{A}}_{\mathrm{ccv}}(\xi^{\mathrm{M}}, \varepsilon^{\mathrm{M}}_{\mathrm{pl}}; \kappa = 0.05, \varepsilon^{\mathrm{M}}_{\mathrm{pl,sat}} = 0.1)$ are chosen here, see Figure 4.3. The calculations are carried out at constant temperature of $\theta = 283\,\mathrm{K}$.

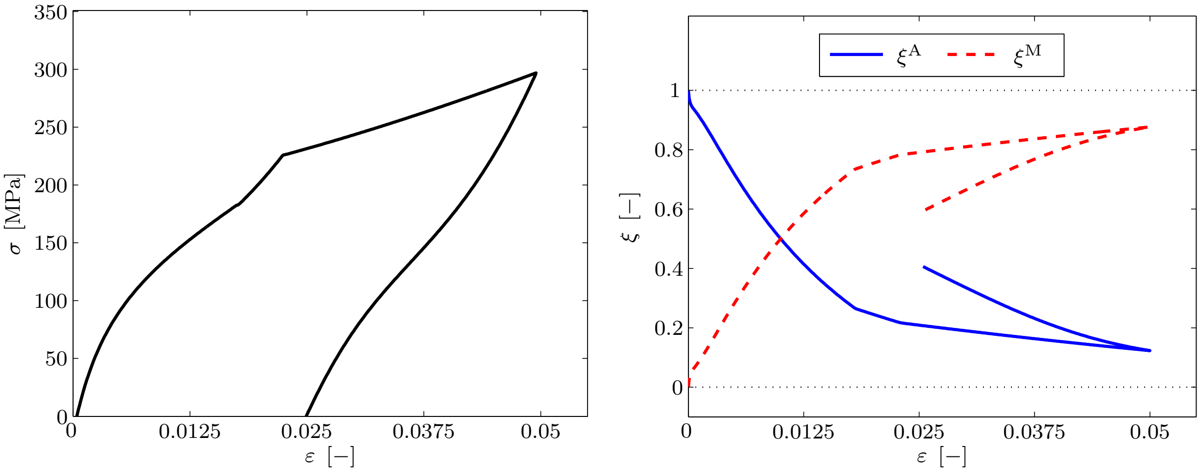

(a) Stress-strain diagram.

(b) Evolution of volume fractions.

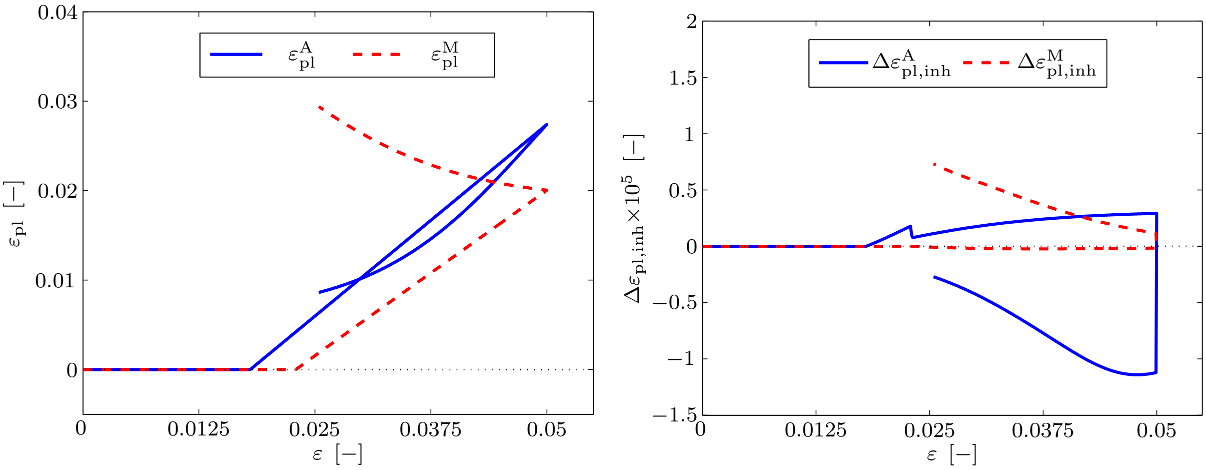

(c) Evolution of plastic strains.

(d) Change of plastic strains due to inheritance.

Figure 4.6: Phase-transformations in SMA: stress-strain diagram (a), evolution of volume fractions (b), evolution of plastic strains (c) and change of plastic strains due to inheritance (d) resulting from the evolution of phases obtained by applying a maximum tension of $\varepsilon_{\max} = 0.05$. Note that convex inheritance probability functions $\mathit{\Pi}^{\mathrm{A}\to\mathrm{M}} = \widehat{\mathit{\Pi}}_{\mathrm{cvx}}^{\mathrm{A}\to\mathrm{M}}(\xi^{\mathrm{A}}, \varepsilon_{\mathrm{pl}}^{\mathrm{A}}; \kappa = 0.1)$ and $\mathit{\Pi}^{\mathrm{M}\to\mathrm{A}} = \widehat{\mathit{\Pi}}_{\mathrm{cvx}}^{\mathrm{M}\to\mathrm{A}}(\xi^{\mathrm{M}}, \varepsilon_{\mathrm{pl}}^{\mathrm{M}}; \kappa = 0.1)$ are chosen here, see Fig. 4.2. The calculations are carried out at constant temperature of $\theta = 283\,\mathrm{K}$.

martensite starts to decrease, while the austenitic phase is now evolving. Furthermore, the evolution of plasticity stops—the change of plastic strains is now solely driven by inheritance resulting from the evolution of the austenitic phase, see Fig. 4.5(b). Due to the concave inheritance function applied, a part of the plastic strains is pushed to the martensitic phase, while the other part is inherited by austenite. Physically speaking, the dislocations pushed by the phase front lead to an increased plastic distortion of the martensitic phase such that the martensitic plastic strains increase, cf. Fig. 4.5(c). On the other hand, at $\varepsilon = 0.05$ the martensitic plastic strains are smaller than those in austenite. Thus the inheritance initially leads to a decrease of plastic strains in austenite. As the martensitic plastic strains increase futher, at $\varepsilon \approx 0.03$ also the austenitic plastic strains start to increase again. In line with Fig. 4.5(a), at $\varepsilon \approx 0.0225$ the stress reaches $\sigma = 0$ and the load cycle is completed.

Assuming a convex inheritance probability function means that dislocations are rather pushed than inherited by trend, compare Figs. 4.2 and 4.3. Fig. 4.6 provides the results obtained for SMA using a convex inheritance probability function. Comparison of Figs. 4.6(c) and 4.5(c) shows that the convex inheritance function leads to a slightly stronger increase of plastic strains in martensite, with at the same time stronger decrease of plastic strains in austenite. This corresponds to the assumption, that—by trend—the convex inheritance function rather pushes dislocations to the decreasing phase, while less dislocations remain for inheritance by the increasing phase. Comparison of Figs. 4.6(a) and 4.5(a) and Figs. 4.6(b) and 4.5(b), respectively, shows that the plasticity inheritance function has an influence also on the macroscopic response of the material. Not only the zero stress state is reached at different strains, but also the evolution of phases differs. To be specific, after reverting the load austenite is much more likely to evolve assuming concave inheritance, while for convex inheritance the austenitic volume fraction evolves with less intensity, cf. Figs. 4.5(b) and 4.6(b).

4.3.3 TRIP steel – phase-transformations with plasticity

Apart from SMA, we also investigate the behaviour of the material model when material constants as provided in Table 4.2 are applied. These are adapted to what is known for TRIP steels. As initial conditions, we once more assume the material to consist of pure austenite, i.e. ${}^{0}\boldsymbol{\xi} = [\,\xi^{\mathrm{A}}|_0,\, \xi^{\mathrm{M}}|_0\,]^{\mathrm{t}} = [\,1,\, 0\,]^{\mathrm{t}}$. Furthermore, we restrict ourselves to the tensile regime and non-negative stresses in the following. The calculation is done at a constant temperature of $\theta = 283\,\mathrm{K}$.

Figure 4.7 shows the results obtained for a concave inheritance probability function. Initially, the material behaves purely elastic, as neither phase-transformations occur nor plastic strains evolve, see Figs. 4.7(b) and 4.7(c), respectively. Then, at a strain of $\varepsilon \approx 0.005$, austenite starts to deform plastically, Fig. 4.7(c), as soon as the evolution of the martensitic tensile phase is triggered, Fig. 4.7(b). For further increased strain, both phases and thus the overall macroscopic material is undergoing plastic flow. As the load reverses, the volume fractions as well as the plastic strains remain constant, resulting in a purely elastic deformation back to the unloaded state at which external forces vanish identically, i.e. $\sigma = 0$. This result coincides with the experimentally observed fact that TRIP steels do not show the pseudo-elastic hysteresis behaviour as in the case of SMA. Comparison of Figs. 4.5(b) and 4.5(c) and 4.7(b) and 4.7(c), respectively, shows that for SMA the material initiates phase-transformations as soon as the load is applied and subsequently starts yielding when a given critical macroscopic load is reached. In contrast to that, when applied to TRIP steel the model predicts that the material starts yielding and transformation simultaneously.

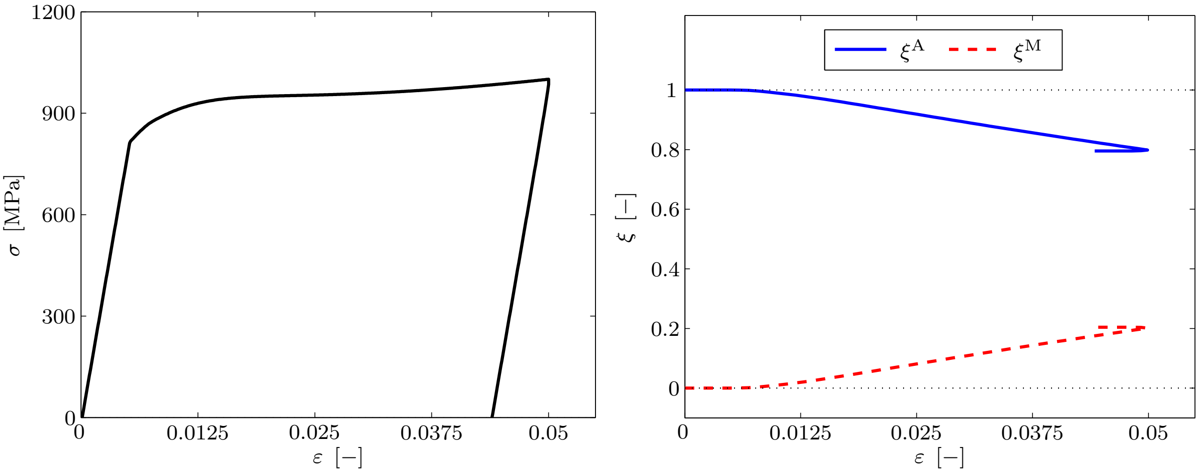

(a) Stress-strain diagram.

(b) Evolution of volume fractions.

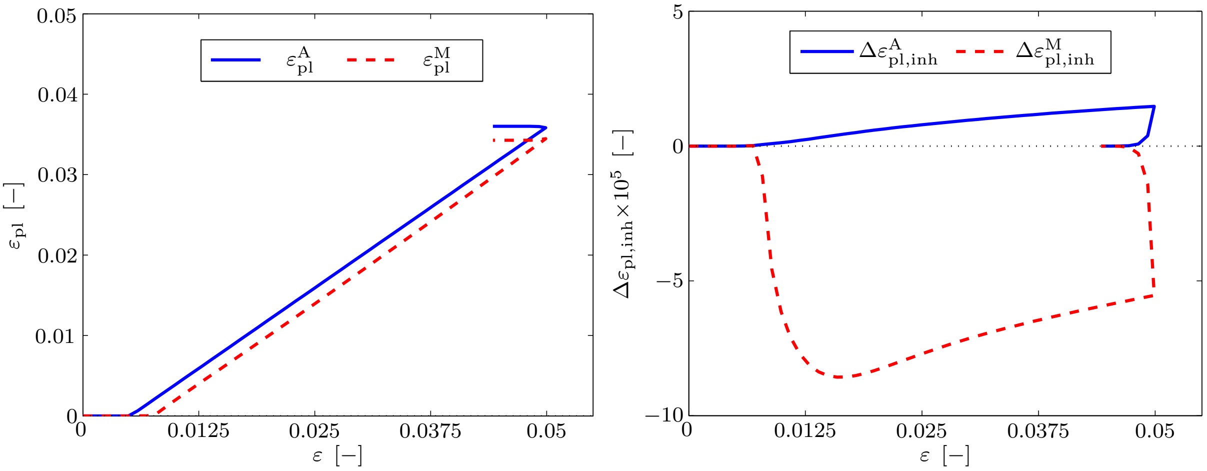

(c) Evolution of plastic strains.

(d) Change of plastic strains due to inheritance.

Figure 4.7: Model based on TRIP steel material parameters: stress-strain diagram (a), evolution of volume fractions (b), evolution of plastic strains (c) and change of plastic strains due to inheritance (d) resulting from the evolution of phases obtained by applying a maximum tension of $\varepsilon_{\max} = 0.05$. Note that concave inheritance probability functions $\Pi^{\mathrm{A}\to\mathrm{M}} = \widehat{\Pi}^{\mathrm{A}\to\mathrm{M}}_{\mathrm{ccv}}(\xi^{\mathrm{M}}, \varepsilon^{\mathrm{M}}_{\mathrm{pl}}; \kappa = 0.05, \varepsilon^{\mathrm{M}}_{\mathrm{pl,sat}} = 0.1)$ and $\Pi^{\mathrm{M}\to\mathrm{A}} = \widehat{\Pi}^{\mathrm{M}\to\mathrm{A}}_{\mathrm{ccv}}(\xi^{\mathrm{A}}, \varepsilon^{\mathrm{A}}_{\mathrm{pl}}; \kappa = 0.05, \varepsilon^{\mathrm{A}}_{\mathrm{pl,sat}} = 0.1)$ are chosen here, see Figure 4.3. The calculations are carried out at constant temperature of $\theta = 283\,\mathrm{K}$.

4.4 Summary

The main goal of this chapter is to develop a coupled model for the interaction of phase-transformations and plasticity. As a basis, we make use of the one-dimensional micromechanically motivated potential-based phase-transformation model introduced in Chapter 2. Based on this model, we extend the Helmholtz free energy function of the material in order to account for the influence of evolving plastic strains. Furthermore, we use a von-Mises type plasticity model in terms of the driving forces for each phase as related to the overall potential. For the plasticity model, we consider linear proportional hardening, facilitating to transpose the backward-Euler based evolution law in such way, that explicit updates of the plastic strains as well as plastic history variables are enabled in each load step. Together with the A-stable explicit update of the volume fractions, the overall model turns out to be numerically efficient.

The influence of the inheritance probability function is discussed in detail for SMA, where it is shown, that the type of inheritance law has an influence not only on the macroscopic stress response, but also on the evolution of volume fractions. Besides the application to SMA, we also apply the model to TRIP steel material parameters. In case of TRIP steel, the correlation between simulated stress-strain response and experimentally observed stress-strain behaviour shows a good agreement, where in particular the ongoing hardening up to large strains is represented by the model, see e.g. [34]. It turns out that for SMA the material first transforms and then yields, while for TRIP the material initiates yielding and transformation basically simultaneously. Although the underlying phase-transformation model was originally established for SMA, see [51], the application of the coupled phase-transformation plasticity model to TRIP steel gives promising results in view of future enhancements of the model.

In view of the chapters to follow, the correlation between simulation and experiment is expected to become more exact by additionally taking into account a martensitic compression phase, which—as discussed in [101]—is expected to increase the accurracy of the simulation results and allows to take into account the compression regime in addition. Also an extension of the model to the three-dimensional case, e.g. by means of a micro-sphere approach, will contribute to a generalisation of the macroscopic material response.

As elaborated in Section 4.3, the chosen inheritance law has a severe influence on the macroscopic material response. To this end, it is necessary to carry out detailed micromechanical experiments that reveal the complex interactions between evolving phase fronts and moving dislocations, eventually giving insight to the physical inheritance probability law depending on the volume fractions and dislocation densities as well as—in general—also on the temperatures of the involved phases.

4.5 Appendix

4.5.1 Material parameters

The material parameters used in this chapter are provided in Table 4.1 for SMA and in Table 4.2 for the TRIP steel simulations. Note that TRIP steel is considered to provide a higher Young's modulus and initial yield stress when compared to SMA. The experimentally observed high strength of the martensitic phase in TRIP steel is accounted for by means of the higher initial yield stress.

Table 4.1: SMA material parameters considered in Section 4.3.2, compare, e.g., [20, 51].

SMA phase	material parameter	symbol	value
austenite A (parent phase)	Young's modulus	E^{A}	67 GPa
	hardening modulus	H^{A}	$\mathsf{E}^{\mathrm{A}}/6$
	initial yield stress	Y_0^{A}	1200 MPa
	transformation strain	$\varepsilon_{\mathrm{tr}}^{\mathrm{A}}$	0
	latent heat	λ_T^{A}	0
martensite M	Young's modulus	E^{M}	26.3 GPa
	hardening modulus	H^{M}	$\mathsf{E}^{\mathrm{M}}/3$
	initial yield stress	Y_0^{M}	600 MPa
	transformation strain	$\varepsilon_{\mathrm{tr}}^{\mathrm{M}}$	0.025
	latent heat	λ_T^{M}	14500 J/kg
common parameters	coefficient of thermal expansion	ζ	12×10^{-7} K^{-1}
	reference temperature	θ_0	273 K
	heat capacity	c_p	400 J/kgK
	transition attempt frequency	ω	1.6 s^{-1}
	transformation region's volume	Δv	2.71×10^{-18} mm^3
	Boltzmann's constant	k	1.381×10^{-23} J/K

Table 4.2: Specific TRIP steel material parameters considered, compare [79].

TRIP steel phase	material parameter	symbol	value
austenite A (parent phase)	Young's modulus	E^{A}	160 GPa
	hardening modulus	H^{A}	$\mathsf{E}^{\mathrm{A}}/4$
	initial yield stress	Y_0^{A}	800 MPa
	transformation strain	$\varepsilon_{\mathrm{tr}}^{\mathrm{A}}$	0
martensite M	Young's modulus	E^{M}	160 GPa
	hardening modulus	H^{M}	$\mathsf{E}^{\mathrm{M}}/12$
	initial yield stress	Y_0^{M}	1200 MPa
	transformation strain	$\varepsilon_{\mathrm{tr}}^{\mathrm{M}}$	0.04
common parameters:	transition attempt frequency	ω	16 s^{-1}

4.5.2 Algorithmic flowchart

```
while $t < t_{\max}$ do
    set $t = {}^{n+1}t = {}^{n}t + \Delta t \in [\,0,\, t_{\max}\,]$
    given ${}^{n}\boldsymbol{\xi} = \left[{}^{n}\xi^{\mathrm{A}}, {}^{n}\xi^{\mathrm{M}}\right]^{\mathrm{t}}$, ${}^{n}\boldsymbol{\varepsilon}^{\mathrm{1d}}_{\mathrm{pl}} = \left[{}^{n}\varepsilon^{\mathrm{A}}_{\mathrm{pl}}, {}^{n}\varepsilon^{\mathrm{M}}_{\mathrm{pl}}\right]^{\mathrm{t}}$, ${}^{n}\boldsymbol{\gamma} = \left[{}^{n}\gamma^{\mathrm{A}}, {}^{n}\gamma^{\mathrm{M}}\right]^{\mathrm{t}}$, ${}^{n+1}\varepsilon$
    get ${}^{n+1}\boldsymbol{\xi}$                                                ▷ see (4.33)
    if $\Delta\xi^{\mathrm{M}} = {}^{n+1}\xi^{\mathrm{M}} - {}^{n}\xi^{\mathrm{M}} > 0$ then
        set increasing phase $\alpha :=$ M, decreasing phase $\beta :=$ A
    else
        set increasing phase $\alpha :=$ A, decreasing phase $\beta :=$ M
    end if
    get $\varPi^{\beta\to\alpha} = \widehat{\varPi}^{\beta\to\alpha}({}^{n+1}\xi^{\beta}, {}^{n}\varepsilon^{\beta}_{\mathrm{pl}}; \ldots)$        ▷ plastic inheritance probability
    get ${}^{n}\tilde{\varepsilon}^{\alpha}_{\mathrm{pl}}$ and ${}^{n}\tilde{\varepsilon}^{\beta}_{\mathrm{pl}}$                              ▷ see (4.26) and (4.28)
    set $\Delta\varepsilon^{\alpha}_{\mathrm{pl,inh}}$ and $\Delta\varepsilon^{\beta}_{\mathrm{pl,inh}}$                          ▷ see (4.40)
    set ${}^{n}\tilde{\gamma}^{\alpha} = \widehat{\tilde{\gamma}}^{\alpha}({}^{n}\gamma^{\alpha}, {}^{n}\tilde{\varepsilon}^{\alpha}_{\mathrm{pl}}, {}^{n}\varepsilon^{\alpha}_{\mathrm{pl}})$ and ${}^{n}\tilde{\gamma}^{\beta} = \widehat{\tilde{\gamma}}^{\beta}({}^{n}\gamma^{\beta}, {}^{n}\tilde{\varepsilon}^{\beta}_{\mathrm{pl}}, {}^{n}\varepsilon^{\beta}_{\mathrm{pl}})$    ▷ see (4.39)
    get $\tilde{\varPsi} := \widehat{\varPsi}({}^{n+1}\varepsilon, {}^{n}\tilde{\boldsymbol{\varepsilon}}^{\mathrm{1d}}_{\mathrm{pl}}, \theta, {}^{n+1}\boldsymbol{\xi})$          ▷ intermediate state potential
    get $q^{\alpha}_{\mathrm{pl},\varPsi,\mathrm{tri}}$ and $q^{\beta}_{\mathrm{pl},\varPsi,\mathrm{tri}}$                         ▷ see (4.36)
    get ${}^{n+1}\lambda^{\alpha}$ and ${}^{n+1}\lambda^{\beta}$                                 ▷ see (4.38)
    get ${}^{n+1}\varepsilon^{\alpha}_{\mathrm{pl}}$ and ${}^{n+1}\gamma^{\alpha}$                            ▷ see (4.35) and (4.38)
    set ${}^{n+1}\sigma = \left.\dfrac{\partial\widehat{\varPsi}({}^{n+1}\varepsilon, {}^{n+1}\boldsymbol{\varepsilon}^{\mathrm{1d}}_{\mathrm{pl}}, \theta, {}^{n+1}\boldsymbol{\xi})}{\partial\, {}^{n+1}\varepsilon}\right|_{\theta, {}^{n+1}\boldsymbol{\varepsilon}^{\mathrm{1d}}_{\mathrm{pl}}}$    ▷ see (4.22)
    return ${}^{n+1}\boldsymbol{\xi}$, ${}^{n+1}\boldsymbol{\varepsilon}^{\mathrm{1d}}_{\mathrm{pl}}$, ${}^{n+1}\boldsymbol{\gamma}$, ${}^{n+1}\sigma$
    set $n \leftarrow n + 1$
end while
```

Algorithm 3: Update scheme for the one-dimensional coupled phase-transformation plasticity model.

5 An affine micro-sphere model for phase-transformations interacting with plasticity

In this chapter, we use the one-dimensional, thermodynamically consistent phase-transformation model based on statistical physics that was originally introduced in [51] and that we used as a basis for the micro-sphere model presented in Chapter 2. Moreover, we consider the extension to plasticity by enhancing the Helmholtz free energy functions of the material phases considered as introduced in Chapter 4. We apply the coupled model to the simulation of phase-transformations between an austenitic parent phase A and a martensitic tension and compression phase, $\mathrm{M_t}$ and $\mathrm{M_c}$ in TRIP steel.

For conceptual simplicity, we assume von Mises-type plasticity with linear proportional hardening, where the plastic driving forces acting in each phase are derived from the overall free energy potential of the mixture. The coupled systems of evolution equations are evaluated using a staggered solution approach, where the change in plastic strains directly resulting from changing phase fractions is considered by means of a physically motivated plasticity inheritance law, cf. Chapter 4.

The one-dimensional model capturing phase-transformations and plasticity is embedded into an affine micro-sphere formulation in order to simulate three-dimensional boundary value problems—a technique well-established in the context of computational inelasticity at small strains, see e.g. [17] and [75]. The particular formulation proposed as this chapter proceeds does not exhibit a volumetric-deviatoric split in the kinematics—note that the general framework is extended to capture different strain modes in Chapter 3. For the solution of the underlying system of evolution equations, we use a Newmark-based explicit integration scheme which was proved unconditionally A-stable [101]. In addition to homogeneous deformation states investigated in Sections 5.1 and 5.2, representative finite element examples are discussed in Section 5.3. It is shown that the model is capable of reflecting the experimentally observed behaviour of TRIP steel.

5.1 One-dimensional model for phase-transformations interacting with plasticity

The phases considered are presumed to show thermo-elasto-plastic behaviour. In this context, a Helmholtz free energy function $\psi^\alpha = \widehat{\psi}^\alpha(\varepsilon, \varepsilon^\alpha_{\mathrm{pl}}, \theta)$ of the form

$$\psi^\alpha = \frac{1}{2}\,\mathsf{E}^\alpha[\varepsilon - \varepsilon^\alpha_{\mathrm{tr}} - \varepsilon^\alpha_{\mathrm{pl}}]^2 - \zeta^\alpha\,\mathsf{E}^\alpha\,[\varepsilon - \varepsilon^\alpha_{\mathrm{tr}} - \varepsilon^\alpha_{\mathrm{pl}}][\theta - \theta_0] + C^\alpha \tag{5.1}$$

is assigned to each phase α. Here, we consider

$$C^\alpha = \rho_0\, c^\alpha_p\, \theta \left[1 - \log\left(\frac{\theta}{\theta_0}\right)\right] - \rho_0\, \lambda^\alpha_T \left[1 - \frac{\theta}{\theta_0}\right] \tag{5.2}$$

the chemical energy, E^α the Young's modulus, $\varepsilon = \nabla_x u$ the total strains, $\varepsilon_{\mathrm{tr}}$ the transformation strains, $\varepsilon_{\mathrm{pl}}$ the plastic strains, ζ the coefficient of thermal expansion, θ the current absolute temperature, θ_0 the reference temperature, c_p the heat capacity, and λ_T the latent heat of the respective material phase. Since the distortional energy of the phase boundaries is neglected here, the overall free energy of the mixture $\varPsi = \sum_\alpha \xi^\alpha \psi^\alpha$ follows directly from the free energy contributions of the constituents.

The Gibbs potential G is obtained by carrying out the Legendre-transformation

$$G = \sum_{\alpha=1}^{\nu} \xi^\alpha\,[\psi^\alpha - \sigma\,\varepsilon] \quad , \tag{5.3}$$

where $\sigma = \partial\varPsi/\partial\varepsilon|_{\theta,\varepsilon_{\mathrm{pl}}}$ is the stress acting in the one-dimensional continuum considered. As introduced in Chapter 2, transformation probabilities are computed and assembled to a transformation probability matrix $\boldsymbol{Q} \in \mathbb{R}^{3\times3}$, facilitating to derive the evolution of volume fractions as $\dot{\boldsymbol{\xi}} = \boldsymbol{Q} \cdot \boldsymbol{\xi}$, wherein $\boldsymbol{\xi} = [\xi^{\mathrm{A}}, \xi^{\mathrm{M_t}}, \xi^{\mathrm{M_c}}]^{\mathrm{t}}$ in line with Chapters 2 and 3. Here, A denotes austenite, whereas $\mathrm{M_t}$ and $\mathrm{M_c}$ refer to the martensitic tension and compression phase. See Section 2.1.2 for details on the algorithmical treatment of this system of evolution equations.

To incorporate plasticity, the individual plastic driving force $q^\alpha_{\mathrm{pl},\varPsi}$ of each phase α is derived from the overall energy potential $\varPsi$ according to $q^\alpha_{\mathrm{pl},\varPsi} = -\,\partial\varPsi/\partial\varepsilon^\alpha_{\mathrm{pl}}\big|_{\theta,\varepsilon,\xi}$. With the driving force and the current yield stress Y^α at hand, the yield function $\varPhi^\alpha$ determining the admissible elastic domain in phase α is given as

$$\widehat{\varPhi}^\alpha(q^\alpha_{\mathrm{pl},\varPsi}, Y^\alpha) = |q^\alpha_{\mathrm{pl},\varPsi} - \xi^\alpha\, b^\alpha| - \xi^\alpha\, Y^\alpha \leq 0 \tag{5.4}$$

with an equilibrium back stress

$$b^\alpha := \widehat{\sigma}^\alpha(\varepsilon = 0, \varepsilon^\alpha_{\mathrm{pl}} = 0, \theta) = -\mathsf{E}^\alpha\varepsilon^\alpha_{\mathrm{tr}} + \zeta^\alpha\mathsf{E}^\alpha\varepsilon^\alpha_{\mathrm{tr}}[\theta - \theta_0] \quad . \tag{5.5}$$

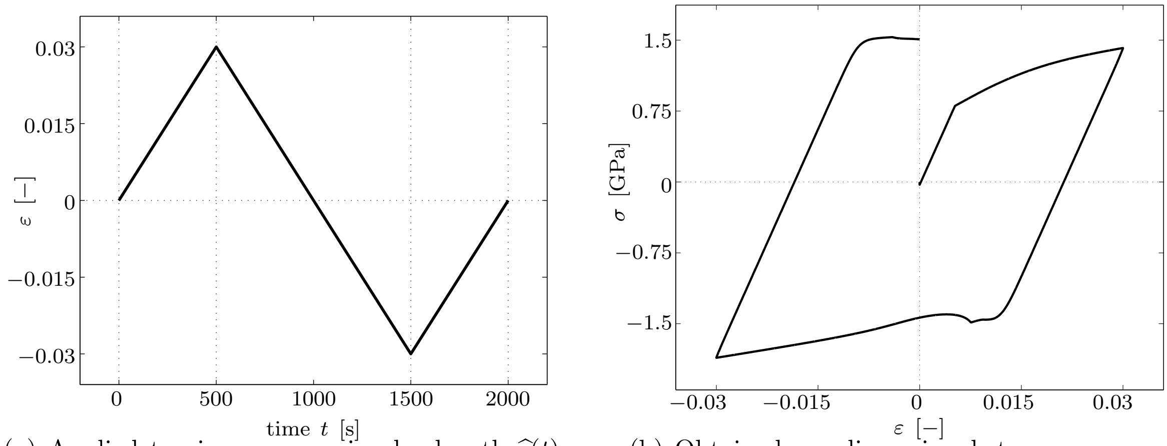

(a) Applied tension-compression load path $\hat{\varepsilon}(t)$ with constant strain rate and a maximum strain of $\varepsilon_{\max} = 0.03$.

(b) Obtained one-dimensional stress response.

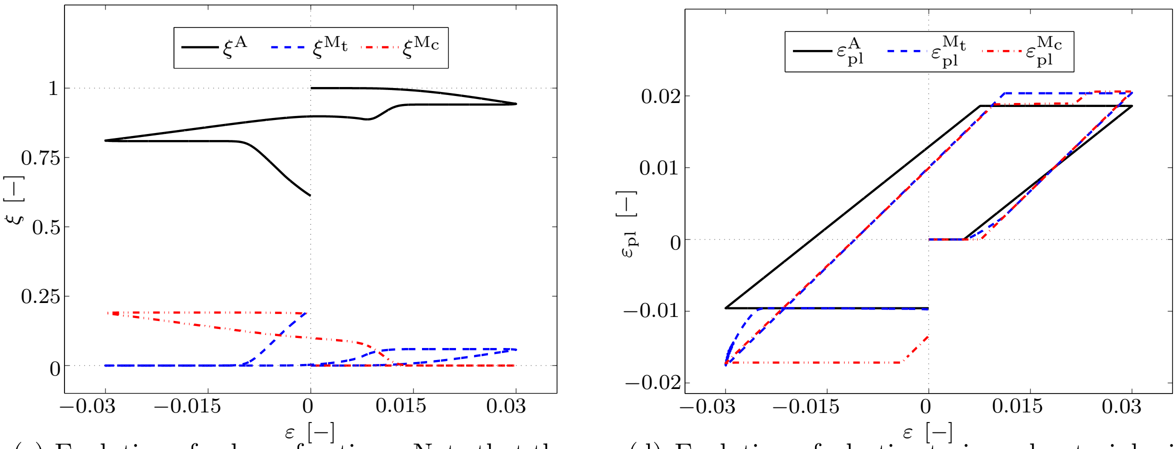

(c) Evolution of volume fractions. Note that the martensitic volume fractions in TRIP steel tend to increase with the number of load cycles applied.

(d) Evolution of plastic strains—due to inheritance from austenite, $\varepsilon_{\mathrm{pl}}^{\mathrm{M_c}}$ increases during tension and acts as a starting value for plasticity in the $\mathrm{M_c}$ phase.

Figure 5.1: One-dimensional tension-compression load cycle applied to the underlying one-dimensional coupled model for the simulation of phase-transformations and plasticity. The load path provided in (a) shows the scalar-valued strain that is applied at a constant strain rate with maximum strain $\varepsilon_{\max} = 0.03$. The obtained stress-strain response is provided in (b) and corresponds to experimentally observed macroscopic TRIP steel responses. Moreover, we provide the evolution of volume fractions and plastic strains in (c) and (d), respectively.

We assume linear proportional hardening for conceptual simplicity, facilitating to derive the current yield stress as $Y^\alpha = Y^0 + \varepsilon^\alpha_{\text{pl,acc}} H^\alpha$, with Y^0 the initial yield stress, $\varepsilon^\alpha_{\text{pl,acc}}$ the accumulated plastic strains and H^α the hardening modulus. For the evolution of plastic strains, we obtain

$$\dot{\varepsilon}^\alpha_{\text{pl}} = \dot{\lambda}^\alpha \, \frac{\partial \varPhi^\alpha}{\partial q^\alpha_{\text{pl},\varPsi}} = \dot{\lambda}^\alpha \, \text{sgn}\left(q^\alpha_{\text{pl},\varPsi} - \xi^\alpha \, b^\alpha\right) \tag{5.6}$$

with an appropriate Lagrangian multiplier $\dot{\lambda}^\alpha \geq 0$. Further details on the numerical evaluation as well as all material parameters considered are provided in Table 4.2. Besides that, in the current chapter we assume $\varepsilon^{\text{M}_\text{c}}_{\text{tr}} = -0.04$ for the transformation strains of the newly introduced martensitic compression phase.

In addition to the evolution of plastic strains, we also consider incremental changes in plastic strains resulting from incremental changes in volume fractions—a mechanism we call plastic inheritance. The basic concept of plastic inheritance is the idea that plastic strains—or rather dislocations—can be either inherited or pushed by a propagating phase front. The inheritance probability $\varPi$, i.e. the probability of plastic strains being inherited to a propagating phase, is assumed to depend on current volume fractions ξ, the amount of the volume fraction increment $\Delta\xi$, the density of plastic strains ε_{pl} and specific material parametres. Based on these quantities, an inheritance probability function can be evaluated, resulting in a specific inheritance probability value $\varPi \in [0,1] \subset \mathbb{R}$. Since we here consider three solid material phases, the plastic inheritance law valid for two phases—as derived in Section 4.1.3—is now generalised to capture inheritance interactions between three independent material phases. For more details on the derivation of the three-phase plasticity inheritance law, see Section 6.2.

Consider the discrete update from time ${}^{n}t$ to ${}^{n+1}t$, with $\Delta t := {}^{n+1}t - {}^{n}t > 0$. Suppose that the volume fraction of one phase $\alpha \in \{\text{A}, \text{M}_\text{t}, \text{M}_\text{c}\}$ increases from step n to $n+1$, i.e. $\Delta\xi^\alpha = {}^{n+1}\xi^\alpha - {}^{n}\xi^\alpha > 0$ and that the two remaining phases β and γ decrease, i.e. $\Delta\xi^\beta < 0$ and $\Delta\xi^\gamma < 0$, with $\beta, \gamma \in \{\text{A}, \text{M}_\text{t}, \text{M}_\text{c}\}$. The updated plastic strains $\tilde{\varepsilon}_{\text{pl}}$ resulting from an incremental change in volume fractions can then be computed from

$$\tilde{\varepsilon}^\alpha_{\text{pl}} = \frac{1}{{}^{n+1}\xi^\alpha} \left[{}^{n}\varepsilon^\alpha_{\text{pl}} \, {}^{n}\xi^\alpha - \varPi^{\beta\to\alpha} \, \Delta\xi^\beta \, {}^{n}\varepsilon^\beta_{\text{pl}} - \varPi^{\gamma\to\alpha} \Delta\xi^\gamma \, {}^{n}\varepsilon^\gamma_{\text{pl}} \right] \quad , \tag{5.7}$$

$$\tilde{\varepsilon}^\beta_{\text{pl}} = \frac{1}{{}^{n+1}\xi^\beta} \left[{}^{n}\xi^\beta + \varPi^{\beta\to\alpha} \, \Delta\xi^\beta \right] {}^{n}\varepsilon^\beta_{\text{pl}} \quad , \tag{5.8}$$

$$\tilde{\varepsilon}^\gamma_{\text{pl}} = \frac{1}{{}^{n+1}\xi^\gamma} \left[{}^{n}\xi^\gamma + \varPi^{\gamma\to\alpha} \, \Delta\xi^\gamma \right] {}^{n}\varepsilon^\gamma_{\text{pl}} \quad . \tag{5.9}$$

In case that we have one decreasing phase α and two increasing phases, β and γ, it follows

$$\tilde{\varepsilon}_{\mathrm{pl}}^{\alpha} = \frac{{}^{n}\varepsilon_{\mathrm{pl}}^{\alpha}}{{}^{n+1}\xi^{\alpha}} \left[{}^{n}\xi^{\alpha} - \Pi^{\alpha\to\beta}\,\Delta\xi^{\beta} - \Pi^{\alpha\to\gamma}\Delta\xi^{\gamma} \right] \quad , \tag{5.10}$$

$$\tilde{\varepsilon}_{\mathrm{pl}}^{\beta} = \frac{1}{{}^{n+1}\xi^{\beta}} \left[{}^{n}\varepsilon_{\mathrm{pl}}^{\beta}\,{}^{n}\xi^{\beta} + \Pi^{\alpha\to\beta}\,\Delta\xi^{\beta}\,{}^{n}\varepsilon_{\mathrm{pl}}^{\alpha} \right] \quad , \tag{5.11}$$

$$\tilde{\varepsilon}_{\mathrm{pl}}^{\gamma} = \frac{1}{{}^{n+1}\xi^{\gamma}} \left[{}^{n}\varepsilon_{\mathrm{pl}}^{\gamma}\,{}^{n}\xi^{\gamma} + \Pi^{\alpha\to\gamma}\,\Delta\xi^{\gamma}\,{}^{n}\varepsilon_{\mathrm{pl}}^{\alpha} \right] \quad , \tag{5.12}$$

for the consistently updated plastic strains.

A numerical example depicting the behaviour of the one-dimensional material model is provided in Fig. 5.1. Here, we use a quasi-static strain rate of $\dot{\varepsilon} = 6 \times 10^{-5}\,\mathrm{s}^{-1}$ with a load path provided in Fig. 5.1(a). The obtained stress-strain response is depicted in Fig. 5.1(b), whereas the evolution of volume fractions ξ is shown in Fig. 5.1(c). It is shown that the martensitic tensile phase $\mathrm{M_t}$ evolves during the tensile load cycle, while the martensitic compression phase $\mathrm{M_c}$ evolves during the compression load cycle. Moreover, the evolution of individual plastic strains for each phase is provided in Fig. 5.1(d).

5.2 Micro-sphere application

To extend the one-dimensional coupled model to three dimensions, it is embedded into a kinematically constrained affine micro-sphere formulation using, e.g., 21 integration directions, cf. [75, 92]. In this context, the one-dimensional micro-sphere strains ε are obtained using projections of the macro-scale strain tensor $\boldsymbol{\varepsilon}$ with respect to the underlying integration directions $\boldsymbol{r} \in \mathbb{U}^2$. To be specific, $\varepsilon = [\boldsymbol{r} \otimes \boldsymbol{r}] : \boldsymbol{\varepsilon}$ represents the affine strain in the direction of $\boldsymbol{r}$ being transferred to the micro-sphere level, cf. Section 2.2.

Apart from the transfer of macroscopic strains to the micro level, the relevant quantities computed at the micro level, i.e. stresses, volume fractions and plastic strains, have to be transferred back to the macro level. The macroscopic stresses $\boldsymbol{\sigma} = \widehat{\boldsymbol{\sigma}}(\sigma)$, volume fractions $\Xi^{\alpha} = \widehat{\Xi}^{\alpha}(\xi^{\alpha})$ and plastic strains $\varepsilon_{\mathrm{pl}}^{\mathrm{mac},\alpha} = \widehat{\varepsilon}_{\mathrm{pl}}^{\mathrm{mac},\alpha}(\varepsilon_{\mathrm{pl}}^{\alpha})$ are derived as

$$\boldsymbol{\sigma} = \frac{1}{4\pi} \int_{\mathbb{U}^2} \sigma\, \boldsymbol{r} \otimes \boldsymbol{r}\, \mathrm{d}a \quad , \tag{5.13}$$

$$\Xi^{\alpha} = \frac{1}{4\pi} \int_{\mathbb{U}^2} \xi^{\alpha}\, \mathrm{d}a \quad , \tag{5.14}$$

$$\varepsilon_{\mathrm{pl}}^{\mathrm{mac},\alpha} = \frac{1}{4\pi} \int_{\mathbb{U}^2} \varepsilon_{\mathrm{pl}}^{\alpha}\, \mathrm{d}a \quad , \tag{5.15}$$

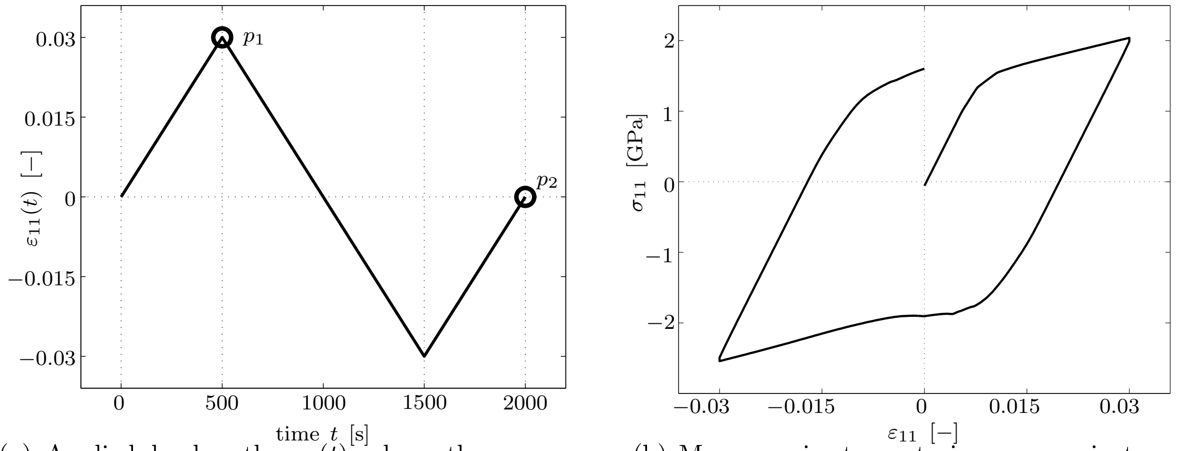

(a) Applied load path $\varepsilon_{11}(t)$ where the macroscopic strain tensor is prescribed as $\widehat{\boldsymbol{\varepsilon}}(t) = \varepsilon_{11}(t)\, \boldsymbol{e}_1 \otimes \boldsymbol{e}_1$.

(b) Macroscopic stress-strain response in terms of the σ_{11} micro-sphere stress component. Note that this macroscopic response nicely reflects experimentally observed behaviour of TRIP steel.

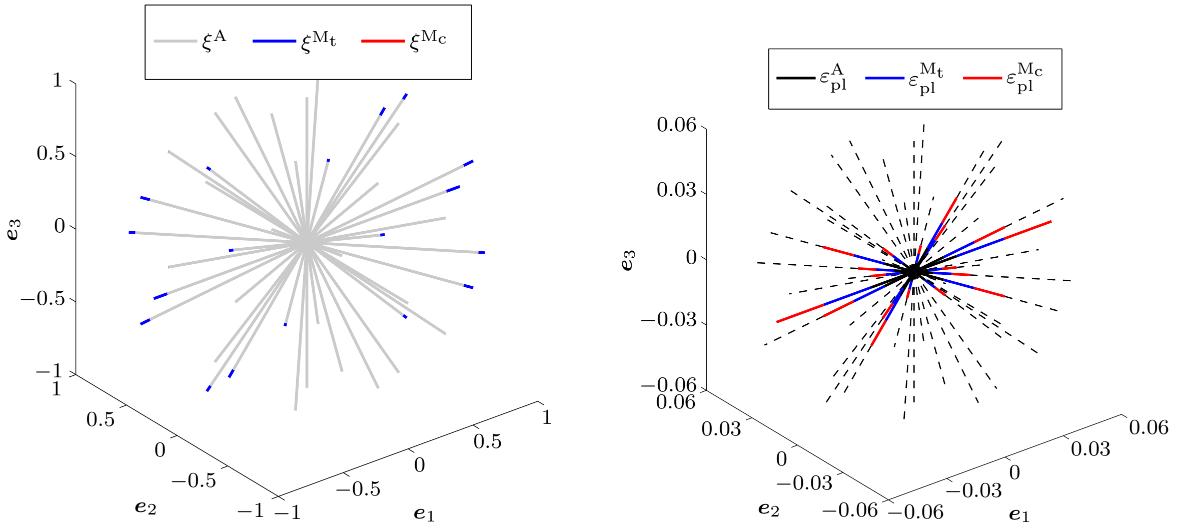

(c) Spatial distribution of volume fractions at maximum tension, i.e. state p_1 in (a). During the first tensile cycle, only a small austenitic volume fraction transforms to martensite.

(d) Spatial distribution of plastic strains obtained at maximum tension, i.e. state p_1 in (a).

Figure 5.2: Application of the one-dimensional coupled model for the simulation of phase-transformations and plasticity in an affine micro-sphere framework using 21 integration directions. A mixed volumetric-deviatoric load is applied where the macroscopic strain tensor is prescribed in terms of $\widehat{\boldsymbol{\varepsilon}}(t) = \varepsilon_{11}(t)\, \boldsymbol{e}_1 \otimes \boldsymbol{e}_1$ with a maximum strain of $\varepsilon_{11,\max} = 0.03$ (a). The corresponding σ_{11} stress component is provided in (b). The spatial distribution of volume fractions and plastic strains, (c) and (d), respectively, are obtained for the state of maximum tension, i.e. state p_1 in (a).

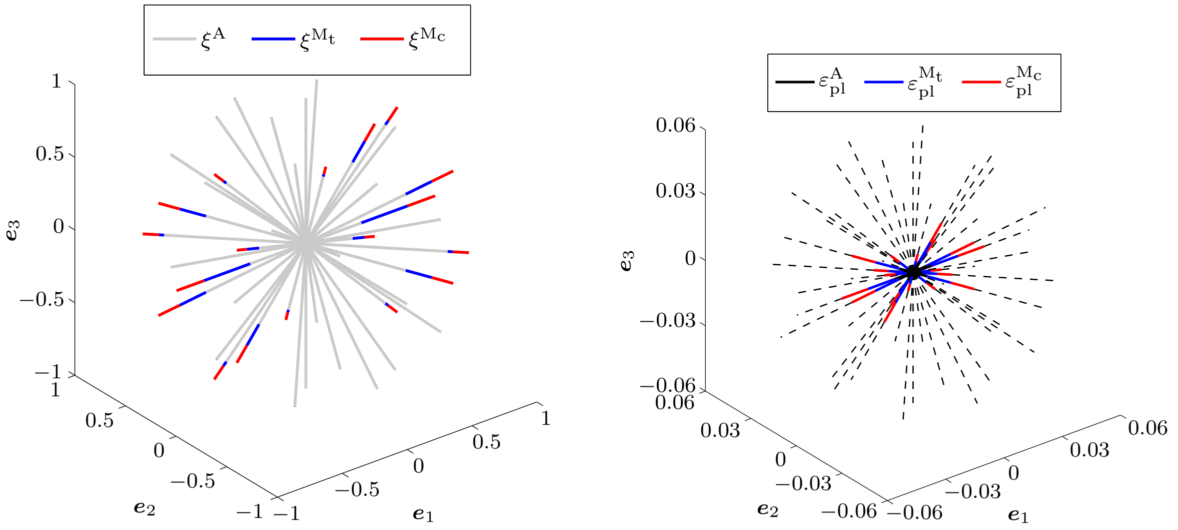

(a) Spatial distribution of volume fractions at maximum compression, i.e. state p_2 in Fig. 5.2(a). The visualisation shows that both the martensitic tensile and compression phase have evolved within the TRIP steel polycrystal.

(b) Spatial distribution of plastic strains obtained at maximum compression, i.e. state p_2 in Fig. 5.2(a)

Figure 5.3: Application of the one-dimensional coupled model for the simulation of phase-transformations and plasticity in an affine micro-sphere framework using 21 integration directions: spatial distribution of volume fractions and plastic strains obtained within the polycrystal after one tension-compression load cycle, see state p_2 in Fig. 5.2(a).

facilitating a numerical approximation via

$$\boldsymbol{\sigma} = \sum_{i=1}^{n_r} \sigma_i \, \bar{w}_i \, \boldsymbol{r}_i \otimes \boldsymbol{r}_i \quad , \tag{5.16}$$

$$\varXi^{\alpha} = \sum_{i=1}^{n_r} \xi_i^{\alpha} \, \bar{w}_i \quad , \tag{5.17}$$

$$\varepsilon_{\mathrm{pl}}^{\mathrm{mac},\alpha} = \sum_{i=1}^{n_r} \varepsilon_{\mathrm{pl},i}^{\alpha} \, \bar{w}_i \quad , \tag{5.18}$$

with σ_i the micro stress acting in ith integration direction, ξ_i^{α} and $\varepsilon_{\mathrm{pl},i}^{\alpha}$ the volume fraction and plastic strains of phase α situated in the ith integration direction $\boldsymbol{r}_i$, and $\bar{w}_i$ the weighting factors depending on the micro-sphere integration scheme used.

A computational example showing the material behaviour at the macro-scale level is depicted in Figs. 5.2 and 5.3. In the example provided, a homogeneous, mixed volumetric-deviatoric load is applied, where the prescribed macroscopic strain tensor $\boldsymbol{\varepsilon}$ is set to

$$\widehat{\boldsymbol{\varepsilon}}(t) = \varepsilon_{11}(t)\, \boldsymbol{e}_1 \otimes \boldsymbol{e}_1 \quad . \tag{5.19}$$

Here, $\varepsilon_{11}(t)$ is linearly varied with a strain rate of $\dot{\varepsilon}_{11} = 6 \times 10^{-5}\,\mathrm{s}^{-1}$ according to the load path provided in Fig. 5.2(a). The stress-strain response in terms of the σ_{11} stress component is given in Fig. 5.2(b). The obtained spatial distributions of volume fractions and plastic strains at maximum tension, i.e. at state p_1 in Fig. 5.2(a), are provided in Figs. 5.2(c) and 5.2(d). It is shown that the martensitic tensile phase starts to evolve during the tensile load cycle as corresponding to the observations made in Fig. 5.1(c). Moreover, the results show that plastic strains evolve mainly in the direction of maximum applied load, i.e. the $\boldsymbol{e}_1$-direction. The distributions of volume fractions and plastic strains at the end of the load cycle, i.e. at state p_2 in Fig. 5.2(a), are given in Fig. 5.3.

5.3 Finite element implementation

For the finite element implementation, the fourth-order algorithmic tangent operator needs to be computed. In the affine micro-sphere context, the algorithmic tangent operator is assembled based on the scalar-valued microscopic tangent moduli $\mathsf{E}^{\mathrm{alg}} := \mathrm{d}\sigma / \mathrm{d}\varepsilon$ according to

$$\boldsymbol{\mathsf{E}}^{\mathrm{alg}} := \frac{\mathrm{d}\boldsymbol{\sigma}}{\mathrm{d}\boldsymbol{\varepsilon}} = \frac{1}{4\pi} \int_{\mathbb{U}^2} \mathsf{E}^{\mathrm{alg}}\, \boldsymbol{r} \otimes \boldsymbol{r} \otimes \boldsymbol{r} \otimes \boldsymbol{r}\, \mathrm{d}a \quad , \tag{5.20}$$

enabling a numerical approximation via

$$\boldsymbol{\mathsf{E}}^{\mathrm{alg}} = \sum_{i=1}^{n_r} \mathsf{E}_i^{\mathrm{alg}}\, \bar{w}_i\, \boldsymbol{r}_i \otimes \boldsymbol{r}_i \otimes \boldsymbol{r}_i \otimes \boldsymbol{r}_i \quad . \tag{5.21}$$

The microscopic tangent moduli $\mathsf{E}_i^{\mathrm{alg}}$ for each integration direction $\boldsymbol{r}_i$ are obtained from the elastic stiffness contributions of the individual phases as we make use of the Voigt assumption here, cf. (5.1). To this end, we express $\mathsf{E}_i^{\mathrm{alg}}$ in terms of

$$\mathsf{E}_i^{\mathrm{alg}} = \sum_{\alpha=1}^{\nu} \xi_i^{\alpha}\, \mathsf{E}^{\mathrm{alg},\alpha} \quad , \tag{5.22}$$

where the elasto-plastic tangent modulus $\mathsf{E}^{\mathrm{alg},\alpha}$ of each phase α takes the form

$$\mathsf{E}^{\mathrm{alg},\alpha} = \begin{cases} \mathsf{E}^{\alpha} & , \text{ if } \dot{\lambda}_i^{\alpha} = 0 \\ \dfrac{\mathsf{E}^{\alpha} H^{\alpha}}{\mathsf{E}^{\alpha} + H^{\alpha}} & , \text{ if } \dot{\lambda}_i^{\alpha} > 0 \end{cases} \tag{5.23}$$

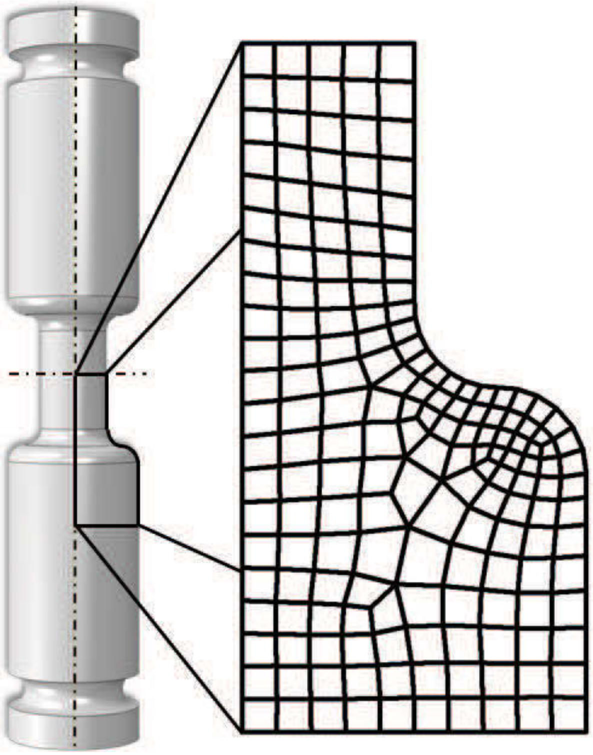

Figure 5.4: Considered tensile specimen and its numerical approximation with axisymmetric finite elements. As boundary conditions, we apply Dirichlet constraints to the top and bottom edge of the discretised model, where the bottom edge is spatially fixed in loading direction and the top edge of the model—corresponding to the horizontal center line of the overall specimen—is loaded with a prescribed tension/compression displacement u_c. The height of the discretised model is 4 mm, i.e. the maximum applied tensile deformation $u_c = 0.12\,\mathrm{mm}$ corresponds to a macroscopic strain of 3%. Note that the deformations provided in Figs. 5.6–5.11 are scaled with a factor of 5.

due to the linear proportional hardening assumed. Here, E^α is the Young's modulus and H^α the hardening modulus of phase α.

As a representative finite element example, a full tension-compression cycle of an axisymmetric rod is elaborated. Fig. 5.4 shows the considered geometry and its finite element approximation, where we make use of axisymmetric finite elements in order to capture the axisymmetric geometry of the tensile specimen considered. Moreover, due to symmetry reasons, it is sufficient to restrict the simulation to just one quarter of the rod, enabling an efficient solution of the macroscopic boundary value problem. The macroscopic mechanical response of the material is provided in Fig. 5.5 in terms of a force-displacement diagram. The macroscopic mechanical response reflects the experimentally observed mechanical behaviour of TRIP steel.

For a detailed investigation of the evolution of internal variables within the specimen, we provide contour plots of representative internal quantities for the states of maximum tension and maximum compression, as well as for the final material state obtained after

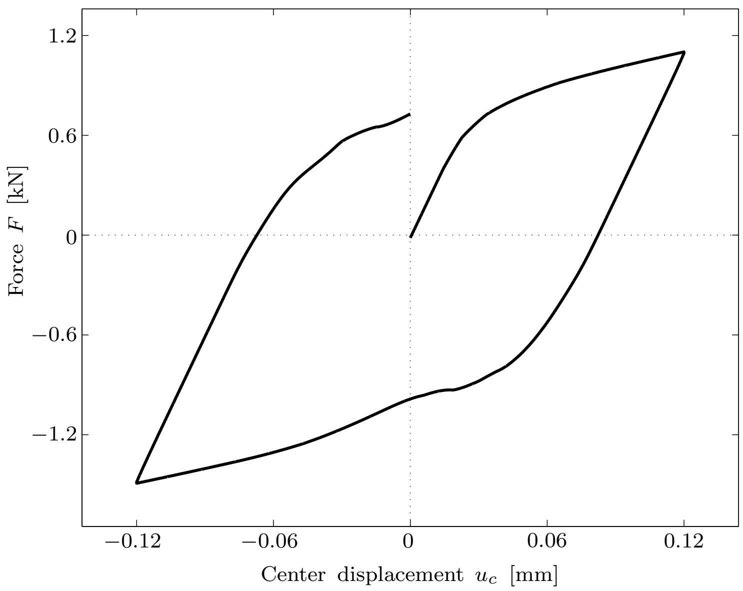

Figure 5.5: Force-displacement relation obtained during one tension-compression load cycle of the considered axisymmetric tensile specimen, cf. Fig. 5.4. The center displacement u_c corresponds to the center of the overall specimen, i.e. the top edge of the axi-symmetric finite element approximation of the body.

one complete tension-compression load cycle. To this end, the evolution of the largest principal stress component σ_I is provided in Fig. 5.6, whereas the obtained tensile stress component σ_{zz} is displayed in Fig. 5.7. Both figures show that the highest stresses are obtained in the constricted central cross-section of the specimen.

To assess the reduction of the parent phase resulting from the mechanical loading applied to the specimen, we provide contour plots of the macroscopic austenitic volume fraction Ξ^{A} in Fig. 5.8. During tension, the austenitic volume fraction if reduced by only few percents, with a further decrease as the load cycle proceeds. The plastic strains evolving within the austenitic parent phase are given in Fig. 5.9. During tension, plastic tensile strains evolve within austenite, while in the compression regime compressive plastic strains are observed.

Finally, we visualise the evolution of the macroscopic martensitic tensile and compression phase, $\Xi^{\mathrm{M_t}}$ and $\Xi^{\mathrm{M_c}}$, in Figs. 5.10 and 5.11, respectively. As expected, the figures show that the martensitic tensile phase evolves in the tensile load states whereas the compression phase evolves in the compressive load states.

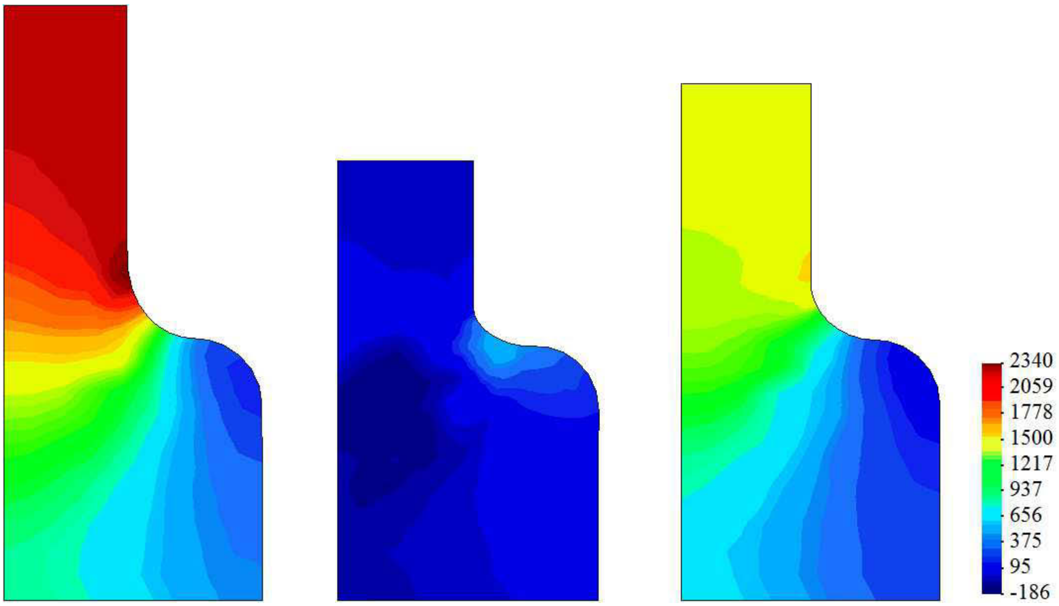

Figure 5.6: Distribution of the largest principal stress component σ_I [MPa] within the specimen. The left figure corresponds to the state of maximum tension with $u_c = 0.12\,\mathrm{mm}$, the plot in the center is obtained for maximum compression at $u_c = -0.12\,\mathrm{mm}$, and the visualisation on the right corresponds to the final state obtained after one complete tension-compression load cycle, $u_c = 0$, see Fig. 5.5.

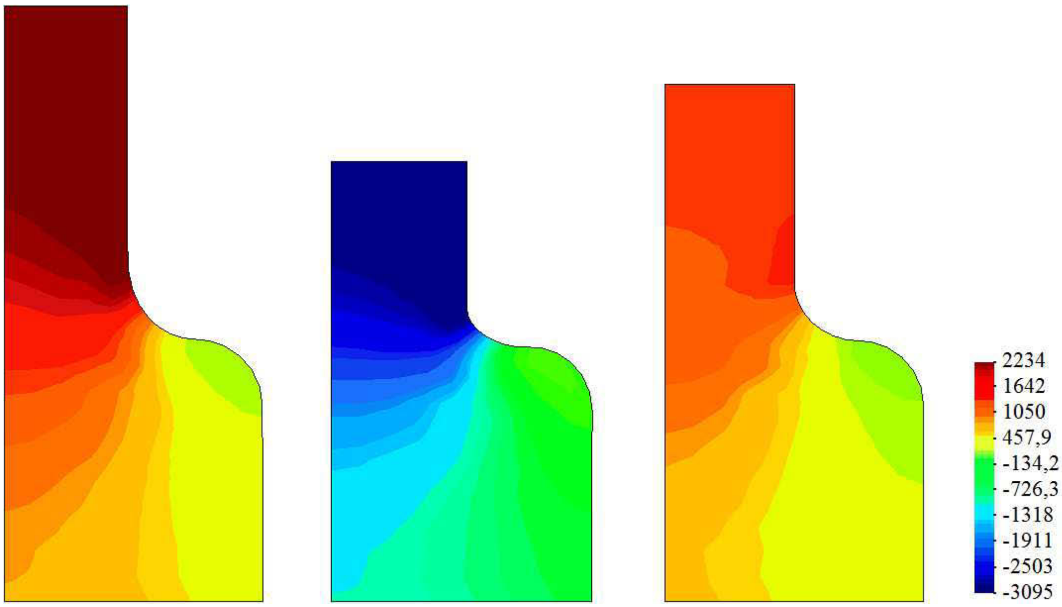

Figure 5.7: Distribution of the axial stress component σ_{zz} [MPa] within the specimen. The left figure corresponds to the state of maximum tension with $u_c = 0.12\,\mathrm{mm}$, the plot in the center is obtained for maximum compression at $u_c = -0.12\,\mathrm{mm}$, and the visualisation on the right corresponds to the final state obtained after one complete tension-compression load cycle, $u_c = 0$, see Fig. 5.5.

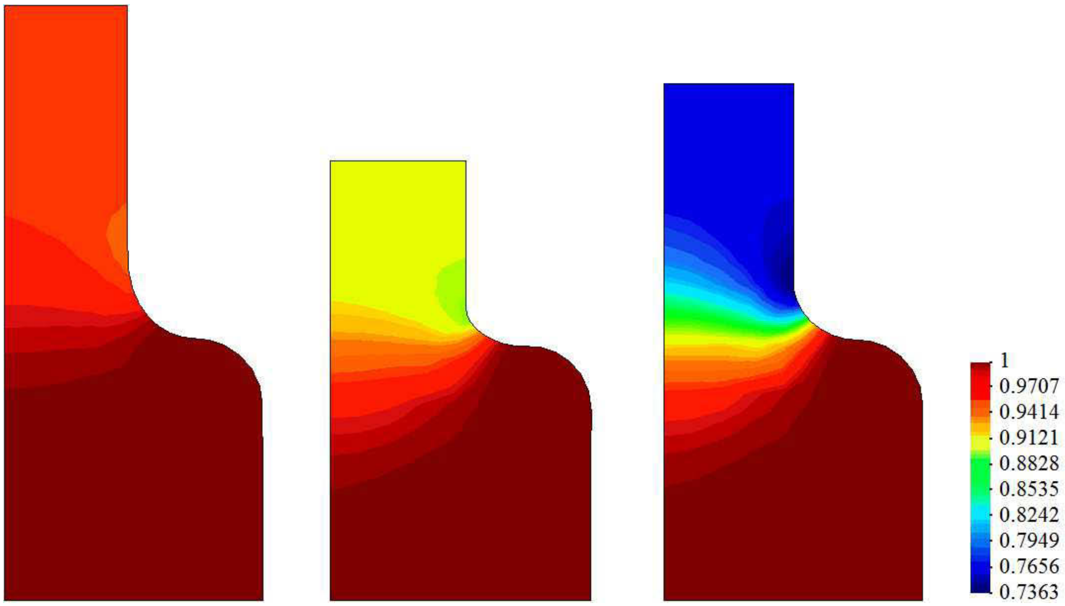

Figure 5.8: Distribution of the macroscopic austenitic volume fraction Ξ^{A} [–] within the specimen. The left figure corresponds to the state of maximum tension with $u_c = 0.12\,\mathrm{mm}$, the plot in the center is obtained for maximum compression at $u_c = -0.12\,\mathrm{mm}$, and the visualisation on the right corresponds to the final state obtained after one complete tension-compression load cycle, $u_c = 0$, see Fig. 5.5.

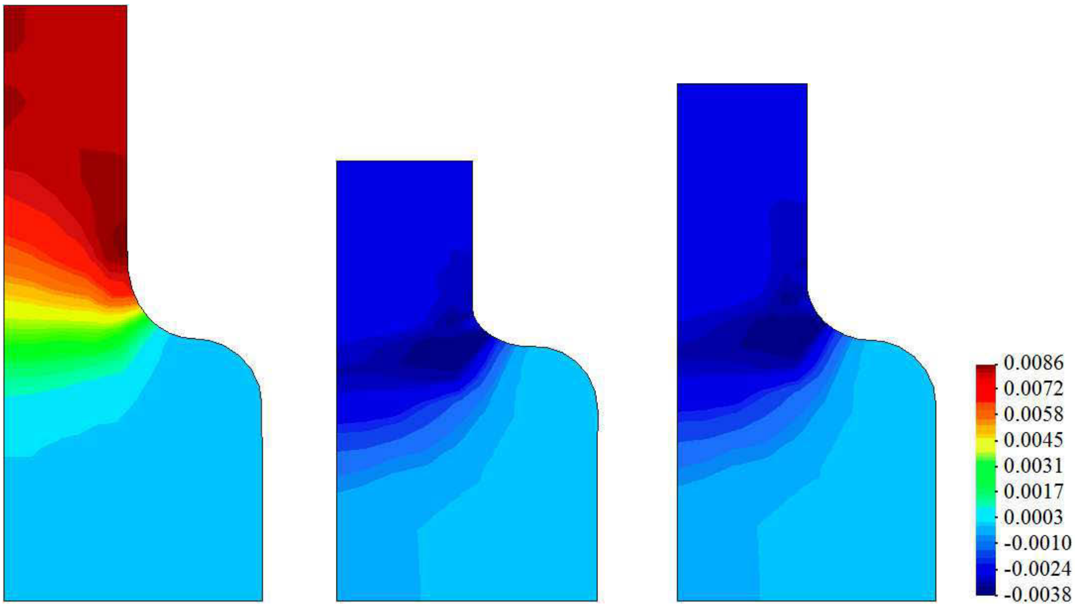

Figure 5.9: Distribution of the macroscopic austenitic plastic strains $\varepsilon^{\mathrm{A}}_{\mathrm{pl}}$ [–] within the specimen. The left figure corresponds to the state of maximum tension with $u_c = 0.12\,\mathrm{mm}$, the plot in the center is obtained for maximum compression at $u_c = -0.12\,\mathrm{mm}$, and the visualisation on the right corresponds to the final state obtained after one complete tension-compression load cycle, $u_c = 0$, see Fig. 5.5.

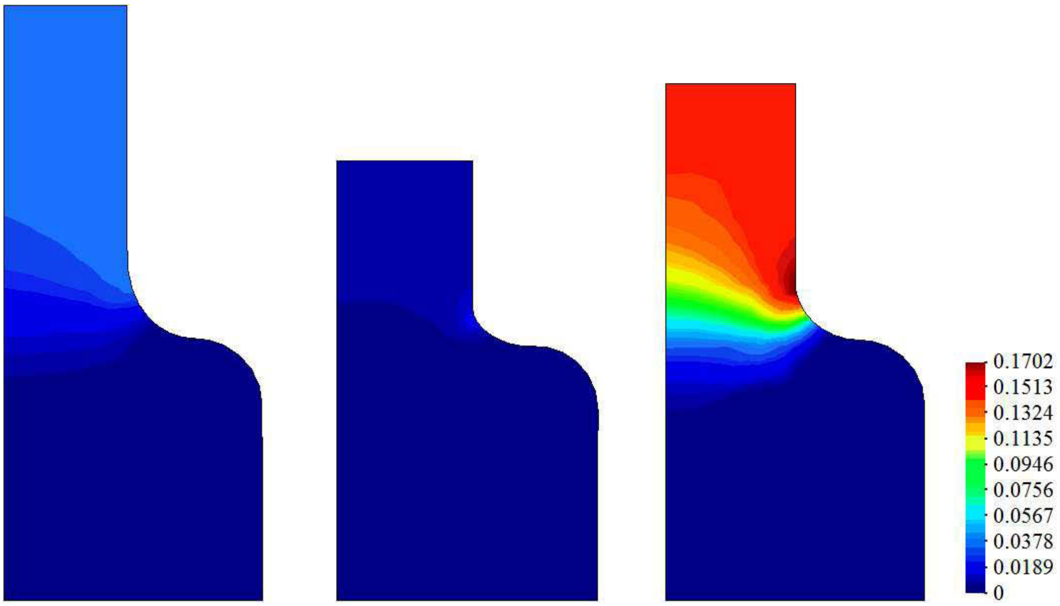

Figure 5.10: Distribution of the macroscopic martensitic tensile phase $\Xi^{\mathrm{M_t}}$ [–] within the specimen. The left figure corresponds to the state of maximum tension with $u_c = 0.12\,\mathrm{mm}$, the plot in the center is obtained for maximum compression at $u_c = -0.12\,\mathrm{mm}$, and the visualisation on the right corresponds to the final state obtained after one complete tension-compression load cycle, $u_c = 0$, see Fig. 5.5.

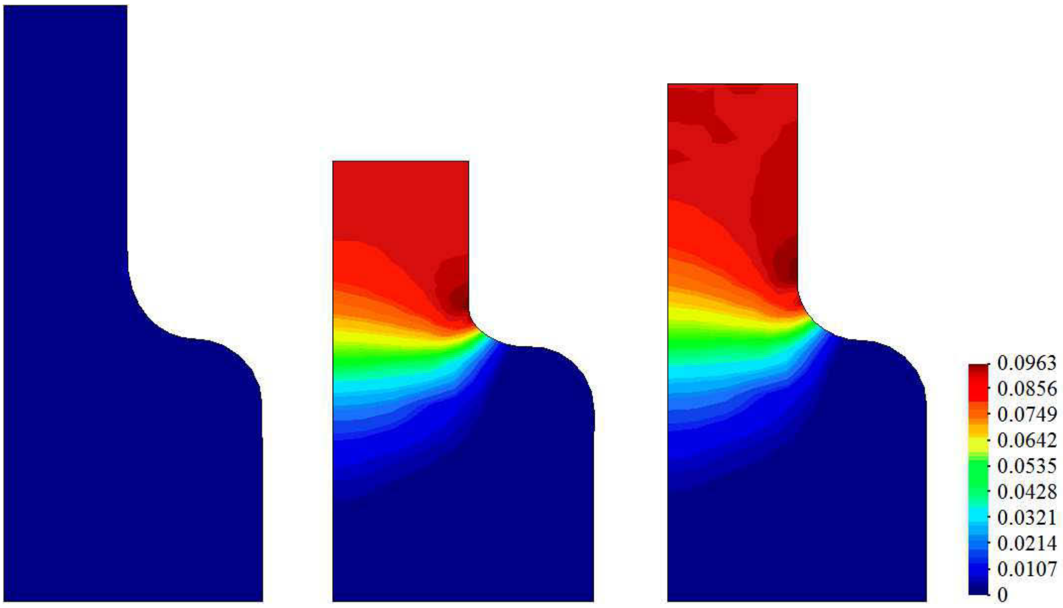

Figure 5.11: Distribution of the macroscopic martensitic compression phase $\Xi^{\mathrm{M_c}}$ [–] within the specimen. The left figure corresponds to the state of maximum tension with $u_c = 0.12\,\mathrm{mm}$, the plot in the center is obtained for maximum compression at $u_c = -0.12\,\mathrm{mm}$, and the visualisation on the right corresponds to the final state obtained after one complete tension-compression load cycle, $u_c = 0$, see Fig. 5.5.

5.4 Summary

The main goal of this chapter is to establish the coupled phase-transformation and plasticity model presented in Chapter 4 for three solid phases using TRIP steel material parameters. To this end, a more generalised plasticity inheritance law—consistently capturing the inheritance interactions of three individual phases—is considered. The overall one-dimensional model is embedded into an affine micro-sphere formulation and representative examples under homogeneous deformation are provided for both the micro-scale and the macro-level. Moreover, finite element simulations are performed, and selected representative results are shown. In summary, the results presented show the capability of the established model to capture the macroscopic behaviour of TRIP steel [39].

However, the use of the affine micro-sphere framework as presented in this chapter involves two restrictions that are adressed in Chapter 6. On the one hand, the macroscopic Poisson's ratio of the material is still restricted to $\nu_{\mathrm{P}} = 0.25$ as elaborated in Chapter 2. On the other hand, volumetric load states result in an evolution of plasticity since the current framework does not allow for the distinction between volumetric and deviatoric load states. An extension of the current, affine micro-sphere model to a non-affine version considering a volumetric-deviatoric split in kinematics is not trivial due to the underlying, physically motivated scheme that is used for the evolution of volume fractions. To be precise, an extension to a non-affine micro-sphere framework requires noteworthy changes with respect to the computation of the underlying Gibbs energy barriers that determine the transformation probabilities between the considered phases and thereby drive the evolution of volume fractions. To overcome the aforementioned model restrictions, an extension of the model to non-affine kinematics was presented in Chapter 3. This model extension allows to capture the actual macroscopic Poisson's ratio of the material and, at the same time, serves as the foundation for the implementation of a solely deviatoric plasticity coupling in Chapter 6.

6 A non-affine micro-sphere model for phase-transformations interacting with plasticity

In order to extend the model presented in Chapter 3 that allows for the simulation of the austenitic-martensitic tranformations in NiTi-based alloys to the simulation of the austenitic-martensitic transformation in TRIP steels, several key aspects have to be considered. First, the interactions between plasticity and phase-transformations play a key role in the simulation of TRIP steels undergoing phase-transitions, see e.g. [34, 39, 84, 86, 103, 138] amongst others. Therefore, the model introduced in Chapter 3 has to be extended to take into account multi-phase plasticity as incorporated in Section 6.1.3. Moreover, the coupled interactions of plasticity and phase-transformations must be considered as elaborated in Section 6.2. Secondly, the non-zero volume change of TRIP steel observed during phase-transformation is accounted for by introducing a non-zero volumetric transformation strain in the modelling framework at hand, cf. Section 6.1.1. Note that SMA—in contrast to TRIP steel—does not exhibit volumetric changes during austenitic-martensitic transformation. Finally, the characteristic work hardening observed for TRIP steels is captured by an appropriately chosen plastic hardening law.

The chapter at hand is organised as follows, cf. [105]. In Section 6.1, we extend the formulations proposed in Chapters 2 and 3 to a coupled scalar-valued phase-transformation-plasticity model, where Section 6.1.1 focuses on the enhanced Helmholtz and Gibbs energy potentials that are assigned to each phase. Section 6.1.2 gives a brief outline of the physically-motivated evolution law that we consider for the evolution of volume fractions. Subsequently, the incorporation of plasticity is discussed in detail in Section 6.1.3. The aforementioned interactions between plasticity and phase-transformations are motivated and elaborated in Section 6.2 by means of a consistent three-phase plasticity inheritance framework that we propose in this work. To capture the material response at polycrystal level, we use the micro-sphere framework elaborated in [49, 74, 91, 92] in Section 6.3. To this end, we briefly outline the kinematic approach and the micro-macro relations in Sections 6.3.1 and 6.3.2, respectively. The required algorithmic tangent modulus and its elastic contribution that allows for the assessment of the elastic anisotropy evolution of the material, see e.g. [142], are introduced in Section 6.3.3, facilitating the simulation of uniaxial stress states resembling a macroscopic tensile test on a homogeneous level. The micro-sphere simulations are carried out for both SMA and TRIP steel; the results are presented in Section 6.3.4, where Section 6.3.4.1 focuses on the SMA simulation and Section 6.3.4.2 discusses the TRIP steel results. The sensitivity of the results with respect to the order of the underlying micro-sphere integration scheme is discussed in Section 6.3.5. Finally, we demonstrate a finite element implementation of the overall constitutive model where the results of representative inhomogeneous boundary value problems in terms of shear and tension of a plate with hole are presented for both SMA and TRIP steel in Section 6.4. The chapter is concluded by a summary given in Section 6.5.

6.1 Scalar-valued phase-transformation model with volumetric-deviatoric split and plasticity

The one-dimensional phase-transformation model is based on mixture theory and follows the basic ideas introduced in [51]. For the phases considered, we make use of the Voigt assumption, i.e. all material phases α are subjected to the same strain measures. The model is capable of handling an arbitrary amount of material phases, where the non-negative volume fraction

$$\xi^\alpha := \lim_{v \to 0} \left(\frac{v^\alpha}{v} \right) \tag{6.1}$$

of each phase $\alpha \in \{1, \dots, \nu\} \subset \mathbb{N}$ is subject to the usual physical restrictions, including conservation of mass, namely

$$\xi^\alpha \in \ [0,1] \subset \mathbb{R} \quad , \quad \sum_{\alpha=1}^{\nu} \xi^\alpha = \ 1 \quad , \text{ so that } \quad \sum_{\alpha=1}^{\nu} \dot{\xi}^\alpha = \ 0 \quad . \tag{6.2}$$

6.1.1 Helmholtz and Gibbs energy potentials of the individual phases

We start by assigning a Helmholtz free energy potential $\psi^\alpha = \widehat{\psi}^\alpha(\varepsilon_{\text{dev}}, \varepsilon_{\text{vol}}, \varepsilon^\alpha_{\text{pl}}, \theta)$ of the form

$$\psi^\alpha = \psi^\alpha_{\text{dev}} + \psi^\alpha_{\text{vol}} + \psi^\alpha_{\text{therm}} + \psi^\alpha_{\text{chem}} \tag{6.3}$$

to each phase α, where we consider a split of elastic energies into deviatoric and volumetric contributions, $\psi^\alpha_{\text{dev}} = \widehat{\psi}^\alpha_{\text{dev}}(\varepsilon_{\text{dev}}, \varepsilon^\alpha_{\text{pl}})$ and $\psi^\alpha_{\text{vol}} = \widehat{\psi}^\alpha_{\text{vol}}(\varepsilon_{\text{vol}})$, respectively. Furthermore, we account for energy related to thermal expansion, $\psi^\alpha_{\text{therm}} = \widehat{\psi}^\alpha_{\text{therm}}(\varepsilon_{\text{dev}}, \varepsilon_{\text{vol}}, \varepsilon^\alpha_{\text{pl}}, \theta)$, and temperature-dependent chemical energies $\psi^\alpha_{\text{chem}} = \widehat{\psi}^\alpha_{\text{chem}}(\theta)$. Note that the plastic strains $\varepsilon^\alpha_{\text{pl}}$ are—besides their influence in thermal expansion—accounted for in each phase solely within the deviatoric energy term but not in the volumetric energy contribution. To be specific, the energy contributions take the form

$$\psi^\alpha_{\text{dev}} = \frac{1}{2}\,\mathsf{E}^\alpha_{\text{dev}}\left[\varepsilon_{\text{dev}} - \varepsilon^\alpha_{\text{tr,dev}} - \varepsilon^\alpha_{\text{pl}}\right]^2 \tag{6.4}$$

$$\psi^\alpha_{\text{vol}} = \frac{1}{2}\,\mathsf{E}^\alpha_{\text{vol}}\left[\varepsilon_{\text{vol}} - \varepsilon^\alpha_{\text{tr,vol}}\right]^2 \tag{6.5}$$

$$\psi^\alpha_{\text{therm}} = -\zeta^\alpha\,\mathsf{E}^\alpha\left[\varepsilon - \varepsilon^\alpha_{\text{tr}} - \varepsilon^\alpha_{\text{pl}}\right]\left[\theta - \theta_0\right] \tag{6.6}$$

$$\psi^\alpha_{\text{chem}} = \rho_0\,c^\alpha_p\,\theta\left[1 - \log\left(\frac{\theta}{\theta_0}\right)\right] - \rho_0\,\lambda^\alpha_T\left[1 - \frac{\theta}{\theta_0}\right] \tag{6.7}$$

for each phase α, cf. Sections 3.1.1 and 4.1. We consider a volumetric-deviatoric-type split of total strains $\varepsilon = \varepsilon_{\text{dev}} + \varepsilon_{\text{vol}}$ as well as transformation strains $\varepsilon^\alpha_{\text{tr}} = \varepsilon^\alpha_{\text{tr,dev}} + \varepsilon^\alpha_{\text{tr,vol}}$. The volumetric contribution $\varepsilon^\alpha_{\text{tr,vol}}$ of the total transformation strain $\varepsilon^\alpha_{\text{tr}}$ is chosen to be zero for SMA, as no change in volume is observed for SMA during phase-transformation. In contrast, for the consistent capture of the transformation behaviour of TRIP steel, a non-zero volumetric transformation strain is considered, see the material parameters provided in Tables 6.1 and 6.2, respectively.

The considered strain measures ε_{dev} and ε_{vol} are obtained from projections of the macroscopic strain tensor in the context of the micro-sphere approach presented in Section 6.3. Here, we denote $\mathsf{E}^\alpha_{\text{dev}}$ and $\mathsf{E}^\alpha_{\text{vol}}$ as deviatoric and volumetric elasticity coefficients on the micro-level, see [27, 104]. Moreover, we consider ζ^α the coefficient of thermal expansion, θ the current absolute temperature and θ_0 the reference temperature. The temperature-dependent chemical energy $\psi^\alpha_{\text{chem}}$ further accounts for the heat capacity c^α_p and the latent heat λ^α_T of the respective material phase α, cf. [51].

The overall phase potential $\Psi = \widehat{\Psi}(\varepsilon_{\text{dev}}, \varepsilon_{\text{vol}}, \boldsymbol{\xi}, \boldsymbol{\varepsilon}^{\text{1d}}_{\text{pl}}, \theta)$ is obtained from the contributions of the constituents and can be expressed as

$$\Psi = \sum_{\alpha=1}^{\nu} \xi^\alpha \psi^\alpha \quad , \tag{6.8}$$

where $\boldsymbol{\xi} = [\xi^1, \ldots, \xi^\nu]^{\text{t}} \in \mathbb{R}^{\nu\times 1}$ is the collection of the volume fractions and $\boldsymbol{\varepsilon}^{\text{1d}}_{\text{pl}} = [\varepsilon^1_{\text{pl}}, \ldots, \varepsilon^\nu_{\text{pl}}]^{\text{t}} \in \mathbb{R}^{\nu\times 1}$ is the collection of the individual one-dimensional plastic strains assigned to each phase in the given material mixture.

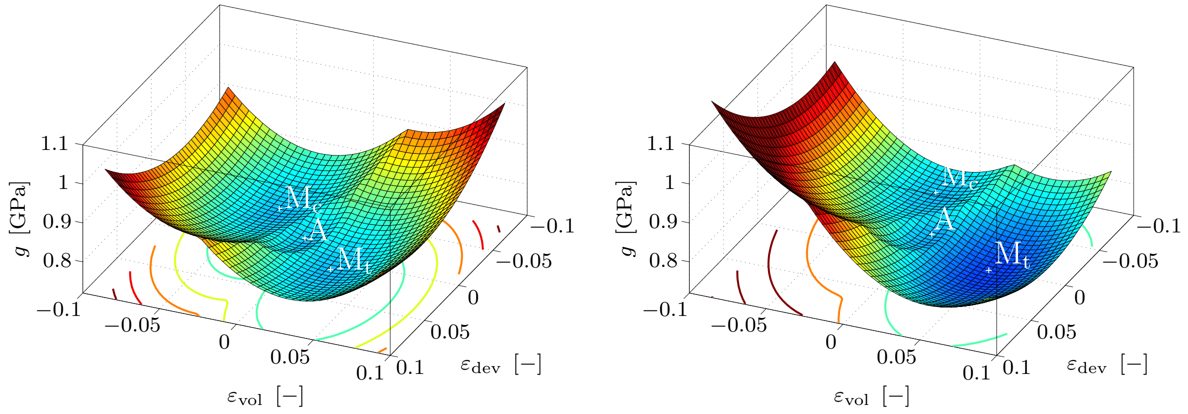

(a) Initial state.

(b) Tensile state.

Figure 6.1: Visualisation of the contributions to the overall Gibbs free energy potential G of the three-phase material mixture considered in this work. The initial state (a) shows the energy minimum of the austenitic parent phase A to be located between both martensite minima. After a tensile deformation is applied to the material, the martensitic tensile phase $\mathrm{M_t}$ becomes energetically favourable as shown in (b). Analogously, for an applied compression load state the martensitic compression phase $\mathrm{M_c}$ takes the distinct energy minimum.

Carrying out a Legendre-transformation of the Helmholtz free energy of the mixture yields the overall Gibbs potential

$$\begin{aligned}\widehat{G}(\partial_{\varepsilon_{\mathrm{dev}}}\Psi, \partial_{\varepsilon_{\mathrm{vol}}}\Psi) &= \Psi - \left.\frac{\partial \Psi}{\partial \varepsilon_{\mathrm{dev}}}\right|_{\varepsilon_{\mathrm{dev}},\theta} \varepsilon_{\mathrm{dev}} - \left.\frac{\partial \Psi}{\partial \varepsilon_{\mathrm{vol}}}\right|_{\varepsilon_{\mathrm{vol}},\theta} \varepsilon_{\mathrm{vol}} \\ &= \sum_{\alpha=1}^{\nu} \xi^\alpha \psi^\alpha - \sum_{\alpha=1}^{\nu} \xi^\alpha \left.\frac{\partial \psi^\alpha}{\partial \varepsilon_{\mathrm{dev}}}\right|_{\varepsilon_{\mathrm{dev}},\theta} \varepsilon_{\mathrm{dev}} - \sum_{\alpha=1}^{\nu} \xi^\alpha \left.\frac{\partial \psi^\alpha}{\partial \varepsilon_{\mathrm{vol}}}\right|_{\varepsilon_{\mathrm{vol}},\theta} \varepsilon_{\mathrm{vol}} \\ &= \sum_{\alpha=1}^{\nu} \xi^\alpha g^\alpha \quad , \end{aligned} \tag{6.9}$$

where use has been made of the additive decomposition given in (6.8). Here,

$$\widehat{g}^\alpha(\partial_{\varepsilon_{\mathrm{dev}}}\psi^\alpha, \partial_{\varepsilon_{\mathrm{vol}}}\psi^\alpha) = \psi^\alpha - \left.\frac{\partial \psi^\alpha}{\partial \varepsilon_{\mathrm{dev}}}\right|_{\varepsilon_{\mathrm{dev}},\theta} \varepsilon_{\mathrm{dev}} - \left.\frac{\partial \psi^\alpha}{\partial \varepsilon_{\mathrm{vol}}}\right|_{\varepsilon_{\mathrm{vol}},\theta} \varepsilon_{\mathrm{vol}} \tag{6.10}$$

is the contribution of phase α to the overall Gibbs potential G. Due to the quadratic nature of the Helmholtz potential, the obtained Gibbs potential is also of quadratic nature, precisely, the Gibbs potential g^α of every individual phase α has the form of an elliptic paraboloid with $\varepsilon_{\mathrm{dev}}$ and $\varepsilon_{\mathrm{vol}}$ as functional parameters. The contributions to the overall Gibbs energy G of the material accordingly have three local minima for a 3-phase material as visualised in Fig. 6.1.

6.1.2 Evolution of volume fractions

The evolution equations for the volume fractions ξ^α are derived in a similar way to the derivations introduced in Section 2.1, cf. [51], and to the extensions thereof presented in Chapter 3, cf. [104]. For the sake of completeness of this chapter, we will however briefly summarise the main relations in the following.

The modelling approach introduces a transformation probability matrix $\boldsymbol{Q} \in \mathbb{R}^{\nu\times\nu}$, which drives the evolution of volume fractions in terms of $\dot{\boldsymbol{\xi}} = \boldsymbol{Q}\cdot\boldsymbol{\xi}$. In line with the previous chapters, we restrict the formulation to three material phases for the sake of simplicity—the model and its numerical implementation is not restricted to a specific number of phases. We consider an austenitic parent phase A and a martensitic tension and compression phase $\mathrm{M_t}$ and $\mathrm{M_c}$, respectively, so that the transformation probability matrix $\boldsymbol{Q} \in \mathbb{R}^{3\times3}$, cf. (2.6), refers to $\boldsymbol{\xi} = [\xi^{\mathrm{A}}, \xi^{\mathrm{M_t}}, \xi^{\mathrm{M_c}}]^{\mathrm{t}} \in \mathbb{R}^{3\times1}$ as the arrangement of components in the vector of volume fractions $\boldsymbol{\xi}$.

As introduced in Chapter 2, the transformation probabilities used for the components of $\boldsymbol{Q}$ are derived from

$$P_{\alpha\to\beta} = \exp\left(\frac{-\Delta v\, b_{\alpha\to\beta}}{k\,\theta}\right) \quad , \tag{6.11}$$

with Δv the constant transformation region's volume, $b_{\alpha\to\beta}$ the energy barrier for the transformation from phase α to phase β, k the Boltzmann constant, and θ the given temperature. Note that, in general, $b_{\alpha\to\beta} \neq b_{\beta\to\alpha}$ and thus $P_{\alpha\to\beta} \neq P_{\beta\to\alpha}$ holds.

Following the derivations introduced in [104], the computation of an energy barrier $b_{\alpha\to\beta}$—characterising the energy barrier that needs to be overcome for the transformation from one phase α to another phase β—is described briefly in the following. The Gibbs energy barrier makes use of the minimum value of the intersection curve of two elliptic paraboloids. To be precise, the Gibbs potentials g^α and g^β of the two involved phases α and β are evaluated in volumetric and deviatoric strain space. To this end, we assume that the paraboloids intersect and are not identical. The intersection of both elliptic paraboloids can then be expressed by means of a parametric curve.

Equating the Gibbs potentials of the two phases α and β,

$$\widehat{g}^{\alpha}(\varepsilon_{\mathrm{dev}}, \varepsilon_{\mathrm{vol}}, \varepsilon^{\alpha}_{\mathrm{pl}}, \theta) = \widehat{g}^{\beta}(\varepsilon_{\mathrm{dev}}, \varepsilon_{\mathrm{vol}}, \varepsilon^{\beta}_{\mathrm{pl}}, \theta) \quad , \tag{6.12}$$

results in an equation for the two unknowns $\varepsilon_{\mathrm{dev}}$ and $\varepsilon_{\mathrm{vol}}$ for given plastic strains, $\varepsilon^{\alpha}_{\mathrm{pl}}$ and $\varepsilon^{\beta}_{\mathrm{pl}}$, and temperature θ in the current material state. By rearranging terms, the deviatoric strains $\varepsilon^{\mathrm{isc}}_{\mathrm{dev}}$ at which g^α and g^β intersect can be expressed in terms of the volumetric strains

$$\varepsilon^{\mathrm{isc}}_{\mathrm{dev}} = \widehat{\varepsilon}^{\mathrm{isc}}_{\mathrm{dev}}(\varepsilon_{\mathrm{vol}}) \quad , \tag{6.13}$$

where the superscript “isc” refers to *intersection curve*. Considering this relation together with (6.10) allows the expression of the actual value of both Gibbs potentials along the intersection curve in terms of

$$\begin{aligned} \widehat{g}^{\text{isc},\alpha,\beta}(\varepsilon_{\text{vol}})\big|_{\varepsilon^{\alpha}_{\text{pl}},\varepsilon^{\beta}_{\text{pl}},\theta} &:= \widehat{g}^{\alpha}(\widehat{\varepsilon}^{\text{isc}}_{\text{dev}}(\varepsilon_{\text{vol}}),\varepsilon_{\text{vol}},\varepsilon^{\alpha}_{\text{pl}},\theta) && (6.14)\\ &\equiv \widehat{g}^{\beta}(\widehat{\varepsilon}^{\text{isc}}_{\text{dev}}(\varepsilon_{\text{vol}}),\varepsilon_{\text{vol}},\varepsilon^{\beta}_{\text{pl}},\theta) \quad . && (6.15) \end{aligned}$$

To obtain the energy barrier $b_{\alpha\to\beta}$ required for the evolution of volume fractions, we seek for the minimum of the Gibbs energy along this parametric curve, i.e.

$$g^{\text{isc},\alpha,\beta}_{\min} := \min_{\varepsilon_{\text{vol}}}\left(\widehat{g}^{\text{isc},\alpha,\beta}(\varepsilon_{\text{vol}})\big|_{\varepsilon^{\alpha}_{\text{pl}},\varepsilon^{\beta}_{\text{pl}},\theta}\right) \quad . \tag{6.16}$$

Due to the implicit nature of the equations, it is not possible to obtain an analytical solution for this problem. Hence, the minimisation of (6.15) is carried out numerically using, e.g., a Newton scheme as discussed in detail in [104]. The ansatz for the extension of this scheme to the plasticity-extended model proposed in this work is given in 6.6.2. With the minimum $g^{\text{isc},\alpha,\beta}_{\min}$ of the intersection curve of the Gibbs potentials of both phases α and β at hand, the energy barriers are computed according to

$$b_{\alpha\to\beta} = g^{\text{isc},\alpha,\beta}_{\min} - g^{\alpha}_{\min} \tag{6.17}$$

and

$$b_{\beta\to\alpha} = g^{\text{isc},\alpha,\beta}_{\min} - g^{\beta}_{\min} \quad , \tag{6.18}$$

where $g^{\alpha}_{\min}$ and $g^{\beta}_{\min}$ denote the absolute minima of the Gibbs potentials g^{α} and g^{β}, respectively. For details on the analytical derivation of the minima of the considered elliptic Gibbs energy paraboloids, the reader may refer to [104].

6.1.3 Incorporation of plasticity

For the incorporation of plasticity, we use a von Mises-type plasticity approach, where we—for conceptual simplicity—assume linear proportional hardening. The plastic driving force $q^{\alpha}_{\text{pl},\varPsi}$ is derived from the overall Helmholtz potential for each individual phase as

$$\begin{aligned} q^{\alpha}_{\text{pl},\varPsi} &= -\left.\frac{\partial\widehat{\varPsi}(\varepsilon_{\text{dev}},\varepsilon_{\text{vol}},\boldsymbol{\xi},\boldsymbol{\varepsilon}^{\text{1d}}_{\text{pl}},\theta)}{\partial\varepsilon^{\alpha}_{\text{pl}}}\right|_{\varepsilon_{\text{dev}},\varepsilon_{\text{vol}},\boldsymbol{\xi},\theta}\\ &= -\xi^{\alpha}\left.\frac{\partial\widehat{\psi}^{\alpha}(\varepsilon_{\text{dev}},\varepsilon_{\text{vol}},\varepsilon^{\alpha}_{\text{pl}},\theta)}{\partial\varepsilon^{\alpha}_{\text{pl}}}\right|_{\varepsilon_{\text{dev}},\varepsilon_{\text{vol}},\theta}\\ &= \xi^{\alpha}\left[\mathsf{E}^{\alpha}_{\text{dev}}\left[\varepsilon_{\text{dev}} - \varepsilon^{\alpha}_{\text{tr,dev}} - \varepsilon^{\alpha}_{\text{pl}}\right] - \zeta^{\alpha}\mathsf{E}^{\alpha}\left[\theta-\theta_0\right]\right] \quad . \end{aligned} \tag{6.19}$$

Note that the ξ^α coefficient in the driving force ensures that the driving force is zero for a volume fraction of zero value, i.e. no plasticity can evolve within a phase of zero volume fraction.

With the driving force and the current yield stress Y^α at hand, the yield function $\varPhi^\alpha = \widehat{\varPhi}^\alpha(Y^\alpha, q^\alpha_{\mathrm{pl},\varPsi})$ determining the admissible elastic domain in phase α, takes the form

$$\widehat{\varPhi}^\alpha(q^\alpha_{\mathrm{pl},\varPsi}, Y^\alpha) = |q^\alpha_{\mathrm{pl},\varPsi} - B^\alpha| - \xi^\alpha\, Y^\alpha \leq 0 \quad . \tag{6.20}$$

The current yield stress $Y^\alpha = \widehat{Y}^\alpha(\varepsilon^\alpha_{\mathrm{pl,acc}}) = Y^\alpha_0 + H^\alpha\, \varepsilon^\alpha_{\mathrm{pl,acc}}$ is given by the initial yield stress Y^α_0 which is then modified by $H^\alpha\, \varepsilon^\alpha_{\mathrm{pl,acc}}$ due to accumulated plastic strains $\varepsilon^\alpha_{\mathrm{pl,acc}}$ of the respective material phase, where H^α denotes the constant hardening modulus of phase α. The individual back stress B^α is additionally considered in order to prevent plastic flow occurring in the initial equilibrium state. To be specific, the underlying Voigt assumption leads to an initial driving force of

$$\begin{aligned} B^\alpha &:= q^\alpha_{\mathrm{pl},\varPsi}\big|_{\varepsilon_{\mathrm{dev}}=\varepsilon_{\mathrm{vol}}=\varepsilon^\alpha_{\mathrm{pl}}=0,\theta} \\ &= -\,\xi^\alpha \left[\mathsf{E}^\alpha_{\mathrm{dev}}\, \varepsilon^\alpha_{\mathrm{tr,dev}} + \zeta^\alpha \mathsf{E}^\alpha[\theta - \theta_0]\right] \end{aligned} \tag{6.21}$$

that acts in each phase α and, in consequence, is considered as a back stress in the yield function. Based on the yield function presented, we use an associated flow rule, facilitating the derivation of the evolution law for the plastic strain in phase α by means of

$$\dot{\varepsilon}^\alpha_{\mathrm{pl}} = \dot{\lambda}^\alpha \frac{\partial \widehat{\varPhi}^\alpha(q^\alpha_{\mathrm{pl},\varPsi}, Y^\alpha)}{\partial q^\alpha_{\mathrm{pl},\varPsi}} = \dot{\lambda}^\alpha \operatorname{sgn}\left(q^\alpha_{\mathrm{pl},\varPsi} - B^\alpha\right) \tag{6.22}$$

with an appropriate Lagrange multiplier $\dot{\lambda}^\alpha \geq 0$ and $\dot{\lambda}^\alpha\, \varPhi^\alpha = 0$. Note that we neglect the contribution of the mechanical dissipation to the evolution of temperature. Moreover, for the temperature range considered in this work, the yield stress of the material does not depend on the temperature.

Consider now the discrete update from time ${}^n t$ to ${}^{n+1}t$, with $\Delta t := {}^{n+1}t - {}^n t > 0$. In case of plastic loading, the Lagrange multiplier can be expressed in terms of the trial value of the yield function $\varPhi^\alpha_{\mathrm{tri}} = \widehat{\varPhi}^\alpha(q^\alpha_{\mathrm{pl},\varPsi,\mathrm{tri}}, {}^n Y^\alpha)$, with the trial plastic driving force $q^\alpha_{\mathrm{pl},\varPsi,\mathrm{tri}}$ and ${}^n Y^\alpha = \widehat{Y}^\alpha({}^n\varepsilon^\alpha_{\mathrm{pl,acc}})$ the yield stress of phase α at time ${}^n t$. For the derivation of the trial plastic driving force, we use the intermediate state potential

$$\widetilde{\varPsi} := \widehat{\varPsi}({}^{n+1}\varepsilon_{\mathrm{dev}}, {}^{n+1}\varepsilon_{\mathrm{vol}}, {}^{n+1}\boldsymbol{\xi}, {}^n\tilde{\boldsymbol{\varepsilon}}^{\mathrm{1d}}_{\mathrm{pl}}, \theta) \quad , \tag{6.23}$$

where the updated volume fractions ${}^{n+1}\boldsymbol{\xi}$ are considered. Here, ${}^n\tilde{\boldsymbol{\varepsilon}}^{\mathrm{1d}}_{\mathrm{pl}} = [{}^n\tilde{\varepsilon}^1_{\mathrm{pl}}, \ldots, {}^n\tilde{\varepsilon}^\nu_{\mathrm{pl}}]$ is the collection of current plastic strains as obtained from plastic evolution and subsequent transformation-induced plastic inheritance, cf. Section 6.2. Thus, the trial plastic driving force for phase α results in

$$\begin{aligned} {}^{n+1}q^{\alpha}_{\mathrm{pl},\varPsi,\mathrm{tri}} &= -\left.\frac{\partial\widehat{\varPsi}({}^{n+1}\varepsilon_{\mathrm{dev}},{}^{n+1}\varepsilon_{\mathrm{vol}},{}^{n+1}\boldsymbol{\xi},{}^{n}\tilde{\boldsymbol{\varepsilon}}^{\mathrm{1d}}_{\mathrm{pl}},\theta)}{\partial\,{}^{n}\varepsilon^{\alpha}_{\mathrm{pl}}}\right|_{\theta} \\ &= -\,{}^{n+1}\xi^{\alpha}\left.\frac{\partial\widehat{\psi}^{\alpha}({}^{n+1}\varepsilon_{\mathrm{dev}},{}^{n+1}\varepsilon_{\mathrm{vol}},{}^{n}\varepsilon^{\alpha}_{\mathrm{pl}},\theta)}{\partial\,{}^{n}\varepsilon^{\alpha}_{\mathrm{pl}}}\right|_{{}^{n}\tilde{\varepsilon}^{\alpha}_{\mathrm{pl}},\theta} \\ &= {}^{n+1}\xi^{\alpha}\left[\mathsf{E}^{\alpha}_{\mathrm{dev}}\left[{}^{n+1}\varepsilon_{\mathrm{dev}}-\varepsilon^{\alpha}_{\mathrm{tr,dev}}-{}^{n}\tilde{\varepsilon}^{\alpha}_{\mathrm{pl}}\right]-\zeta^{\alpha}\mathsf{E}^{\alpha}\left[\theta-\theta_{0}\right]\right] \quad . \end{aligned} \tag{6.24}$$

Based on this, the trial value $\varPhi^{\alpha}_{\mathrm{tri}}$ of the yield function can be evaluated, facilitating—in the case of plastic loading—the expression of the Lagrange multiplier as

$${}^{n+1}\lambda^{\alpha}=\frac{\widehat{\varPhi}^{\alpha}({}^{n+1}q^{\alpha}_{\mathrm{pl},\varPsi,\mathrm{tri}},{}^{n}Y^{\alpha})}{{}^{n+1}\xi^{\alpha}\,[\mathsf{E}^{\alpha}+H^{\alpha}]} \quad . \tag{6.25}$$

The plastic strains $\varepsilon^{\alpha}_{\mathrm{pl}}$ in each phase α can, in consequence, be directly updated from time ${}^{n}t$ to ${}^{n+1}t$ according to

$${}^{n+1}\varepsilon^{\alpha}_{\mathrm{pl}}={}^{n}\tilde{\varepsilon}^{\alpha}_{\mathrm{pl}}+{}^{n+1}\lambda^{\alpha}\,\mathrm{sgn}\left({}^{n+1}q^{\alpha}_{\mathrm{pl},\varPsi}-B^{\alpha}\right) \quad , \tag{6.26}$$

whereas the accumulated plastic strains ${}^{n+1}\varepsilon^{\alpha}_{\mathrm{pl,acc}}$ are obtained from

$${}^{n+1}\varepsilon^{\alpha}_{\mathrm{pl,acc}}={}^{n}\tilde{\varepsilon}^{\alpha}_{\mathrm{pl,acc}}+{}^{n+1}\lambda^{\alpha} \quad . \tag{6.27}$$

Here, the consistency of history variables is accounted for by considering the intermediate accumulated plastic strains

$${}^{n}\tilde{\varepsilon}^{\alpha}_{\mathrm{pl,acc}}=\widehat{\tilde{\varepsilon}}^{\alpha}_{\mathrm{pl,acc}}({}^{n}\varepsilon^{\alpha}_{\mathrm{pl,acc}},{}^{n}\tilde{\varepsilon}^{\alpha}_{\mathrm{pl}},{}^{n}\varepsilon^{\alpha}_{\mathrm{pl}}):={}^{n}\varepsilon^{\alpha}_{\mathrm{pl,acc}}+|{}^{n}\tilde{\varepsilon}^{\alpha}_{\mathrm{pl}}-{}^{n}\varepsilon^{\alpha}_{\mathrm{pl}}| \quad , \tag{6.28}$$

see Section 6.2 for details on the derivation of intermediate plastic strains $\tilde{\varepsilon}^{\alpha}_{\mathrm{pl}}$ resulting from plastic inheritance caused by incremental changes of volume fractions.

6.2 Consistent plasticity inheritance law for three phases

In this section, we extend the inheritance law introduced in [102] to $\nu=3$ phases. Due to mass conservation—as implied by (6.2)b—the sum of all volume fractions yields

$$\xi^{\alpha}+\xi^{\beta}+\xi^{\gamma}=1 \quad \text{with} \quad \alpha,\beta,\gamma\in\{\,\mathrm{A},\,\mathrm{M_c},\,\mathrm{M_t}\,\} \quad \text{and} \quad \alpha\neq\beta\neq\gamma \quad . \tag{6.29}$$

For the derivation of the extended inheritance law, we consider again the discrete update from time ${}^{n}t$ to ${}^{n+1}t$, with $\Delta t := {}^{n+1}t - {}^{n}t > 0$. It follows

$$ {}^{n+1}\xi^{\alpha} + {}^{n+1}\xi^{\beta} + {}^{n+1}\xi^{\gamma} = {}^{n}\xi^{\alpha} + {}^{n}\xi^{\beta} + {}^{n}\xi^{\gamma} \tag{6.30} $$

as well as ${}^{n+1}\xi^{\bullet}, {}^{n}\xi^{\bullet} \geq 0$. Using the definition $\Delta\xi^{\bullet} := {}^{n+1}\xi^{\bullet} - {}^{n}\xi^{\bullet}$ for the volume fraction increments, (6.30) can be expressed as

$$ \Delta\xi^{\alpha} + \Delta\xi^{\beta} + \Delta\xi^{\gamma} = 0 \quad , \tag{6.31} $$

which reflects (6.2)c.

First, we assume the volume fraction of one phase, say α, to increase from step n to $n+1$, i.e. $\Delta\xi^{\alpha} = {}^{n+1}\xi^{\alpha} - {}^{n}\xi^{\alpha} > 0$. Inserting this relation in (6.31) then yields

$$ \Delta\xi^{\beta} + \Delta\xi^{\gamma} < 0 \tag{6.32} $$

One possibility to fulfil this inequality is to have the volume fractions of both phases β and γ decreasing, i.e. $\Delta\xi^{\beta} < 0$ and $\Delta\xi^{\gamma} < 0$. Besides, if we assume that the volume fraction of one phase, say β, increases, i.e. $\Delta\xi^{\beta} > 0$, then the volume fraction of the remaining phase γ must decrease such that (6.31) is fulfilled, i.e. $\Delta\xi^{\gamma} < 0$. In summary, we either have one increasing and two decreasing phases, or two increasing and one decreasing phase if we initially assume that one phase α increases from step n to $n+1$.

Next, we assume the volume fraction of phase α to decrease from step n to $n+1$, i.e. $\Delta\xi^{\alpha} = {}^{n+1}\xi^{\alpha} - {}^{n}\xi^{\alpha} < 0$. From (6.31) one obtains

$$ \Delta\xi^{\beta} + \Delta\xi^{\gamma} > 0 \tag{6.33} $$

as a constraint. On the one hand, this inequality can be fulfilled if the volume fractions of both phases β and γ increase, i.e. $\Delta\xi^{\beta} > 0$ and $\Delta\xi^{\gamma} > 0$ such that (6.31) is fulfilled. On the other hand, if we assume that the volume fraction of one phase,say β, decreases, i.e. $\Delta\xi^{\beta} < 0$, then the volume fraction of the remaining phase γ must increase, i.e. $\Delta\xi^{\gamma} > 0$. In summary, these results show that an incremental change of volume fractions can be expressed either in terms of one decreasing and two increasing phases, or in terms of one increasing and two decreasing phases. The special case of one phase remaining constant—while only two phases evolve—is captured by the inheritance rules presented in sections 6.2.1 and 6.2.2 and is briefly discussed in Section 6.2.3.

6.2.1 Derivation of inheritance rules in the case of one increasing and two decreasing phases

We assume that the volume fraction of phase α increases, while phases β and γ decrease, i.e. $\Delta\xi^{\alpha} > 0$ and $\Delta\xi^{\beta} \leq 0$ as well as $\Delta\xi^{\gamma} \leq 0$, cf. Fig. 6.2, such that (6.31) is fulfilled. The amount of plastic strains ${}^{n}\varepsilon_{\mathrm{pl}}^{\beta}$ of phase β assigned to the (non-negative) part $|\Delta\xi^{\beta}|$

of the volume fraction ${}^n\xi^\beta$ at time ${}^n t$ is given as $|\Delta\xi^\beta|\,{}^n\varepsilon^\beta_{\mathrm{pl}}$ and inherited to the growing phase α with a certain inheritance probability $\Pi^{\beta\to\alpha}$. The same holds for the plastic strains of phase γ, facilitating the expression of the updated intermediate plastic strains $\tilde{\varepsilon}^\alpha_{\mathrm{pl}}$ present in phase α in terms of

$$\tilde{\varepsilon}^\alpha_{\mathrm{pl}}\,{}^{n+1}\xi^\alpha = {}^n\varepsilon^\alpha_{\mathrm{pl}}\,{}^n\xi^\alpha + \Pi^{\beta\to\alpha}|\Delta\xi^\beta|\,{}^n\varepsilon^\beta_{\mathrm{pl}} + \Pi^{\gamma\to\alpha}|\Delta\xi^\gamma|\,{}^n\varepsilon^\gamma_{\mathrm{pl}} \quad , \tag{6.34}$$

where we consider a physically reasonable concave ("ccv") inheritance probability function

$$\Pi^{\beta\to\alpha} = \widehat{\Pi}^{\beta\to\alpha}_{\mathrm{ccv}}({}^{n+1}\xi^\beta, {}^n\varepsilon^\beta_{\mathrm{pl}}; \kappa, \varepsilon^\beta_{\mathrm{pl,sat}}) = \frac{1-\exp\left(\dfrac{-\kappa\,[1-{}^{n+1}\xi^\beta]}{\varepsilon^\beta_{\mathrm{pl,sat}} - |{}^n\varepsilon^\beta_{\mathrm{pl}}|}\right)}{1-\exp\left(\dfrac{-\kappa}{\varepsilon^\beta_{\mathrm{pl,sat}} - |{}^n\varepsilon^\beta_{\mathrm{pl}}|}\right)} \quad . \tag{6.35}$$

For a detailed discussion, including an alternative convex inheritance probability function, we refer to [102].

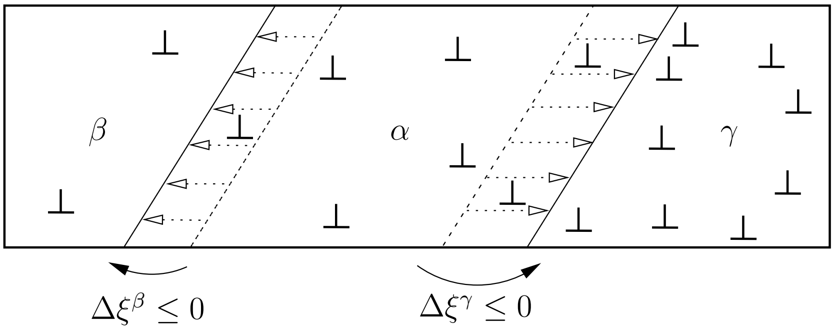

Figure 6.2: Phase α increases, while phases β and γ decrease.

In consequence, the intermediate plastic strains $\tilde{\varepsilon}^\bullet_{\mathrm{pl}}$ within both decreasing phases β and γ are reduced due to the aforementioned part of plastic strains inherited to the increasing phase α. For phases β and γ we obtain

$$\tilde{\varepsilon}^\bullet_{\mathrm{pl}}\,{}^{n+1}\xi^\bullet = {}^n\varepsilon^\bullet_{\mathrm{pl}}\,{}^n\xi^\bullet - \Pi^{\bullet\to\alpha}|\Delta\xi^\bullet|\,{}^n\varepsilon^\bullet_{\mathrm{pl}} \quad . \tag{6.36}$$

Considering the signs of the volume fraction increments, $\Delta\xi^\beta \leq 0$ and $\Delta\xi^\gamma \leq 0$, the intermediate plastic strains resulting from an incremental change of volume fractions as given in (6.34) and (6.36) finally result in

$$
\begin{aligned}
\tilde{\varepsilon}^\alpha_{\text{pl}} &= \frac{1}{{}^{n+1}\xi^\alpha} \left[{}^n\varepsilon^\alpha_{\text{pl}}\, {}^n\xi^\alpha - \mathit{\Pi}^{\beta\to\alpha}\, \Delta\xi^\beta\, {}^n\varepsilon^\beta_{\text{pl}} - \mathit{\Pi}^{\gamma\to\alpha} \Delta\xi^\gamma\, {}^n\varepsilon^\gamma_{\text{pl}} \right] \quad , && (6.37)\\
\tilde{\varepsilon}^\beta_{\text{pl}} &= \frac{1}{{}^{n+1}\xi^\beta} \left[{}^n\xi^\beta + \mathit{\Pi}^{\beta\to\alpha}\, \Delta\xi^\beta \right] {}^n\varepsilon^\beta_{\text{pl}} \quad , && (6.38)\\
\tilde{\varepsilon}^\gamma_{\text{pl}} &= \frac{1}{{}^{n+1}\xi^\gamma} \left[{}^n\xi^\gamma + \mathit{\Pi}^{\gamma\to\alpha}\, \Delta\xi^\gamma \right] {}^n\varepsilon^\gamma_{\text{pl}} && (6.39)
\end{aligned}
$$

in case of one increasing phase α, and two decreasing phases, β and γ. Note that the overall plastic strains of the one-dimensional continuum considered remain constant in terms of

$$
\sum_{\alpha,\beta,\gamma} \tilde{\varepsilon}^\bullet_{\text{pl}}\, {}^{n+1}\xi^\bullet = \sum_{\alpha,\beta,\gamma} {}^n\varepsilon^\bullet_{\text{pl}}\, {}^n\xi^\bullet \quad . \tag{6.40}
$$

In physical terms, this corresponds to the assumption that dislocations are neither generated nor annihilated by an evolving phase front that propagates due to diffusion-less lattice shearing that drives the evolution of phases.

6.2.2 Derivation of inheritance rules in the case of one decreasing and two increasing phases

In contrast to Section 6.2.1, we now assume that the volume fraction of one phase—here denoted as α without loss of generality—decreases, while the remaining phases—β and γ—increase, i.e. $\Delta\xi^\alpha < 0$ with appropriate $\Delta\xi^\beta \geq 0$ and $\Delta\xi^\gamma \geq 0$, cf. Fig. 6.3, such that the mass conservation constraint (6.31) is fulfilled. Consider first the phases β and γ, which increase their volume fractions at the expense of phase α. The volume fraction increments $\Delta\xi^\bullet$ of both phases β and γ inherit the plastic strains ${}^n\varepsilon^\alpha_{\text{pl}}$ present in phase α at time ${}^nt$, thus for the intermediate plastic strains of phases β and γ

$$
\tilde{\varepsilon}^\bullet_{\text{pl}}\, {}^{n+1}\xi^\bullet = {}^n\varepsilon^\bullet_{\text{pl}}\, {}^n\xi^\bullet + \mathit{\Pi}^{\alpha\to\bullet}\, \Delta\xi^\bullet\, {}^n\varepsilon^\alpha_{\text{pl}} \tag{6.41}
$$

holds, with $\mathit{\Pi}^{\alpha\to\bullet}$ the probability for the inheritance from phase α to phases β and γ, respectively. In consequence—in order to fulfil the requirement that the amount of plastic strains remains constant in the context of (6.40)—the plastic strains present in the decreasing phase α change according to

$$
\tilde{\varepsilon}^\alpha_{\text{pl}}\, {}^{n+1}\xi^\alpha = {}^n\varepsilon^\alpha_{\text{pl}}\, {}^n\xi^\alpha - \mathit{\Pi}^{\alpha\to\beta}\, \Delta\xi^\beta\, {}^n\varepsilon^\alpha_{\text{pl}} - \mathit{\Pi}^{\alpha\to\gamma}\, \Delta\xi^\gamma\, {}^n\varepsilon^\alpha_{\text{pl}} \quad . \tag{6.42}
$$

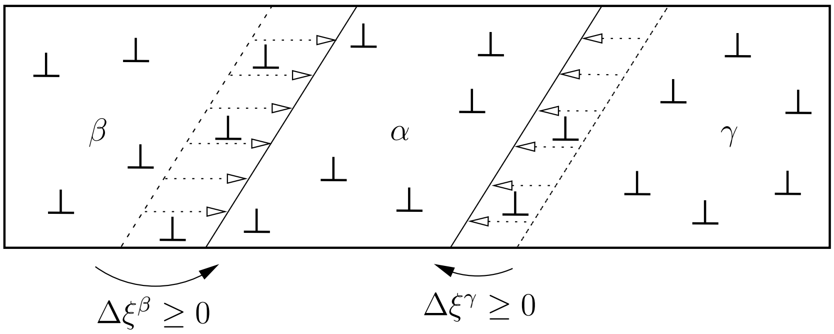

Figure 6.3: Phase α decreases, while phases β and γ increase.

In summary, the intermediate plastic strains in the case of one decreasing phase α, and two increasing phases, β and γ, result in

$$\tilde{\varepsilon}^{\alpha}_{\text{pl}} = \frac{1}{{}^{n+1}\xi^{\alpha}} \left[{}^{n}\xi^{\alpha} - \Pi^{\alpha\to\beta}\,\Delta\xi^{\beta} - \Pi^{\alpha\to\gamma}\Delta\xi^{\gamma} \right] {}^{n}\varepsilon^{\alpha}_{\text{pl}} \quad , \tag{6.43}$$

$$\tilde{\varepsilon}^{\beta}_{\text{pl}} = \frac{1}{{}^{n+1}\xi^{\beta}} \left[{}^{n}\varepsilon^{\beta}_{\text{pl}}\, {}^{n}\xi^{\beta} + \Pi^{\alpha\to\beta}\,\Delta\xi^{\beta}\, {}^{n}\varepsilon^{\alpha}_{\text{pl}} \right] \quad , \tag{6.44}$$

$$\tilde{\varepsilon}^{\gamma}_{\text{pl}} = \frac{1}{{}^{n+1}\xi^{\gamma}} \left[{}^{n}\varepsilon^{\gamma}_{\text{pl}}\, {}^{n}\xi^{\gamma} + \Pi^{\alpha\to\gamma}\,\Delta\xi^{\gamma}\, {}^{n}\varepsilon^{\alpha}_{\text{pl}} \right] \quad , \tag{6.45}$$

as obtained from (6.41) and (6.42).

6.2.3 Remarks on the inheritance rules

It can be shown that the inheritance rules consistently take into account the special case of two evolving phases, while the third phase remains constant. Consider on the one hand—without loss of generality—that phase α evolves, i.e. $\Delta\xi^{\alpha} > 0$, while phase γ remains constant, $\Delta\xi^{\gamma} = 0$, inducing $\Delta\xi^{\beta} = -\Delta\xi^{\alpha} < 0$ from (6.31). The related inheritance laws, (6.37), (6.38), (6.39), then reduce to

$$\tilde{\varepsilon}^{\alpha}_{\text{pl}} = \frac{1}{{}^{n+1}\xi^{\alpha}} \left[{}^{n}\varepsilon^{\alpha}_{\text{pl}}\, {}^{n}\xi^{\alpha} + \Pi^{\beta\to\alpha}\,\Delta\xi^{\alpha}\, {}^{n}\varepsilon^{\beta}_{\text{pl}} \right] \quad , \tag{6.46}$$

$$\tilde{\varepsilon}^{\beta}_{\text{pl}} = \frac{1}{{}^{n+1}\xi^{\beta}} \left[{}^{n}\xi^{\beta} + \Pi^{\beta\to\alpha}\,\Delta\xi^{\beta} \right] {}^{n}\varepsilon^{\beta}_{\text{pl}} \quad , \tag{6.47}$$

$$\tilde{\varepsilon}^{\gamma}_{\text{pl}} = {}^{n}\varepsilon^{\gamma}_{\text{pl}} \quad , \tag{6.48}$$

where $\Delta\xi^{\gamma} = 0$ is considered in (6.46), (6.47), (6.48), while in addition $\Delta\xi^{\beta} = -\Delta\xi^{\alpha}$ and ${}^{n+1}\xi^{\gamma} = {}^{n}\xi^{\gamma}$ are considered in (6.46) and (6.48), respectively.

On the other hand, if we assume the volume fraction of phase α to decrease, $\Delta\xi^{\alpha} < 0$, while—again without loss of generality—γ remains constant, i.e. $\Delta\xi^{\gamma} = 0$, we obtain

$\Delta\xi^\beta = -\Delta\xi^\alpha > 0$ for phase β from (6.31). The inheritance rules derived for this case, (6.43), (6.44), (6.45), result in

$$\tilde{\varepsilon}^\alpha_{\text{pl}} = \frac{1}{{}^{n+1}\xi^\alpha}\left[{}^n\xi^\alpha + \mathit{\Pi}^{\alpha\to\beta}\,\Delta\xi^\alpha\right]{}^n\varepsilon^\alpha_{\text{pl}} \quad , \tag{6.49}$$

$$\tilde{\varepsilon}^\beta_{\text{pl}} = \frac{1}{{}^{n+1}\xi^\beta}\left[{}^n\varepsilon^\beta_{\text{pl}}\,{}^n\xi^\beta + \mathit{\Pi}^{\alpha\to\beta}\,\Delta\xi^\beta\,{}^n\varepsilon^\alpha_{\text{pl}}\right] \quad , \tag{6.50}$$

$$\tilde{\varepsilon}^\gamma_{\text{pl}} = {}^n\varepsilon^\gamma_{\text{pl}} \quad , \tag{6.51}$$

with $\Delta\xi^\gamma = 0$ being considered in (6.49), (6.50), (6.51). In addition, $\Delta\xi^\beta = -\Delta\xi^\alpha$ and ${}^{n+1}\xi^\gamma = {}^n\xi^\gamma$ is accounted for in (6.49) and (6.51), respectively. Comparison of (6.48) and (6.51) shows that no plastic strains are inherited within a phase of constant volume fraction in either case. Furthermore, in the case of one phase remaining constant, the inheritance rules (6.37), (6.38), (6.39) and (6.43), (6.44), (6.45) consistently reduce to the inheritance law applicable for just two evolving phases as derived in [102]. Moreover, it is clear that equations (6.46) and (6.47) (with α as the increasing phase and β as the decreasing phase) are equivalent to (6.50) and (6.49) (with α as the decreasing phase and β as the increasing phase), respectively. In consequence, the presented physically motivated inheritance rules are self-consistent and capture all special cases that may occur with respect to the possible transformation states of the three phases considered.

6.3 Micro-sphere application

The scalar-valued model for the interaction of phase-transformations and plasticity established in Section 6.1 is embedded into a non-affine micro-sphere framework to allow the simulation of three-dimensional homogeneous load cases and for the solution of three-dimensional boundary value problems. The definition of affine, respectively non-affine models is not uniquely introduced in the literature. From the perspective of a given spatial micro-sphere integration direction, in the current model not only the strain corresponding to the macroscopic stretch projected onto the same direction is considered, but two strain measures are transferred to the micro-level even though both are determined from the macro-strains. In this sense, the strain measures used for each integration direction do not only depend on the macro-strains projected in this direction alone. This motivates the use of the term *non-affine.*

In the context of a small strain non-affine micro-sphere framework, the local deformation state $\boldsymbol{\varepsilon} := \nabla^{\text{sym}}_{\boldsymbol{x}}\boldsymbol{u}$ is split into volumetric and deviatoric parts in terms of $\boldsymbol{\varepsilon} = \boldsymbol{\varepsilon}_{\text{vol}} + \boldsymbol{\varepsilon}_{\text{dev}}$ with $\boldsymbol{\varepsilon}_{\text{vol}} = 1/3\,\text{tr}(\boldsymbol{\varepsilon})\boldsymbol{I}$ and $\boldsymbol{\varepsilon}_{\text{dev}} = \boldsymbol{\varepsilon} - 1/3\,\text{tr}(\boldsymbol{\varepsilon})\boldsymbol{I}$, where $\boldsymbol{I}$ denotes the second-order identity tensor. Both tensorial quantities are then projected onto each spatial integration direction $\boldsymbol{r}_i \in \mathbb{U}^2$ considered for the numerical micro-sphere integration scheme as briefly presented in Section 6.3.1.

6.3.1 Kinematics

For the material model proposed, we use a kinematically constrained non-affine micro-sphere model, where the vector norm of the projection $\boldsymbol{\varepsilon}_{r_i} = [\boldsymbol{r}_i \cdot \boldsymbol{\varepsilon} \cdot \boldsymbol{r}_i]\, \boldsymbol{r}_i$ of the strain tensor $\boldsymbol{\varepsilon}$ onto each integration direction $\boldsymbol{r}_i$ is split into the volumetric and deviatoric contributions $\varepsilon_{\text{dev},i}$ and ε_{vol}. To be precise, $\boldsymbol{r}_i \cdot \boldsymbol{\varepsilon} \cdot \boldsymbol{r}_i = \varepsilon_{\text{dev},i} + \varepsilon_{\text{vol}}$ with $\varepsilon_{\text{dev},i} = \boldsymbol{r}_i \cdot \boldsymbol{\varepsilon} \cdot \boldsymbol{r}_i - 1/3\,\text{tr}(\boldsymbol{\varepsilon})$ and $\varepsilon_{\text{vol}} = 1/3\,\text{tr}(\boldsymbol{\varepsilon})$. Applying this kinematic constraint in combination with volumetric and deviatoric elasticity coefficients on the micro-level, $\mathsf{E}_{\text{vol}} = \mathsf{E}/[1 - 2\,\nu_{\text{P}}]$ and $\mathsf{E}_{\text{dev}} = \mathsf{E}/[1 + \nu_{\text{P}}]$, facilitates the capturing of different Young's moduli E and Poisson's ratios ν_{P} on the macro-level as shown in [27].

Note that this split of the projection of the macroscopic strain induces $\varepsilon_{\text{dev}}(\boldsymbol{r}_i) = \varepsilon_{\text{dev}}(-\boldsymbol{r}_i)$, whereas ε_{vol} does not depend on $\boldsymbol{\varepsilon}$ and a single direction $\boldsymbol{r}_i$ alone but on the trace of $\boldsymbol{\varepsilon}$. In consequence, the strain history obtained for any spatial integration direction $\boldsymbol{r}_i$ is identical to the strain history obtained in the opposite direction $-\boldsymbol{r}_i$ of the micro-sphere. As a result, for symmetric initial conditions in terms of the material's initial state, the constitutive response obtained in one spatial direction is identical to the response of the opposite spatial direction for every load state. Thus, the symmetry of the kinematic projections in combination with symmetric initial conditions for the material state allows for the application of efficient micro-sphere integration schemes that require the numerical integration to be carried out solely on one hemisphere as presented in Section 6.3.5.

6.3.2 Micro-macro-relations

In this section we review how stresses, state-dependent variables, and derived quantities obtained at the micro-level are transferred to the macro-scale. Section 6.3.2.1 shows the derivation of the macroscopic stress tensor based on the overall Helmholtz free energy potentials of the phase mixtures assigned to the individual micro-sphere integration directions. Sections 6.3.2.2 and 6.3.2.3 show how volume fractions and plastic strains obtained at the micro-level are transferred to the macro-level, where we introduce higher-order moments and a deviatoric macroscopic plastic strain tensor.

6.3.2.1 Stresses

In the context of the micro-sphere approach, the macroscopic stress tensor $\boldsymbol{\sigma}$ is obtained by integration over the unit sphere, resulting in the numerical approximation

$$\boldsymbol{\sigma} = \frac{1}{4\pi} \int_{\mathbb{U}^2} \frac{\partial \varPsi}{\partial \boldsymbol{\varepsilon}}\, \text{d}a \approx \sum_{i=1}^{n_r} \frac{\partial \varPsi_i}{\partial \boldsymbol{\varepsilon}}\, \bar{w}_i = \sum_{i=1}^{n_r} \boldsymbol{\sigma}_i \tag{6.52}$$

with the help of a finite number i of spatial integration directions, cf., e.g., [75, 92, 101, 104]. The constitutive relation is evaluated in every such direction, where the individual strain- and history-dependent material response related to each integration direction $\boldsymbol{r}_i$

contributes to the overall macroscopic stress tensor $\boldsymbol{\sigma}$. Here, $\partial\Psi_i/\partial\boldsymbol{\varepsilon}$ is the contribution of the i'th integration direction weighted by the numerical integration weight $\bar{w}_i$ with $\sum_i \bar{w}_i = 1$. Note that $\Psi_i = \widehat{\Psi}_i(\varepsilon_{\text{dev},i}, \varepsilon_{\text{vol}}, \boldsymbol{\xi}_i, \boldsymbol{\varepsilon}^{\text{1d}}_{\text{pl},i})$ is the overall Helmholtz potential of the specific phase mixture situated in integration direction $\boldsymbol{r}_i$, where $\boldsymbol{\xi}_i = [\xi_i^{(1)}, \ldots, \xi_i^{(\nu)}]^{\text{t}} \in \mathbb{R}^{\nu\times 1}$ and $\boldsymbol{\varepsilon}^{\text{1d}}_{\text{pl},i} = [\varepsilon^{(1)}_{\text{pl},i}, \ldots, \varepsilon^{(\nu)}_{\text{pl}}]$ are the corresponding collections of volume fractions and individual plastic strains per phase, respectively. Applying the chain rule to the partial derivative of the overall phase potential Ψ_i with respect to the macroscopic strain tensor $\boldsymbol{\varepsilon}$ yields

$$\frac{\partial\Psi_i}{\partial\boldsymbol{\varepsilon}} = \frac{\partial\Psi_i}{\partial\varepsilon_{\text{vol}}}\frac{\partial\varepsilon_{\text{vol}}}{\partial\boldsymbol{\varepsilon}} + \frac{\partial\Psi_i}{\partial\varepsilon_{\text{dev},i}}\frac{\partial\varepsilon_{\text{dev},i}}{\partial\boldsymbol{\varepsilon}} = \frac{\partial\Psi_i}{\partial\varepsilon_{\text{vol}}}\frac{1}{3}\boldsymbol{I} + \frac{\partial\Psi_i}{\partial\varepsilon_{\text{dev},i}}\left[\boldsymbol{r}_i\otimes\boldsymbol{r}_i - \frac{1}{3}\boldsymbol{I}\right] \quad . \tag{6.53}$$

Considering (6.8) together with (6.3), the terms $\partial\Psi_i/\partial\varepsilon_{\text{vol}}$ and $\partial\Psi_i/\partial\varepsilon_{\text{dev}}$ in (6.53) take the form

$$\frac{\partial\Psi_i}{\partial\varepsilon_{\text{vol}}} = \sum_{\alpha=1}^{\nu}\xi_i^\alpha\left[\mathsf{E}^\alpha_{\text{vol}}\left[\varepsilon_{\text{vol}} - \varepsilon^\alpha_{\text{tr,vol}}\right] - \zeta^\alpha\mathsf{E}^\alpha\left[\theta-\theta_0\right]\right] \quad \text{and} \tag{6.54}$$

$$\frac{\partial\Psi_i}{\partial\varepsilon_{\text{dev},i}} = \sum_{\alpha=1}^{\nu}\xi_i^\alpha\left[\mathsf{E}^\alpha_{\text{dev}}\left[\varepsilon_{\text{dev},i} - \varepsilon^\alpha_{\text{tr,dev}} - \varepsilon^\alpha_{\text{pl},i}\right] - \zeta^\alpha\mathsf{E}^\alpha\left[\theta-\theta_0\right]\right] \quad , \tag{6.55}$$

where the volumetric strain projection ε_{vol} is identical for all integration directions. Note that for every integration direction $\boldsymbol{r}_i$ of the micro-sphere, the deviatoric strain projections $\varepsilon_{\text{dev},i}$, the volume fractions of all phases ξ_i^α and the plastic strains $\varepsilon^\alpha_{\text{pl},i}$ need to be considered and evaluated individually. The numerical micro-sphere approximation of the macroscopic stress tensor finally results in

$$\boldsymbol{\sigma} \approx \sum_{i=1}^{n_r}\boldsymbol{\sigma}_i = \sum_{i=1}^{n_r}\sum_{\alpha=1}^{\nu}\xi_i^\alpha\boldsymbol{\sigma}_i^\alpha \quad , \tag{6.56}$$

with

$$\begin{aligned}\boldsymbol{\sigma}_i^\alpha &= \left[\frac{1}{3}\left[\mathsf{E}^\alpha_{\text{vol}}\left[\varepsilon_{\text{vol}} - \varepsilon^\alpha_{\text{tr,vol}}\right] - \zeta^\alpha\,\mathsf{E}^\alpha\left[\theta-\theta_0\right]\right]\boldsymbol{I}\right.\\ &\quad + \left.\left[\mathsf{E}^\alpha_{\text{dev}}\left[\varepsilon_{\text{dev},i} - \varepsilon^\alpha_{\text{tr,dev}} - \varepsilon^\alpha_{\text{pl},i}\right] - \zeta^\alpha\,\mathsf{E}^\alpha\left[\theta-\theta_0\right]\right]\left[\boldsymbol{r}_i\otimes\boldsymbol{r}_i - \frac{1}{3}\boldsymbol{I}\right]\right]\bar{w}_i\end{aligned} \tag{6.57}$$

the tensor-valued stress contribution of phase α situated in the ith micro-sphere integration direction.

6.3.2.2 Macroscopic volume fractions

A scalar measure for the macroscopic volume fractions $\Xi^\alpha = \widehat{\Xi}^\alpha(\xi^\alpha)$ is obtained by integration over the unit sphere in terms of

$$\Xi^\alpha = \sum_{i=1}^{n_r} \xi_i^\alpha \, \bar{w}_i \quad , \tag{6.58}$$

resulting in a structural tensor of zeroth order that corresponds to a simple arithmetic averaging of the micro-quantities, where ξ_i^α is the volume fraction of phase α situated in the i th integration direction $\boldsymbol{r}_i$. From a macroscopic point of view, a more detailed insight into the anisotropy of the material is obtained by computing higher-order structural tensors that give additional information on the spatial distribution of volume fractions.

6.3.2.3 Macroscopic plastic strains

As in the case of the macroscopic volume fractions, cf. Section 6.3.2.2, the macroscopic plastic strains can be derived in terms of structural tensors of different order. For example, a scalar macroscopic plastic strain measure $\varepsilon_{\text{pl}}^{\alpha,\text{mac}}$ is obtained from

$$\varepsilon_{\text{pl}}^{\alpha,\text{mac}} = \sum_{i=1}^{n_r} \varepsilon_{\text{pl},i}^\alpha \, \bar{w}_i \quad , \tag{6.59}$$

while the macroscopic plastic strain tensor of second-order can be derived as

$$\boldsymbol{\varepsilon}_{\text{pl}}^{\alpha,\text{mac}} = \sum_{i=1}^{n_r} \varepsilon_{\text{pl},i}^\alpha \, [\boldsymbol{r}_i \otimes \boldsymbol{r}_i] \, \bar{w}_i \quad . \tag{6.60}$$

Note that the second-order plastic strain tensor obtained in this manner is not necessarily purely deviatoric. To ensure a purely deviatoric second-order macroscopic plastic strain tensor, (6.60) can be modified with the help of the fourth-order deviatoric projection operator I^{dev}, resulting in

$$\begin{aligned}
\boldsymbol{\varepsilon}_{\text{pl,dev}}^{\alpha,\text{mac}} &= \sum_{i=1}^{n_r} \varepsilon_{\text{pl},i}^\alpha \, [\boldsymbol{r}_i \otimes \boldsymbol{r}_i] : \mathsf{I}^{\text{dev}} \, \bar{w}_i && (6.61)\\
&= \sum_{i=1}^{n_r} \varepsilon_{\text{pl},i}^\alpha \, [\boldsymbol{r}_i \otimes \boldsymbol{r}_i] : \left[\mathsf{I}^{\text{sym}} - \frac{1}{3} \boldsymbol{I} \otimes \boldsymbol{I} \right] \bar{w}_i && (6.62)\\
&= \sum_{i=1}^{n_r} \varepsilon_{\text{pl},i}^\alpha \left[\boldsymbol{r}_i \otimes \boldsymbol{r}_i - \frac{1}{3} \boldsymbol{I} \right] \bar{w}_i \quad , && (6.63)
\end{aligned}$$

with I^{sym} denoting the fourth-order symmetric identity tensor and $\boldsymbol{I}$ the second-order identity tensor. However, as this work proceeds—especially in view of the finite element results presented in Section 6.4—we restrict the illustrations to the scalar averaging of the microscopic plastic strains according to (6.59) in order to assess the amount of plastic strains generated at a given material point.

6.3.3 Anisotropic elasticity tensor and tangent operator

The algorithmic tangent operator E^{alg} is required for the iterative determination of uniaxial stress states within a constitutive driver framework, facilitating the simulation of tensile tests with uniaxial stress states in homogeneous simulations as shown in Section 6.3.4. Moreover, it is required for the finite element implementation presented in Section 6.4. For the model framework proposed in this work, the tangent operator can be split into elastic and inelastic contributions, $\mathsf{E}^{\text{alg}} = \mathsf{E}_{\text{el}} + \mathsf{E}^{\text{alg}}_{\text{pl}}$. To be precise,

$$\begin{aligned} \mathsf{E}^{\text{alg}} &:= \frac{\mathrm{d}\boldsymbol{\sigma}}{\mathrm{d}\boldsymbol{\varepsilon}} && (6.64)\\ &= \mathsf{E}_{\text{el}} + \mathsf{E}^{\text{alg}}_{\text{pl}} && (6.65)\\ &= \sum_{i=1}^{n_r} \frac{\partial \boldsymbol{\sigma}_i}{\partial \boldsymbol{\varepsilon}} + \sum_{i=1}^{n_r}\sum_{\alpha=1}^{\nu} \frac{\partial \boldsymbol{\sigma}}{\partial \boldsymbol{s}_i^\alpha} \cdot \frac{\partial \boldsymbol{s}_i^\alpha}{\partial \boldsymbol{\varepsilon}} \quad , && (6.66) \end{aligned}$$

with $\boldsymbol{s}_i^\alpha = [\xi_i^\alpha, \varepsilon^\alpha_{\text{pl},i}, \varepsilon^\alpha_{\text{pl,acc},i}]$ representing the state-dependent variables of phase α located in integration direction $\boldsymbol{r}_i$. The elastic part $\mathsf{E}_{\text{el}} = \partial\boldsymbol{\sigma}/\partial\boldsymbol{\varepsilon}$ of the algorithmic tangent modulus corresponds to the anisotropic elasticity tensor of the material. The reader is referred to [104], respectively Chapter 3, for a detailed elaboration on its derivation. The inelastic contribution $\mathsf{E}^{\text{alg}}_{\text{pl}}$ to the tangent modulus can be derived in a component-by-component manner based on (6.66) as shown in, e.g., [118].

To assess the evolution of anisotropy within the material, we visualise the fourth-order anisotropic elasticity tensor by means of Young's modulus surface plots as shown in, e.g., [23, 31, 142]. To this end, the fourth-order compliance tensor $\mathsf{C}_{\text{el}} := \mathsf{E}_{\text{el}}^{-1}$ is projected onto spatial directions $\boldsymbol{d}$, where the latter are unit vectors obtained from a parametrisation of the unit sphere $\mathbb{U}^2$. The projection $\delta^{\mathsf{C}_{\text{el}}}(\mathsf{C}_{\text{el}}, \boldsymbol{d})$ of the fourth-order compliance tensor onto each unit vector,

$$\delta^{\mathsf{C}_{\text{el}}}(\mathsf{C}_{\text{el}}, \boldsymbol{d}) = [\boldsymbol{d}\otimes\boldsymbol{d}] : \mathsf{C}_{\text{el}} : [\boldsymbol{d}\otimes\boldsymbol{d}] \quad , \tag{6.67}$$

results in the scalar compliance of the material in the specific spatial direction $\boldsymbol{d}$, the inverse of which yields the sought Young's modulus $\mathsf{E}(\boldsymbol{d})$ in direction $\boldsymbol{d}$,

$$\mathsf{E}(\boldsymbol{d}) = \delta^{-1\mathsf{C}_{\text{el}}}(\mathsf{C}_{\text{el}}, \boldsymbol{d}) = \big[\,[\boldsymbol{d}\otimes\boldsymbol{d}] : \mathsf{C}_{\text{el}} : [\boldsymbol{d}\otimes\boldsymbol{d}]\,\big]^{-1} \quad . \tag{6.68}$$

Graphical representations of $\mathsf{E}(\boldsymbol{d})$ for selected representative deformation states for both SMA and TRIP steel are provided in Figs. 6.7(a), 6.7(b), 6.10(a), and 6.10(b).

6.3.4 Micro-sphere application – numerical examples

In this section, the constitutive response of the previously described model is presented for a characteristic homogeneous load case. Cyclic tension and compression of the material is applied to the polycrystal, i.e. at the micro-sphere level, while maintaining uniaxial stress states with the help of a constitutive driver. To this end, we prescribe the deformation in terms of the ε_{11} strain component while iteratively adapting ε_{22} and ε_{33} so that the uniaxiality $\boldsymbol{\sigma} = \sigma_{11}\, \boldsymbol{e}_1 \otimes \boldsymbol{e}_1$ of the stress tensor is ensured in every load step.

The cyclic tension-compression simulations of the polycrystal are performed for both SMA and TRIP steel material parameters at a room temperature of 20°C with a high-order micro-sphere integration scheme providing $n_r = 350$ spatial integration directions. The results obtained for SMA are discussed in Section 6.3.4.1, the results for TRIP steel are elaborated in Section 6.3.4.2.

6.3.4.1 Application to NiTi-based shape memory alloy

For the investigation of the SMA response at polycrystal level we apply the loading path shown in Fig. 6.4(a) with a quasi-static cycle duration of $T = 1600\,\mathrm{s}$ to the ε_{11} component of the macroscopic strain tensor. As initial condition we consider a purely austenitic initial state, i.e. $\xi^{\mathrm{A}}|_{t_0} = 1$, inducing $\xi^{\mathrm{M_t}}|_{t_0} = \xi^{\mathrm{M_c}}|_{t_0} = 0$ at a room temperature of $\theta = 20\,^\circ\mathrm{C}$. The material parameters used for the simulation of SMA are provided in Table 6.1.

The resulting uniaxial stress response σ_{11} of the material as depicted in Fig. 6.4(b) corresponds to the macroscopic mechanical response typically observed for SMA material at room temperature. At a maximum strain of $\varepsilon_{11} = 0.04$ a stress of $\sigma_{11} = 200\,\mathrm{MPa}$ is observed for the polycrystalline SMA.

Apart from the stress response, we show the evolution of internal variables in the direction of maximum load, i.e. the $\boldsymbol{e}_1$-direction, as well as the homogenised macroscopic counterparts of these quantities. To be precise, Fig. 6.5(a) shows the evolution of volume fractions $\xi^{\alpha}_{\boldsymbol{e}_1}$ in the $\boldsymbol{e}_1$-direction while Fig. 6.5(c) presents the evolution of plastic strains $\varepsilon^{\alpha}_{\mathrm{pl},\boldsymbol{e}_1}$ in the same direction. The macroscopic volume fractions Ξ^{α} shown in Fig. 6.5(b) are computed according to (6.58), i.e. we show the obtained scalar averaged quantities here. The macroscopic plastic strains $\varepsilon^{\alpha,\mathrm{mac}}_{\mathrm{pl}}$ given in Fig. 6.5(d) are obtained in an analogous manner according to (6.59) for the sake of simplicity.

The evolution of volume fractions in the underlying $\boldsymbol{e}_1$ integration direction, see Fig. 6.5(a), shows how the onset of plasticity, cf. Fig. 6.5(c), represses the evolution of the martensitic tensile phase during the tensile load cycle. Moreover, Figs. 6.5(c) and 6.5(d) show the effects of the plasticity inheritance framework introduced in Section 6.2. For example, as the initial tensile load is applied, the martensitic compression phase $\mathrm{M_c}$ remains zero in the $\boldsymbol{e}_1$ integration direction, as does the corresponding plastic strain $\varepsilon^{\mathrm{M_c}}_{\mathrm{pl},\boldsymbol{e}_1}$. As the load reverses and the martensitic compression phase starts to grow

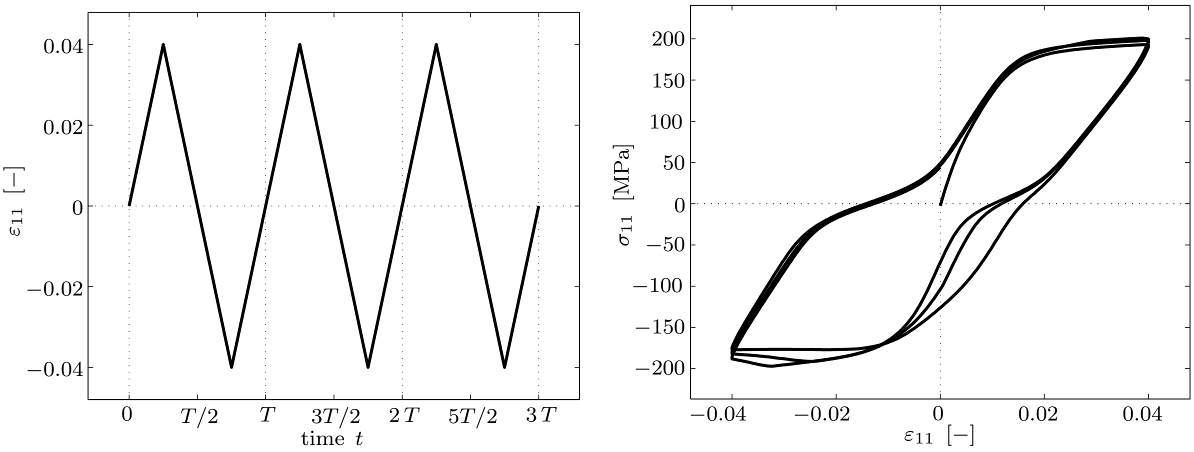

(a) Loading path prescribed in $\boldsymbol{e}_1$-direction.

(b) Uniaxial stress-strain response.

Figure 6.4: Three-dimensional SMA micro-sphere simulation with constitutive driver maintaining an uniaxial macroscopic stress state in $\boldsymbol{e}_1$-direction during all load steps. The results are obtained at $\theta = 20\,°\mathrm{C}$ for 350 equally distributed micro-sphere integration directions. Shown is the prescribed load path (a) and the obtained uniaxial macroscopic stress response (a). See Fig. 6.5 for the corresponding evolution of volume fractions and plastic strains within the material.

at the cost of both the austenitic and the martensitic tensile phase, it inherits the plastic strains of the latter phases as suggested by the corresponding close-to-vertical line depicted in Fig. 6.5(c).

Figures 6.6 and 6.7 provide visualisations of the internal state of the simulated SMA polycrystal at two representative loading states, namely at the state of maximum tension, $\varepsilon_{11} = 0.04$ reached at $t = T/4$, and at the state of maximum compression, $\varepsilon_{11} = -0.04$ reached at $t = 3/4\,T$, cf. Fig. 6.4(a). For both states, we provide the spatial distribution of volume fractions, the spatial distribution of plastic strains and a Young's modulus surface plot, thereby facilitating the assessment of the elastic anisotropy evolution.

The spatial distribution of volume fractions at maximum tension, Fig. 6.6(a), shows how the initially purely austenitic crystal transforms to the tensile martensite variant in the tensile direction, i.e. in direction of the $\boldsymbol{e}_1$-axis. Orthogonal to this axis, i.e. in the $\boldsymbol{e}_2$-$\boldsymbol{e}_3$-plane, the evolution of the martensitic compression variant is observed due to the constitutive driver controlling the lateral compression deformation. The corresponding spatial distribution of plastic strains in the same material state depicted in Fig. 6.6(c) shows the evolution of plasticity in the austenitic parent phase and in the martensitic tensile phase in a cone around the $\boldsymbol{e}_1$-axis. The corresponding elastic anisotropy of the material in the given state is presented in Fig. 6.7(a).

At the state of maximum compression in $\boldsymbol{e}_1$-direction, the spatial distribution of volume fractions within the polycrystal, see Fig. 6.6(b), is dominated by compression martensite in the compression direction, whereas in the orthogonal $\boldsymbol{e}_2$-$\boldsymbol{e}_3$-plane, the martensitic tensile variant evolves as a result of the positive lateral deformation induced

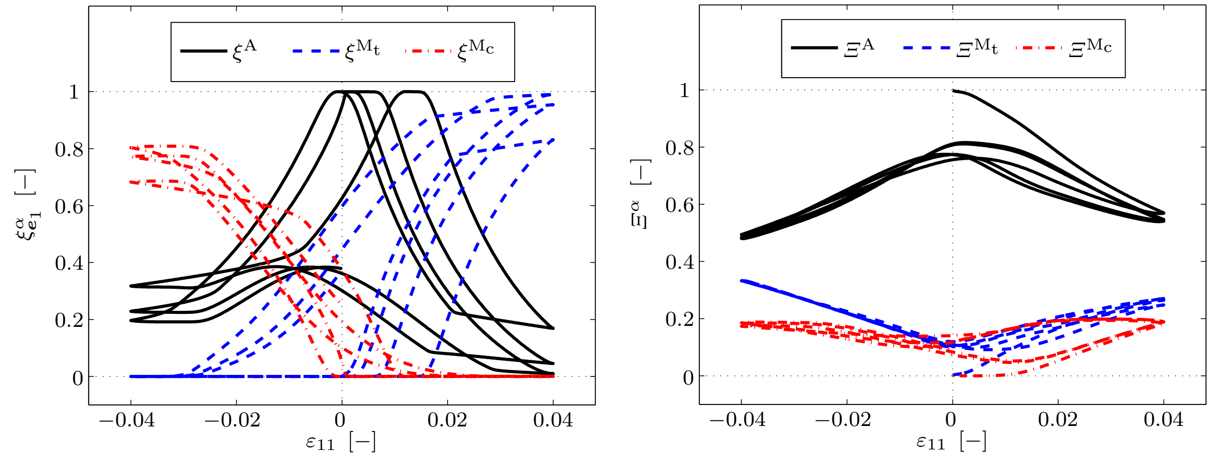

(a) Volume fractions in $\boldsymbol{e}_1$-direction. (b) Macroscopic volume fractions.

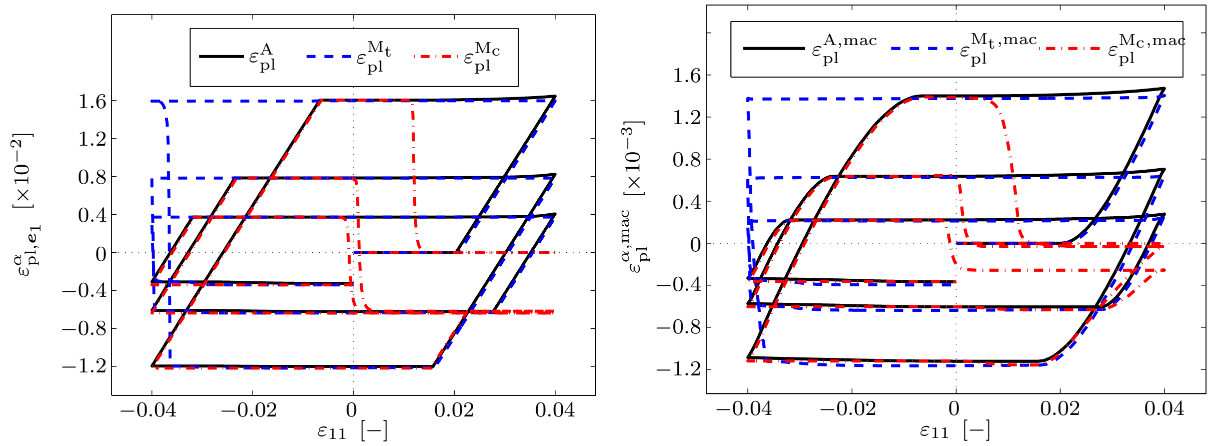

(c) Plastic strains in $\boldsymbol{e}_1$-direction. (d) Macroscopic plastic strains.

Figure 6.5: Three-dimensional SMA micro-sphere simulation with constitutive driver maintaining an uniaxial macroscopic stress state in $\boldsymbol{e}_1$-direction during all load steps. The results are obtained at $\theta = 20\,^{\circ}\mathrm{C}$ for 350 equally distributed micro-sphere integration directions for the load path provided in 6.4(a). Shown are the the internal variables in the direction of maximum load, (a) and (c), as well as the homogenised macroscopic variables in terms of volume fractions and plastic strains, (b) and (d), respectively.

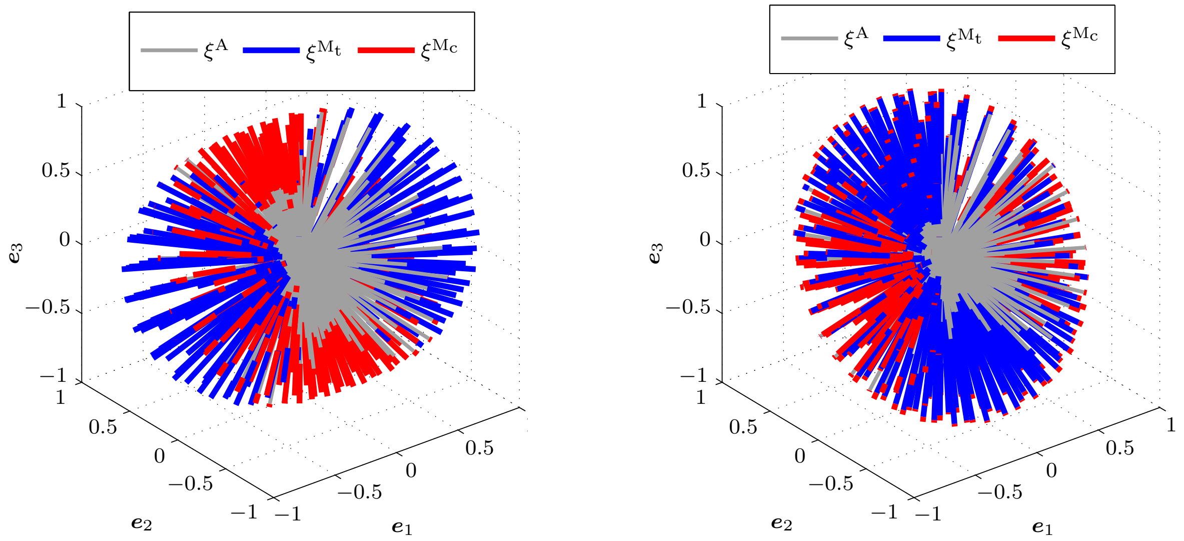

(a) Spatial distribution of volume fractions at maximum tension $\varepsilon_{11} = 0.04$, i.e. $t = T/4$, cf. Fig. 6.4(a).

(b) Spatial distribution of volume fractions at maximum compression $\varepsilon_{11} = -0.04$, i.e. $t = 3/4\,T$, cf. Fig. 6.4(a).

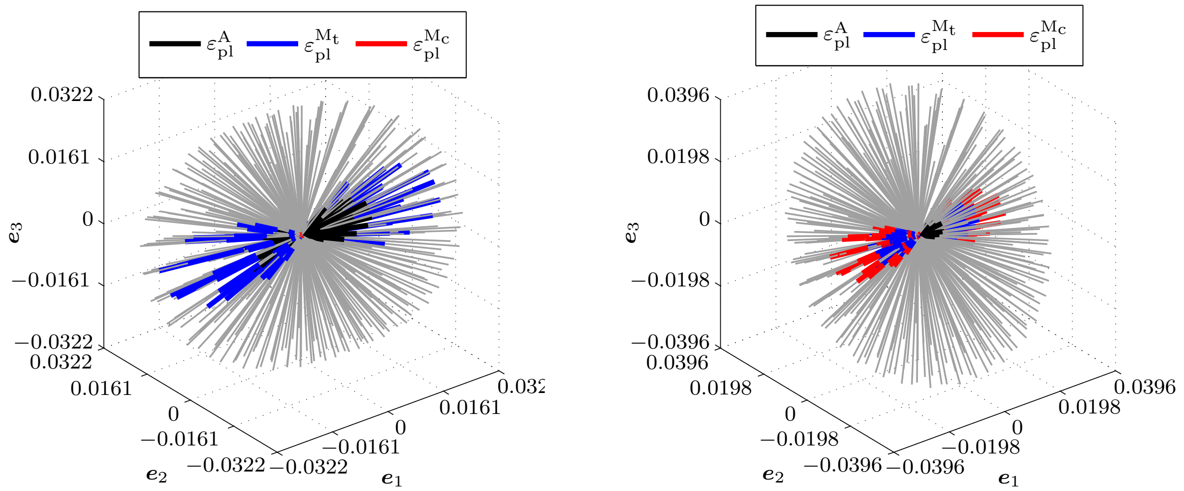

(c) Spatial distribution of plastic strains at maximum tension $\varepsilon_{11} = 0.04$, i.e. $t = T/4$, cf. Fig. 6.4(a).

(d) Spatial distribution of plastic strains at maximum compression $\varepsilon_{11} = -0.04$, i.e. $t = 3/4\,T$, cf. Fig. 6.4(a).

Figure 6.6: Three-dimensional SMA simulation with constitutive driver enforcing a uniaxial stress state: results in terms of the spatial distributions of volume fractions and plastic strains obtained at $\theta = 20\,^\circ\mathrm{C}$ for 350 equally distributed micro-sphere integration directions.

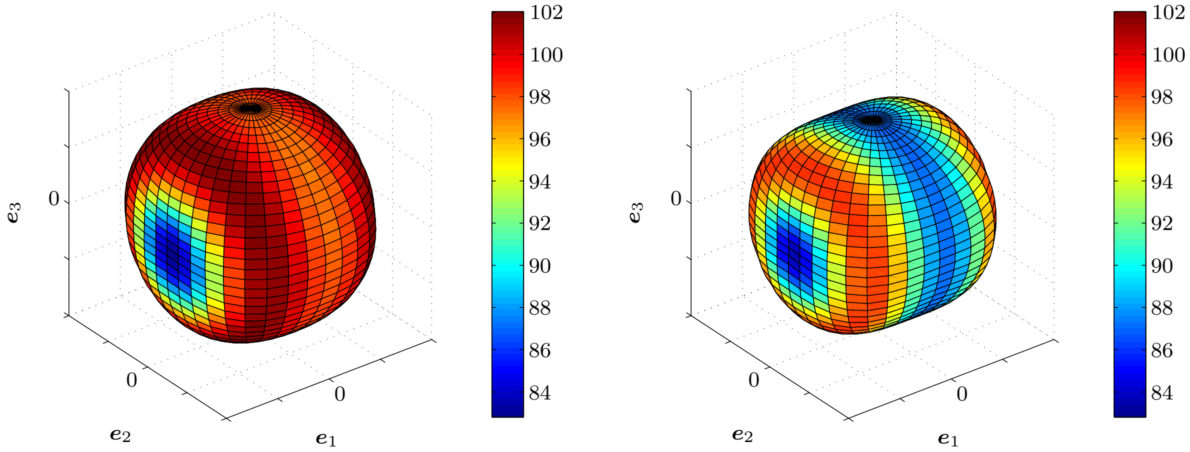

(a) Young's modulus surface plot $\mathsf{E}(\boldsymbol{d})$ [GPa] at maximum tension $\varepsilon_{11} = 0.04$, i.e. $t = T/4$, cf. Fig. 6.4(a).

(b) Young's modulus surface plot $\mathsf{E}(\boldsymbol{d})$ [GPa] at maximum compression $\varepsilon_{11} = -0.04$, i.e. $t = 3/4\,T$, cf. Fig. 6.4(a).

Figure 6.7: Three-dimensional SMA simulation with constitutive driver enforcing a uniaxial stress state: results in terms of the Young's modulus surface plot obtained at $\theta = 20\,°\mathrm{C}$ for 350 equally distributed micro-sphere integration directions.

by the constitutive driver. The spatial distribution of plastic strains in this material state is given in Fig. 6.6(d). It shows that the martensite compression phase has not only evolved, but also is subject to plastic strains. Moreover, the plastic strains in austenite and tensile martensite as obtained during the previously applied tensile load are still present to some extent. The Young's modulus surface plot depicted in Fig. 6.7(b) shows the significant elastic anisotropy obtained in the material's compression state.

6.3.4.2 Application to TRIP steel

For the simulation of TRIP steel at polycrystal level, we draw on the TRIP steel material parameters provided in Table 6.2. As boundary conditions, we choose a tension-compression loading path with a maximum strain magnitude of $\varepsilon_{11} = 0.04$ where we start with a purely austenitic initial state, i.e. $\xi^{\mathrm{A}}|_{t_0} = 1$, thus $\xi^{\mathrm{M_t}}|_{t_0} = \xi^{\mathrm{M_c}}|_{t_0} = 0$. As in the SMA simulation provided in Section 6.3.4.1, we investigate the material behaviour at a room temperature of $\theta = 20\,°\mathrm{C}$. The constitutive routine is embedded in a constitutive driver for the simulation of uniaxial stress states corresponding to experimental tensile tests.

In addition to the loading path applied, see Fig. 6.8(a), we show the obtained uniaxial stress response in Fig. 6.8(b), a visualisation of the plastic strains evolving in the direction of maximum load, i.e. the $\boldsymbol{e}_1$-direction, during the load cycles—cf. Fig. 6.8(c)—and the evolution of macroscopic volume fractions as provided in Fig. 6.8(d). The uniaxial stress response shows that the macroscopic mechanical hardening effect typically observed for TRIP steels is captured by the modelling framework. For an increased number

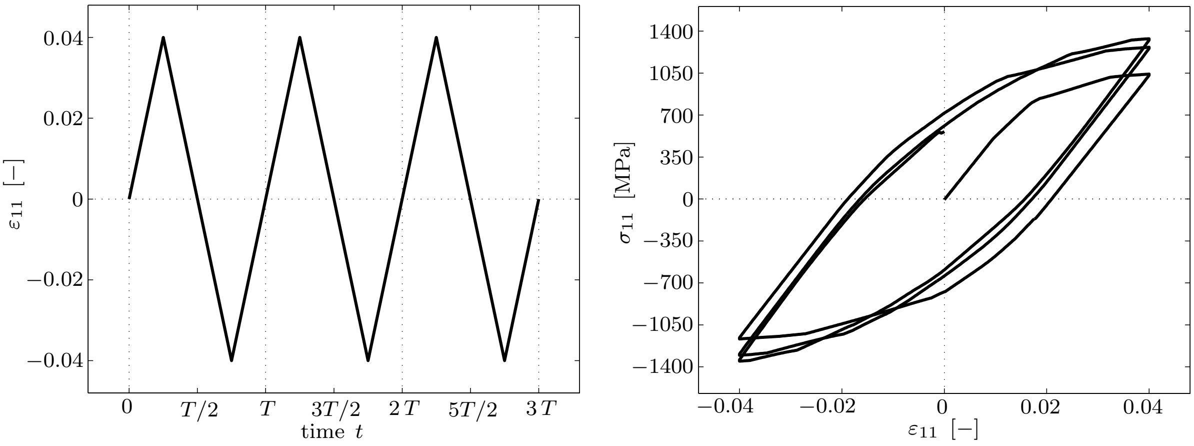

(a) Loading path prescribed in $\boldsymbol{e}_1$-direction.

(b) Uniaxial stress-strain response.

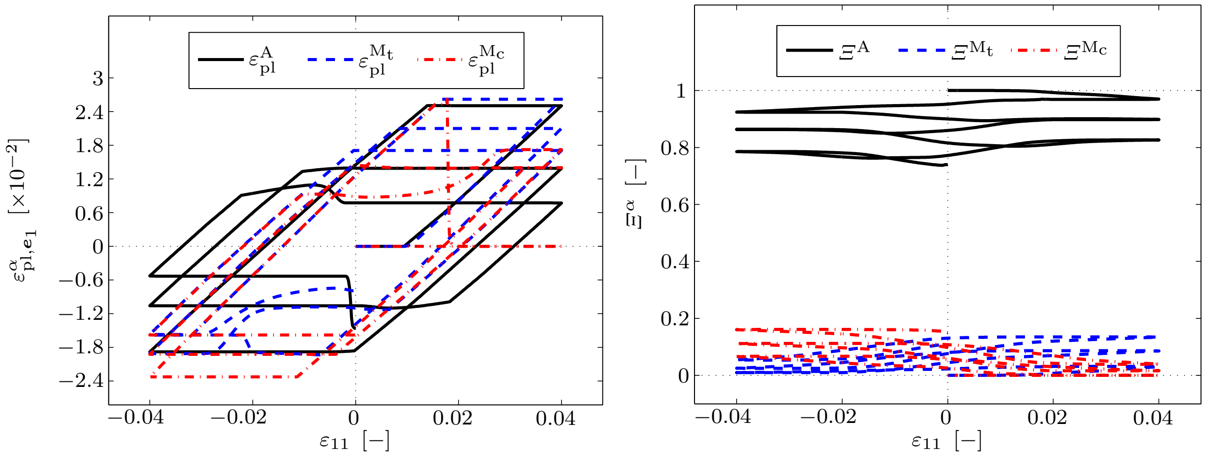

(c) Plastic strains in $\boldsymbol{e}_1$-direction.

(d) Macroscopic volume fractions.

Figure 6.8: Three-dimensional TRIP steel micro-sphere simulation with constitutive driver maintaining an uniaxial macroscopic stress state in $\boldsymbol{e}_1$-direction during all load steps. The results are obtained at $\theta = 20\,°\mathrm{C}$ for 350 equally distributed micro-sphere integration directions. Shown are the obtained uniaxial macroscopic stress response (b), the evolution of plastic strains in the direction of maximum load (c) and the evolution of the homogenised macroscopic volume fractions (d).

of tensile-compression load cycles, the obtained maximum and minimum stress values increase by magnitude, coinciding with the experimental results depicted in Fig. 1.5. Physically speaking, this effect results from the accumulation of plastic strains—or rather dislocations—within the material. Note that we consider isotropic strain hardening to model the hardening behaviour, thus the non-linearities in the evolution of plastic strains that are observed in Fig. 6.8(c) result from the application of the plasticity inheritance framework that we introduced in Section 6.2.

The obtained evolution of macroscopic volume fractions depicted in Fig. 6.8(d) is significantly different from the evolution of volume fractions observed for SMA, cf. Fig. 6.5(b). In the case of TRIP steel, the simulation results show that the transformation is less intense but accumulates with the number of tension-compression loading cycles. For a larger amount of cycles, we observe saturation effects, i.e. the accumulation of the martensite variants continues up to a certain level. Both effects predicted by the model, i.e. the accumulation of the martensitic volume fractions with a growing number of cycles as well as the saturation effect, are in line with experimental results reported in the literature for multi-cyclic TRIP steel responses as presented in, e.g., [48, 136].

Figures 6.9 and 6.10 visualise the internal state of the simulated TRIP steel polycrystal at two representative loading states: the state of maximum tension $\varepsilon_{11} = 0.04$ obtained at $t = T/4$, and the state of maximum compression $\varepsilon_{11} = -0.04$ at $t = 3/4\,T$, cf. Fig. 6.8(a). For both states, we show the spatial distribution of volume fractions and the spatial distribution of plastic strains within the polycrystal, as well as a Young's modulus surface plot which gives insight into the elastic anisotropy evolution.

The spatial distribution of volume fractions obtained for TRIP steel at the $\varepsilon_{11} = 0.04$ tensile state is depicted in Fig. 6.9(a). The figure shows that only a small amount of austenite transforms to the martensitic tensile variant in the first tensile cycle as suggested by the small amount of macroscopic martensitic volume fraction observed in Fig. 6.8(d). The transformations take place in a relatively wide cone around the tensile axis. As the load reverses and the state of maximum compression is reached at $\varepsilon_{11} = -0.04$, the martensitic compression variant evolves, cf. Fig. 6.9(b). A comparison with Figs. 6.6(a) and 6.6(b) shows that the phase-transformations observed for TRIP steel are significantly less intense than those observed for SMA.

However, for TRIP steel the plasticity effects are more pronounced as highlighted in Figs. 6.9(c) and 6.9(d). The spatial distribution of plastic strains in the tensile state provided in Fig. 6.9(c) shows the evolution of plasticity to take place in a cone around the tensile axis. Note that the plastic strains shown for the martensitic tensile phase correspond to the small martensitic volume fractions given in Fig. 6.9(a), i.e. the overall constitutive response of the TRIP steel polycrystal is mainly governed by the austenitic volume fraction and the plastic strains therein. As the load reverses and the compression load state is reached, cf. Fig. 6.9(d), the constitutive driver leads to positive lateral deformation of the crystal. In contrast to the distribution of plastic strains in SMA, see Fig. 6.6(d), in the case of TRIP steel we observe plasticity in the lateral direction as well.

The Young's modulus surface plots displayed in Figs. 6.10(a) and 6.10(b) visualise how the elastic anisotropy of the polycrystal evolves. The initially isotropic austenitic crystal shows only small amounts of anisotropy in the loading directions in the first tensile state as depicted in Fig. 6.10(a). As the load reverses and the compression state of the material is reached, the elastic anisotropy becomes more pronounced as provided in Fig. 6.10(b).

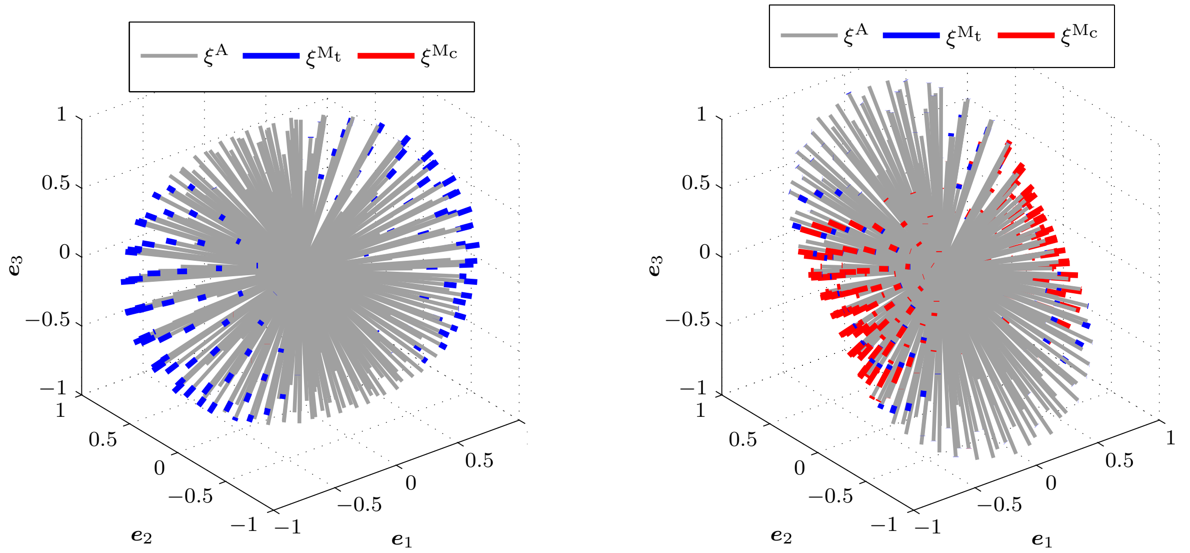

(a) Spatial distribution of volume fractions at maximum tension $\varepsilon_{11} = 0.04$, i.e. $t = T/4$, cf. Fig. 6.8(a).

(b) Spatial distribution of volume fractions at maximum compression $\varepsilon_{11} = -0.04$, i.e. $t = 3/4\,T$, cf. Fig. 6.8(a).

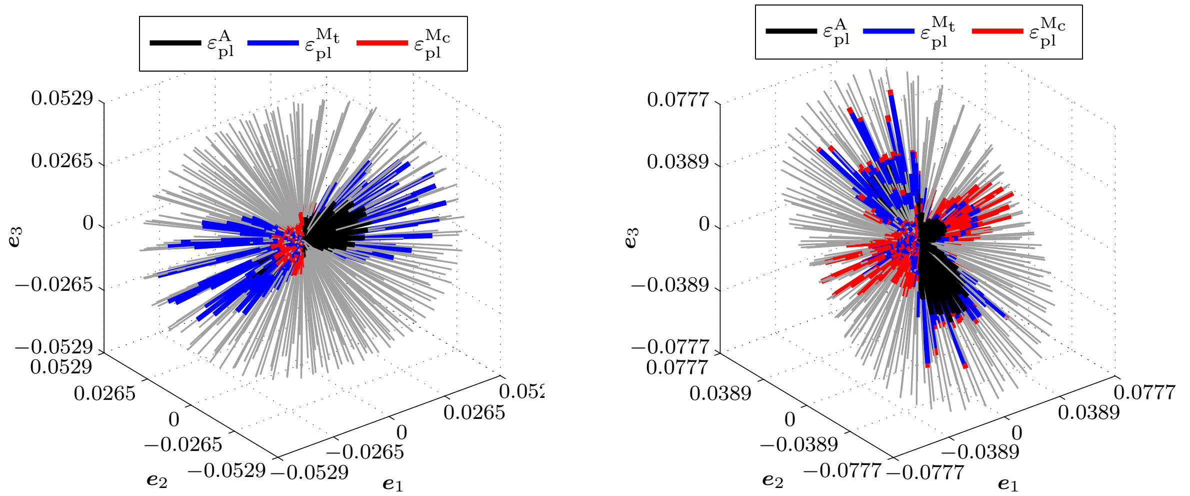

(c) Spatial distribution of plastic strains at maximum tension $\varepsilon_{11} = 0.04$, i.e. $t = T/4$, cf. Fig. 6.8(a).

(d) Spatial distribution of plastic strains at maximum compression $\varepsilon_{11} = -0.04$, i.e. $t = 3/4\,T$, cf. Fig. 6.8(a).

Figure 6.9: Three-dimensional TRIP steel simulation with constitutive driver enforcing a uniaxial stress state: results in terms of spatial distributions of volume fractions and plastic strains obtained at $\theta = 20\,^{\circ}\mathrm{C}$ for 350 equally distributed micro-sphere integration directions.

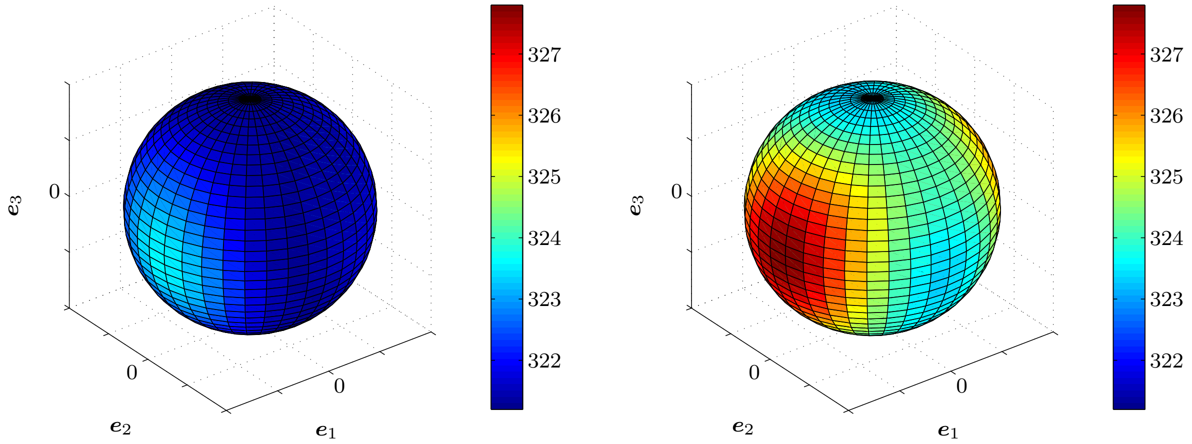

(a) Young's modulus surface plot $\mathsf{E}(\boldsymbol{d})$ [GPa] at maximum tension $\varepsilon_{11} = 0.04$, i.e. $t = T/4$, cf. Fig. 6.8(a).

(b) Young's modulus surface plot $\mathsf{E}(\boldsymbol{d})$ [GPa] at maximum compression $\varepsilon_{11} = -0.04$, i.e. $t = 3/4\,T$, cf. Fig. 6.8(a).

Figure 6.10: Three-dimensional TRIP steel simulation with constitutive driver enforcing a uniaxial stress state: results in terms of Young's modulus surface plots obtained at $\theta = 20\,°\mathrm{C}$ for 350 equally distributed micro-sphere integration directions.

6.3.5 Sensitivity of the macroscopic constitutive response with respect to the underlying micro-sphere integration scheme

In this section, we show to what extent the constitutive response of the model depends on the micro-sphere integration scheme used. This is important in view of choosing an efficient, yet sufficiently accurate micro-sphere integration scheme for the later finite element application presented in Section 6.4.

In order to emphasise the dependencies of the constitutive response of the polycrystal on the numerical integration scheme used, we carry out computations with four different micro-sphere integration schemes as depicted in Fig. 6.11. The most efficient scheme we consider makes use of $n_r = 21$ integration directions specifically distributed on only one hemisphere, see Fig. 6.11(d). This scheme is applicable due to symmetry considerations and has been frequently used in the literature [17, 75, 92].

The highest-order scheme we consider accounts for $n_r = 1000$ spatial integration directions equally distributed on the unit sphere, see Fig. 6.11(a). Apart from this scheme, we consider schemes with $n_r = 350$ and $n_r = 100$ equally distributed integration directions, cf. Figs. 6.11(b) and 6.11(c), respectively. For these schemes, the weighting factors introduced in Section 3.2.1.2 are given by $\bar{w}_i = 1/n_r$. Note that these schemes are computationally not efficient as they do not take advantage of the hemisphere symmetry. However, in this section we focus on the numerical accuracy instead of computational efficiency. As schemes with equally distributed integration directions for the unit sphere are straightforward to generate and the integration weights take a simple form, we will consider these schemes for simplicity. Note that the computational effort for the evaluation of the constitutive response at the local level scales approximately linearly with the number of micro-sphere integration directions considered. The required storage space for the state-dependent variables—i.e. volume fractions, plastic strains, and hardening variables for each phase in each integration direction—accumulates to $3 \times \nu \times n_r$ variables. For example, for the three-phase material evaluated with $n_r = 1000$ integration directions, we have to store $3 \times 3 \times 1000$ independent scalar state variables.

Representative results of the sensitivity analysis are presented in Fig. 6.12. In Figs. 6.12(a), 6.12(c), and 6.12(e) we show the evolution of the axial stress component $\sigma_{11}^{(n_r)}$, the macroscopic austenitic volume fraction $\Xi^{\mathrm{A}(n_r)}$ and the macroscopic plastic strains in austenite $\varepsilon_{\mathrm{pl}}^{\alpha,\mathrm{mac}(n_r)}$, respectively, for the different micro-sphere integration schemes considered. Moreover, we evaluate relative deviations of the named quantities by relating them to the results obtained for the $n_r = 1000$ scheme in Figs. 6.12(b), 6.12(d), and 6.12(f).

The main result of the sensitivity study is that the deviations between the $n_r = 100$, $n_r = 350$ and $n_r = 1000$ integration schemes are on average below 1 % for the uniaxial stress response and the macroscopic austenitic volume fraction as presented in Figs. 6.12(b) and 6.12(d). Here and in the following, the relative deviation $\Delta\bullet(t)$ of a time-dependent quantity $\bullet(t)$ obtained for one integration scheme, say i_1, with respect to another scheme, say i_2, is computed from

$$\Delta\bullet^{(i_1)}(t) := \left[\bullet^{(i_1)}(t) - \bullet^{(i_2)}(t)\right] / \max_{\tau\in[0,\,t_{\max}]} \left(\left|\,\bullet^{(i_2)}\,(\tau)\right|\right) \quad . \tag{6.69}$$

For the macroscopic plastic strains in austenite an error that accumulates over several load cycles is observed for the $n_r = 350$ scheme, see Fig. 6.12(f). However, in view of the finite element implementation to be carried out at a later stage, we are especially interested in the numerical reliability of the efficient $n_r = 21$ scheme. Note that this scheme is—in view of the computational effort—about 50 times as efficient as the $n_r = 1000$ scheme and still about 5 times as efficient as the $n_r = 100$ scheme.

The sensitivity analysis also shows that the $n_r = 21$ scheme over-estimates the stress magnitude both during the tensile cycle and during the compression cycle, see Fig. 6.12(b). Interestingly, the deviation of the stress response $\sigma_{11}^{(21)}$ obtained at the end of a load cycle, e.g. at $t = T$, is smaller than 1 %. Moreover, with a growing number of cycles, the effect of the stress over-estimation becomes less significant. As Fig. 6.12(d) shows, the macroscopic austenitic volume fraction is under-estimated by the $n_r = 21$ scheme by about 2.5 % in average. However, the most significant numerical deviation is observed for the plastic strains. Fig. 6.12(f) suggests an under-estimation of plasticity in the tensile regime and an over-estimation in the compression regime. The maximum deviation of the $n_r = 21$ scheme with respect to the results obtained for the $n_r = 1000$ reference scheme reaches up to 30 % in this case. The reason is that the plasticity evolving in a cone-like surrounding of the loading axis is not captured accurately for the given load case since plasticity is triggered only in one integration direction when using the $n_r = 21$ scheme in combination with a tensile load in $\boldsymbol{e}_1$-direction as briefly summarised in Fig. 6.13.

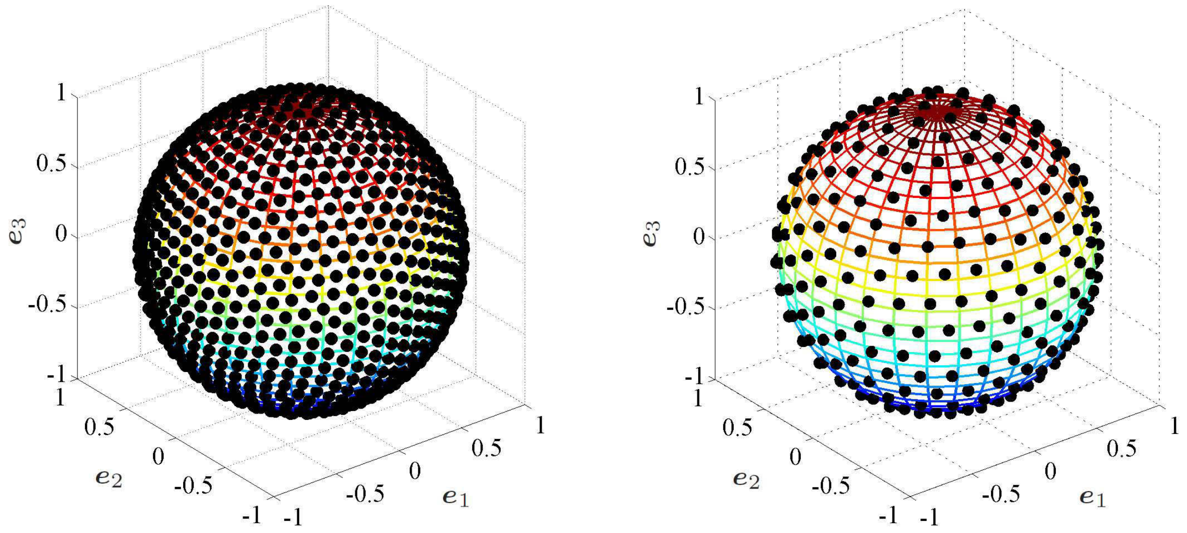

(a) 1000 homogeneously distributed integration directions.

(b) 350 homogeneously distributed integration directions.

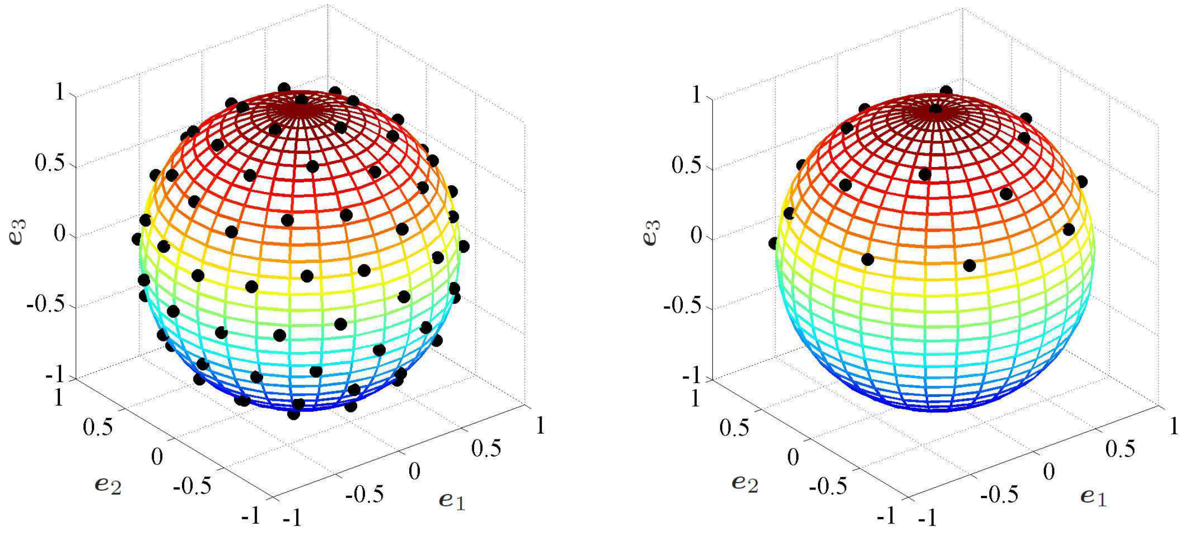

(c) 100 homogeneously distributed integration directions.

(d) 21 integration directions distributed only on one hemisphere.

Figure 6.11: Micro-sphere integration schemes utilised for assessing the numerical sensitivity of the macroscopic constitutive response with respect to the underlying micro-sphere scheme, where the computational effort required for the evaluation of the constitutive response scales linearly with the number of micro-sphere integration directions used. The scheme shown in (d) is applicable since $\varepsilon_{\text{dev}}(\boldsymbol{r}_i) = \varepsilon_{\text{dev}}(-\boldsymbol{r}_i)$ and $\varepsilon_{\text{vol}} \neq f(\boldsymbol{r}_i)$, see Section 6.3.1. Use of this symmetry relation between both hemispheres facilitates the efficient numerical evaluation of the constitutive response.

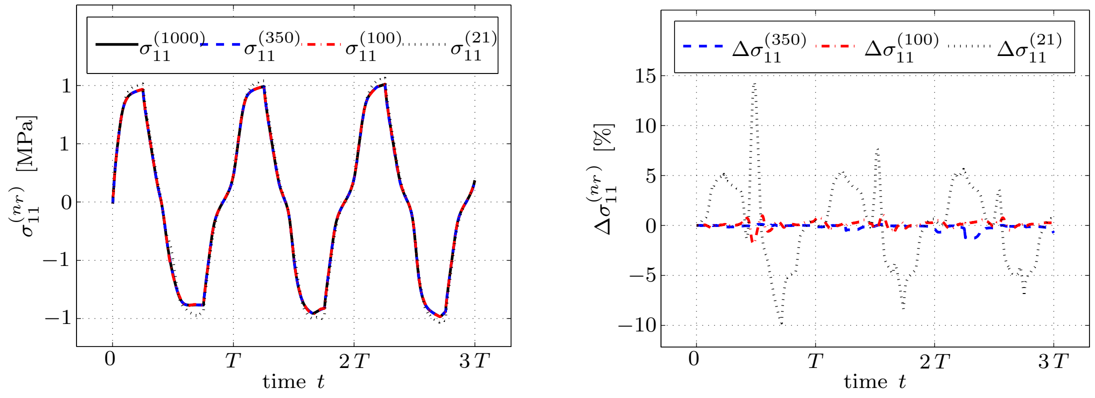

(a) Uniaxial cyclic stress responses.

(b) Relative deviation of the cyclic stress responses w.r.t. the $n_r = 1000$ scheme.

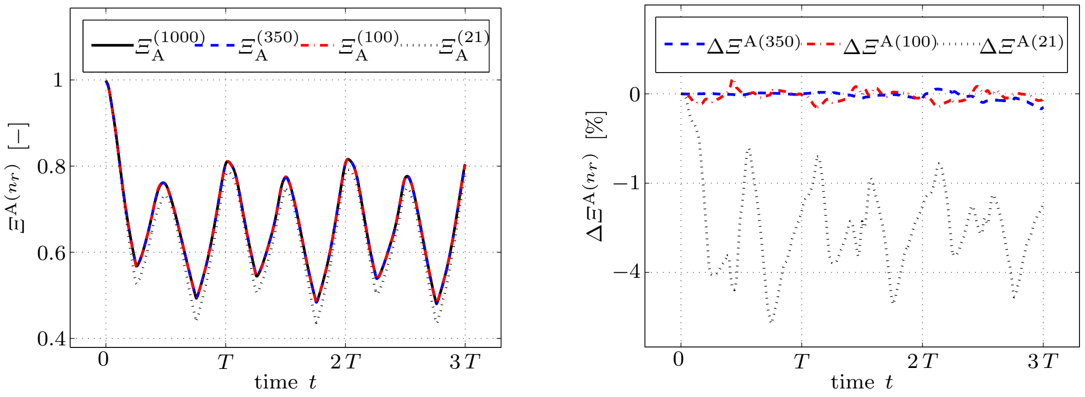

(c) Evolution of the macroscopic austenitic volume fraction.

(d) Relative deviation of the macroscopic austenitic volume fraction w.r.t. the $n_r = 1000$ scheme.

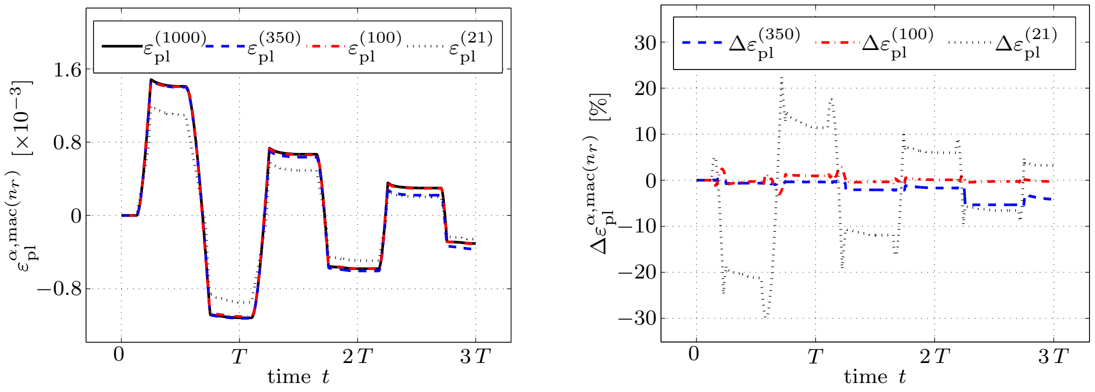

(e) Evolution of macroscopic plastic strains in austenite.

(f) Relative deviation of the macroscopic plastic strains in austenite w.r.t. the $n_r = 1000$ scheme.

Figure 6.12: Macroscopic material response in terms of uniaxial stress σ_{11} (a), evolution of austenite Ξ^{A} (c), and evolution of macroscopic plasticity in austenite $\varepsilon_{\mathrm{pl}}^{\alpha,\mathrm{mac}}$ (e) for the four different micro-sphere integration schemes provided in Fig. 6.11. The simulation setup is the same as in Fig. 6.4 with the loadpath given in Fig. 6.4(a). The relative differences, (b), (d), and (f), are computed with respect to the results obtained for the highest-order scheme, i.e. $n_r = 1000$.

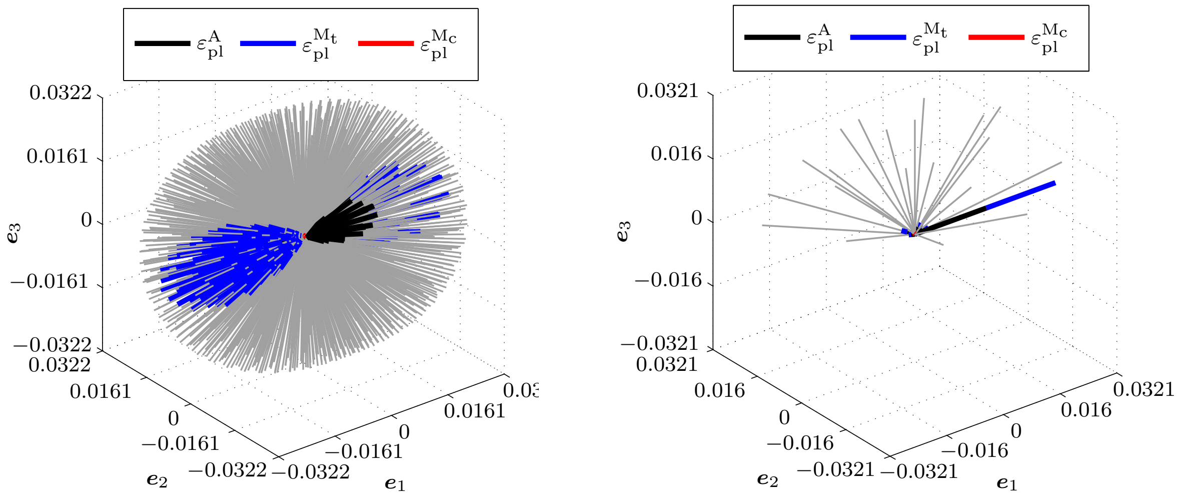

(a) Spatial distribution of plastic strains at maximum tension, i.e. $t = T/4$, cf. Fig. 6.4(a), obtained for $n_r = 1000$ micro-sphere integration directions.

(b) Spatial distribution of plastic strains at maximum tension, i.e. $t = T/4$, cf. Fig. 6.4(a), obtained for $n_r = 21$ micro-sphere integration directions.

Figure 6.13: The sensitivity of the macroscopic plastic strains with respect to the micro-sphere integration scheme, cf. Fig. 6.12(f), results from the fact that plasticity is activated in a cone-like surrounding of the loading axis, i.e. the $\boldsymbol{e}_1$-axis (a) where, in the case of the reduced integration scheme with $n_r = 21$ spatial integration directions, plasticity is captured in only one integration direction for the specific tensile load case chosen (b).

6.4 Finite element implementation

As a test specimen for the investigation of inhomogeneous load cases we choose a plate of the size $4 \times 4 \times 1$ mm with a central hole with a diameter of 2 mm. For the finite element discretisation we use a mesh of 768 hexahedral elements. We apply Dirichlet boundary conditions to the $y = -2$ and $y = 2$ face of the body, where the $y = -2$ face is chosen to be spatially fixed such that $u_x|_{y=-2} = u_y|_{y=-2} = u_z|_{y=-2} = 0$ and the $y = 2$ face is loaded in terms of prescribed nodal displacements, $u_y|_{y=2} = u$. We investigate both tension and shear of the plate with hole as load cases for both material types considered in this work, i.e. for both SMA and TRIP steel. The obtained nodal displacement fields of the test specimen at maximum load for tension and shear are shown in Figs. 6.15(a) and 6.17(a), respectively.

For the tension test, we apply a macroscopic tensile displacement of $u_{\max} = 0.2$ mm to the specimen of 4 mm of length, corresponding to a macroscopic strain of 5 %. The obtained macroscopic reaction forces are presented in Figs. 6.14(a) and 6.14(b) for both materials considered. Note that the maximum tensile force for SMA reaches up to $F_{y,\max} = 250$ N, Fig. 6.14(a), whereas the maximum tensile force for TRIP steel reaches $F_{y,\max} = 1500$ N, Fig. 6.14(b). After the maximum tensile load is applied, the load is reversed until the tensile force F_y reaches zero value. The figures show that the macroscopic tensile deformation that remains after reversal of the tensile load is higher for the TRIP steel. The detailed results in terms of contour plots of strain, stress, volume fractions and plastic strains obtained at the state of maximum tension are presented in Section 6.4.1 for SMA and in Section 6.4.2 for TRIP steel. Comparison of Figs. 6.15(c) and 6.16(c) shows that the maximum tensile stress for SMA is $\sigma_{yy,\max} = 273\,\text{MPa}$, whereas for TRIP steel material parameters a maximum tensile stress value of $\sigma_{yy,\max} = 1591.7\,\text{MPa}$ is obtained for a macroscopic specimen strain of $5\,\%$. For SMA, the austenitic parent phase is reduced to up to $30\,\%$, see Fig. 6.15(d), whereas for TRIP steel the volume fraction of the parent phase does not come below $91.6\,\%$, cf. Fig. 6.16(d). Due to the more pronounced transformation behaviour of SMA already highlighted in Section 6.3.4, both the macroscopic martensitic tensile and compression phases evolve as depicted in Figs. 6.15(e) and 6.15(f). In contrast, for TRIP steel mainly the martensitic tensile phase evolves, cf. Figs. 6.16(e) and 6.16(f). Moreover, comparison of Figs. 6.15(h) and 6.15(i) with Figs. 6.16(h) and 6.16(i) shows that the TRIP steel simulation predicts a more pronounced evolution of plastic strains especially in the martensitic phases.

The shear test is conducted with a maximum shear displacement of $u_{\max} = 0.2\,\text{mm}$ applied to the loaded face, corresponding to a macroscopic shear angle of $\tau_{\max} = 0.05$. Figs. 6.14(c) and 6.14(d) show the macroscopic reaction forces obtained during one complete shear cycle, i.e. increase of the shear angle up to the maximum value of $\tau_{\max} = 0.05$, then reversal of the shear displacement until $\tau_{\min} = -0.05$ is reached, and finally deformation of the specimen back into its original shape. The obtained maximum macroscopic shear force F_x takes a value of $F_{x,\max} = 100\,\text{N}$ for SMA, see Fig. 6.14(c), and $F_{x,\max} = 500\,\text{N}$ for TRIP steel, see Fig. 6.14(d). The detailed shear test results in terms of contour plots of strain, stress, volume fractions and plastic strains are given in Section 6.4.3 for SMA and in Section 6.4.4 for TRIP steel each at the state of maximum shear. The maximum shear stress obtained for SMA is $\sigma_{xy,\max} = 129.17\,\text{MPa}$, whereas for TRIP steel the maximum shear stress reaches $\sigma_{xy,\max} = 520\,\text{MPa}$, see Figs. 6.17(c) and 6.18(c), respectively. Moreover, in line with the results previously obtained in this work, the phase-transformations are more intense for SMA, compare Figs. 6.17(d) and 6.18(d). In contrast, for the TRIP steel simulations a more pronounced evolution of plastic strains is observed especially in martensite, compare Figs. 6.17(h) and 6.17(i) with Figs. 6.18(h) and 6.18(i), respectively.

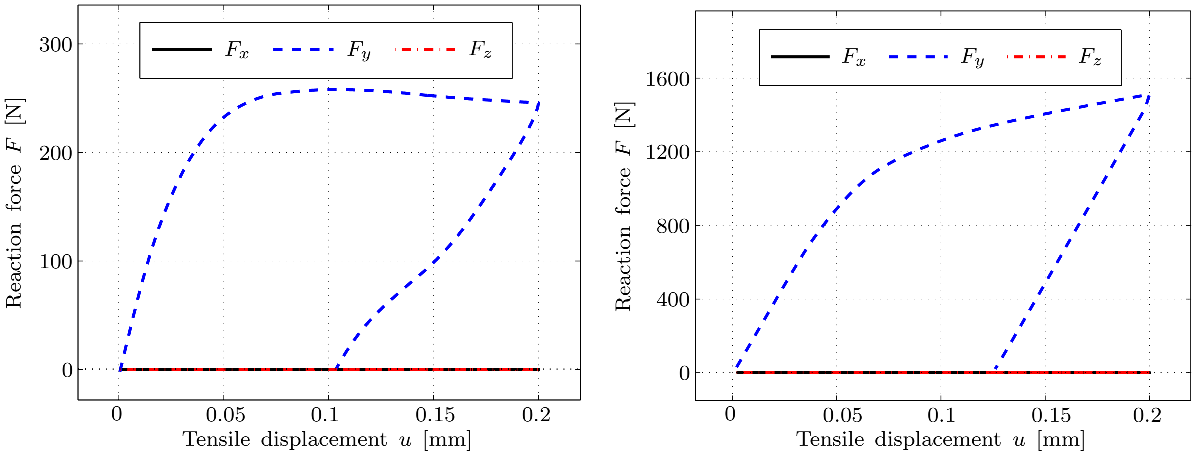

(a) SMA – tensile reaction force. (b) TRIP steel – tensile reaction force.

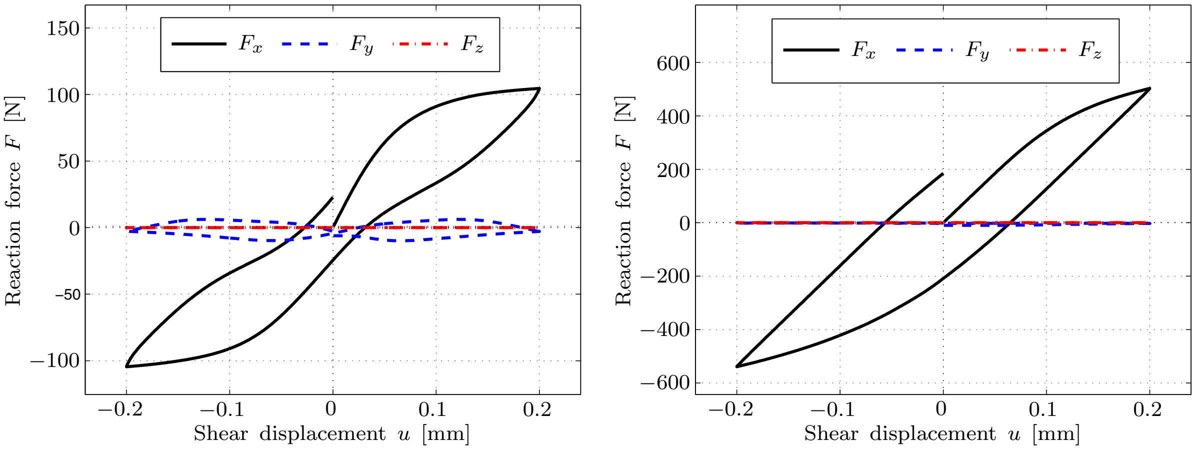

(c) SMA – shear reaction force. (d) TRIP steel – shear reaction force.

Figure 6.14: Macroscopic mechanical response of the test specimen obtained for SMA and TRIP steel for both tensile and shear tests. Shown are the macroscopic reaction force components F_x, F_y, and F_z for SMA under tension (a), TRIP under tension (b), SMA under shear (c), and TRIP under shear (d). The maximum tensile displacement corresponds to a macroscopic tensile strain of $5\,\%$, whereas the maximum shear displacement corresponds to a macroscopic shear angle of $\tau_{\max} = 0.05$ of the specimen.

6.4.1 Plate with hole under tension – SMA

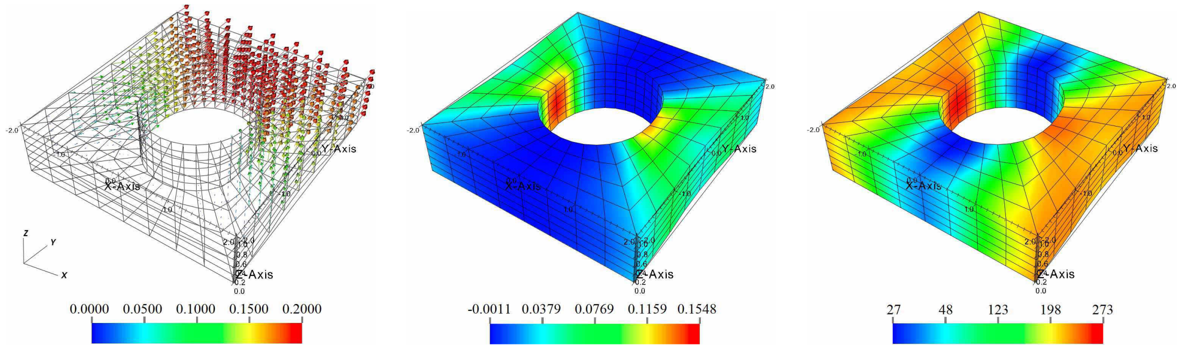
0.0000 0.0500 0.1000 0.1500 0.2000
-0.0011 0.0379 0.0769 0.1159 0.1548
27 48 123 198 273
X-Axis
Y-Axis
Z-Axis

(a) Displacement field $\boldsymbol{u}$ [mm]. (b) Tensile strain ε_{yy} [–]. (c) Tensile stress σ_{yy} [MPa].

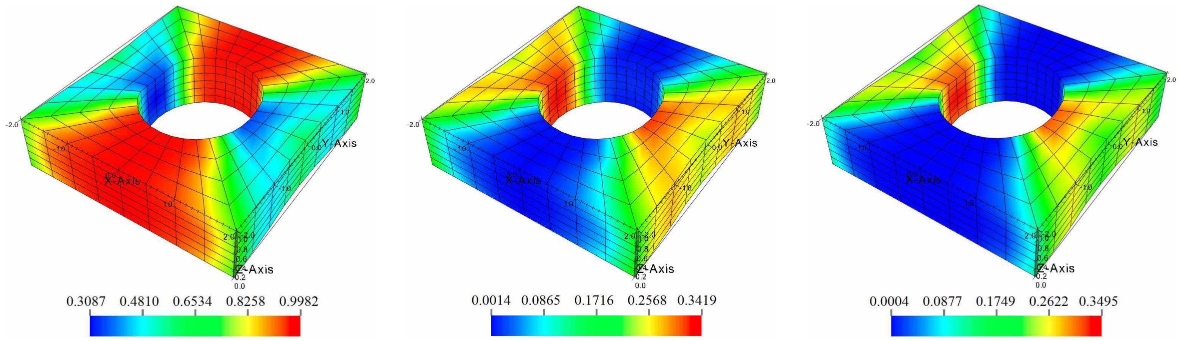
0.3087 0.4810 0.6534 0.8258 0.9982
0.0014 0.0865 0.1716 0.2568 0.3419
0.0004 0.0877 0.1749 0.2622 0.3495
X-Axis
Y-Axis
Z-Axis

(d) Austenite Ξ^{A} [–]. (e) Tensile martensite $\Xi^{\mathrm{M_t}}$ [–]. (f) Compression martensite $\Xi^{\mathrm{M_c}}$ [–].

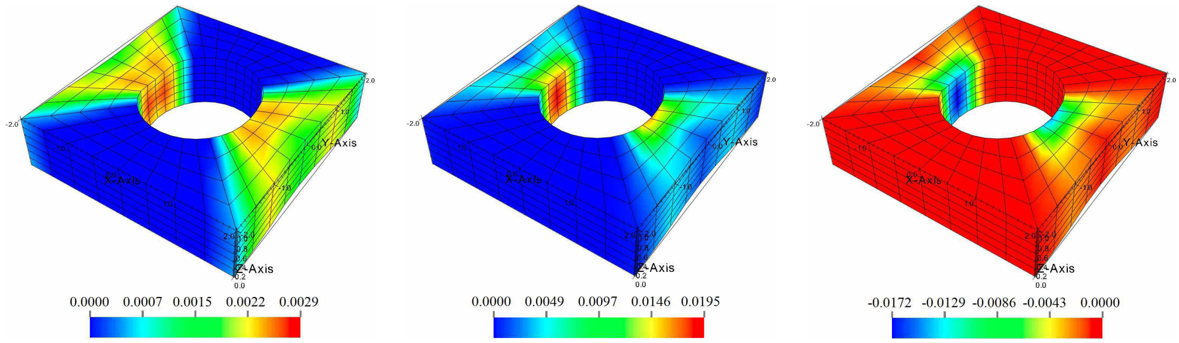
0.0000 0.0007 0.0015 0.0022 0.0029
0.0000 0.0049 0.0097 0.0146 0.0195
-0.0172 -0.0129 -0.0086 -0.0043 0.0000
X-Axis
Y-Axis
Z-Axis

(g) Austenite plasticity $\varepsilon_{\mathrm{pl}}^{\mathrm{A,mac}}$ [–]. (h) Plasticity in martensite tensile phase $\varepsilon_{\mathrm{pl}}^{\mathrm{M_t,mac}}$ [–]. (i) Plasticity in martensite compression phase $\varepsilon_{\mathrm{pl}}^{\mathrm{M_c,mac}}$ [–].

Figure 6.15: SMA – finite element simulation of a plate with hole under tension. The results depicted are obtained for the state of maximum tension, cf. Fig. 6.14(a). The displacement field (a) shows the loading direction, (b) and (c) show the resulting strains and stresses in tensile direction, respectively. In the region of maximum tension, the austenitic volume fraction is reduced to 30 % (d), corresponding to the evolution of the martensitic tensile and compression phase, (e) and (f), respectively. The obtained distributions of macroscopic plastic strains are displayed in (g), (h), and (i).

6.4.2 Plate with hole under tension – TRIP steel

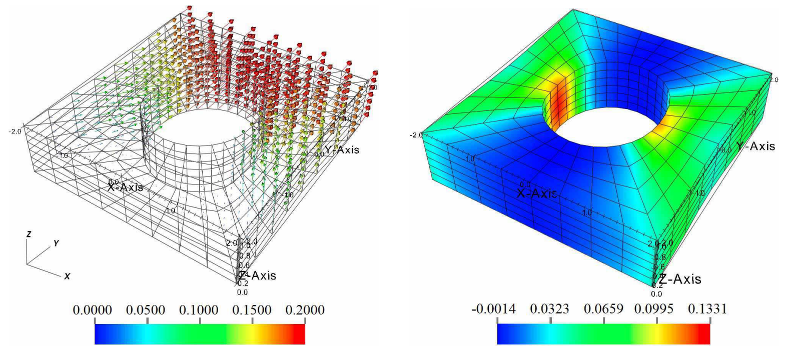
X-Axis
Y-Axis
Z-Axis
0.0000 0.0500 0.1000 0.1500 0.2000
-0.0014 0.0323 0.0659 0.0995 0.1331
84,5 334,5 753,5 1172,5 1591,7

(a) Displacement field $\boldsymbol{u}$ [mm]. (b) Tensile strain ε_{yy} [–]. (c) Tensile stress σ_{yy} [MPa].

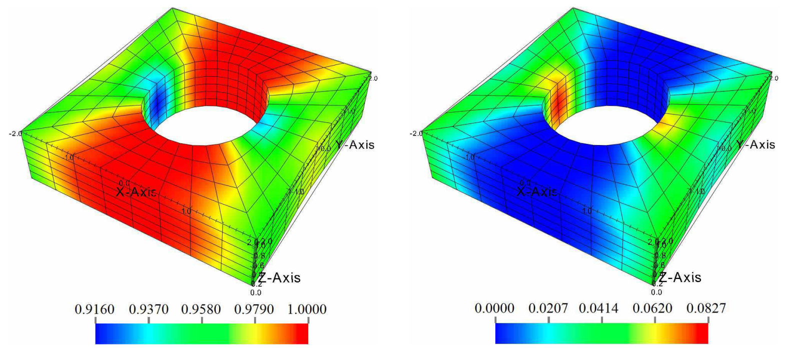
X-Axis
Y-Axis
Z-Axis
0.9160 0.9370 0.9580 0.9790 1.0000
0.0000 0.0207 0.0414 0.0620 0.0827
0.0000 0.0007 0.0014 0.0020 0.0027

(d) Austenite $\varXi^{\mathrm{A}}$ [–]. (e) Tensile martensite $\varXi^{\mathrm{M_t}}$ [–]. (f) Compression martensite $\varXi^{\mathrm{M_c}}$ [–].

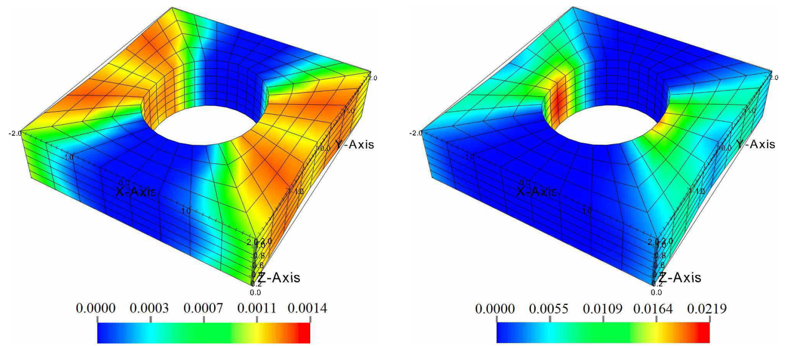
X-Axis
Y-Axis
Z-Axis
0.0000 0.0003 0.0007 0.0011 0.0014
0.0000 0.0055 0.0109 0.0164 0.0219
-0.0345 -0.0259 -0.0173 -0.0086 0.0000

(g) Austenite plasticity $\varepsilon_{\mathrm{pl}}^{\mathrm{A,mac}}$ [–]. (h) Plasticity in martensite tensile phase $\varepsilon_{\mathrm{pl}}^{\mathrm{M_t,mac}}$ [–]. (i) Plasticity in martensite compression phase $\varepsilon_{\mathrm{pl}}^{\mathrm{M_c,mac}}$ [–].

Figure 6.16: TRIP steel – finite element simulation of a plate with hole under tension. The results depicted are obtained for the state of maximum tension, cf. Fig. 6.14(b). The displacement field (a) shows the loading direction, (b) and (c) show the resulting strains and stresses in tensile direction, respectively. In the region of maximum tension, the austenitic volume fraction is reduced to 91.6 % (d), corresponding to the evolution of the martensitic tensile and compression phase, (e) and (f), respectively. The obtained distributions of macroscopic plastic strains are given in (g), (h), and (i).

6.4.3 Plate with hole under shear deformation – SMA

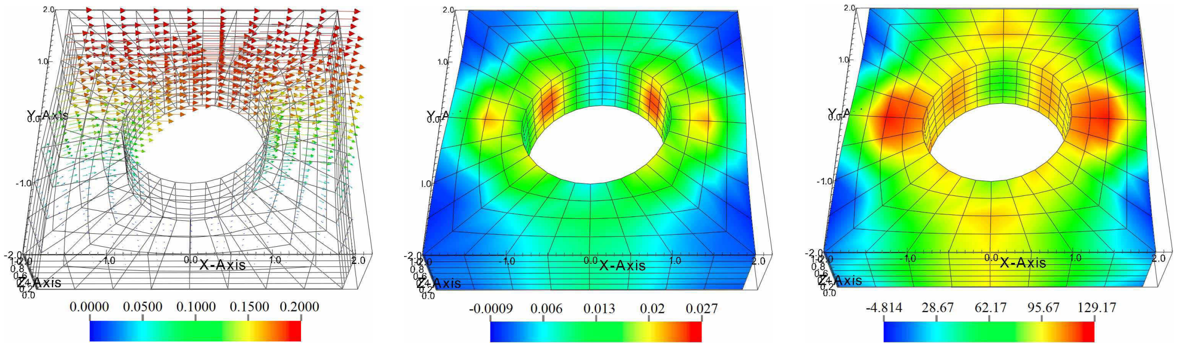

(a) Displacement field $\boldsymbol{u}$ [mm]. (b) In-plane shear strain ε_{xy} [–]. (c) In-plane shear stress σ_{xy} [MPa].

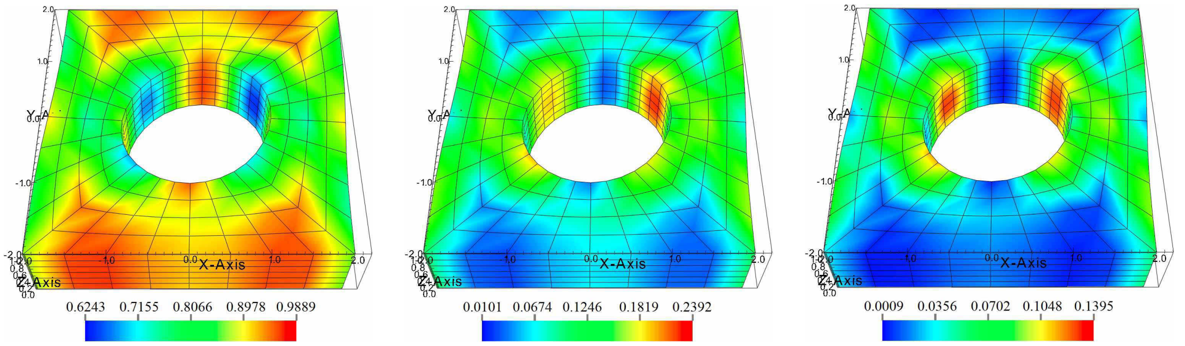

(d) Austenite Ξ^{A} [–]. (e) Tensile martensite $\Xi^{\mathrm{M_t}}$ [–]. (f) Compression martensite $\Xi^{\mathrm{M_c}}$ [–].

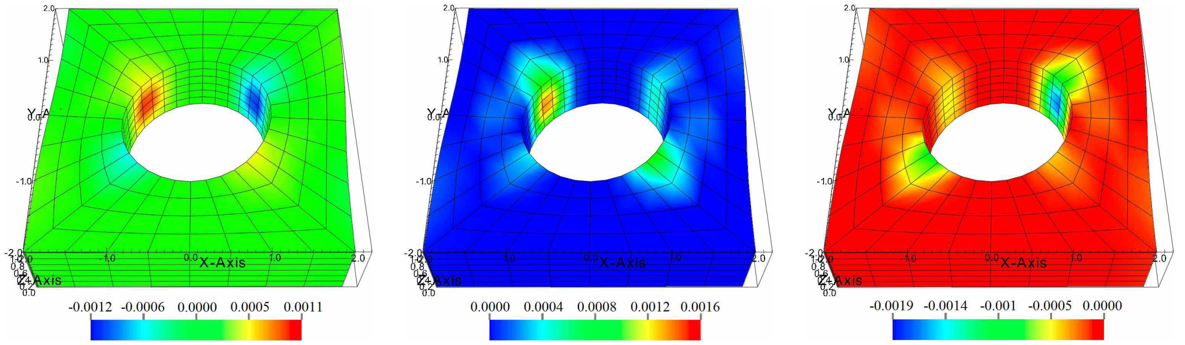

(g) Austenite plasticity $\varepsilon_{\mathrm{pl}}^{\mathrm{A,mac}}$ [–]. (h) Plasticity in martensite tensile phase $\varepsilon_{\mathrm{pl}}^{\mathrm{M_t,mac}}$ [–]. (i) Plasticity in martensite compression phase $\varepsilon_{\mathrm{pl}}^{\mathrm{M_c,mac}}$ [–].

Figure 6.17: SMA – finite element simulation of a plate with hole under shear deformation. The results shown are obtained for the state of maximum shear, cf. Fig. 6.14(c). The displacement field (a) shows the shear direction, (b) and (c) show the resulting shear strains and stresses in the shear plane. In the region of maximum shear strain, the austenitic volume fraction is reduced to 62 % (d), corresponding to the evolution of the martensitic tensile and compression phase, (e) and (f), respectively. The obtained distributions of macroscopic plastic strains are presented in (g), (h), and (i).

6.4.4 Plate with hole under shear deformation – TRIP steel

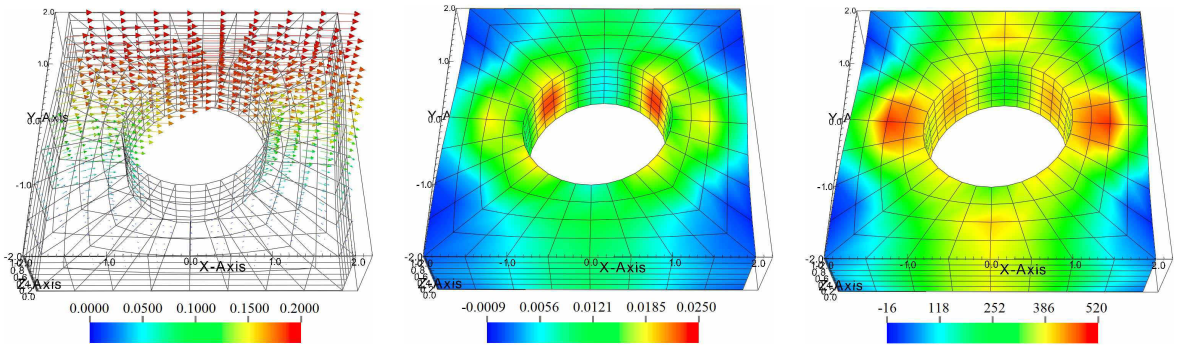

(a) Displacement field $\boldsymbol{u}$ [mm]. (b) In-plane shear strain ε_{xy} [–]. (c) In-plane shear stress σ_{yy} [MPa].

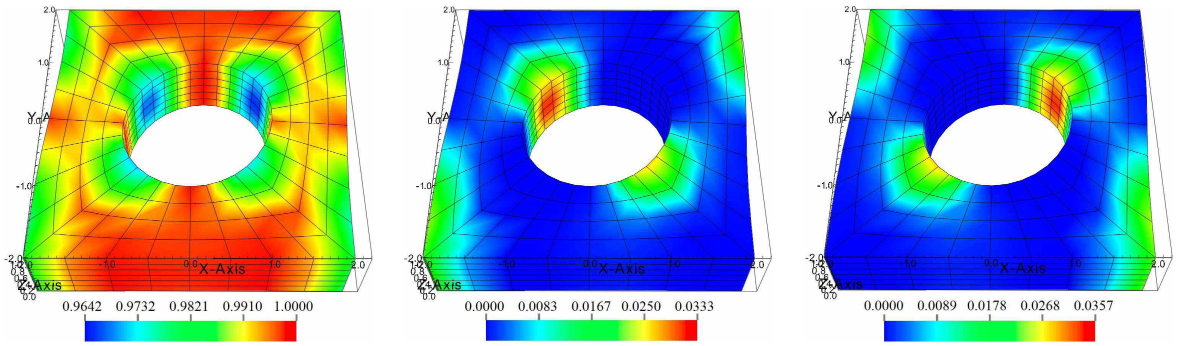

(d) Austenite $\varXi^{\mathrm{A}}$ [–]. (e) Tensile martensite $\varXi^{\mathrm{M_t}}$ [–]. (f) Compression martensite $\varXi^{\mathrm{M_c}}$ [–].

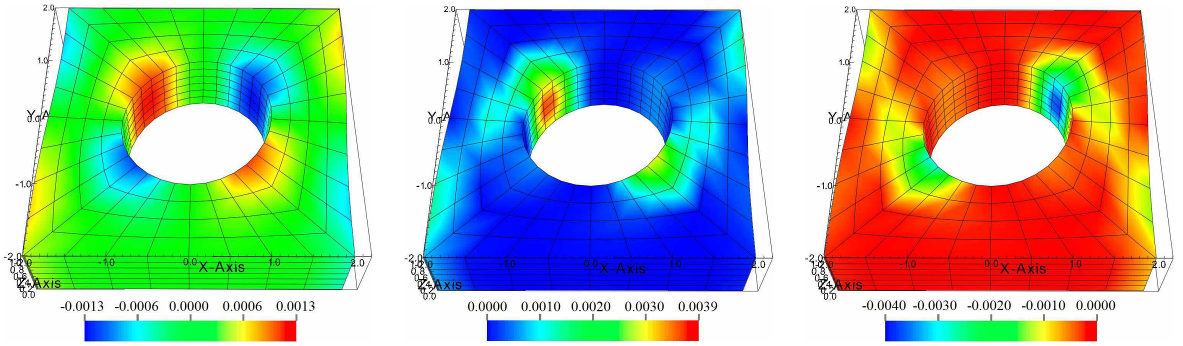

(g) Austenite plasticity $\varepsilon_{\mathrm{pl}}^{\mathrm{A,mac}}$ [–]. (h) Plasticity in martensite tensile phase $\varepsilon_{\mathrm{pl}}^{\mathrm{M_t,mac}}$ [–]. (i) Plasticity in martensite compression phase $\varepsilon_{\mathrm{pl}}^{\mathrm{M_c,mac}}$ [–].

Figure 6.18: TRIP steel – finite element simulation of a plate with hole under shear deformation. The results shown are obtained for the state of maximum shear, cf. Fig. 6.14(d). The displacement field (a) shows the shear direction, (b) and (c) show the resulting shear strains and stresses in the shear plane. In the region of maximum shear strain, the austenitic volume fraction is reduced to 96.4 % (d), corresponding to the evolution of the martensitic tensile and compression phase, (e) and (f), respectively. The obtained distributions of macroscopic plastic strains are shown in (g), (h), and (i).

6.5 Summary and conclusions

In this chapter, we introduce an enhanced multi-scale and multi-phase approach for the modelling and simulation of the interactions of martensitic phase-transformations and plasticity. The phase-transformation scheme applied in this chapter is based on statistical physics and was first applied to a one-dimensional phase-transformation model for shape memory alloys in [51]. In the previous chapters, we extended this model to three dimensions—starting with an affine micro-sphere approach, see Chapter 2, which we then extended to a non-affine micro-sphere framework by means of a volumetric-deviatoric split of macroscopic strain projections in Chapter 3. In the latter chapter, we showed that the established modelling framework facilitates the reproduction of the characteristic SMA stress-strain-temperature response, temperature-dependent pseudo-elastic and pseudo-plastic effects, and stress-strain minor loops for tensile step tests that are experimentally observed for shape memory alloys [62, 77]. This chapter therefore serves as the foundation for the current chapter, where we extend the framework by the incorporation of plasticity interactions in order to additionally capture multi-cyclic stress-strain responses as well as the characteristic behaviour of TRIP steel.

The capturing of plasticity phenomena is established by introducing individual evolution equations for each of the phases considered. The volumetric-deviatoric split of strain measures considered in the non-affine micro-sphere modelling framework applied in this work allows for the incorporation of plasticity solely in the deviatoric Helmholtz free energy contributions of the individual phases. Moreover, deviatoric and volumetric contributions of the transformation strains can be accounted for separately. A further coupling between phase-transformations and plasticity is established by means of the consistent plasticity inheritance framework introduced in Section 6.2. These framework extensions enable us to additionally capture the macroscopic behaviour of TRIP steels as it highly depends on the interactions between phase-transformations and plasticity as introduced in Section 1.1.2.

The capabilities of the extended model established in this work are discussed in Section 6.3.4 by analysis and discussion of cyclic tension-compression simulations applied to both SMA and TRIP steel material parameters. The simulations are carried out on the micro-sphere level in order to capture the response of polycrystalline material conglomerates. Moreover, we study states under homogeneous deformation, enabling us to approximate the conditions applied in experimental tensile tests. A finite element implementation of the overall model including representative inhomogeneous simulations for both SMA and TRIP steel is provided in Section 6.4, see Fig. 1.6 for an illustration of the overall multi-scale scheme.

The results show that this work successfully extends previous works towards the simulation of TRIP steel. Unlike SMA, TRIP steels are known to show a pronounced work hardening behaviour under multicyclic loading as introduced in Section 1.1.2. The

TRIP steel simulation results obtained for homogeneous deformation states presented in Section 6.3.4.2 underline that the physically sound model established in this work reproduces the typical stress-strain behaviour as well as macroscopic work hardening observed for polycrystalline TRIP steels as provided in Fig. 6.8(b). Moreover, the extended model captures the fact that TRIP steels show a slowly accumulating martensite volume fraction with an increasing number of tension-compression load cycles. To this end, we show the accumulating evolution of macroscopic martensite in Fig. 6.8(d), which is in line with observations made in, e.g., [48, 136].

6.6 Appendix

6.6.1 Material parameters

In general, the material parameters of SMA do not only depend on alloy components, but also on the heat treatment applied [73]. In this chapter, we use the parameters given in Table 6.1 which are consistent with the parameters provided and used in previous works, e.g., [20, 51, 104]. To be specific, we consider the elastic properties in terms of Young's moduli for austenite and martensite in line with the basic underlying modelling approach introduced in [51]. Additionally, the latent heat, coefficient of thermal expansion, mass density, and heat capacity considered within the physically sound material model are all chosen according to values provided in the aforementioned literature. The volumetric transformation strains are—unlike the TRIP steel values—set to zero for all SMA phases, since experiments show that no change of volume occurs during the phase-transformation of SMA. The initial yield stresses are adapted to the Young's moduli of the individual phases, i.e. for SMA we assume a higher yield stress for austenite than for martensite.

To model TRIP steel, we take the parameters shown in Table 6.1 as a basis, but we introduce the modifications presented in Table 6.2. The main differences between the material parameters used for NiTi-based SMA and TRIP steel are considered by means of the Young's moduli, initial yield stresses, and the volumetric transformation strains of the respective material phases. Note that for steels the martensitic phase is known to be the harder phase when compared to austenite. This is reflected by the higher Young's moduli and initial yield stresses chosen for the simulation of TRIP steel for both the martensitic tension and compression phase. Moreover, experiments have proved that TRIP steels—unlike NiTi-based SMAs—show changes in volume when transforming from austenite to martensite. We consider this by means of the non-zero volumetric transformation strains $\varepsilon^{\bullet}_{\mathrm{tr,vol}} \neq 0$ used for the martensitic phases in TRIP steel, see Table 6.2.

Table 6.1: SMA material parameters considered in this chapter—compare, e.g., [20, 51, 104].

SMA phase	material parameter	symbol	value
austenite A (parent phase)	Young's modulus	E^{A}	67 GPa
	hardening modulus	H^{A}	$\mathsf{E}^{\mathrm{A}}/3$
	initial yield stress	Y_0^{A}	1 GPa
	deviatoric transformation strain	$\varepsilon_{\mathrm{tr,dev}}^{\mathrm{A}}$	0
	volumetric transformation strain	$\varepsilon_{\mathrm{tr,vol}}^{\mathrm{A}}$	0
	latent heat	λ_T^{A}	0
tensile martensite $\mathrm{M_t}$	Young's modulus	$\mathsf{E}^{\mathrm{M_t}}$	26.3 GPa
	hardening modulus	$H^{\mathrm{M_t}}$	$\mathsf{E}^{\mathrm{M_t}}/3$
	initial yield stress	$Y_0^{\mathrm{M_t}}$	400 MPa
	deviatoric transformation strain	$\varepsilon_{\mathrm{tr,dev}}^{\mathrm{M_t}}$	0.025
	volumetric transformation strain	$\varepsilon_{\mathrm{tr,vol}}^{\mathrm{M_t}}$	0
	latent heat	$\lambda_T^{\mathrm{M_t}}$	14500 J/kg
compression martensite $\mathrm{M_c}$	Young's modulus	$\mathsf{E}^{\mathrm{M_c}}$	26.3 GPa
	hardening modulus	$H^{\mathrm{M_c}}$	$\mathsf{E}^{\mathrm{M_c}}/3$
	initial yield stress	$Y_0^{\mathrm{M_c}}$	400 MPa
	deviatoric transformation strain	$\varepsilon_{\mathrm{tr,dev}}^{\mathrm{M_c}}$	-0.04
	volumetric transformation strain	$\varepsilon_{\mathrm{tr,vol}}^{\mathrm{M_c}}$	0
	latent heat	$\lambda_T^{\mathrm{M_c}}$	14500 J/kg
common parameters	coefficient of thermal expansion	ζ	12×10^{-6} K^{-1}
	mass density	ρ_0	6448 kg/m^3
	macroscopic Poisson's ratio	ν_{P}	0.33
	reference temperature	θ_0	273 K
	heat capacity	c_p	400 J/kgK
	transition attempt frequency	ω	1.6 s^{-1}
	transformation region's volume	Δv	2.71×10^{-18} mm^3
	Boltzmann's constant	k	1.381×10^{-23} J/K

Table 6.2: TRIP steel material parameters considered in this chapter—cf. [43, 79, 85, 110, 149].

TRIP steel phase	material parameter	symbol	value
austenite A (parent phase)	Young's modulus	E^{A}	160 GPa
	hardening modulus	H^{A}	$\mathsf{E}^{\mathrm{A}}/4$
	initial yield stress	Y_0^{A}	1000 MPa
	deviatoric transformation strain	$\varepsilon_{\mathrm{tr,dev}}^{\mathrm{A}}$	0
	volumetric transformation strain	$\varepsilon_{\mathrm{tr,vol}}^{\mathrm{A}}$	0
tensile martensite $\mathrm{M_t}$	Young's modulus	$\mathsf{E}^{\mathrm{M_t}}$	200 GPa
	hardening modulus	$H^{\mathrm{M_t}}$	$\mathsf{E}^{\mathrm{M_t}}/12$
	initial yield stress	$Y_0^{\mathrm{M_t}}$	1400 MPa
	deviatoric transformation strain	$\varepsilon_{\mathrm{tr,dev}}^{\mathrm{M_t}}$	0.02
	volumetric transformation strain	$\varepsilon_{\mathrm{tr,vol}}^{\mathrm{M_t}}$	0.02
compression martensite $\mathrm{M_c}$	Young's modulus	$\mathsf{E}^{\mathrm{M_c}}$	200 GPa
	hardening modulus	$H^{\mathrm{M_c}}$	$\mathsf{E}^{\mathrm{M_c}}/12$
	initial yield stress	$Y_0^{\mathrm{M_c}}$	1400 MPa
	deviatoric transformation strain	$\varepsilon_{\mathrm{tr,dev}}^{\mathrm{M_c}}$	-0.02
	volumetric transformation strain	$\varepsilon_{\mathrm{tr,vol}}^{\mathrm{M_c}}$	-0.02
common parameters:	mass density	ρ_0	7850 kg/m^3

6.6.2 Computation of Gibbs energy barriers

To compute the Gibbs energy barriers $b_{\alpha\to\beta}$ and $b_{\beta\to\alpha}$ between two phases α and β (here, $\alpha, \beta \in \{\mathrm{A}, \mathrm{M_t}, \mathrm{M_c}\}$), we start by deriving a compact representation of the Helmholtz free energy potential by means of

$$\widehat{\psi}^\bullet(\varepsilon_{\mathrm{dev}}, \varepsilon_{\mathrm{vol}})|_{\varepsilon^\bullet_{\mathrm{pl}},\theta} = a^\bullet_\psi \, {\varepsilon_{\mathrm{dev}}}^2 + b^\bullet_\psi \, \varepsilon_{\mathrm{dev}} + c^\bullet_\psi \, {\varepsilon_{\mathrm{vol}}}^2 + d^\bullet_\psi \, \varepsilon_{\mathrm{vol}} + e^\bullet_\psi \quad , \tag{6.70}$$

with appropriate Helmholtz coefficients $a^\alpha_\psi, ..., e^\alpha_\psi$ that are obtained from rearranging terms in (6.7). The application of the Legendre transformation to the Helmholtz potential conserves the quadratic nature of the potential, though a new set of Gibbs energy coefficients is obtained. The simplified Gibbs energy coefficients $a^\alpha, ..., e^\alpha$ implicitly defined by

$$\widehat{g}^\bullet(\varepsilon_{\mathrm{dev}}, \varepsilon_{\mathrm{vol}})|_{\varepsilon^\bullet_{\mathrm{pl}},\theta} = a^\bullet \, {\varepsilon_{\mathrm{dev}}}^2 + b^\bullet \, \varepsilon_{\mathrm{dev}} + c^\bullet \, {\varepsilon_{\mathrm{vol}}}^2 + d^\bullet \, \varepsilon_{\mathrm{vol}} + e^\bullet \tag{6.71}$$

here take a very similar format to the coefficients that are presented in detail in Chapter 3. To be more precise, the additional consideration of plastic strains in the deviatoric elastic energy contribution $\psi^\alpha_{\mathrm{dev}}$, see (6.7), finally leads to the simplified Gibbs energy coefficients

$$a^\bullet = a^\bullet_\psi \tag{6.72}$$

$$\begin{aligned} b^\bullet &= b^\bullet_\psi - \xi^\bullet \left[\mathsf{E}^\bullet_{\mathrm{dev}} \, \varepsilon_{\mathrm{dev}}|_t - \mathsf{E}^\bullet_{\mathrm{dev}} \left[\varepsilon^\bullet_{\mathrm{tr,dev}} + \varepsilon^\bullet_{\mathrm{pl}}\right] - \zeta^\bullet \, \mathsf{E}^\bullet \, [\theta - \theta_0]\right] \\ &= -\left[1 - \xi^\bullet\right] \left[\varepsilon^\bullet_{\mathrm{tr,dev}} + \varepsilon^\bullet_{\mathrm{pl}}\right] \, \mathsf{E}^\bullet_{\mathrm{dev}} - \xi^\bullet \mathsf{E}^\bullet_{\mathrm{dev}} \, \varepsilon_{\mathrm{dev}}|_t - \zeta^\bullet \, \mathsf{E}^\bullet \, [\theta - \theta_0] \end{aligned} \tag{6.73}$$

$$c^\bullet = c^\bullet_\psi \tag{6.74}$$

$$\begin{aligned} d^\bullet &= d^\bullet_\psi - \xi^\bullet \left[\mathsf{E}^\bullet_{\mathrm{vol}} \, \varepsilon_{\mathrm{vol}}|_t - \mathsf{E}^\bullet_{\mathrm{vol}} \, \varepsilon^\bullet_{\mathrm{tr,vol}} - \zeta^\bullet \, \mathsf{E}^\bullet \, [\theta - \theta_0]\right] \\ &= -\left[1 - \xi^\bullet\right] \, \mathsf{E}^\bullet_{\mathrm{vol}} \, \varepsilon^\bullet_{\mathrm{tr,vol}} - \xi^\bullet \mathsf{E}^\bullet_{\mathrm{vol}} \, \varepsilon_{\mathrm{vol}}|_t - \zeta^\bullet \, \mathsf{E}^\bullet \, [\theta - \theta_0] \end{aligned} \tag{6.75}$$

$$e^\bullet = e^\bullet_\psi \tag{6.76}$$

which then allow for the numerical computation of the minimum of the intersection curve of two elliptic-paraboloidal Gibbs energy potentials. This specific minimum value which is required for the computation of the energy barriers driving the evolution law, see (6.17), can be obtained with the help of a proper numerical scheme that allows for the minimisation of non-linear implicit functions. For a detailed elaboration on the application of the Newton scheme to the problem class at hand the reader is referred to Chapter 3.

6.6.3 Algorithmic scheme for the numerical constitutive update

Algorithm 4 provides pseudo-code for the constitutive update of the coupled phase-transformation plasticity model proposed in this chapter. Based on a given set of history variables and a given three-dimensional deformation state, the algorithm facilitates the computation of the updated history variables as well as the corresponding Cauchy stress tensor and the algorithmic tangent modulus. For the uniaxial micro-sphere computations provided in Section 6.3.4, the provided strain-driven algorithm is embedded into a constitutive driver routine that iteratively adapts the deformation state ${}^{n+1}\boldsymbol{\varepsilon}$ with the help of the algorithmic tangent operator ${}^{n+1}\mathsf{E}^{\mathrm{alg}}$ so that the resulting macroscopic stress tensor ${}^{n+1}\boldsymbol{\sigma}$—as the constitutive driver routine has converged—corresponds to a uniaxial stress state.

```
given: deformation $^{n+1}\boldsymbol{\varepsilon}$ and material state, i.e. $\left[{}^{n}\boldsymbol{\xi}_i, {}^{n}\boldsymbol{\varepsilon}^{\rm 1d}_{{\rm pl},i}, {}^{n}\boldsymbol{\varepsilon}^{\rm 1d}_{{\rm pl,acc},i}\right]$ $\forall\, i \in \{1,\dots,n_r\}$
set $^{n+1}t = {}^{n}t + \Delta t \in [\,0,\, t_{\max}\,]$, initialise $^{n+1}\boldsymbol{\sigma} = \mathbf{0}$ and $^{n+1}\boldsymbol{\mathsf{E}}^{\rm alg} = \mathbf{0}$
for every micro-sphere direction $i = 1 \dots n_r$ do
    given: $^{n}\boldsymbol{\xi}_i$, $^{n}\boldsymbol{\varepsilon}^{\rm 1d}_{{\rm pl},i}$, $^{n}\boldsymbol{\varepsilon}^{\rm 1d}_{{\rm pl,acc},i}$ at time $^{n}t$
    compute $^{n+1}\varepsilon_{{\rm dev},i}$ and $^{n+1}\varepsilon_{\rm vol}$ from given $^{n+1}\boldsymbol{\varepsilon}$, see Section 6.3.1
    for all combinations $(\alpha,\beta) \in [{\rm A}, {\rm M_t}, {\rm M_c}]$, $\alpha \neq \beta$ do
        get energy barriers $^{n+1}b_{\alpha\to\beta,i}$, see (6.17) and 6.6.2
        get transformation probabilities $^{n+1}P_{\alpha\to\beta,i}$, see (6.11)
    end for
    assemble $^{n+1}\boldsymbol{Q}_i$ and obtain $^{n+1}\boldsymbol{\xi}_i$, see (2.6), (2.15), and, e.g., [101]
    get inheritance probabilities $\Pi_i^{\beta\to\alpha}$ $\forall\,(\alpha,\beta) \in [{\rm A}, {\rm M_t}, {\rm M_c}]$, $\alpha \neq \beta$ (6.35)
    if number of increasing phases $n_{\rm inc} < 2$ then
        define $\alpha$ as increasing and $\beta$ and $\gamma$ as non-increasing phases
        get intermediate plastic strains $^{n}\tilde{\boldsymbol{\varepsilon}}^{\rm 1d}_{{\rm pl},i}$ from (6.37), (6.38), (6.39)
    else
        define $\alpha$ as decreasing and $\beta$ and $\gamma$ as non-decreasing phases
        get intermediate plastic strains $^{n}\tilde{\boldsymbol{\varepsilon}}^{\rm 1d}_{{\rm pl},i}$ from (6.43), (6.44), (6.45)
    end if
    get intermediate accumulated plastic strains $^{n}\tilde{\boldsymbol{\varepsilon}}^{\rm 1d}_{{\rm pl,acc},i}$
    compute intermediate potential $\widetilde{\Psi}_i = \widehat{\Psi}_i({}^{n+1}\varepsilon_{{\rm dev},i}, {}^{n+1}\varepsilon_{\rm vol}, {}^{n+1}\boldsymbol{\xi}, {}^{n}\tilde{\boldsymbol{\varepsilon}}^{\rm 1d}_{{\rm pl},i}, \theta)$ (6.23)
    for each phase $\alpha$ do
        obtain trial plastic driving force $^{n+1}q^{\alpha}_{{\rm pl},\Psi,{\rm tri}}$ from (6.24)
        if for yield function (6.20) holds $\widehat{\Phi}^{\alpha}(q^{\alpha}_{{\rm pl},\Psi}, Y^{\alpha}) > 0$ then
            compute Lagrange multiplier $^{n+1}\lambda^{\alpha}$, see (6.25)
            update $^{n+1}\boldsymbol{\varepsilon}^{\rm 1d}_{{\rm pl},i}$ and $^{n+1}\boldsymbol{\varepsilon}^{\rm 1d}_{{\rm pl,acc},i}$ according to (6.26) and (6.27)
        end if
    end for
    add $^{n+1}\boldsymbol{\sigma} \leftarrow {}^{n+1}\boldsymbol{\sigma} + {}^{n+1}\boldsymbol{\sigma}_i$ and $^{n+1}\boldsymbol{\mathsf{E}}^{\rm alg} \leftarrow {}^{n+1}\boldsymbol{\mathsf{E}}^{\rm alg} + {}^{n+1}\boldsymbol{\mathsf{E}}^{\rm alg}_i$, see (6.56) and (6.66)
end for
return history arrays, i.e. $\left[{}^{n+1}\boldsymbol{\xi}_i, {}^{n+1}\boldsymbol{\varepsilon}^{\rm 1d}_{{\rm pl},i}, {}^{n+1}\boldsymbol{\varepsilon}^{\rm 1d}_{{\rm pl,acc},i}\right]$ $\forall\, i$ as well as $^{n+1}\boldsymbol{\sigma}$ and $^{n+1}\boldsymbol{\mathsf{E}}^{\rm alg}$
```

Algorithm 4: Update scheme for the coupled phase-transformation plasticity model embedded into a strain-driven non-affine micro-sphere framework. For the uniaxial stress computations provided in Section 6.3.4, a superordinate constitutive driver algorithm is used.

7 A finite strain model for phase-transformations interacting with plasticity based on representative transformation directions

In this chapter we implement a constitutive model for polycrystalline materials undergoing martensitic phase transformations that is based on representative crystal orientations. The model is derived in a thermodynamically consistent framework as elaborated in detail in [14]. The crystallographic considerations that this model is based on are presented in Section 7.1. In Section 7.2, we present the basics of the thermo-elastoplastic constitutive model, including the strongly coupled, highly non-linear system of evolution equations that governs the inelastic constitutive response. The numerical solution of the system of differential equations is introduced in Section 7.3, where we show representative simulation results in Section 7.3.2 followed by a convergence study regarding the fulfillment of algebraic inequality constraints elaborated in Section 7.4. A finite element implementation of the overall model is provided in Section 7.5.

7.1 Crystallographic considerations

The goal of the model implemented in this chapter is to consider actual crystallographic properties of the polycrystalline material. To this end, we introduce a reference transformation strain $\boldsymbol{U}^{\mathrm{tr}}_{\mathrm{ref}}$ that is observed when a cubic austenitic unit cell transforms to a tetragonal unit cell of martensite. The transformation strain related to this transformation is known as Bain strain and can be expressed as

$$\boldsymbol{U}^{\mathrm{tr}}_{\mathrm{ref}} = U^{\mathrm{tr}}_{\mathrm{lon}} \boldsymbol{e}_1 \otimes \boldsymbol{e}_1 + U^{\mathrm{tr}}_{\mathrm{lat}} \left[\boldsymbol{e}_2 \otimes \boldsymbol{e}_2 + \boldsymbol{e}_3 \otimes \boldsymbol{e}_3 \right] \tag{7.1}$$

within a given Cartesian coordinate system $\{\boldsymbol{e}_1, \boldsymbol{e}_2, \boldsymbol{e}_3\}$, where the first vector $\boldsymbol{e}_1$ is aligned with the crystallographic [100] direction by using Miller indices. Here, the longitudinal transformation stretch is $U^{\text{tr}}_{\text{lon}} < 1$, while $U^{\text{tr}}_{\text{lat}} > 1$ holds for the lateral transformation stretch. As a result of $\boldsymbol{F}^{\text{t}} \cdot \boldsymbol{F} = \boldsymbol{U}^{\text{t}} \cdot \boldsymbol{U}$, the related logarithmic transformation strain measure takes the form

$$\boldsymbol{H}^{\text{tr}}_{\text{ref}} = \ln(\boldsymbol{U}^{\text{tr}}_{\text{ref}}) \quad . \tag{7.2}$$

The elastic properties of one martensitic unit cell with above named orientation are similarly considered by means of an associated referential fourth order elasticity tensor E_{ref}.

To derive the properties of a polycrystal based on these referential unit cell properties, we introduce a spatial arrangement of unit cells, where we rotate the reference properties of the unit cell in terms of the reference transformation strain $\boldsymbol{H}^{\text{tr}}_{\text{ref}}$ as well as the related reference elasticity tensor E_{ref} into different spatial directions by using orthogonal rotation tensors $\boldsymbol{R}_{ij}$. The index i refers to a spatial direction whereas index j accounts for a specific rotation of the crystal around the ith spatial direction. A visualisation of the arrangement of martensitic unit cells considered in this chapter is provided in Fig. 7.1.

With the help of proper rotation tensors $\boldsymbol{R}_{ij}$, which rotate referential quantities into spatial direction i and simultaneously provide a variant rotation j around the spatial direction i, the logarithmic transformation strain of the jth martensitic variant oriented towards the ith spatial direction takes the form

$$\boldsymbol{H}^{\text{tr}}_{ij} = \boldsymbol{R}_{ij} \cdot \boldsymbol{H}^{\text{tr}}_{\text{ref}} \cdot \boldsymbol{R}^{\text{t}}_{ij} \quad , \tag{7.3}$$

while the corresponding elasticity tensor reads

$$\mathsf{E}_{ij} = [\boldsymbol{R}_{ij} \,\overline{\otimes}\, \boldsymbol{R}_{ij}] : \mathsf{E}_{\text{ref}} : \left[\boldsymbol{R}^{\text{t}}_{ij} \,\overline{\otimes}\, \boldsymbol{R}^{\text{t}}_{ij}\right] \quad , \tag{7.4}$$

By assigning an individual volume fraction $\xi_{ij} \in [0,1]$ to each martensitic variant j in every direction i, the pre-homogenised elasticity tensor $\bar{\mathsf{E}}_{\text{M}}$ of the overall martensitic crystal conglomerate as depicted in Figs. 7.1, 7.2, and 7.3, takes the form

$$\bar{\mathsf{E}}_{\text{M}} := \frac{1}{\xi_{\text{M}}} \sum_{i=1}^{n_d} \sum_{j=1}^{n_v} \xi_{ij} \, w_{ij} \, \mathsf{E}_{ij} \quad . \tag{7.5}$$

with the overall martensitic volume fraction $\xi_{\text{M}} \in [0,1]$ being defined as

$$\xi_{\text{M}} := \sum_{i=1}^{n_d} \sum_{j=1}^{n_v} \xi_{ij} \tag{7.6}$$

and the weighting factors $w_{ij} > 0$, which are constrained by $\sum w_{ij} = 1$.

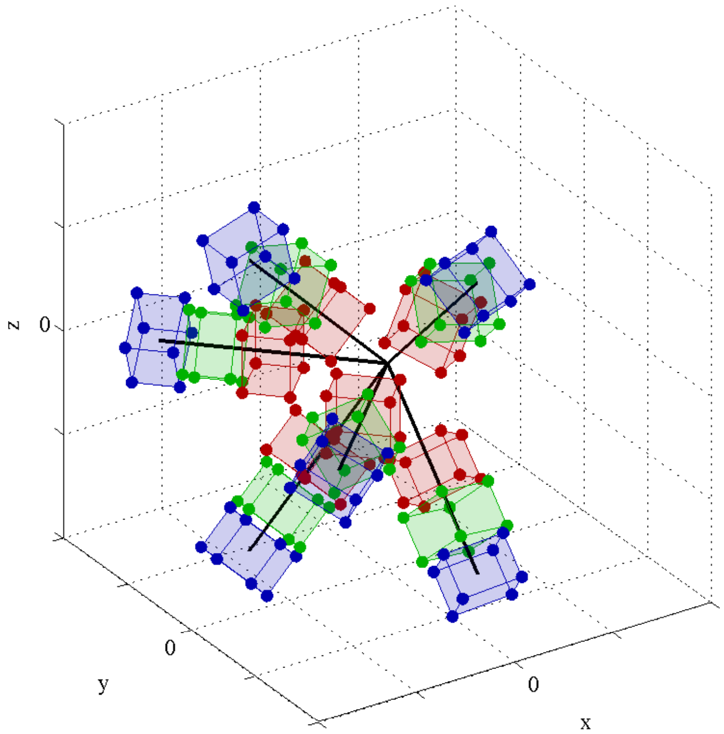

Figure 7.1: Martensitic polycrystal considered in this chapter, consisting of the depicted spatial arrangement of martensitic unit cells. The model implemented in this chapter is capable of handling an arbitrary amount of martensitic orientations and variants. However, we restrict the formulation to the depicted six spatial directions with three martensitic variants each, resulting in 18 individual, coupled evolution equations for the martensitic volume fractions ξ_{ij}.

7.2 Basics of the constitutive model

This section gives a brief review of the constitutive model. The model is based on a mixture theory with respect to the Helmholtz free energy densities $\varPsi_{\mathrm{A}}$ of the parent austenite phase and $\varPsi_{\mathrm{M}}$ of a representative martensite phase which yields the macroscopic energy density of the phase mixture

$$\varPsi = \xi_{\mathrm{A}}\, \varPsi_{\mathrm{A}} + \xi_{\mathrm{M}}\, \varPsi_{\mathrm{M}} \quad , \tag{7.7}$$

where ξ_{M} with $0 \leq \xi_{\mathrm{M}} \leq 1$ and $\xi_{\mathrm{A}} = 1 - \xi_{\mathrm{M}}$ with $0 \leq \xi_{\mathrm{A}} \leq 1$ denote the overall volume fractions of martensite and austenite, respectively. To be more specific, the phase energy densities

$$\varPsi_{\mathrm{A}} = \widehat{\varPsi}_{\mathrm{A}}^{\mathrm{elas}} \left(\boldsymbol{H}_{\mathrm{A}}, \boldsymbol{H}_{\mathrm{A}}^{\mathrm{pl}} \right) + \widehat{\varPsi}_{\mathrm{A}}^{\mathrm{chem}} \left(\theta \right) + \widehat{\varPsi}_{\mathrm{A}}^{\mathrm{hard}} \left(\alpha_{\mathrm{A}}^{\mathrm{pl}} \right) \tag{7.8}$$

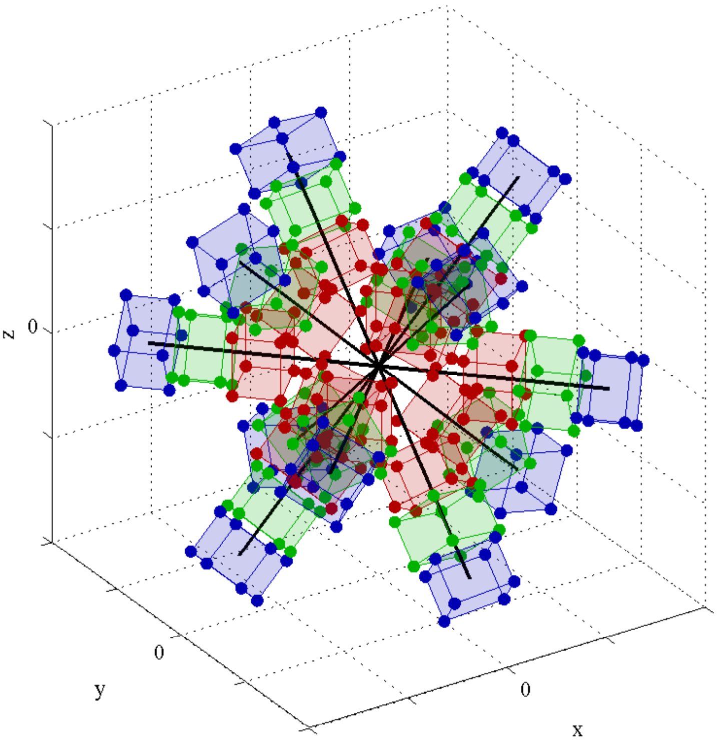

Figure 7.2: Visualisation of a martensitic polycrystal that is macroscopically isotropic in terms of its averaged Young's modulus $\bar{\mathsf{E}}_{\mathrm{M}}$ for equally distributed martensitic volume fractions, i.e. $\xi_{ij} = \mathrm{const} = 1/[n_r\, n_v]\ \forall\ (i,j)$. Considering the symmetry of this arrangement and adapting appropriate weighting factors w_{ij} for the individual variants, the numerical simulation can be reduced to the solution of the simplified crystal provided in Fig. 7.1.

and

$$\Psi_{\mathrm{M}} = \widehat{\Psi}^{\mathrm{elas}}_{\mathrm{M}}\left(\boldsymbol{H}_{\mathrm{M}}, \boldsymbol{H}^{\mathrm{pl}}_{\mathrm{M}}, \boldsymbol{H}^{\mathrm{tr}}_{\mathrm{M}}\right) + \widehat{\Psi}^{\mathrm{chem}}_{\mathrm{M}}\left(\theta\right) + \widehat{\Psi}^{\mathrm{hard}}_{\mathrm{M}}\left(\alpha^{\mathrm{pl}}_{\mathrm{M}}\right) \tag{7.9}$$

are additively decomposed into elastic parts $\Psi^{\mathrm{elas}}_{\bullet}$, into temperature-dependent chemical parts $\Psi^{\mathrm{chem}}_{\bullet}$ and into contributions $\Psi^{\mathrm{hard}}_{\bullet}$ related to plastic hardening. In this context, θ denotes the absolute temperature and $\alpha^{\mathrm{pl}}_{\bullet}$ are monotonically increasing variables that account for isotropic hardening.

As strain measures we introduce Hencky-type logarithmic strains in terms of $\boldsymbol{H} = 1/2\,\ln(\boldsymbol{U}^2) = \ln(\boldsymbol{U})$ where $\boldsymbol{U}$ denotes the right stretch tensor which is linked to the deformation gradient via $\boldsymbol{F} = \boldsymbol{R}\cdot\boldsymbol{U}$, and where $\boldsymbol{R} \in \mathbb{O}^3_+$ is a proper orthogonal rotation tensor. The total strains $\boldsymbol{H}_{\bullet}$ of the respective phases are additively decomposed into elastic strains $\boldsymbol{H}^{\mathrm{el}}_{\bullet}$, plastic strains $\boldsymbol{H}^{\mathrm{pl}}_{\bullet}$, and into transformation strains $\boldsymbol{H}^{\mathrm{tr}}_{\bullet}$, i.e. $\boldsymbol{H}_{\bullet} = \boldsymbol{H}^{\mathrm{el}}_{\bullet} + \boldsymbol{H}^{\mathrm{pl}}_{\bullet} + \boldsymbol{H}^{\mathrm{tr}}_{\bullet}$.

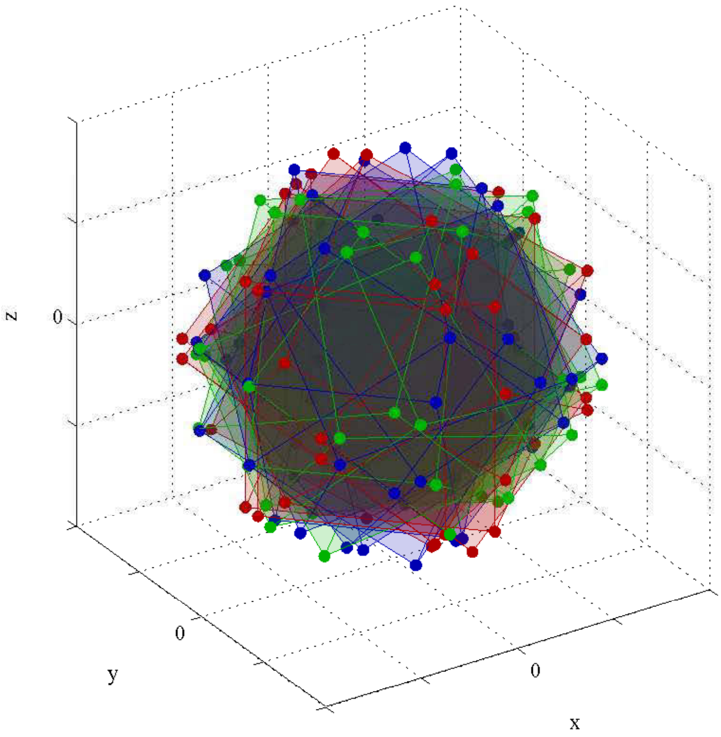

Figure 7.3: Pre-homogenisation of the martensitic polycrystal depicted in Fig. 7.1. In the model implemented in this chapter, the martensitic conglomerate is pre-homogenised according to the Voigt assumption, resulting in an averaged macroscopic Young's modulus $\bar{\mathsf{E}}_{\rm M}$. The depicted anisotropic martensitic conglomerate with the overall volume fraction $\xi_{\rm M}$ is embedded into an isotropic austenitic parent phase of volume fraction $\xi_{\rm A} = 1 - \xi_{\rm M}$, where the mixture of both phases is subject to the Reuss assumption.

The energy contributions for austenite are chosen as

$$\varPsi_{\rm A}^{\rm elas} := \frac{1}{2}\left[\boldsymbol{H}_{\rm A} - \boldsymbol{H}_{\rm A}^{\rm pl}\right] : \mathsf{E}_{\rm A} : \left[\boldsymbol{H}_{\rm A} - \boldsymbol{H}_{\rm A}^{\rm pl}\right] \quad , \tag{7.10}$$

$$\varPsi_{\rm A}^{\rm chem} := -\,c_{\rm A}\,\theta\,\ln(\theta) - \lambda_0^A\left[1 - \frac{\theta}{\theta_0^{\rm tr}}\right] \quad , \tag{7.11}$$

$$\varPsi_{\rm A}^{\rm hard} := \left[\mathsf{Y}_{\rm A}^{\rm sat} - \mathsf{Y}_{\rm A}^{\rm init}\right]\left[\alpha_{\rm A}^{\rm pl} + \frac{1}{\kappa_{\rm A}}\left[\exp\left(-\kappa_{\rm A}\,\alpha_{\rm A}^{\rm pl}\right) - 1\right]\right] \quad , \tag{7.12}$$

and the martensitic counterparts are set to

$$\varPsi_{\rm M}^{\rm elas} := \frac{1}{2}\left[\boldsymbol{H}_{\rm M} - \boldsymbol{H}_{\rm M}^{\rm pl} - \bar{\boldsymbol{H}}_{\rm M}^{\rm tr}\right] : \bar{\mathsf{E}}_{\rm M} : \left[\boldsymbol{H}_{\rm M} - \boldsymbol{H}_{\rm M}^{\rm pl} - \bar{\boldsymbol{H}}_{\rm M}^{\rm tr}\right] \quad , \tag{7.13}$$

$$\varPsi_{\rm M}^{\rm chem} := -\,c_{\rm M}\,\theta\,\ln(\theta) - \lambda_0^M\left[1 - \frac{\theta}{\theta_0^{\rm tr}}\right] \quad , \tag{7.14}$$

$$\varPsi_{\rm M}^{\rm hard} := \left[\mathsf{Y}_{\rm M}^{\rm sat} - \mathsf{Y}_{\rm M}^{\rm init}\right]\left[\alpha_{\rm M}^{\rm pl} + \frac{1}{\kappa_{\rm M}}\left[\exp\left(-\kappa_{\rm M}\,\alpha_{\rm M}^{\rm pl}\right) - 1\right]\right] \quad . \tag{7.15}$$

In the above equations, we denote $c_\bullet$ as the specific heat capacity, $\lambda_0^\bullet$ as the latent heat, θ_0^{tr} as a reference temperature, $\mathsf{Y}_\bullet^{\mathrm{sat}}$ and $\mathsf{Y}_\bullet^{\mathrm{init}}$ as the saturated and initial plastic yield limit as well as $\kappa_\bullet$ as a decay parameter introduced for the saturation-type hardening behaviour.

Convexifying the underlying double-well potential in the logarithmic strain space yields

$$\begin{aligned} \varPsi^C &= \|\boldsymbol{H} - \xi_\mathrm{A}\boldsymbol{H}_\mathrm{A}^{\mathrm{pl}} - \xi_\mathrm{M}\left[\boldsymbol{H}_\mathrm{M}^{\mathrm{pl}} + \bar{\boldsymbol{H}}_\mathrm{M}^{\mathrm{tr}}\right]\|_{\bar{\mathsf{E}}}^2 \\ &+ \xi_\mathrm{A}\left[\varPsi_\mathrm{A}^{\mathrm{chem}} + \varPsi_\mathrm{A}^{\mathrm{hard}}\right] \\ &+ \xi_\mathrm{M}\left[\varPsi_\mathrm{M}^{\mathrm{chem}} + \varPsi_\mathrm{M}^{\mathrm{hard}}\right] \quad , \end{aligned} \tag{7.16}$$

where we introduce the notation

$$\|\boldsymbol{X}\|_{\bar{\mathsf{E}}}^2 := \frac{1}{2}\boldsymbol{X} : \bar{\mathsf{E}} : \boldsymbol{X} \quad , \tag{7.17}$$

with

$$\bar{\mathsf{E}} := \mathsf{E}_\mathrm{A} : \widehat{\mathsf{E}}^{-1} : \bar{\mathsf{E}}_\mathrm{M} \quad , \quad \text{wherein} \quad \widehat{\mathsf{E}} := \xi_\mathrm{A}\,\bar{\mathsf{E}}_\mathrm{M} + \xi_\mathrm{M}\,\mathsf{E}_\mathrm{A} \quad . \tag{7.18}$$

The definition of the convexified Helmholtz energy $\varPsi^C$ facilitates the derivation of the elastic stresses $\boldsymbol{T}$ energy-conjugated to $\boldsymbol{H}$ in terms of

$$\boldsymbol{T} = \partial_{\boldsymbol{H}}\varPsi^C = \bar{\mathsf{E}} : \left[\boldsymbol{H} - \xi_\mathrm{A}\boldsymbol{H}_\mathrm{A}^{\mathrm{pl}} - \xi_\mathrm{M}\left[\boldsymbol{H}_\mathrm{M}^{\mathrm{pl}} + \bar{\boldsymbol{H}}_\mathrm{M}^{\mathrm{tr}}\right]\right] \quad . \tag{7.19}$$

The total strains $\boldsymbol{H}_\bullet$ within each phase are determined according to the Reuss assumption, so that the stresses are homogeneously distributed among the phases. The precise expressions for the total strains are omitted here but can be obtained according to [14]. With all the above-mentioned relations at hand, the constitutive model is defined except for the evolution of internal variables which will be defined in the following section.

7.2.1 Inelastic material behaviour

For the load-driven evolution of the underlying internal variables, i.e. plastic strains $\boldsymbol{H}_\bullet^{\mathrm{pl}}$ and the martensitic volume fractions ξ_{ij}, we adopt a Perzyna-type viscoplastic format which results in

$$\dot{\boldsymbol{H}}_\bullet^{\mathrm{pl}} = \frac{1}{\eta_\bullet^{\mathrm{pl}}}\,\langle \varPhi_\bullet^{\mathrm{pl}} \rangle\,\frac{\mathsf{A}_\bullet : \boldsymbol{T}}{\sqrt{\boldsymbol{T} : \mathsf{A}_\bullet : \boldsymbol{T}}} \quad , \tag{7.20}$$

$$\dot{\xi}_{ij} = \frac{1}{\eta_{ij}^{\xi}}\,\langle \varPhi_{ij}^{\xi} \rangle\,\mathrm{sign}(\tau_{ij}^{\xi}) \quad , \tag{7.21}$$

$$\dot{\alpha}^{\rm pl}_{\bullet} = \frac{1}{\xi_{\bullet}\,\eta^{\rm pl}_{\bullet}}\,\langle \varPhi^{\rm pl}_{\bullet} \rangle \quad , \tag{7.22}$$

$$\dot{\theta} = \frac{1}{c}\,\mathcal{D}_{\rm mech} \quad . \tag{7.23}$$

In these equations, $\eta^{\circ}_{\bullet}$ denotes viscosity-type quantities, $\varPhi^{\circ}_{\bullet}$ reflects yield functions, and $\boldsymbol{\mathsf{A}}_{\bullet}$ are Hill-type fourth order tensors which enables us to take into account the incompressibility of plastic deformations and, if desired, anisotropic behaviour. Finally, $\boldsymbol{T}$ is the stress measure conjugated to the logarithmic strain $\boldsymbol{H}$ as defined in (7.19). The driving forces τ^{ξ}_{ij} for the evolution of the individual martensitic volume fractions ξ_{ij} follow from

$$\tau^{\xi}_{ij} := -\frac{\partial \varPsi^{C}}{\partial \xi_{ij}} \quad , \tag{7.24}$$

whereas the mechanical dissipation rate density $\mathcal{D}_{\rm mech}$ that governs the evolution of temperature θ (7.23) takes the form

$$\mathcal{D}_{\rm mech} = \sum_{i=1}^{n_d}\sum_{j=1}^{n_v} \frac{1}{\eta^{\xi}_{ij}}\,\langle \varPhi^{\xi}_{ij} \rangle \left[\varPhi^{\xi}_{ij} + \mathsf{Y}^{\xi}_{ij}\right] + \sum_{\bullet\in\{\rm A,M\}} \frac{\xi_{\bullet}}{\eta^{\rm pl}_{\bullet}}\,\langle \varPhi^{\rm pl}_{\bullet} \rangle \left[\varPhi^{\rm pl}_{\bullet} + \mathsf{Y}^{\rm init}_{\bullet}\right] \quad . \tag{7.25}$$

The yield functions associated to phase-transformations, $\varPhi^{\xi}_{ij}$, and to plasticity in martensite and austenite, $\varPhi^{\rm pl}_{\rm M}$ and $\varPhi^{\rm pl}_{\rm A}$, respectively, are specified as

$$\varPhi^{\xi}_{ij} := |\tau^{\xi}_{ij}| - \mathsf{Y}^{\xi}_{ij} \quad , \tag{7.26}$$

$$\varPhi^{\rm pl}_{\rm M} := \sqrt{\boldsymbol{T} : \boldsymbol{\mathsf{A}}_{\rm M} : \boldsymbol{T}} - \mathsf{Y}^{\rm init}_{\rm M} - \left[\mathsf{Y}^{\rm sat}_{\rm M} - \mathsf{Y}^{\rm init}_{\rm M}\right]\left[1 - \exp(-\kappa_{\rm M}\,\alpha^{\rm pl}_{\rm M})\right] \quad , \tag{7.27}$$

$$\varPhi^{\rm pl}_{\rm A} := \sqrt{\boldsymbol{T} : \boldsymbol{\mathsf{A}}_{\rm A} : \boldsymbol{T}} - \mathsf{Y}^{\rm init}_{\rm A} - \left[\mathsf{Y}^{\rm sat}_{\rm A} - \mathsf{Y}^{\rm init}_{\rm A}\right]\left[1 - \exp(-\kappa_{\rm A}\,\alpha^{\rm pl}_{\rm A})\right] \tag{7.28}$$

$$+\,\varPhi^{\rm GWJ}_{\rm A} \quad , \tag{7.29}$$

where the Greenwood-Johnson effect of the material is considered by means of the additional contribution $\varPhi^{\rm GWJ}_{\rm A}$ incorporated into the yield function of austenite, precisely

$$\varPhi^{\rm GWJ}_{\rm A} = \xi_{\rm M}\sqrt{\left[\boldsymbol{\mathsf{E}}_{\rm A} : \bar{\boldsymbol{H}}^{\rm tr}_{\rm M}\right] : \boldsymbol{\mathsf{A}}_{\rm A} : \left[\boldsymbol{\mathsf{E}}_{\rm A} : \bar{\boldsymbol{H}}^{\rm tr}_{\rm M}\right]} \quad . \tag{7.30}$$

In the above equations, $\mathsf{Y}^{\circ}_{\bullet}$ denotes initial and saturation yield stresses for phase-transformations and plasticity, $\kappa_{\bullet}$ is a decay parameter connected to the chosen exponential saturation-type plasticity hardening rule, and $\alpha^{\rm pl}_{\bullet}$ refers to the accumulated plastic strains (7.22).

In the current chapter, we consider $n_d = 6$ spatial orientations with $n_v = 3$ martensitic variants each as visualised in Fig. 7.1, resulting in 18 individually evolving martensitic volume fractions ξ_{ij}. Moreover, the independently evolving tensor-valued logarithmic plastic strains $\boldsymbol{H}_{\bullet}^{\mathrm{pl}}$ for both austenite A and pre-homogenised martensite M—cf. (7.6)—have six independent tensorial quantities for both phases, resulting in 12 additional internal variables. Finally, considering the evolution of the scalar hardening variables $\alpha_{\bullet}^{\mathrm{pl}}$ for both phases and the local temperature θ, the overall number of independently evolving variables considered locally is 33. Note that further martensitic variants can be taken into account. However, the results provided in this chapter are restricted to the case of 18 independent martensitic volume fractions for the sake of simplicity.

In view of a numerical implementation of the model formulation, the system of the named 33 independent, strongly coupled differential equations, (7.20)–(7.23), must be solved with a stable and thus preferably implicit numerical time-integration scheme. Moreover, the system of differential equations to be solved is partially subject to algebraic inequality constraints in terms of

$$\xi_{ij} \geq 0 \ \forall \ (i,j) \tag{7.31}$$

and

$$\xi_{\mathrm{M}} = \sum_{i=1}^{n_d} \sum_{j=1}^{n_v} \xi_{ij} \leq 1 \quad , \tag{7.32}$$

which can equivalently be denoted in the standard form

$$h_{ij} := -\,\xi_{ij} \leq 0 \ \forall \ (i,j) \tag{7.33}$$

and

$$\bar{h} := \xi_{\mathrm{M}} - 1 = \sum_{i=1}^{n_d} \sum_{j=1}^{n_v} \xi_{ij} - 1 \leq 0 \quad , \tag{7.34}$$

facilitating the expression of the constraints in terms of the Macaulay brackets $\langle \bullet \rangle := \max\{0, \bullet\}$ viz.

$$\langle h_{ij} \rangle = 0 \ \forall \ (i,j) \tag{7.35}$$

and

$$\langle \bar{h} \rangle = 0 \quad , \tag{7.36}$$

respectively. Expressing the inequality constraints for the volume fractions ξ_{ij} in terms of Macaulay brackets enables a compact representation of the residual function R_p that is required in view of the later numerical solution scheme, namely

$$R_p(\boldsymbol{\xi}) := \langle \bar{h} \rangle + \sum_{i=1}^{n_d} \sum_{j=1}^{n_v} \langle h_{ij} \rangle = 0 \quad , \tag{7.37}$$

where $\boldsymbol{\xi} = [\xi_{11}, \ldots, \xi_{n_r n_v}]$ is the collection of the considered individual martensitic volume fractions. The numerical application of this residual function within a penalty iteration scheme is provided in Algorithm 7.

No separate constraints on the austenitic volume fractions are necessary, since from $\xi_\mathrm{A} := 1 - \xi_\mathrm{M}$ it follows that (7.31) induces $\xi_\mathrm{A,max} \to 1$ in case of $\xi_{ij} \to 0 \; \forall \, (i,j) \Rightarrow \xi_\mathrm{M} \to 0$. Moreover, from (7.32) it follows that $\xi_\mathrm{A,min} \to 0$ in case of $\xi_\mathrm{M} \to 1$, i.e. the enforcement of (7.31) and (7.32) already guarantees $\xi_\mathrm{A} \in [0,1]$. The solution of the system of differential equations (7.20)–(7.23) subject to the inequality contraints (7.31) and (7.32) is presented and discussed in Section 7.3.

7.3 Numerical solution of the constitutive equations

In this Section, an algorithmic solution scheme is provided for the solution of the coupled system of ordinary differential equations (ODE system), (7.20)–(7.23), subject to the inequality constraints (7.31) and (7.32). We use an iterative implicit backward Euler update scheme for the solution of the ODE system. The backward Euler scheme is embedded into a superordinate penalty iteration scheme, consistently enforcing the physical constraints (7.31) and (7.32) on the phase fractions.

7.3.1 Algorithmic solution scheme

In view of the time-discretisation of (7.20)–(7.23), we rewrite the ODE system as

$$\dot{\boldsymbol{v}} = \boldsymbol{f}(\boldsymbol{v}) \tag{7.38}$$

with $\boldsymbol{v}$ representing the vector-valued collection of the internal variables, including the temperature θ. For the system at hand, $\boldsymbol{v} \in \mathbb{R}^{33 \times 1}$ stores 33 individual variables as introduced in Section 7.2.1. Note that the ODE system derived within the provided modelling framework is autonomous, i.e. the right-hand side of (7.38) is not an explicit function of time t. For the implicit time-update from time t_n to t_{n+1} with $\Delta t := t_{n+1} - t_n$ we apply the backward-Euler ansatz

$$\boldsymbol{v}_{n+1} = \boldsymbol{v}_n + \Delta t \, \boldsymbol{f}(\boldsymbol{v}_{n+1}) \quad , \tag{7.39}$$

yielding a non-linear vector-valued equation system to be solved for $\boldsymbol{v}_{n+1}$. For the solution of (7.39) we iteratively solve for the residual function

$$\boldsymbol{R}(\boldsymbol{v}_{n+1}) := \boldsymbol{v}_{n+1} - \boldsymbol{v}_n - \Delta t \, \boldsymbol{f}(\boldsymbol{v}_{n+1}) = \boldsymbol{0} \tag{7.40}$$

using a Newton scheme.

```
given: $k$th Newton approximation $\boldsymbol{v}_{n+1}^{(k)}$ to the sought solution $\boldsymbol{v}_{n+1}$
initialise $\boldsymbol{J}^{(k)} = \text{zeros}(\dim(\boldsymbol{v}), \dim(\boldsymbol{v}))$
compute current non-perturbed residual vector $\boldsymbol{R}(\boldsymbol{v}_{n+1}^{(k)})$ from (7.40)
for $i = 1 \ldots \dim(\boldsymbol{v})$ do
    perturb component $i$ of $\boldsymbol{v}_{n+1}^{(k)}$, i.e. set $\boldsymbol{v}_{\text{pert},i} := \boldsymbol{v}_{n+1}^{(k)} + \epsilon_{\text{pert}}\, \boldsymbol{e}_i$ with $\epsilon_{\text{pert}} = 10^{-8}$
    compute $i$th perturbed residual vector $\boldsymbol{R}(\boldsymbol{v}_{\text{pert},i})$ from (7.40)
    compute differential quotient $\mathrm{d}\boldsymbol{R}_i := \left[\boldsymbol{R}(\boldsymbol{v}_{\text{pert},i}) - \boldsymbol{R}(\boldsymbol{v}_{n+1}^{(k)})\right] / \epsilon_{\text{pert}}$
    insert $\mathrm{d}\boldsymbol{R}_i$ into the $i$th column of $\boldsymbol{J}^{(k)}$, i.e. $\boldsymbol{J}^{(k)}(1 : \dim(\boldsymbol{v}), i) \leftarrow \mathrm{d}\boldsymbol{R}_i$
end for
return approximate Jacobian $\boldsymbol{J}^{(k)}$ for the Newton scheme, see Algorithm 6
```

Algorithm 5: Numerical approximation of the Jacobian $\boldsymbol{J}^{(k)}$ used for the backward-Euler update (7.41) of the ODE system (7.20)–(7.23), cf. Algorithm 6.

Following the Newton scheme, the update rule for the solution of (7.40) takes the form

$$\boldsymbol{v}_{n+1}^{(k+1)} = \boldsymbol{v}_{n+1}^{(k)} - [\boldsymbol{J}^{(k)}]^{-1} \cdot \boldsymbol{R}(\boldsymbol{v}_{n+1}^{(k)}) \tag{7.41}$$

with

$$\boldsymbol{J}^{(k)} := \left.\frac{\mathrm{d}\boldsymbol{R}(\boldsymbol{v})}{\mathrm{d}\boldsymbol{v}}\right|_{\boldsymbol{v}=\boldsymbol{v}_{n+1}^{(k)}} \in \mathbb{R}^{33\times 33} \tag{7.42}$$

the Jacobian of $\boldsymbol{R}$ evaluated at the current point $\boldsymbol{v}_{n+1}^{(k)}$. As a starting value for the Newton scheme we initialise $\boldsymbol{v}_{n+1}^{(0)} := \boldsymbol{v}_n$, see Algorithm 6. Due to the algebraic complexity of the $33 \times 33 = 1089$ entries of the Jacobian, the latter is not derived analytically but rather approximated numerically by using a numerical perturbation scheme as provided in Algorithm 5, cf. [40].

To consistently account for the algebraic inequality constraints introduced in (7.31) and (7.32), the convexified Helmholtz energy potential Ψ^C (7.16) is extended properly, yielding the Lagrangian

$$\mathcal{L} := \Psi^C + \sum_{i=1}^{n_d} \sum_{j=1}^{n_v} \frac{1}{2\,\gamma_{ij}} \left[\langle \mu_{ij} + \gamma_{ij}\, h_{ij} \rangle^2 - \mu_{ij}^2\right] - \frac{1}{2\,\bar{\gamma}} \left[\langle \bar{\mu} + \bar{\gamma}\, \bar{h} \rangle^2 - \bar{\mu}^2\right] \quad , \tag{7.43}$$

```
given: equilibrium state $\boldsymbol{v}_n$ at time $t_n$, time increment $\Delta t$, deformation $\boldsymbol{F}^{(n+1)}$
set $k = 0$, initialise $\boldsymbol{v}_{n+1}^{(k=0)} = \boldsymbol{v}_n$
compute initial residual vector $\boldsymbol{R}(\boldsymbol{v}_{n+1}^{(k=0)})$ using (7.40)
while $\left|\boldsymbol{R}(\boldsymbol{v}_{n+1}^{(k)})\right| > \epsilon$ with $\epsilon = 10^{-8}$ do
    approximate Jacobian $\boldsymbol{J}^{(k)}$, see (7.42), numerically following Algorithm 5
    compute $\mathrm{d}\boldsymbol{v}^{(k)} := -[\boldsymbol{J}^{(k)}]^{-1} \cdot \boldsymbol{R}(\boldsymbol{v}_{n+1}^{(k)})$ by solving $\boldsymbol{J}^{(k)} \cdot \mathrm{d}\boldsymbol{v}^{(k)} = -\boldsymbol{R}(\boldsymbol{v}_{n+1}^{(k)})$
    update $\boldsymbol{v}_{n+1}^{(k+1)} = \boldsymbol{v}_{n+1}^{(k)} + \mathrm{d}\boldsymbol{v}^{(k)}$ in line with (7.41)
    compute new residual $\boldsymbol{R}(\boldsymbol{v}_{n+1}^{(k+1)})$ for convergence check/in view of
    next Newton iteration using (7.40)
    set $k \leftarrow k + 1$
end while
after Newton convergence, return $\boldsymbol{v}_{n+1} = \boldsymbol{v}_{n+1}^{(k)}$ as solution at time $t_{n+1} = t_n + \Delta t$
```

Algorithm 6: Newton scheme facilitating the iterative solution of the non-linear algebraic equation system (7.40), yielding an updated set of state variables $\boldsymbol{v}_{n+1}$ that fulfill the backward-Euler update rule (7.39) for the numerically stable, implicit solution of the ODE system (7.20)–(7.23) governing the inelastic constitutive response of the material model. Note that parts of this solution might violate the algebraic inequality constraints (7.33) and (7.34), thus an iterative solution refinement using the superordinate penalty strategy provided in Algorithm 7 is generally required.

which leads to the desired modification of the driving force (7.24) that drives the evolution of the martensitic volume fractions in terms of

$$\bar{\tau}_{ij}^{\xi} := -\frac{\partial \mathcal{L}}{\partial \xi_{ij}} = \tau_{ij} + \langle \mu_{ij} + \gamma_{ij}\, h_{ij} \rangle - \langle \bar{\mu} + \bar{\gamma}\, \bar{h} \rangle \quad . \tag{7.44}$$

Accordingly, the penalised driving force $\bar{\tau}_{ij}^{\xi}$ for a martensitic volume fraction ξ_{ij} as provided in (7.44) increases if the corresponding inequality constraint h_{ij} (7.33) is violated. In that case, $\xi_{ij} < 0$ violated the lower constraint boundary, which is consistently corrected by gradually increasing the driving force and thus the resulting volume fraction until $\xi_{ij} \geq 0 \;\forall\; (i, j)$, cf. [19]. On the other hand, if the upper constraint boundary (7.34) is violated, i.e. $\sum \xi_{ij} > 1$, then the penalty scheme consistently decreases the driving forces of all volume fractions ξ_{ij} until the penalty residuum is zero, i.e. the constraint $\sum \xi_{ij} \leq 1$ is fulfilled again.

The algorithmic implementation of the Bertsekas penalty scheme applied in this work is provided in Algorithm 7. A detailed study on the convergence behaviour of the penalty scheme for both lower and upper constraint boundaries is presented in Section 7.4.

```
given: equilibrium state $\boldsymbol{v}_n$ at time $t_n$, time increment $\Delta t$, deformation $\boldsymbol{F}^{(n+1)}$
initialise penalty interation counter $p = 0$
initialise penalty parameters $\gamma_{ij}^{(p=0)} = \mathcal{C}_\gamma$ and $\bar{\gamma}^{(p=0)} = \mathcal{C}_{\bar{\gamma}}$
with proper penalty coefficients $\mathcal{C}_\gamma$ and $\mathcal{C}_{\bar{\gamma}}$, cf. Section 7.4
while penalty residual $R_p(\boldsymbol{\xi}) > \epsilon_{\text{pen}}$ with $\epsilon_{\text{pen}} = 10^{-6}$, cf. (7.37), do
    obtain $\boldsymbol{v}_{n+1}$ using Algorithm 6 with $\bar{\tau}_{ij}^{\xi}$ (7.44) as the penalised driving force
    considered in the constitutive ODEs (7.21)
    increase penalty parameter $\gamma_{ij}^{(p+1)} = \gamma_{ij}^{(p)} + \mathcal{C}_\gamma \ \forall \ (i,j)$ with $h_{ij} > 0$ (7.33)
    increase penalty parameter $\bar{\gamma}^{(p+1)} = \bar{\gamma}^{(p)} + \mathcal{C}_{\bar{\gamma}}$ if $\bar{h} > 0$ (7.34)
    update penalty parameter $\mu_{ij}^{(p+1)} = \langle \mu_{ij}^{(p)} + \gamma_{ij}^{(p)} \, h_{ij} \rangle$
    update penalty parameter $\bar{\mu}^{(p+1)} = \langle \bar{\mu}^{(p)} + \bar{\gamma}^{(p)} \, \bar{h} \rangle$
end while
after penalty convergence, return the final solution $\boldsymbol{v}_{n+1}$ that now fulfills the
constraints (7.33) and (7.34)
```

Algorithm 7: Bertsekas penalty scheme used to enforce the algebraic inequality constraints (7.33) and (7.34) on the implicit solution of the differential equation system (7.20)–(7.23).

7.3.2 Numerical results for states under homogeneous deformation

This section shows the numerical results obtained by solving the coupled system of evolution equations (7.20)–(7.23) for the considered 33 internal variables subject to the algebraic inequality constraints (7.33) and (7.34) for selected deformation paths. To assess the material behaviour subject to homogeneous deformations, we present two representative load cases, namely isochoric tension in Section 7.3.2.1 and simple shear in Section 7.3.2.2. For both load cases, we investigate two different initial conditions in terms of volume fractions. On the one hand, we start with an initially purely austenitic state, $\xi_{\text{M}}|_{t=0} = 0 \Rightarrow \xi_{\text{A}}|_{t=0} = 1$, as provided in Figures 7.4 and 7.6. On the other hand, we start with an overall martensitic volume fraction of $\xi_{\text{M}}|_{t=0} = 0.5$, inducing an austenitic volume fraction of $\xi_{\text{A}}|_{t=0} = 0.5$ as well. To this end, we consider equally distributed individual martensitic volume fractions ξ_{ij}, where we choose $\xi_{ij}|_{t=0} = 0.5/[n_r \, n_v] \ \forall \ (i,j) \Rightarrow \sum \xi_{ij}|_{t=0} = \xi_{\text{M}}|_{t=0} = 0.5$, see Figures 7.5 and 7.7. Note that we here and in the following focus on the elaboration of the general constitutive properties of the proposed highly non-linear and strongly coupled model, i.e. at this point we do not calibrate material parameters to quantitatively match experimental results.

The results obtained for isochoric tension of an initially purely austenitic polycrystal are provided in Fig. 7.4. The applied load path in terms of components of the deformation gradient $\boldsymbol{F} = F_{11} \, \boldsymbol{e}_1 \otimes \boldsymbol{e}_1 + \left[1/\sqrt{F_{11}}\right] \, [\boldsymbol{e}_2 \otimes \boldsymbol{e}_2 + \boldsymbol{e}_3 \otimes \boldsymbol{e}_3]$ is given in Fig. 7.4(a) and the obtained stress-strain response is provided in Fig. 7.4(b). The coefficients plotted refer to a Cartesian base system $\{\boldsymbol{e}_1, \boldsymbol{e}_2, \boldsymbol{e}_3\}$ such that $F_{kl} = \boldsymbol{e}_k \cdot \boldsymbol{F} \cdot \boldsymbol{e}_l$ and the Cauchy stresses are defined as $\boldsymbol{\sigma} = \det(\boldsymbol{F}^{-1})\, \partial_{\boldsymbol{F}} \varPsi^C \cdot \boldsymbol{F}^{\rm t} = \det(\boldsymbol{F}^{-1})\, \boldsymbol{T} : \partial_{\boldsymbol{F}} \boldsymbol{H} \cdot \boldsymbol{F}^{\rm t}$, cf. (7.19). The maximum deformation applied is $F_{11} = 1.5$, corresponding to a macroscopic strain of 50%, where the overall simulation time is set to $t_{\rm end} = 1$s. The evolution of individual volume fractions ξ_{ij} depicted in Fig. 7.4(c) shows that certain martensitic variants evolve within the polycrystal, while other variants remain zero. As a result of the spatial symmetry of the considered polycrystalline arrangement and the eigenstrain directions remaining constant during the isochoric load cycle, a symmetric—or rather identical—evolution of certain martensitic variants ξ_{ij} is obtained as indicated by solely four unique evolution paths obtained for all 18 variants, see Fig. 7.4(c).

The overall martensitic volume fraction $\xi_{\rm M}$ is given in Fig. 7.4(d). The figure shows that the superordinate penalty algorithm successfully enforces the constraint $\xi_{\rm M} \leq 0$ by suppressing the evolution of the individual volume fractions, Fig. 7.4(c), as a result of the penalised—and thus successively decreased—driving force for the individual volume fractions (7.44), see Algorithm 7. For the sake of simplicity, we focus here on the evolution of plasticity solely in the austenitic parent phase as presented in Fig. 7.4(e). For the calculations provided here, the initial temperature is set to $\theta|_{t=0} = 20$°C, cf. 7.4(f). The evolution of temperature is induced by both the evolution of martensite and the evolution of plasticity within the material and, at this stage, renders temperature levels above physically reasonable values since, among other aspects, no heat flux is accounted for.

Applying the isochoric load to a mixed austenitic-martensitic polycrystal with $\xi_{ij}|_{t=0} = 0.5/[n_r\, n_v]\ \forall\ (i,j) \Rightarrow \xi_{\rm M}|_{t=0} = \xi_{\rm A}|_{t=0} = 0.5$ as shown in Fig. 7.5 results in an overall martensitic volume fraction that further evolves towards the upper constraint boundary $\xi_{\rm M} \to 1$, see Fig. 7.4(d). As a result of the non-zero starting values for the individual martensitic volume fractions ξ_{ij}, all phases increase until the constraint $\xi_{\rm M} \to 1$ is approached. As the constraint is enforced by the penalty scheme, a subset of the individual martensitic volume fractions continues to grow at the cost of other martensitic variants, see Fig. 7.4(c). As the overall amount of dissipation induced by phase-transformations is lower as a result of the already partially martensitic initial state, the obtained final temperature provided in Fig. 7.5(f) is lower when compared to the temperature obtained for the initially purely austenitic crystal that was highlighted before in Fig. 7.4(f).

Figure 7.6 shows the results obtained for a simple shear deformation applied to an initially austenitic crystal. The deformation is set to $\boldsymbol{F} = \boldsymbol{I} + \gamma\, \boldsymbol{e}_1 \otimes \boldsymbol{e}_2$ with a maximum shear number of $\gamma_{\rm max} = 0.5$ as shown in Fig. 7.6(a). The resulting shear stresses are displayed in Fig. 7.6(b). Moreover, we show the individual martensite variants in Fig. 7.6(c). In contrast to the evolution of volume fractions obtained for the isochoric tensile deformation, see Figs. 7.4(c) and 7.5(c), in the case of simple shear a larger variety of independently—or rather non-identically—evolving volume fractions is observed. This results from the fact that the direction of the maximum principal strain is not constant for large-strain shear deformations. Accordingly, the individual martensitic variants considered within the crystal are activated in a non-uniform manner. The maximum overall martensitic volume fraction obtained during the simple shear load cycle is $\xi_{\mathrm{Mmax}} \approx 0.65$, see Fig. 7.6(d). As in the case of the isochoric deformation, we also provide the evolution of plastic strains in austenite, see Fig. 7.6(e), and the evolution of the temperature, cf. Fig. 7.6(f).

The results obtained for a simple shear deformation with an initially mixed martensitic-austenitic polycrystal with $\xi_{ij}|_{t=0} = 0.5/[n_r\, n_v]\ \forall\ (i,j) \Rightarrow \xi_{\mathrm{M}}|_{t=0} = \xi_{\mathrm{A}}|_{t=0} = 0.5$ are given in Fig. 7.7. In line with the results discussed for the isochoric loading path, the increase of the initial martensitic volume fraction within the polycrystal leads to an approach of the upper constraint $\xi_{\mathrm{M}} \rightarrow 1$, see Fig. 7.7(d). Due to the non-constant direction of maximum principal strain, a variety of individually evolving martensite variants is observed, cf. Fig. 7.7(c). It is also interesting to note that the evolution of plasticity in the austenitic phase of the initially mixed austenitic-martensitic crystal, cf. Fig. 7.7(e), is slightly less intense when compared to the plasticity evolution in the initially purely austenitic crystal, cf. Fig. 7.6(e). This is in line with the Greenwood-Johnson effect, which predicts growing plastic strains within the austenitic matrix material due to an ongoing evolution of martensite.

7.3.2.1 Isochoric tension

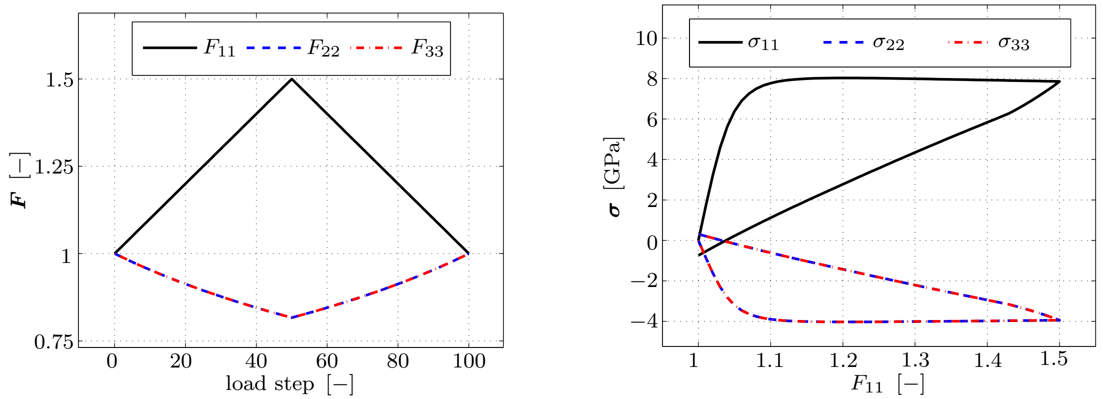

(a) Isochoric tension – load path.

(b) Stress-strain response.

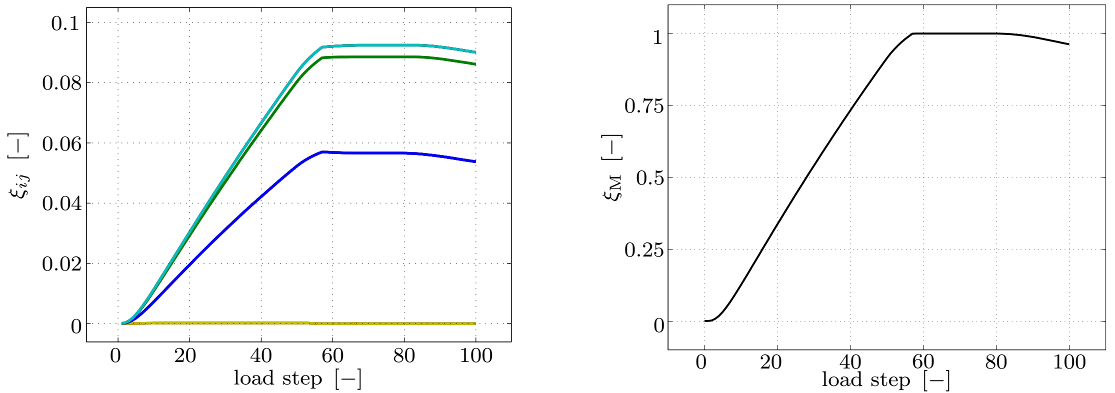

(c) Evolution of individual volume fractions ξ_{ij}.

(d) Evolution of the overall martensitic volume fraction $\xi_{\mathrm{M}} = \sum \xi_{ij}$.

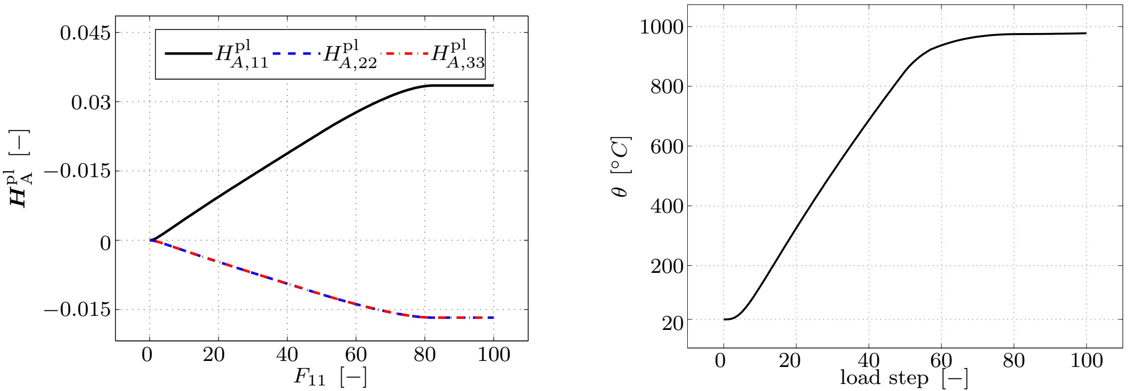

(e) Evolution of plasticity in austenite.

(f) Evolution of temperature.

Figure 7.4: Isochoric tension applied to an initially purely austenitic crystal, i.e. $\xi_{ij}|_{t=0} = 0 \; \forall \; (i,j) \Rightarrow \xi_{\mathrm{M}}|_{t=0} = 0$. Due to symmetry reasons, several of the considered 18 martensitic variants evolve in the same manner, see (c). The penalty scheme successfully enforces the constraints $\xi_{ij} \geq 0$ (c) and $\xi_{\mathrm{M}} \leq 1$ (d).

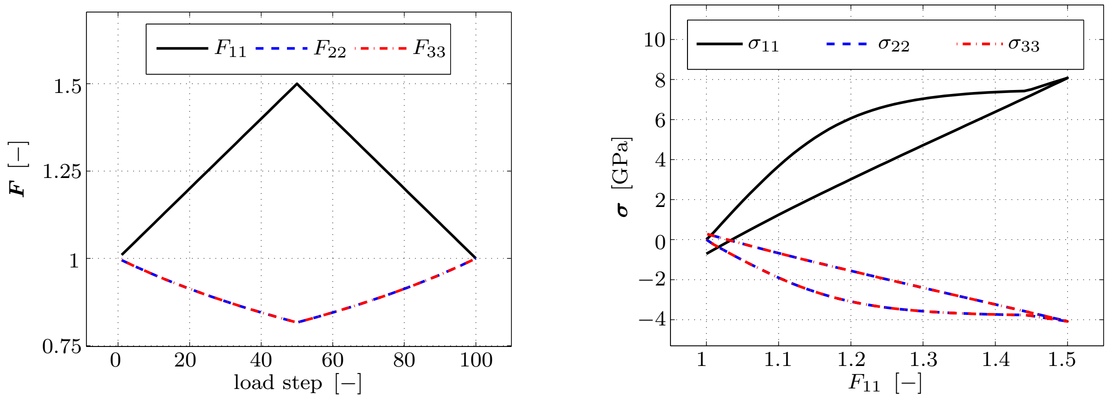

(a) Isochoric tension – load path.

(b) Stress-strain response.

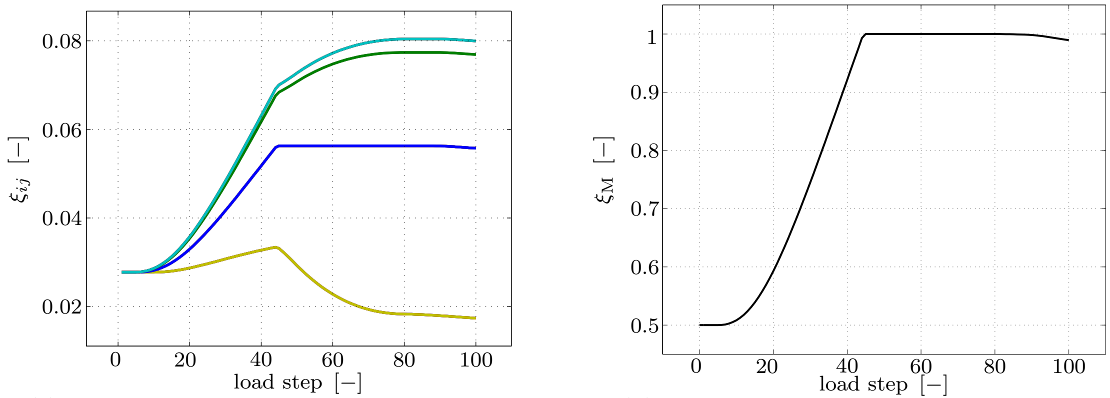

(c) Evolution of individual volume fractions ξ_{ij}.

(d) Evolution of the overall martensitic volume fraction $\xi_{\mathrm{M}} = \sum \xi_{ij}$.

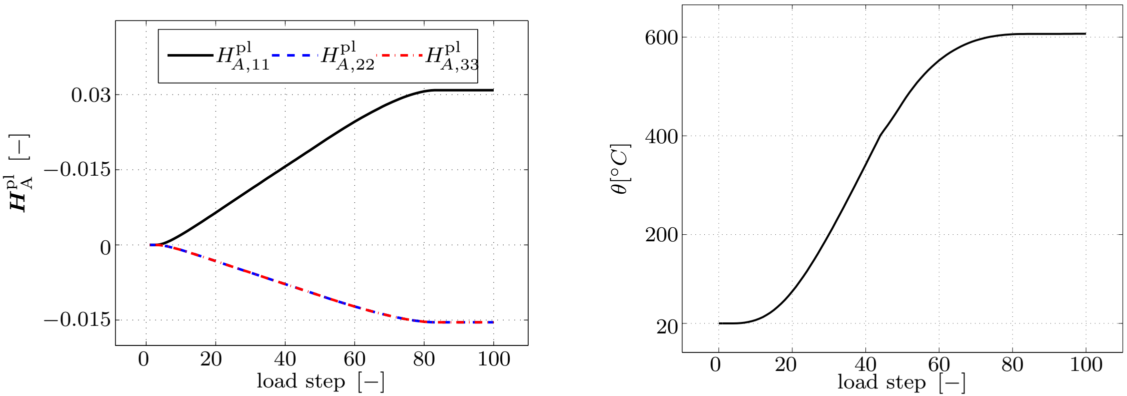

(e) Evolution of plasticity in austenite.

(f) Evolution of temperature.

Figure 7.5: Isochoric tension applied to a mixed austenitic-martensitic crystal with $\xi_{ij}|_{t=0} = 0.5/[n_r\, n_v]\ \forall\ (i,j) \Rightarrow \xi_{\mathrm{M}}|_{t=0} = 0.5$. As the upper constraint boundary $\xi_{\mathrm{M}} \to 1$ is reached (d), certain martensitic variants continue to grow at the cost of other variants (c). Due to the partially martensitic initial state of the crystal, the evolution of temperature (f) is less intense when compared to Fig. 7.4(f).

7.3.2.2 Simple shear

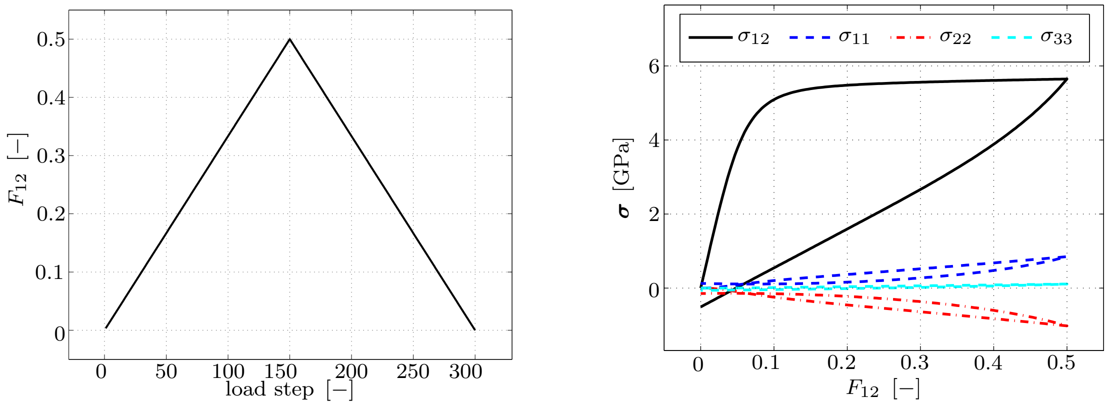

(a) Simple shear – load path.

(b) Stress-strain response.

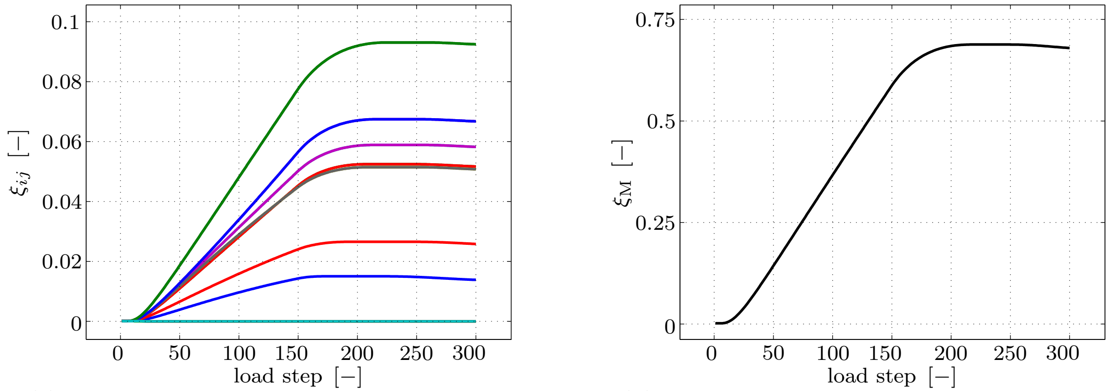

(c) Evolution of individual volume fractions ξ_{ij}.

(d) Evolution of the overall martensitic volume fraction $\xi_M = \sum \xi_{ij}$.

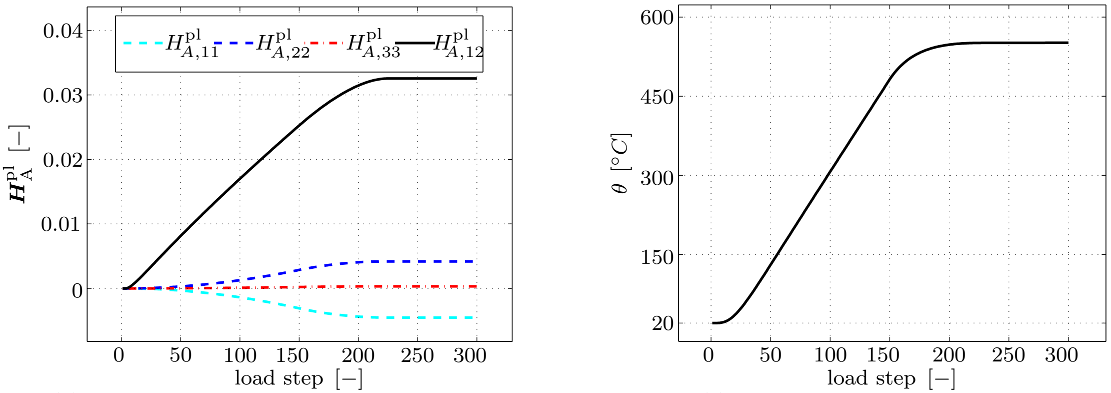

(e) Evolution of plasticity in austenite.

(f) Evolution of temperature.

Figure 7.6: Simple shear applied to an initially purely austenitic crystal, i.e. $\xi_{ij}|_{t=0} = 0 \; \forall \; (i,j) \Rightarrow \xi_M|_{t=0} = 0$. As the direction of maximum principal strain is non-constant for large shear deformations, a broad variety of individually evolving martensitic variants is observed (c).

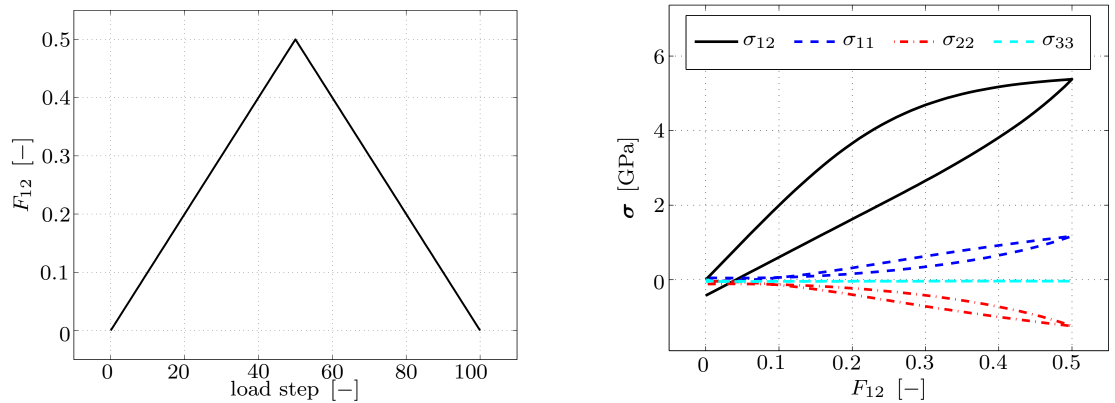

(a) Simple shear – load path.

(b) Stress-strain response.

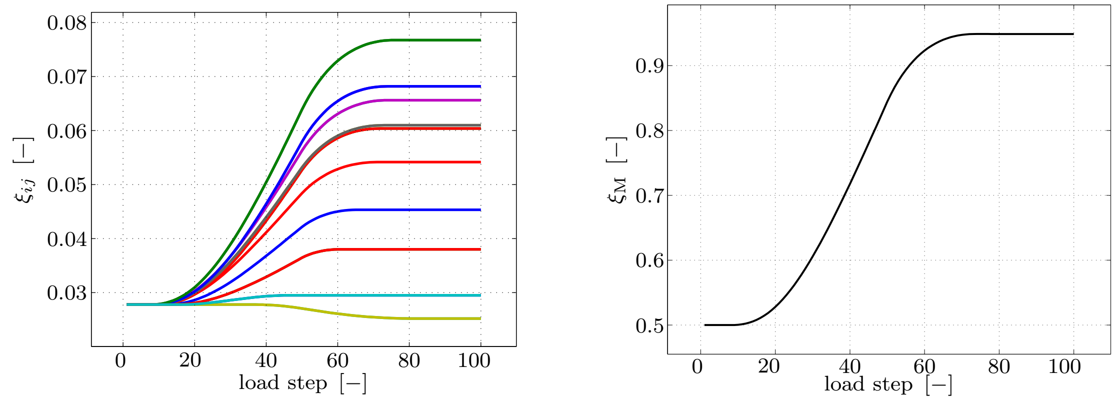

(c) Evolution of individual volume fractions ξ_{ij}.

(d) Evolution of the overall martensitic volume fraction $\xi_{\mathrm{M}} = \sum \xi_{ij}$.

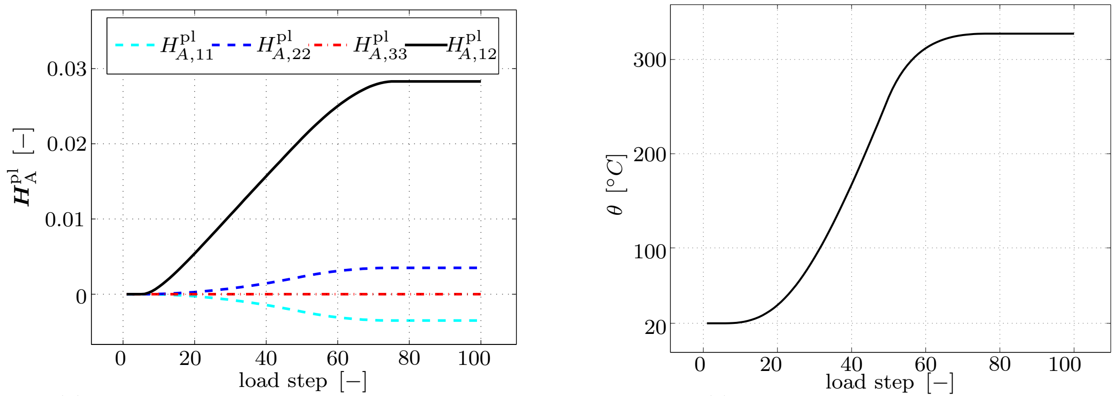

(e) Evolution of plasticity in austenite.

(f) Evolution of temperature.

Figure 7.7: Simple shear applied to a mixed austenitic-martensitic crystal with $\xi_{ij}|_{t=0} = 0.5/[n_r\, n_v]\ \forall\ (i,j) \Rightarrow \xi_{\mathrm{M}}|_{t=0} = 0.5$. As a result of the partially martensitic initial state (d), the evolution of temperature is less intense when compared to Fig. 7.6(f).

7.4 Enforcement of inequality constraints – convergence study

In this section we investigate the numerical behaviour of the penalty scheme provided in Algorithm 7, as the actual convergence behaviour strongly depends on the penalty parameters chosen. In fact, in order to guarantee a robust numerical behaviour of the overall solution algorithm, the inequality constraints (7.31) and (7.32) introduced in Section 7.2.1 are slightly modified. Note that several terms evaluated in the ODE system (7.20)–(7.23) contain expressions of the form $1/\xi_\mathrm{M}$, as e.g. the definition of $\bar{\mathbf{E}}_\mathrm{M}$ in (7.5). As a result, in view of the numerical implementation of the model, the inequality constraint (7.31) is reformulated as

$$\begin{aligned} \xi_{ij} &\geq \epsilon_h \; \forall \; (i,j) & (7.45)\\ \Rightarrow h_{ij} &= -\,\xi_{ij} + \epsilon_h \leq 0 \; \forall \; (i,j) \quad . & (7.46) \end{aligned}$$

Similarly, the expression $1/\xi_\mathrm{A}$ is evaluated within the ODE system, as e.g. in the expression of the mechanical dissipation rate density (7.25). To this end, the upper inequality constraint (7.32) is implemented numerically by

$$\begin{aligned} \xi_\mathrm{M} &= \sum_{i=1}^{n_d}\sum_{j=1}^{n_v} \xi_{ij} \leq 1 - \epsilon_h & (7.47)\\ \Rightarrow \bar{h} &= \xi_\mathrm{M} - 1 + \epsilon_h = \sum_{i=1}^{n_d}\sum_{j=1}^{n_v} \xi_{ij} - 1 + \epsilon_h \leq 0 & (7.48) \end{aligned}$$

with ϵ_h being referred to as the *constraint distance* in the following. To make sure that neither the state $\xi_\mathrm{M} = 0$ nor $\xi_\mathrm{A} = 0$ occurs within any situation, the constraint distance must be larger than the non-zero numerical penalty residuum ϵ_pen that is introduced in Algorithm 7, i.e. $\epsilon_h > \epsilon_\mathrm{pen}$. Moreover, the perturbation scheme applied to compute the numerical tangent operator required for the Newton-Raphson iteration of the implicit ODE system update, see Algorithm 5, has to be considered as well. It needs to be ensured that the perturbation increment ϵ_pert used therein—as it is added to ξ_{ij} among the other state variables—does in no situation lead to $\xi_\mathrm{M} = 0$ or $\xi_\mathrm{A} = 0$. To this end, we set the constraint distance to

$$\epsilon_h = \epsilon_\mathrm{pen} + \epsilon_\mathrm{pert} + 10^{-8} \qquad (7.49)$$

which ensures a numerically stable solution of the overall model formulation.

Note that the penalty values γ_{ij} and $\bar{\gamma}$ that are considered in the driving force of each martensitic variant—as introduced in (7.44)—are updated incrementally by adding the penalty parameters $\mathcal{C}_\gamma$ and $\mathcal{C}_{\bar{\gamma}}$, respectively, see Algorithm 7. In the following, we investigate how the choice of the penalty parameters $\mathcal{C}_\gamma$ and $\mathcal{C}_{\bar{\gamma}}$ influences the convergence behaviour of the overall penalty scheme for different loading conditions. As the actual evolution of martensitic variants within the polycrystal strongly depends on the acting load, cf. Section 7.3.2, we will show that different homogeneous load paths have to be considered for a determination of proper values for the penalty parameters $\mathcal{C}_\gamma$ and $\mathcal{C}_{\bar{\gamma}}$. To this end, in Sections 7.4.1 and 7.4.2, we show the penalty convergence behaviour at both the upper and the lower constraint boundary for an isochoric tensile load. Moreover, in Sections 7.4.3 and 7.4.4, the penalty convergence is elaborated for a homogeneous shear deformation. Note that parameter $\mathcal{C}_{\bar{\gamma}}$ is connected to the penalty-based enforcement of the upper boundary constraint for the sum of all martensitic volume fractions, (7.48), whereas $\mathcal{C}_\gamma$ facilitates the iterative fulfillment of the lower constraint boundary for each individual martensitic variant, (7.46).

For the investigation of the penalty behaviour close to the upper constraint boundary, we start with a high initial martensitic volume fraction of $\xi_\mathrm{M} = 0.9$ with equally distributed martensitic variants, i.e. $\xi_{ij}|_{t=0} = \xi_\mathrm{M}/[n_r\, n_v]\ \forall\ (i,j)$. Figure 7.8 provides the results obtained for an isochoric tensile loading state. The evolution of individual volume fractions given in Fig. 7.8(b) highlights that no variant violates the lower boundary constraint (7.46). The required penalty iterations provided in Figs. 7.8(c) and 7.8(e) are thus required for the sole fulfillment of the upper boundary constraint, (7.48). The results obtained for the isochoric load path suggests that the penalty parameter $\mathcal{C}_{\bar{\gamma}}$ should be chosen in a range of $\mathcal{C}_{\bar{\gamma}} = 20 \ldots 300$. For lower values, the number of necessary penalty iterations increases to higher double-digit values, whereas for higher values $\mathcal{C}_{\bar{\gamma}} \gg 300$ the negative contribution $-\left\langle \bar{\mu}(\mathcal{C}_{\bar{\gamma}}) + \bar{\gamma}\,\bar{h} \right\rangle$ to the driving force of the martensitic variants (7.44) is so significant that the evolution is reversed and the solution starts to be inexact as indicated in Fig. 7.8(f).

To assess the convergence behaviour close to the lower boundary constraint we set the volume fractions of the individual martensitic variants close to zero, where the smallest reasonable starting value coincides with the constraint distance (7.49), i.e. $\xi_{ij}|_{t=0} = \epsilon_h\ \forall\ (i,j)$. The results obtained for an isochoric load are provided in Fig. 7.9. Note that the penalty scheme is activated as $\xi_\mathrm{M} \to 1$, see Figs. 7.9(d) and 7.9(c), respectively. The high number of 60–70 penalty iterations for a penalty parameter $\mathcal{C}_\gamma = 20$ results from the fact that the martensite variants with zero volume fraction are now constrained at $\xi_{ij} \geq \epsilon_h$. In an unconstrained setting, these variants would decrease further as highlighted earlier in Fig. 7.8(b). A resonable choice for the penalty parameter governing the lower constraint is $\mathcal{C}_\gamma = 2000$ as shown in Fig. 7.9(e).

The penalty convergence results obtained for large shear strains as depicted in Figs. 7.10 and 7.11 underline that $\mathcal{C}_{\bar{\gamma}} = 300$ and $\mathcal{C}_\gamma = 2000$ are reasonable values for the penalty parameters used in the applied penalty scheme. Taking a closer look at the definition of the penalised driving force for the individual martensite variants (7.44) shows why $\mathcal{C}_{\bar{\gamma}} \ll \mathcal{C}_\gamma$ has to generally hold for this model. If the upper boundary constraint is violated, then all martensite variants are penalised at the same time—in consequence, the more martensite variants are considered within the crystal, the lower the ratio $\mathcal{C}_{\bar{\gamma}}/\mathcal{C}_\gamma$ has to be to maintain efficient convergency of the overall implementation.

7.4.1 Tensile load – upper constraint boundary

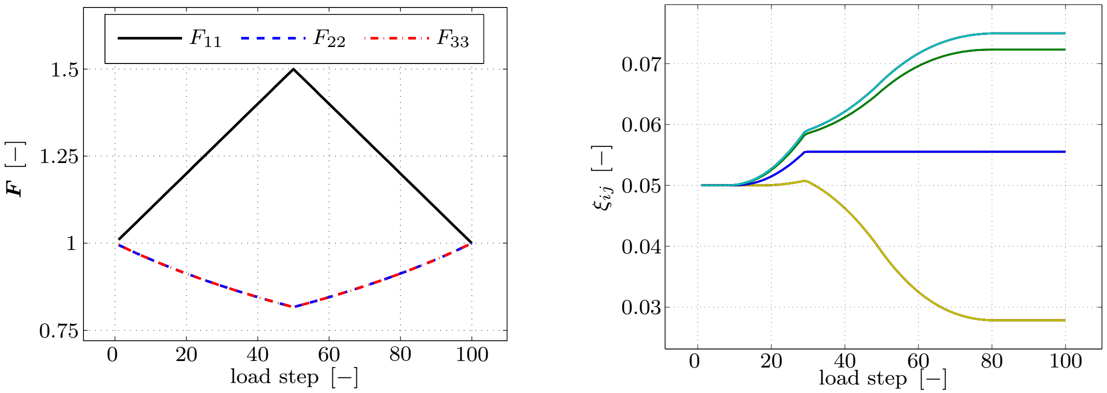

(a) Isochoric tension – load path.

(b) Evolution of individual volume fractions ξ_{ij}.

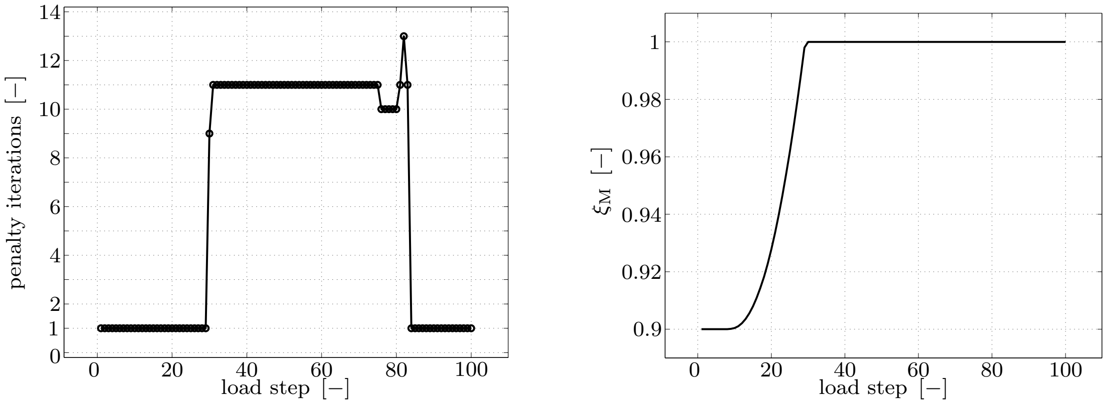

(c) Number of penalty iterations required for each load step with penalty parameter $\mathcal{C}_{\bar{\gamma}} = 20$.

(d) Evolution of bounded quantity $\xi_{\mathrm{M}} \leq 1 - \epsilon_h$ with penalty parameter $\mathcal{C}_{\bar{\gamma}} = 20$.

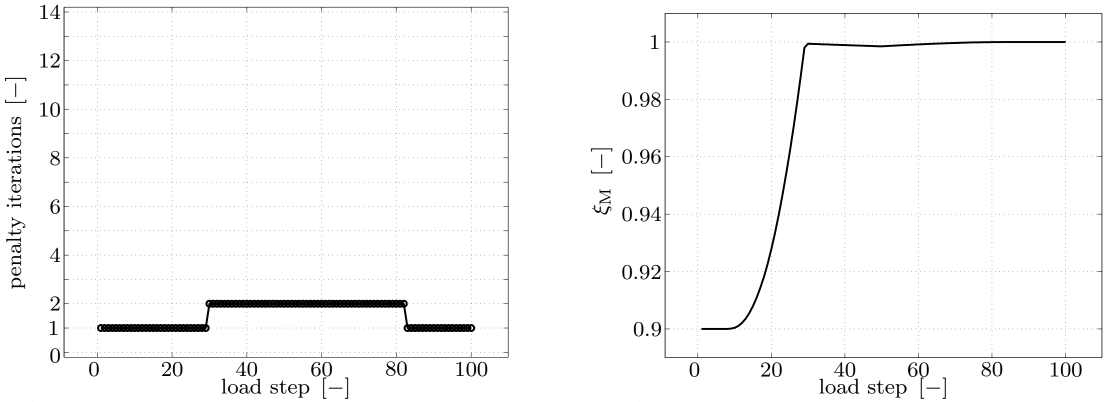

(e) Number of penalty iterations required for each load step with penalty parameter $\mathcal{C}_{\bar{\gamma}} = 300$.

(f) Evolution of bounded quantity $\xi_{\mathrm{M}} \leq 1 - \epsilon_h$ with penalty parameter $\mathcal{C}_{\bar{\gamma}} = 300$.

Figure 7.8: Convergence behaviour of the implemented penalty scheme enforcing $\xi_{\mathrm{M}} \leq 1 - \epsilon_h$ depending on the penalty parameter $\mathcal{C}_{\bar{\gamma}}$ for an isochoric tensile load with $F_{11,\max} = 1.5$ and $t_{\max} = 1\mathrm{s}$, where the martensite variants are initially set to $\xi_{ij}|_{t=0} = 0.9/[n_r\, n_v]\ \forall\ (i,j) \Rightarrow \xi_{\mathrm{M}}|_{t=0} = 0.9$.

7.4.2 Tensile load – lower constraint boundary

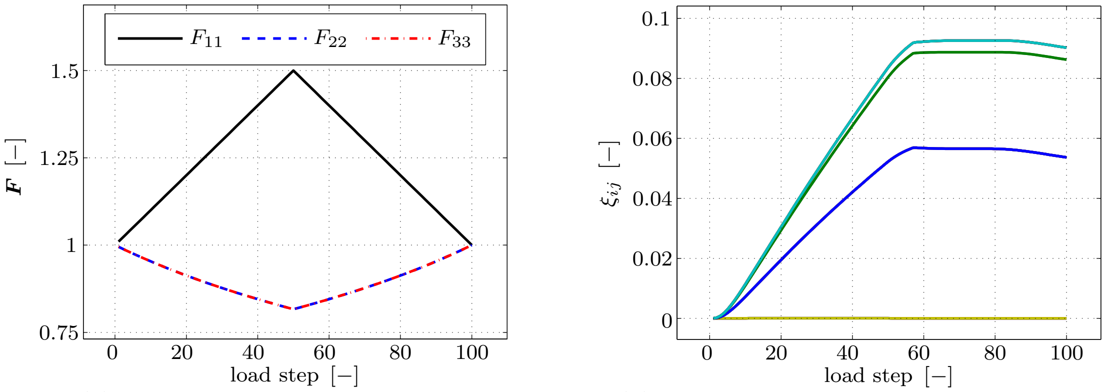

(a) Isochoric tension – load path.

(b) Evolution of individual volume fractions bounded to $\xi_{ij} \geq \epsilon_h$.

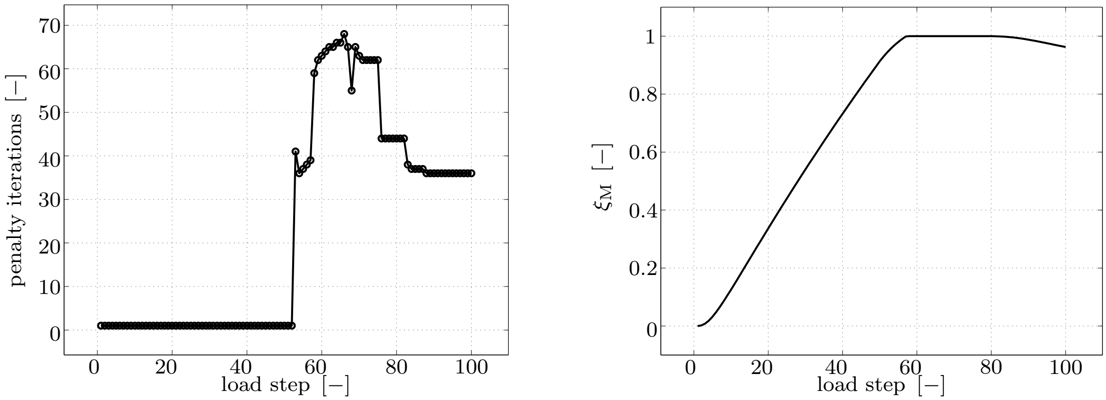

(c) Number of penalty iterations required for each load step with penalty parameter $\mathcal{C}_\gamma = 20$.

(d) Evolution of the overall volume fraction ξ_{M} with penalty parameter $\mathcal{C}_\gamma = 20$.

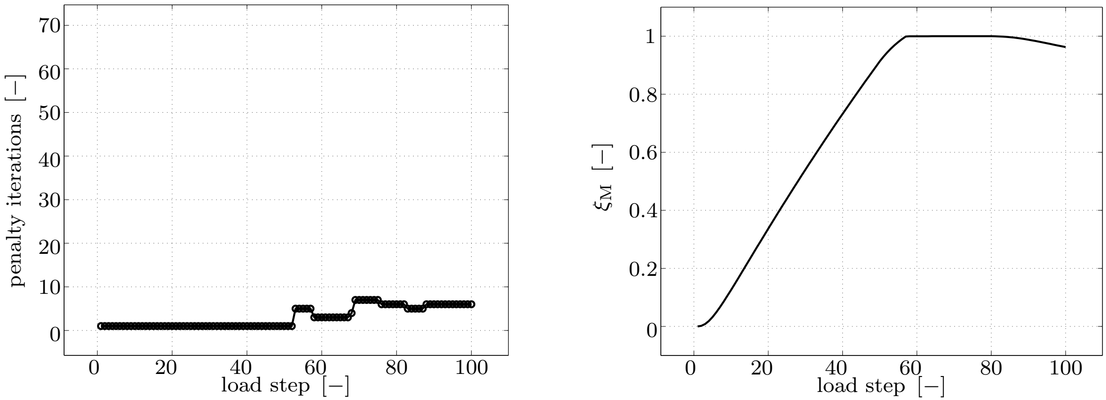

(e) Number of penalty iterations required for each load step with penalty parameter $\mathcal{C}_\gamma = 2000$.

(f) Evolution of the overall volume fraction ξ_{M} with penalty parameter $\mathcal{C}_\gamma = 2000$.

Figure 7.9: Convergence behaviour of the implemented penalty scheme enforcing $\xi_{ij} \geq \epsilon_h$ depending on the penalty parameter $\mathcal{C}_\gamma$ for an isochoric tensile load with $F_{11,\max} = 1.5$ and $t_{\max} = 1\mathrm{s}$, where the martensite variants are initially set to $\xi_{ij}|_{t=0} = \epsilon_h \ \forall \ (i,j) \Rightarrow \xi_{\mathrm{M}}|_{t=0} = n_r \, n_v \, \epsilon_h$.

7.4.3 Shear load – upper constraint boundary

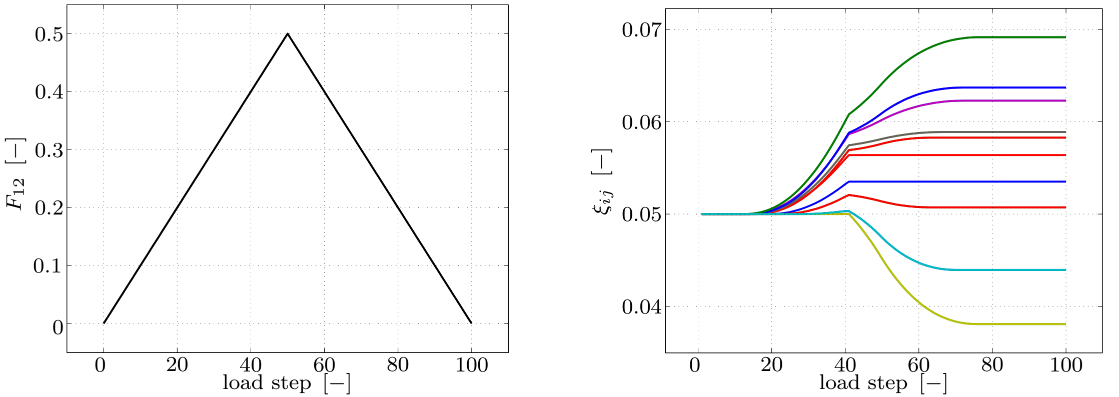

(a) Simple shear – load path.

(b) Evolution of individual volume fractions ξ_{ij}.

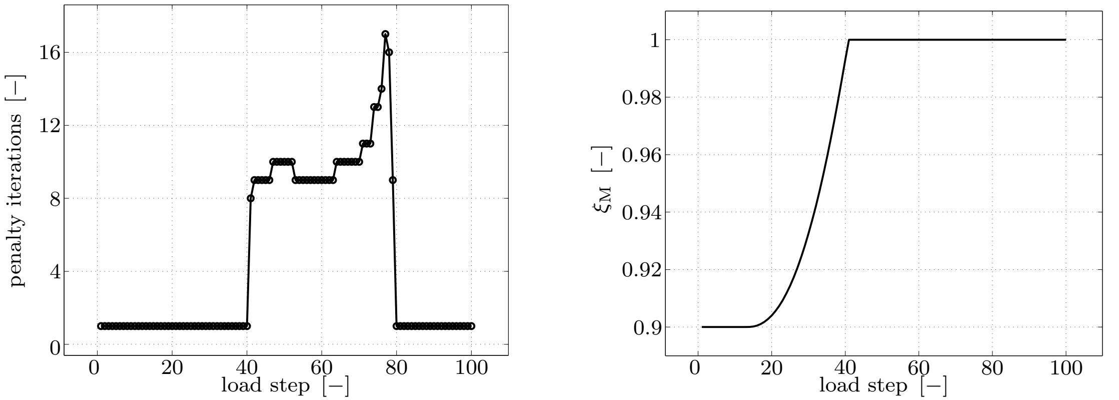

(c) Number of penalty iterations required for each load step with penalty parameter $\mathcal{C}_{\bar{\gamma}} = 20$.

(d) Evolution of bounded quantity $\xi_{\mathrm{M}} \leq 1 - \epsilon_h$ with penalty parameter $\mathcal{C}_{\bar{\gamma}} = 20$.

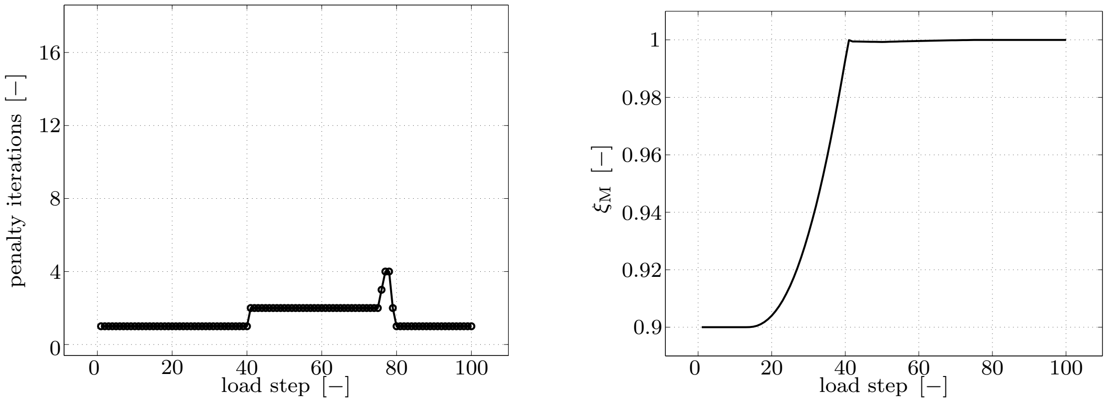

(e) Number of penalty iterations required for each load step with penalty parameter $\mathcal{C}_{\bar{\gamma}} = 300$.

(f) Evolution of bounded quantity $\xi_{\mathrm{M}} \leq 1 - \epsilon_h$ with penalty parameter $\mathcal{C}_{\bar{\gamma}} = 300$.

Figure 7.10: Convergence behaviour of the implemented penalty scheme enforcing $\xi_{\mathrm{M}} \leq 1 - \epsilon_h$ depending on the penalty parameter $\mathcal{C}_{\bar{\gamma}}$ for a simple shear load with $F_{12,\mathrm{max}} = 1.5$ and $t_{\mathrm{max}} = 1\mathrm{s}$, where the martensite variants are initially set to $\xi_{ij}|_{t=0} = 0.9/[n_r\, n_v] \; \forall \; (i,j) \Rightarrow \xi_{\mathrm{M}}|_{t=0} = 0.9$.

7.4.4 Shear load – lower constraint boundary

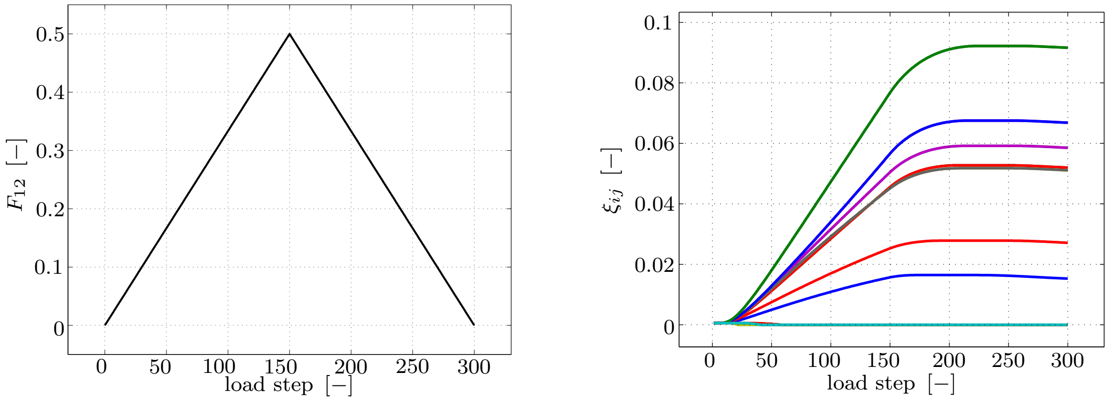

(a) Simple shear – load path.

(b) Evolution of individual volume fractions bounded to $\xi_{ij} \geq \epsilon_h$.

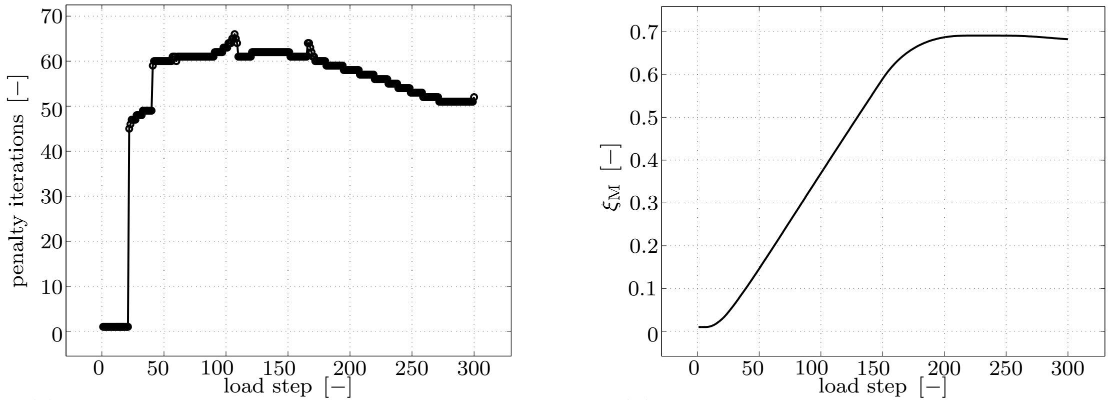

(c) Number of penalty iterations required for each load step with penalty parameter $\mathcal{C}_\gamma = 20$.

(d) Evolution of the overall volume fraction ξ_{M} with penalty parameter $\mathcal{C}_\gamma = 20$.

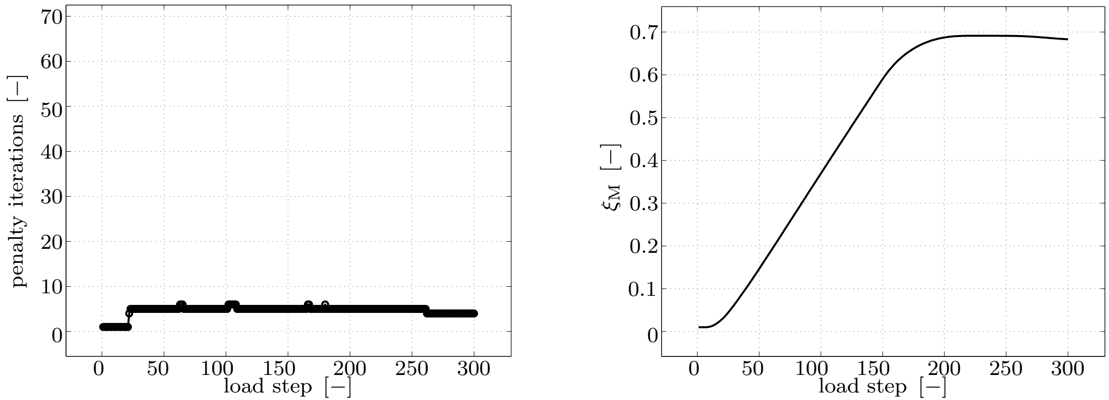

(e) Number of penalty iterations required for each load step with penalty parameter $\mathcal{C}_\gamma = 2000$.

(f) Evolution of the overall volume fraction ξ_{M} with penalty parameter $\mathcal{C}_\gamma = 2000$.

Figure 7.11: Convergence behaviour of the implemented penalty scheme enforcing $\xi_{ij} \geq \epsilon_h$ depending on the penalty parameter $\mathcal{C}_\gamma$ for a simple shear load with $F_{12,\max} = 1.5$ and $t_{\max} = 1\text{s}$, where the martensite variants are initially set to $\xi_{ij}|_{t=0} = \epsilon \ \forall \ (i,j) \Rightarrow \xi_{\mathrm{M}}|_{t=0} = n_r \, n_v \, \epsilon$.

7.5 Finite element implementation

In this section, a finite element implementation of the finite-strain thermo-elasto-plastic phase-transformation model is shown. The previously presented results, see Sections 7.3.2 and 7.4, were obtained with the help of a Fortran-implementation of the overall model formulation. For the implementation into three-dimensional finite elements, the Fortran-based code is linked to the commercial finite element program ABAQUS via the ABAQUS VUMAT interface. The ABAQUS VUMAT interface represents a vectorised user material ('UMAT') routine interface for the efficient explicit solution of dynamic boundary value problems. As industrial process simulations—such as machining or drilling simulations—are often carried out using dynamic simulations with explicit finite element integration schemes, cf. [63, 64], we provide a representative finite element based dynamic solution to an inhomogeneous adiabatic problem by means of a stretched block with hole.

Figure 7.12(a) provides the finite element discretisation of the considered three-dimensional block with hole, where we use three-dimensional 8-node hexahedral ABAQUS C3D8R elements. The Dirichlet boundary conditions given in Fig. 7.12(b) show the fixed bottom plane while tensile displacements are applied to the top plane of the body. The tensile displacement is applied in a short time of $10^{-4}\,\mathrm{s}$, facilitating an explicit solution with consideration of dynamic effects. As initial conditions, we chose $\theta|_{t=0} = 20°\mathrm{C}$ for the initial temperature and $\xi_{ij}|_{t=0} = 0.01 \Rightarrow \xi_\mathrm{M}|_{t=0} = 0.18$ for the initial martensite variant distribution. The obtained von Mises stress distribution σ_vM as well as the evolution of temperature θ at $5\,\%$ macroscopic tensile deformation are provided in Figs. 7.12(c) and 7.12(d), respectively.

The evolution of plastic strains in austenite is depicted in Fig. 7.13 for two deformation states, namely at $5\,\%$ and at $15\,\%$ tensile strain, respectively. For both deformation states we show the distribution of the tensile component $H^\mathrm{pl}_{\mathrm{A},22}$ of the plastic strain tensor $\boldsymbol{H}^\mathrm{pl}_\mathrm{A}$, see Figs. 7.13(a) and 7.13(b). Moreover, the corresponding accumulated plastic strains are provided in Figs. 7.13(c) and 7.13(d), respectively.

For the evolution of volume fractions provided in Fig. 7.14, we restrict the visualisations to the volume fractions of austenite ξ_A and overall martensite ξ_M, i.e. we do not provide seperate visualisations for all 18 martensite variants considered in the presented model implementation. For details on the evolution of individual martensitic variants for different homogeneous load cases, the reader is instead referred to Section 7.3.2.

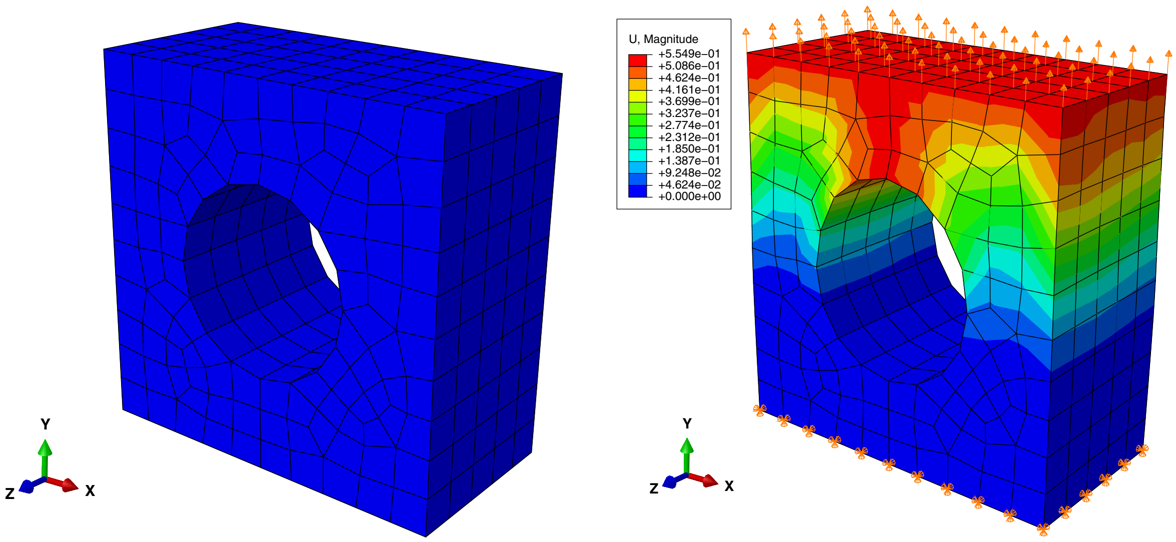
U, Magnitude
+5.549e−01
+5.086e−01
+4.624e−01
+4.161e−01
+3.699e−01
+3.237e−01
+2.774e−01
+2.312e−01
+1.850e−01
+1.387e−01
+9.248e−02
+4.624e−02
+0.000e+00
Y
Z
X
Y
Z
X

(a) Finite element discretisation of the model.

(b) Applied Dirichlet boundary conditions and resulting displacement magnitude $|\boldsymbol{u}|$.

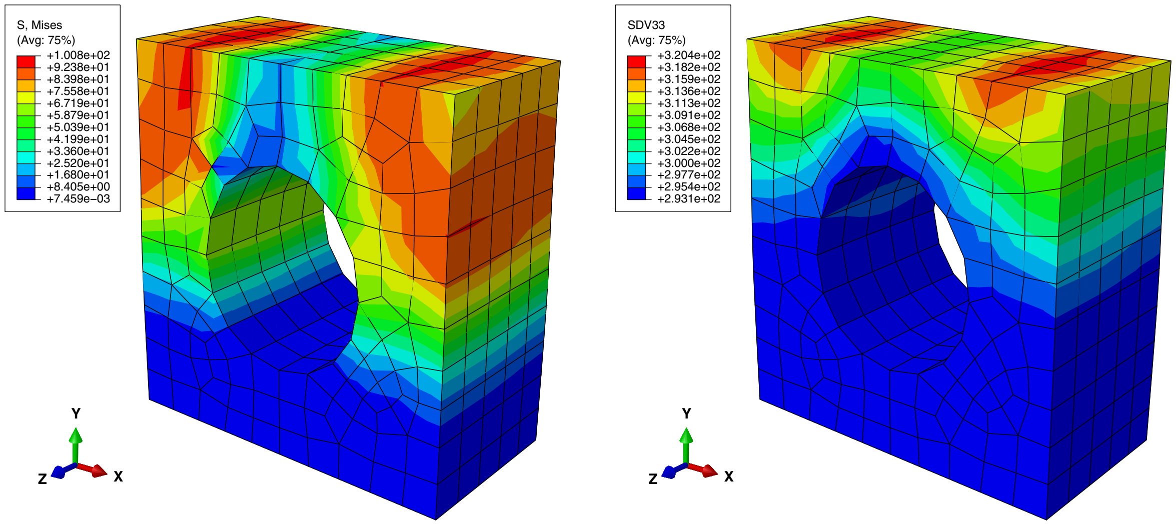
S, Mises
(Avg: 75%)
+1.008e+02
+9.238e+01
+8.398e+01
+7.558e+01
+6.719e+01
+5.879e+01
+5.039e+01
+4.199e+01
+3.360e+01
+2.520e+01
+1.680e+01
+8.405e+00
+7.459e−03
SDV33
(Avg: 75%)
+3.204e+02
+3.182e+02
+3.159e+02
+3.136e+02
+3.113e+02
+3.091e+02
+3.068e+02
+3.045e+02
+3.022e+02
+3.000e+02
+2.977e+02
+2.954e+02
+2.931e+02
Y
Z
X
Y
Z
X

(c) Von Mises equivalent stress σ_{vM} [MPa] obtained at 5 % macroscopic strain.

(d) Temperature θ [°C] obtained at 5 % macroscopic strain.

Figure 7.12: Representative finite element simulation of the thermo-elasto-plastic finite strain model for coupled phase-transformations and plasticity introduced in this chapter. The Fortran-based model implementation is used as an ABAQUS user subroutine via the ABAQUS VUMAT interface. For the evolution of plasticity and volume fractions, see Figs. 7.13 and 7.14, respectively.

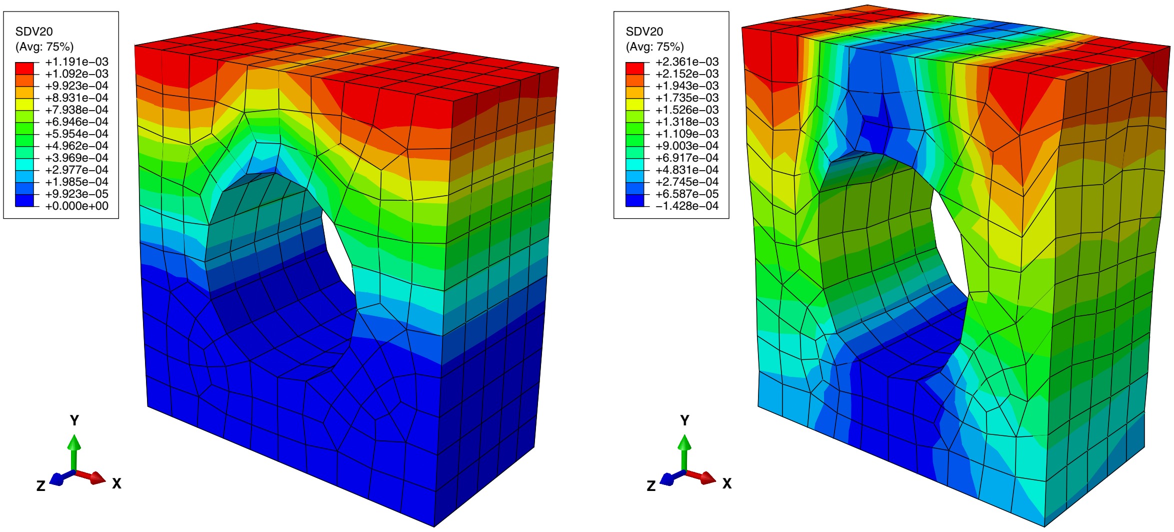
SDV20
(Avg: 75%)
+1.191e−03
+1.092e−03
+9.923e−04
+8.931e−04
+7.938e−04
+6.946e−04
+5.954e−04
+4.962e−04
+3.969e−04
+2.977e−04
+1.985e−04
+9.923e−05
+0.000e+00
Y
Z
X
SDV20
(Avg: 75%)
+2.361e−03
+2.152e−03
+1.943e−03
+1.735e−03
+1.526e−03
+1.318e−03
+1.109e−03
+9.003e−04
+6.917e−04
+4.831e−04
+2.745e−04
+6.587e−05
−1.428e−04
Y
Z
X

(a) Plastic strain in austenite $H^{\mathrm{pl}}_{\mathrm{A},22}$ in tensile direction at 5 % macroscopic strain.

(b) Plastic strain in austenite $H^{\mathrm{pl}}_{\mathrm{A},22}$ in tensile direction at 15 % macroscopic strain.

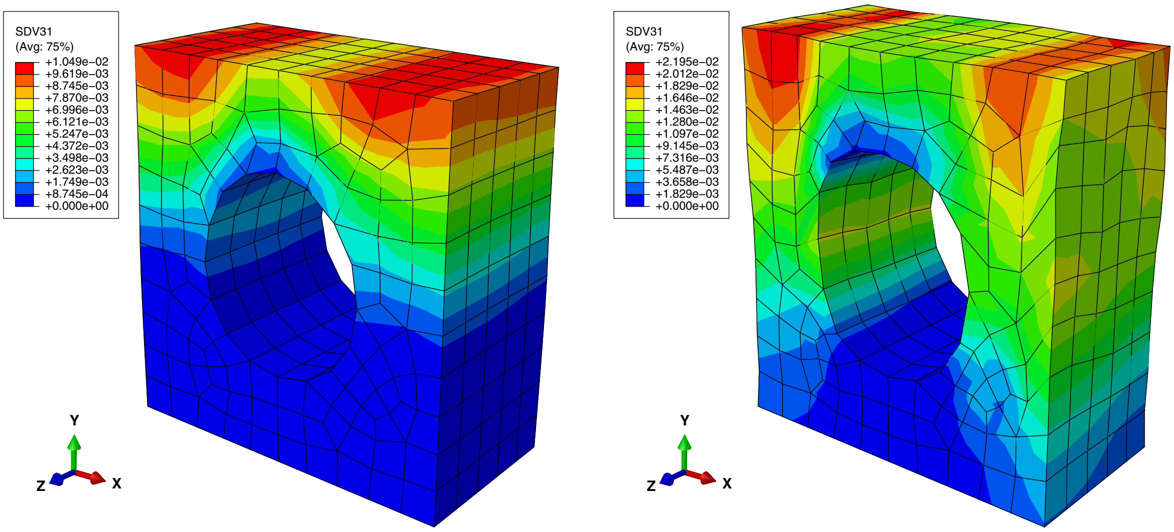
SDV31
(Avg: 75%)
+1.049e−02
+9.619e−03
+8.745e−03
+7.870e−03
+6.996e−03
+6.121e−03
+5.247e−03
+4.372e−03
+3.498e−03
+2.623e−03
+1.749e−03
+8.745e−04
+0.000e+00
Y
Z
X
SDV31
(Avg: 75%)
+2.195e−02
+2.012e−02
+1.829e−02
+1.646e−02
+1.463e−02
+1.280e−02
+1.097e−02
+9.145e−03
+7.316e−03
+5.487e−03
+3.658e−03
+1.829e−03
+0.000e+00
Y
Z
X

(c) Accumulated plastic strain in austenite at 5 % macroscopic strain.

(d) Accumulated plastic strain in austenite at 15 % macroscopic strain.

Figure 7.13: Evolution of plasticity in austenite at different states of deformation. Plasticity in austenite is induced not only by the deformation of the body, but also as a result of the evolution of martensite. This effect—known as Greenwood-Johnson effect—is considered in the yield function of austenite in a thermodynamically consistent manner.

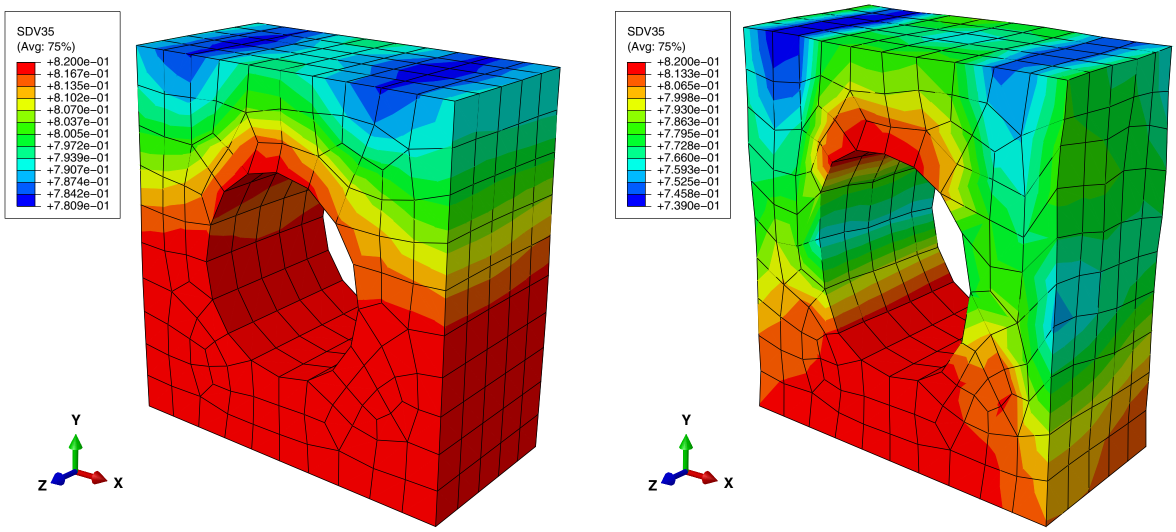
SDV35
(Avg: 75%)
+8.200e−01
+8.167e−01
+8.135e−01
+8.102e−01
+8.070e−01
+8.037e−01
+8.005e−01
+7.972e−01
+7.939e−01
+7.907e−01
+7.874e−01
+7.842e−01
+7.809e−01
Y
Z
X
SDV35
(Avg: 75%)
+8.200e−01
+8.133e−01
+8.065e−01
+7.998e−01
+7.930e−01
+7.863e−01
+7.795e−01
+7.728e−01
+7.660e−01
+7.593e−01
+7.525e−01
+7.458e−01
+7.390e−01
Y
Z
X

(a) Volume fraction of austenite ξ_{A} at 5 % macroscopic strain.

(b) Volume fraction of austenite ξ_{A} at 15 % macroscopic strain.

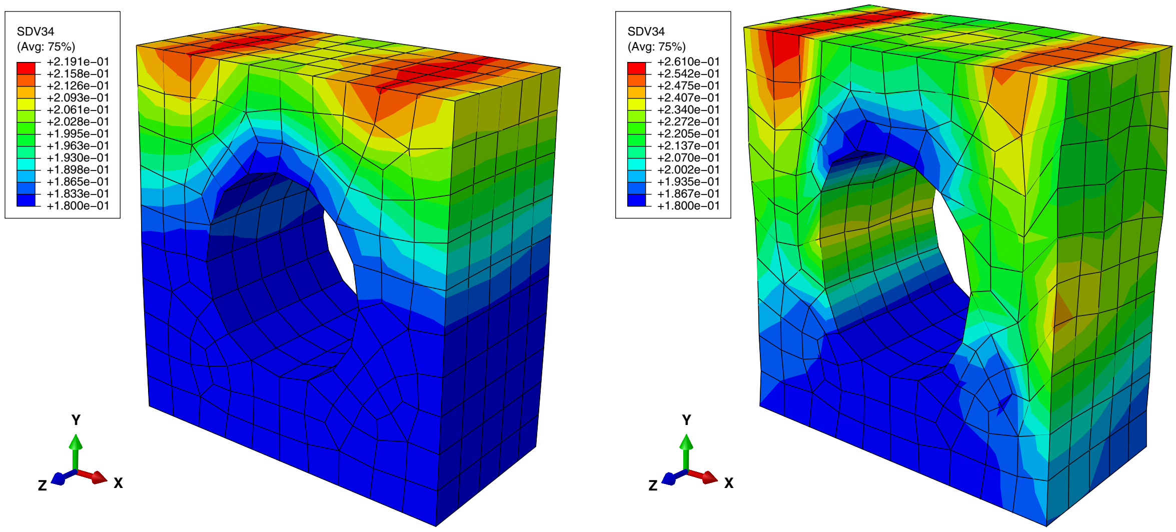
SDV34
(Avg: 75%)
+2.191e−01
+2.158e−01
+2.126e−01
+2.093e−01
+2.061e−01
+2.028e−01
+1.995e−01
+1.963e−01
+1.930e−01
+1.898e−01
+1.865e−01
+1.833e−01
+1.800e−01
Y
Z
X
SDV34
(Avg: 75%)
+2.610e−01
+2.542e−01
+2.475e−01
+2.407e−01
+2.340e−01
+2.272e−01
+2.205e−01
+2.137e−01
+2.070e−01
+2.002e−01
+1.935e−01
+1.867e−01
+1.800e−01
Y
Z
X

(c) Overall volume fraction of martensite ξ_{M} at 5 % macroscopic strain.

(d) Overall volume fraction of martensite ξ_{M} at 15 % macroscopic strain.

Figure 7.14: Evolution of volume fractions within the considered body at different states of deformation. Besides the evolution of austenite shown in (a) and (b), we restrict the visualisation to the evolution of the overall martensite volume fraction $\xi_{\mathrm{M}} = \sum \xi_{ij}$, cf. (c) and (d), i.e. we do not provide seperate visualisations of the individual distributions of all 18 martensite variants that are considered within this simulation.

7.6 Appendix – material parameters

The Bain strains related to the austenite-martensite transformation, see (7.1), are identified as $U^{\text{tr}}_{\text{lon}} = 0.8376$ and $U^{\text{tr}}_{\text{lat}} = 1.1138$. Moreover, the elastic properties of the referential martensitic unit cell—cf. (7.4) and (7.5)—are chosen as

$$
\begin{aligned}
[\mathsf{\mathbf{E}}_{\text{ref}}]_{1111} &= 617\,\text{GPa} \quad , && (7.50)\\
[\mathsf{\mathbf{E}}_{\text{ref}}]_{2222} &= [\mathsf{\mathbf{E}}_{\text{ref}}]_{3333} = 497\,\text{GPa} \quad , && (7.51)\\
[\mathsf{\mathbf{E}}_{\text{ref}}]_{1122} &= [\mathsf{\mathbf{E}}_{\text{ref}}]_{1133} = 265\,\text{GPa} \quad , && (7.52)\\
[\mathsf{\mathbf{E}}_{\text{ref}}]_{2233} &= 405\,\text{GPa} \quad , && (7.53)\\
[\mathsf{\mathbf{E}}_{\text{ref}}]_{1212} &= [\mathsf{\mathbf{E}}_{\text{ref}}]_{1313} = 263\,\text{GPa} \quad , && (7.54)\\
[\mathsf{\mathbf{E}}_{\text{ref}}]_{2323} &= 278\,\text{GPa} \quad , && (7.55)
\end{aligned}
$$

whereas the elastic properties of the isotropic austenite matrix are set to

$$
\begin{aligned}
[\mathsf{\mathbf{E}}_{\text{A}}]_{1111} &= [\mathsf{\mathbf{E}}_{\text{A}}]_{2222} = [\mathsf{\mathbf{E}}_{\text{A}}]_{3333} = 309\,\text{GPa} \quad , && (7.56)\\
[\mathsf{\mathbf{E}}_{\text{A}}]_{1122} &= [\mathsf{\mathbf{E}}_{\text{A}}]_{2233} = [\mathsf{\mathbf{E}}_{\text{A}}]_{1133} = 136\,\text{GPa} \quad , && (7.57)\\
[\mathsf{\mathbf{E}}_{\text{A}}]_{1212} &= [\mathsf{\mathbf{E}}_{\text{A}}]_{2323} = [\mathsf{\mathbf{E}}_{\text{A}}]_{1313} = 87\,\text{GPa} \quad . && (7.58)
\end{aligned}
$$

Moreover, the used scalar-valued parameters are given in Table 7.1.

Table 7.1: TRIP steel material parameters considered in the current chapter.

TRIP steel phase	material parameter	symbol	value
austenite A (parent phase)	latent heat	λ^{M}_0	0
	initial yield stress	$\mathsf{Y}^{\text{init}}_{\text{A}}$	1.65 GPa
	saturation yield stress	$\mathsf{Y}^{\text{sat}}_{\text{A}}$	$2\,\mathsf{Y}^{\text{init}}_{\text{A}}$
martensite M	transformation strain	$\boldsymbol{U}^{\text{tr}}_{\text{ref}}$	200 GPa
	latent heat	λ^{M}_0	0.15 GPa
	initial yield stress	$\mathsf{Y}^{\text{init}}_{\text{M}}$	1.9 GPa
	saturation yield stress	$\mathsf{Y}^{\text{sat}}_{\text{M}}$	$1.5\,\mathsf{Y}^{\text{init}}_{\text{M}}$
common parameters:	heat capacity	$c_\bullet$	5×10^{-3} GPa/K
	hardening decay parameter	$\kappa_\bullet$	$10\,\text{s}^{-2}$
	transformation viscosities	$\eta^\circ_\bullet$	25 GPa/s
	reference temperature	θ^{tr}_0	263.15 K

8 Concluding remarks

In this work, two approaches for the modelling and simulation of phase-transformations in elasto-plastic polycrystals are presented. The model elaborated in the course of Chapters 2-6 is based on statistical physics, where transformation probabilites driving the evolution of volume fractions are computed from Gibbs energy barriers. The model is implemented in a micro-sphere framework for the efficient simulation of polycrystalline materials undergoing austenitic-martensitic phase-transformations, such as shape memory alloys and TRIP steels. In Chapter 7, a finite-strain phase-transformation model based on selected representative transformation directions is implemented and discussed.

The model for the simulation of phase-transformations in polycrystalline SMA presented in **Chapter 2** is based on a one-dimensional, thermodynamically consistent model introduced in [51]. The model is implemented into an affine micro-sphere framework, facilitating the simulation of polycrystalline aggregates within three-dimensional boundary value problems. The tension-compression asymmetry observed in experiments is incorporated by means of individual transformation strains considered for the martensitic tension and compression phase, respectively. Due to an explicit but A-stable integration scheme applied to the system of evolution equations, an efficient yet stable numerical solution of the overall model formulation is obtained. However, it is shown that the affine micro-sphere kinematics induce a macroscopic Poisson's ratio of $\nu_{\mathrm{P}} = 1/4$. To adress this limitation—and in view of the incorporation of purely deviatoric plasticity effects—an extension to a non-affine micro-sphere framework is presented in Chapter 3.

The extension of the aforementioned model to non-affine micro-sphere kinematics is elaborated in **Chapter 3**, where the volumetric-deviatoric split in kinematics facilitates capturing the actual macro-level Poisson's ratio of SMA. However, the introduced split in kinematics has a significant influence on the underlying phase-transformation model—instead of simple parabolas, the Gibbs phase potentials now take the form of elliptical paraboloids in volumetric-deviatoric strain space. As a result, the computation of the Gibbs energy barriers driving the evolution of volume fractions turns into a computationally advanced problem. To this end, we introduce a numerical minimisation scheme to solve for the minimum of the parametric Gibbs energy intersection curves. We show that the model is capable of reproducing the stress-strain-temperature response which is considered as one of the main features of SMA. Moreover, the model captures the pseudo-plastic response of SMA observed at low temperatures and the pseudo-elastic response observed at elevated temperatures. Finally, we simulate tensile step tests, showing that the proposed model captures experimentally observed stress-strain envelopes and appropriate stress-strain minor loops of SMA as well.

In view of the simulation of austenitic-martensitic phase-transformations in TRIP steels, the model has to be extended to the capturing of interactions between phase-transformations and plasticity. The formulation presented in **Chapter 4** shows an extension of the underlying one-dimensional model, where individually evolving plastic strains are considered for each of the material phases by an extension of the Helmholtz free energy functions. Moreover, a so-called plasticity inheritance framework is introduced—motivated by the changes in dislocation densities resulting from an evolving phase front that separates two phases. Numerical results for TRIP steel material parameters are provided and it is shown that the proposed coupling mechanism between phase-transformations and plasticity gives promising results in view of further enhancements of the model.

The coupled phase-transformation plasticity model is embedded into an affine micro-sphere framework in **Chapter 5**, where we show that the three-dimensional extension of the coupled model introduced in Chapter 4 allows to capture the macroscopic response of TRIP steel. Besides homogeneous micro- and meso-level computations, we show a finite element implementation for the solution of inhomogeneous boundary value problems. However, the use of the affine micro-sphere framework induces a macroscopic Poisson's ratio of $\nu_\mathrm{P} = 1/4$ as discussed in Chapter 2. Moreover, the onset of plasticity is not restricted to deviatoric load cases. Both limitations are adressed in Chapter 6.

Chapter 6 provides a model formulation for the interactions between phase-transformations and plasticity in a non-affine micro-sphere framework with volumetric-deviatoric split in kinematics. The incorporation of plasticity is considered solely in the deviatoric Helmholtz free energy contributions of the individual phases and a further coupling between phase-transformations and plasticity is established by means of a consistent plasticity inheritance framework for three phases. We simulate the polycrystalline responses of SMA and TRIP steel for multiple tension-compression load cycles and show that the obtained results are in agreement with the experimentally observed features of both materials, cf. Sections 1.1.1 and 1.1.2, respectively. Precisely speaking, the results obtained for polycrystalline SMA, see Figs. 6.4, 6.5, and 6.6, coincide with experimental findings in terms of the stress-strain response and the maximum macroscopic martensitic volume fraction. The latter reaches around 50 % at 4 % macroscopic strain, corresponding to experimentally observed values for polycrystalline specimen that are subject to the grain-locking effect, cf. Fig. 1.2. The application of the model formulation to TRIP steel material parameters shows that the proposed model captures experimentally observed TRIP steel characteristics as well. The cyclic stress-strain response with work hardening and the cyclic accumulation of martensitic volume fractions shown in Fig. 6.8 coincides with experimental findings, cf. Section 1.1.2. Moreover, the visualisation of the three-dimensional polycrystalline response provided in Fig. 6.9 highlights the intense evolution of plasticity within TRIP steel, whereas the phase-transformation are less intense compared to SMA. Besides these polycrystal-level results, we show a finite element implementation of the overall formulation, where representative inhomogeneous boundary value problems by means of tensile and shear tests of a plate with hole are presented for both classes of material.

A finite-strain model for the simulation of austenitic-martensitic phase-transformations and plasticity in a thermo-elastoplastic framework, taken from [14], is presented in **Chapter 7**. The model aims at the simulation of TRIP steel, where the individual transformation strains—i.e. Bain strains—of spatially arranged martensite unit cells are considered. Representative spatial transformation directions are introduced, where for each spatial direction an arbitrary number of martensite variants can be considered. The minimum amount of transformation directions and martensite variants required to capture macroscopically isotropic polycrystal responses are identified in [14] with the help of an optimisation scheme. The focal point of this chapter is the efficient and robust numerical solution of the strongly coupled system of differential equations—governing the evolution of individual martensite variants, logarithmic plastic strain tensor components for austenite and martensite, respectively, accumulated plastic strains, and temperature. Moreover, algebraic inequality constraints for the evolution of volume fractions are established by means of a penalty scheme. A penalty convergence study is carried out, facilitating the identification of penalty parameter values that enable an efficient enforcement of the physically motivated constraints. Finally, the results of a finite element implementation of the overall model formulation are provided, where the ABAQUS VUMAT subroutine interface for the explicit solution of dynamic boundary value problems is used in view of a later application to macroscopic machining simulations.

Bibliography

[1] R. Abeyaratne and J. Knowles. On the driving traction acting on a surface of strain discontinuity in a continuum. *J. Mech. Phys. Solids*, 38:345–360, 1990. doi:10.1016/0022-5096(90)90003-M.

[2] R. Abeyaratne and J. Knowles. A continuum model of a thermoelastic solid capable of undergoing phase transitions. *J. Mech. Phys. Solids*, 41:541–571, 1993. doi:10.1016/0022-5096(90)90003-M.

[3] R. Abeyaratne and J. Knowles. On the kinetics of an austenite → martensite phase transformation induced by impact in a Cu-Al-Ni shape-memory alloy. *Acta Mater.*, 45:1671–1683, 1997. doi:10.1016/S1359-6454(96)00276-5.

[4] R. Abeyaratne, S. Kim, and J. Knowles. A one-dimensional continuum model for shape-memory alloys. *Int. J. Sol. Struct.*, 31:2229–2249, 1994. doi:10.1016/0020-7683(94)90208-9.

[5] M. Achenbach. A model for an alloy with shape memory. *Int. J. Plasticity*, 5: 371–395, 1989. doi:10.1016/0749-6419(89)90023-5.

[6] V. Alastrué, M. Martínez, A. Menzel, and M. Doblaré. On the use of non–linear transformations for the evaluation of anisotropic rotationally symmetric directional integrals. application to the stress analysis in fibred soft tissues. *Int. J. Numer. Meth. Eng.*, 79(1):474–504, 2009. doi:10.1002/nme.2577.

[7] V. Alastrué, M. Martíneza, M. Doblaré, and A. Menzel. Anisotropic micro-sphere-based finite elasticity applied to blood vessel modelling. *J. Mech. Phys. Solids*, 57: 178–203, 2009. doi:210.1016/j.jmps.2008.09.005.

[8] F. Auricchio and R. Taylor. Shape-memory alloys: modelling and numerical simulations of the finite-strain superelastic behavior. *Comput. Method. Appl. M.*, 143: 175–194, 1997. doi:10.1016/S0045-7825(96)01147-4.

[9] S. C. Baik, S. Kim, Y. S. Jin, and O. Kwon. Effects of alloying elements on mechanical properties and phase transformation of cold rolled TRIP steel sheets. *ISIJ International*, 41(3):290–297, 2001. doi:10.2355/isijinternational.41.290.

[10] E. C. Bain. The nature of martensite. *Trans. AIME*, 70:25–46, 1924.

[11] J. Ball. Convexitiy conditions and existence theorems in nonlinear elasticity. *Arch. Ration. Mech. An.*, 63:337–403, 1977. doi:10.1007/BF00279992.

[12] J. Ball and R. James. Fine phase mixtures as minimizers of energy. *Arch. Ration. Mech. An.*, 100:13–52, 1987. doi:10.1007/BF00281246.

[13] T. Bartel and K. Hackl. A micromechanical model for martensitic phase-transformations in shape-memory alloys based on energy-relaxation. *J. Appl. Math. Mech.*, 89 (10):792–809, 2009. doi:10.1002/zamm.200900244.

[14] T. Bartel and A. Menzel. A finite deformation framework for martensitic phase transformations interacting with plasticity based on representative transformation orientations. *Internal Report, Institute of Mechanics, TU Dortmund*, 2014.

[15] T. Bartel, A. Menzel, and B. Svendsen. Enhanced micromechanical modelling of martensitic phase-transitions considering plastic deformations. In P. Šittner, L. Heller, and V. Paidar, editors, *ESOMAT 2009 - The 8th European Symposium on Martensitic Transformations*, page 03002. EDP Sciences (www.esomat.org), 2009. doi:10.1051/esomat/200903002.

[16] T. Bartel, A. Menzel, and B. Svendsen. Thermodynamic and relaxation-based modeling of the interaction between martensitic phase transformations and plasticity. *J. Mech. Phys. Solids*, 59(5):1004–1019, 2011. ISSN 0022-5096. doi:10.1016/j.jmps.2011.02.006.

[17] Z. Bažant and B. Oh. Efficient numerical integration on the surface of a sphere. *J. Appl. Math. Mech.*, 66(1):37–49, 1986. doi:10.1002/zamm.19860660108.

[18] A. Berezovski and G. Maugin. Moving singularities in thermoelastic solids. *Int. J. Fracture*, 147:191–198, 2007. doi:10.1007/978-1-4020-6929-1_18.

[19] D. Bertsekas. *Constrained Optimization and Lagrange Multiplier Methods*. Athena Scientific, 1996. ISBN 1-886529-04-3.

[20] K. Bhattacharya. *Microstructure of Martensite - Why it forms and how it gives rise to the shape-memory effect*. Oxford University Press, New York, 2003.

[21] P. Blanc and C. Lexcellent. Micromechanical modelling of a CuAlNi shape memory alloy behaviour. *Mat. Sci. Eng. A: Struct.*, 378:465–469, 2004. doi:10.1016/j.msea.2003.11.065.

[22] V. Blank and B. Kulnitskiy. The habit plane of martensite at BCC-HCP phase transformation. *Scripta Mater.*, 37(3):373–376, 1997. ISSN 1359-6462. doi:10.1016/S1359-6462(97)00091-2.

[23] T. Böhlke and C. Brüggemann. Graphical representation of the generalized Hooke's law. *Technische Mechanik*, 21:145–158, 2001. ISSN 0232-3869.

[24] J. Bowles and J. MacKenzie. The crystallography of martensite transformations I and II. *Acta Metall.*, 2:129–137, 1954. doi:10.1016/0001-6160(57)90018-4.

[25] L. Brinson, I. Schmidt, and R. Lammering. Stress-induced transformation behavior of a polycrystalline NiTi shape memory alloy: micro and macromechanical investigations via in situ optical microscopy. *J. Mech. Phys. Solids*, 52(7):1549–1571,

2004. ISSN 0022-5096. doi:10.1016/j.jmps.2004.01.001.

[26] Z. Cai, H. Ding, X. Xue, and Q. Xin. Microstructural evolution and mechanical properties of hot-rolled 11% manganese TRIP steel. *Mat. Sci. Eng. A: Struct.*, 560:388–395, 2013. ISSN 0921-5093. doi:10.1016/j.msea.2012.09.083.

[27] I. Carol and Z. Bažant. Damage and plasticity in microplane theory. *Int. J. Sol. Struct.*, 34:3807–3835, 1997. doi:10.1016/S0020-7683(96)00238-7.

[28] I. Carol, M. Jirásek, and Z. Bažant. A thermodynamically consistent approach to microplane theory. Part I. Free energy and consistent microplane stresses. *Int. J. Sol. Struct.*, 38:2921–2931, 2001. doi:10.1016/S0020-7683(00)00212-2.

[29] I. Carol, M. Jirásek, and Z. Bažant. A framework for microplane models at large strain, with application to hyperelasticity. *Int. J. Sol. Struct.*, 41:511–557, 2004.

[30] C. Carstensen and P. Plechac. Numerical analysis of a relaxed variational model of hysteresis in two-phase solids. *Math. Model. Numer. Anal.*, 35:865–878, 2001. doi:10.1051/m2an:2001139.

[31] A. Cazzani and M. Rovati. Extrema of Young's modulus for cubic and transversely isotropic solids. *Int. J. Sol. Struct.*, 40:1713–1744, 2003. doi:10.1016/S0020-7683(02)00668-6.

[32] M. Cherkaoui, Q. Sun, and G. Song. Micromechanics modeling of composite with ductile matrix and shape memory alloy reinforcement. *Int. J. Sol. Struct.*, 37: 1577–1594, 2000. doi:10.1016/S0020-7683(98)00332-1.

[33] J. Chiang, B. Lawrence, J. D. Boyd, and A. K. Pilkey. Effect of microstructure on retained austenite stability and work hardening of TRIP steels. *Mat. Sci. Eng. A: Struct.*, 528(13-14):4516–4521, 2011. ISSN 0921-5093. doi:10.1016/j.msea.2011.02.032.

[34] K. Choi, W. Liu, X. Sun, and M. Khaleel. Microstructure-based constitutive modeling of TRIP steel: Prediction of ductility and failure modes under different loading conditions. *Acta Mater.*, 57:2592–2604, 2009. doi:10.1016/j.actamat.2009.02.020.

[35] C. Collard and T. Zineb. Simulation of the effect of elastic precipitates in SMA materials based on a micromechanical model. *Comp. Part B: Eng.*, 43(6):2560–2576, 2012. doi:10.1016/j.compositesb.2012.03.015.

[36] B. D. Cooman. Structure-properties relationship in TRIP steels containing carbide-free bainite. *Curr. Opin. Solid St. M.*, 8(3-4):285–303, 2004. ISSN 1359-0286. doi:10.1016/j.cossms.2004.10.002.

[37] B. Dacorogna. Quasiconvexity and relaxation of the nonconvex problems in the calculus of variations. *J. Funct. Anal.*, 46:102–118, 1982. doi:10.1016/0022-1236(82)90046-5.

[38] B. Dacorogna. *Direct Methods in the Calculus of Variations*. Springer, Berlin, 1989.

[39] W. J. Dan, S. H. Li, W. G. Zhang, and Z. Q. Lin. The effect of strain-induced martensitic transformation on mechanical properties of TRIP steel. *Materials and Design*, 29:604–612, 2008. doi:10.1016/j.matdes.2007.02.019.

[40] J. E. Dennis, Jr. and R. B. Schnabel. *Numerical Methods for Unconstrained Optimization and Nonlinear Equations (Classics in Applied Mathematics, 16)*. Soc. for Industrial & Applied Math., 1996. ISBN 0898713641.

[41] A. DeSimone and G. Dolzmann. Material instabilities in nematic polymers. *Physica D*, 136:175–191, 1999. doi:10.1016/S0167-2789(99)00153-0.

[42] A. DeSimone and G. Dolzmann. Macroscopic response of nematic elastomers via relaxation of a class of SO(3)-invariant energies. *Arch. Ration. Mech. An.*, 161: 181–204, 2002. doi:10.1007/s002050100174.

[43] S. Dey, S. Datta, P. Chattopadhyay, and J. Sil. Modeling the properties of TRIP steel using AFIS: A distributed approach. *Comp. Mater. Sci.*, 43(3):501–511, 2008. ISSN 0927-0256. doi:10.1016/j.commatsci.2007.12.009.

[44] E. Emadoddin, A. Akbarzadeh, and G. Daneshi. Effect of cold rolling reduction and intercritical annealing temperature on the bulk texture of two TRIP-aided steel sheets. *J. Mater. Process. Tech.*, 203(1-3):293–300, 2008. ISSN 0924-0136. doi:10.1016/j.jmatprotec.2007.10.041.

[45] F. Fischer. A micromechanical model for transformation plasticity in steels. *Acta Metall. Mater.*, 38(8):1535–1546, 1990. doi:10.1016/0956-7151(90)90121-V.

[46] J. Frenzel, E. George, A. Dlouhy, C. Somsen, M.-X. Wagner, and G. Eggeler. Influence of Ni on martensitic phase transformations in NiTi shape memory alloys. *Acta Mater.*, 58(9):3444–3458, 2010. ISSN 1359-6454. doi:10.1016/j.actamat.2010.02.019.

[47] X. Gao, M. Huang, and L. Brinson. A multivariant micromechanical model for smas part 1. crystallographic issues for single crystal model. *Int. J. Plasticity*, 16: 1345–1369, 2000. doi:10.1016/S0749-6419(00)00013-9.

[48] A. Glage, A. Weidner, and H. Biermann. Effect of austenite stability on the low cycle fatigue behavior and microstructure of high alloyed metastable austenitic cast TRIPsteels. *Procedia Engineering*, 2(1):2085–2094, 2010. ISSN 1877-7058. doi:10.1016/j.proeng.2010.03.224. Fatigue 2010.

[49] S. Göktepe and C. Miehe. A micro-macro approach to rubber-like materials. Part III: The micro-sphere model of anisotropic mullins-type damage. *J. Mech. Phys. Solids*, 53:2259–2283, 2005. doi:10.1016/j.jmps.2005.04.010.

[50] S. Gollerthan, M. Young, A. Baruj, J. Frenzel, W. Schmahl, and G. Eggeler. Fracture mechanics and microstructure in NiTi shape memory alloys. *Acta Mater.*,

57(4):1015–1025, 2009. ISSN 1359-6454. doi:10.1016/j.actamat.2008.10.055.

[51] S. Govindjee and G. Hall. A computational model for shape memory alloys. *Int. J. Sol. Struct.*, 37:735–760, 2000. doi:10.1016/S0020-7683(99)00048-7.

[52] S. Govindjee and C. Miehe. A multi-variant martensitic phase transformation model: formulation and numerical implementation. *Comput. Method. Appl. M.*, 191(3-5):215–238, 2001. doi:10.1016/S0045-7825(01)00271-7.

[53] S. Govindjee, A. Mielke, and G. Hall. The free energy of mixing for n-variant martensitic phase transformations using quasi-convex analysis. *J. Mech. Phys. Solids*, 50:1897–1922, 2002. doi:10.1016/S0022-5096(02)00105-9.

[54] S. Govindjee, K. Hackl, and R. Heinen. An upper bound to the free energy of mixing by twin-compatible lamination for n-variant martensitic phase transformations. *Continuum Mech. Therm.*, 18:443–453, 2007. doi:10.1007/s00161-006-0038-1.

[55] K. Hackl and R. Heinen. An upper bound to the free energy of n-variant polycrystalline shape memory alloys. *J. Mech. Phys. Solids*, 56:2832–2843, 2008. doi:10.1016/j.jmps.2008.04.005.

[56] K. Hackl and M. Schmidt-Baldassari. A micromechanical model for polycrystalline shape-memory alloys. *Mat. Sci. Eng. A: Struct.*, 378:503–506, 2004. doi:10.1016/j.msea.2003.12.047.

[57] D. Hartl and D. Lagoudas. Aerospace applications of shape memory alloys. *P. I. Mech. Eng. G: J. Aer.*, 221:535–552, 2007. doi:10.1243/09544100JAERO211.

[58] D. Hartl and D. Lagoudas. Constitutive modeling and structural analysis considering simultaneous phase transformations and plastic yield in shape memory alloys. *Smart Mater. Struct.*, 18(10):1–17, 2009. doi:10.1088/0964-1726/18/10/104017.

[59] D. Helm. *Formgedächtnislegierungen – Experimentelle Untersuchung, phänomenologische Modellierung und numerische Simulation der thermomechanischen Materialeigenschaften.* Dissertation, Universität Gesamthochschule Kassel, 2001. Berichte des Instituts für Mechanik (Bericht 3/2001).

[60] D. Helm and P. Haupt. Thermomechanical behaviour of shape memory alloys. *Proceedings of SPIEs Smart Structures and Materials*, 4333:302–313, 2001.

[61] D. Helm and P. Haupt. Shape memory behaviour: modelling within continuum mechanics. *Int. J. Sol. Struct.*, 40:827–849, 2003. doi:10.1016/S0020-7683(02)00621-2.

[62] D. Helm and P. Haupt. Thermomechanical behaviour of shape memory alloys. *Proceedings of SPIE Smart Structures and Materials*, 4333:302–313, 2001. doi:10.1117/12.432769.

[63] R. Holtermann, S. Schumann, A. Menzel, and D. Biermann. Modelling, simulation and experimental investigation of chip formation in internal traverse grinding. *Prod. Engineer.*, 7(2-3):251–263, 2013. doi:10.1007/s11740-01.

[64] C. Hortig and B. Svendsen. Simulation of chip formation during high-speed cutting. *J. Mater. Process. Tech.*, 186(1-3):66–76, 2007. ISSN 0924-0136. doi:10.1016/j.jmatprotec.2006.12.018.

[65] M. Huang and L. Brinson. A multivariant model for single crystal shape memory alloy behavior. *J. Mech. Phys. Solids*, 46:1379–1409, 1998. doi:10.1016/S0022-5096(97)00080-X.

[66] Y. Huo and I. Müller. Nonequilibrium thermodynamics of pseudoelasticity. *Continuum Mech. Therm.*, 5:163–204, 1993. doi:10.1007/BF01126524.

[67] P. J. Jacques, F. Delannay, and J. Ladriere. On the influence of interactions between phases on the mechanical stability of retained austenite in transformation-induced plasticity multiphase steels. *Metall. Mater. Trans. A*, 32(11):2759–2768, 2001. ISSN 1543-1940. doi:10.1007/s11661-001-1027-4.

[68] R. James and K. Hane. Martensitic transformations and shape memory materials. *Acta Mater.*, 48:197–222, 2000. doi:10.1016/S1359-6454(99)00295-5.

[69] W. C. Jeong and J. H. Chung. observation of retained austenite by secondary electron imaging in a scanning transmission electron microscope. *Mater. Charact.*, 26(1):53–56, 1991. ISSN 1044-5803. doi:10.1016/1044-5803(91)90008-R.

[70] X. Jiang, M. Hida, Y. Takemoto, A. Sakakibara, H. Yasuda, and H. Mori. In situ observation of stress-induced martensitic transformation and plastic deformation in TiNi alloy. *Mat. Sci. Eng. A: Struct.*, 238(2):303–308, 1997. ISSN 0921-5093. doi:10.1016/S0921-5093(97)00422-X.

[71] J. Kobayashi, H. Tonegawa, and K. Sugimoto. Cold formability of 22SiMnCrB TRIP-aided martensitic sheet steel. *Procedia Engineering*, 81(0):1336–1341, 2014. ISSN 1877-7058. doi:10.1016/j.proeng.2014.10.153. 11th International Conference on Technology of Plasticity, ICTP 2014, 19-24 October 2014, Nagoya Congress Center, Nagoya, Japan.

[72] R. Kohn. The relaxation of a double-well energy. *Continuum Mech. Therm.*, 3: 193–236, 1991. doi:10.1007/BF01135336.

[73] P. Krooß, M. Holzweissig, T. Niendorf, C. Somsen, M. Schaper, Y. Chumlyakov, and H. J. Maier. Thermal cycling behavior of an aged FeNiCoAlTa single-crystal shape memory alloy. *Scripta Mater.*, 81(0):28–31, 2014. ISSN 1359-6462. doi:10.1016/j.scriptamat.2014.02.020.

[74] E. Kuhl, P. Steinmann, and I. Carol. A thermodynamically consistent approach to microplane theory. Part II. Dissipation and inelastic constitutive modeling. *Int. J. Sol. Struct.*, 38:2933–2952, 2001. doi:10.1016/S0020-7683(00)00213-4.

[75] E. Kuhl, P. Steinmann, and I. Carol. A thermodynamically consistent approach to microplane theory. Part II. Dissipation and inelastic constitutive modeling. *Int. J. Sol. Struct.*, 38:2933–2952, 2001. doi:10.1016/S0020-7683(00)00213-4.

[76] I. Kurzhöfer. *Mehrskalen–Modellierung polykristalliner Ferroelektrika basierend auf diskreten Orientierungsverteilungsfunktionen.* PhD thesis, Universität Duisburg–Essen, Institut für Mechanik, Bericht Nr. 4, 2007.

[77] D. Lagoudas. *Shape Memory Alloys – Modeling and Engineering Applications.* Springer, 2008. doi:10.1007/978-0-387-47685-8.

[78] D. Lagoudas, P. Entchev, P. Popov, E. Patoor, L. Brinson, and X. Gao. Shape memory alloys, part II: modeling of polycrystals. *Mech. Mater.*, 38:430–462, 2006. doi:10.1016/j.mechmat.2005.08.003.

[79] H.-G. Lambers, S. Tschumak, H. J. Maier, and D. Canadinc. Tensile properties of 51crv4 steel in martensitic, bainitic and austenitic state. *Hot Sheet Metal Forming of High-Performance Steel*, 2:73–82, 2009.

[80] Q. Liu, D. Tang, H.-T. Jiang, R.-D. Liu, and X.-Y. Tang. Research and development of 780 MPa cold rolling TRIP-aided steel. *International Journal of Minerals, Metallurgy and Materials*, 16(4):399–406, 2009. ISSN 1674-4799. doi:10.1016/S1674-4799(09)60071-6.

[81] Y. Liu, Z. Xie, J. V. Humbeeck, and L. Delaey. Effect of texture orientation on the martensite deformation of NiTi shape memory alloy sheet. *Acta Mater.*, 47 (2):645–660, 1999. ISSN 1359-6454. doi:10.1016/S1359-6454(98)00376-0.

[82] Y. Liu, Z. Xie, J. V. Humbeeck, and L. Delaey. Asymmetry of stress-strain curves under tension and compression for NiTi shape memory alloys. *Acta Mater.*, 46 (12):4325–4338, 1998. ISSN 1359-6454. doi:10.1016/S1359-6454(98)00112-8.

[83] Y. Liu, Z. Xie, and J. V. Humbeeck. Cyclic deformation of NiTi shape memory alloys. *Mat. Sci. Eng. A: Struct.*, 273-275:673–678, 1999. ISSN 0921-5093. doi:10.1016/S0921-5093(99)00347-0.

[84] A. Ma and A. Hartmaier. A study of deformation and phase transformation coupling for trip-assisted steels. *Int. J. Plasticity*, 64:40–55, 2015. ISSN 0749-6419. doi:10.1016/j.ijplas.2014.07.008.

[85] R. Mahnken, A. Schneidt, and T. Antretter. Macro modelling and homogenization for transformation induced plasticity of a low-alloy steel. *Int. J. Plasticity*, 25:183–204, 2009. doi:10.1016/j.ijplas.2008.03.005.

[86] R. Mahnken, M. Wolff, A. Schneidt, and M. Böhm. Multi-phase transformations at large strains – thermodynamic framework and simulation. *Int. J. Plasticity*, 39: 1–26, 2012. ISSN 0749-6419. doi:10.1016/j.ijplas.2012.05.009.

[87] H. J. Maier, B. Donth, M. Bayerlein, H. Mughrabi, B. Meier, and M. Kesten. Optimierte Festigkeitssteigerung eines metastabilen austenitischen Stahles durch wechselverformungsinduzierte Martensit-Umwandlung bei tiefen Temperaturen. *Zeitschrift für Metallkunde*, 84:820–826, 1993.

[88] G. Maugin and A. Berezovski. On the propagation of singular surfaces in thermoelasticity. *J. Therm. Stresses*, 32:557–592, 2009. doi:10.1080/01495730902848631.

[89] A. Menzel and T. Waffenschmidt. A micro-sphere-based remodelling formulation for anisotropic biological tissues. *Philos. T. Roy. Soc. A.*, 367(1902):3499–3523, 2009. doi:10.1098/rsta.2009.0103.

[90] T. Merzouki, A. Duval, and T. Zineb. Finite element analysis of a shape memory alloy actuator for a micropump. *Sim. Mod. Pract. Theory*, 27:112–126, 2012. doi:10.1016/j.simpat.2012.05.006.

[91] C. Miehe and S. Göktepe. A micro-macro approach to rubber-like materials. Part II: The micro-sphere model for finite rubber viscoelasticity. *J. Mech. Phys. Solids*, 53:2231–2258, 2005. doi:10.1016/j.jmps.2005.04.006.

[92] C. Miehe, S. Göktepe, and F. Lulei. A micro-macro approach to rubber-like materials Part I: the non-affine micro-sphere model of rubber elasticity. *J. Mech. Phys. Solids*, 52:2617–2660, 2004. doi:10.1016/j.jmps.2004.03.011.

[93] C. Miehe, S. Göktepe, and J. M. Diez. Finite viscoplasticity of amorphous glassy polymers in the logarithmic strain space. *Int. J. Sol. Struct.*, 46:181–202, 2009. doi:10.1016/j.ijsolstr.2008.08.029.

[94] A. Mielke and F. Theil. A mathematical model for rate-independent phase transformations with hysteresis. In H.-D. Alber, R. Balean, and R. Farwig, editors, *Proceedings of the Workshop on Models of Continuum Mechanics in Analysis and Engineering*, pages 117–129. Shaker-Verlag, 1999.

[95] A. Mielke, F. Theil, and V. Levitas. A variational formulation of rate-independent phase transformations using an extremum principle. *Arch. Ration. Mech. An.*, 162 (2):137–177, 2002. doi:10.1007/s002050200194.

[96] S. Miyazaki. Medical and dental applications of shape memory alloys. *Shape Memory Materials, Cambridge University Press*, 12:267–281, 1999.

[97] C. Morrey. Quasi–convexity and the lower semicontinuity of multiple integrals. *Pac. J. Math.*, 2:25–53, 1952.

[98] C. Müller and O. Bruhns. A thermodynamic finite-strain model for pseudoelastic shape memory alloys. *Int. J. Plasticity*, 22:1658–1682, 2006. doi:10.1016/j.ijplas.2006.02.010.

[99] I. Müller and S. Seelecke. Thermodynamic aspects of shape memory alloys. *Math. Comput. Model.*, 34:1307–1355, 2001. doi:10.1016/S0895-7177(01)00134-0.

[100] M. Ortiz and E. Repetto. Nonconvex energy minimization and dislocation structures in ductile single crystals. *J. Mech. Phys. Solids*, 47:397–462, 1999. doi:10.1016/S0022-5096(97)00096-3.

[101] R. Ostwald, T. Bartel, and A. Menzel. A computational micro-sphere model applied to the simulation of phase-transformations. *J. Appl. Math. Mech.*, 90

(7-8):605–622, 2010. ISSN 1521-4001. doi:10.1002/zamm.200900390.

[102] R. Ostwald, T. Bartel, and A. Menzel. A one-dimensional computational model for the interaction of phase-transformations and plasticity. *Int. J. of Structural Changes in Solids*, 3(1):63–82, 2011.

[103] R. Ostwald, T. Bartel, and A. Menzel. Phase-transformations interacting with plasticity – a micro-sphere model applied to TRIP steel. *Comp. Mater. Sci.*, 64: 12–16, 2012. doi:10.1016/j.commatsci.2012.05.015.

[104] R. Ostwald, T. Bartel, and A. Menzel. A Gibbs-energy-barrier-based computational micro-sphere model for the simulation of martensitic phase-transformations. *Int. J. Numer. Meth. Eng.*, 97:851–877, 2014. doi:10.1002/nme.4601.

[105] R. Ostwald, T. Bartel, and A. Menzel. An energy-barrier-based computational micro-sphere model for phase-transformations interacting with plasticity. *Comput. Method. Appl. M.*, 293:232–265, 2015. doi:10.1016/j.cma.2015.04.008.

[106] K. Otsuka and T. Kakeshita. Science and technology of shape-memory alloys: new developments. *MRS Bull*, 27:91–100, 2002. doi:10.1557/mrs2002.43.

[107] S. Pagano, P. Alart, and O. Maisonneuve. Solid-solid phase transition modelling. local and global minimizations of non-convex and relaxed potentials. isothermal case for shape memory alloys. *Int. J. Eng. Sci.*, 36:1143–1172, 1998. doi:10.1016/S0020-7225(98)00010-X.

[108] E. Patoor, D. Lagoudas, B. P. Entchev, L. Brinson, and X. Gao. Shape memory alloys, part I: General properties and modeling of single crystals. *Mech. Mat.*, 38: 391–429, 2006.

[109] E. Patoor, D. Lagoudas, P. Entchev, L. Brinson, and X. Gao. Shape memory alloys, part I: general properties and modeling of singlecrystals. *Mech. Mater.*, 38: 391–429, 2006. doi:10.1016/j.mechmat.2005.05.027.

[110] S. Petit-Grostabussiat, L. Taleb, and J.-F. Jullien. Experimental results on classical plasticity of steels subjected to structural transformations. *Int. J. Plasticity*, 20(8-9):1371–1386, 2004. ISSN 0749-6419. doi:10.1016/j.ijplas.2003.07.003.

[111] B. Raniecki, C. Lexcellent, and K. Tanaka. Thermodynamic models of pseudoelastic behaviour of shape memory alloys. *Arch. Mech.*, 44:261–284, 1992.

[112] S. Reese and D. Christ. Finite deformation pseudo-elasticity of shape memory alloys – constitutive modelling and finite element implementation. *Int. J. Plasticity*, 24:455–482, 2008. doi:10.1016/j.ijplas.2007.05.005.

[113] Y. Sakuma, D. K. Matlock, and G. Krauss. Intercritically annealed and isothermally transformed 0.15 Pct C steels containing 1.2 Pct Si-1.5 Pct Mn and 4 Pct Ni: Part I. transformation, microstructure, and room-temperature mechanical properties. *Metall. Trans. A*, 23(4):1221–1232, 1992. doi:10.1007/BF02665053.

[114] Y. Sakuma, D. K. Matlock, and G. Krauss. Intercritically annealed and isothermally transformed 0.15 Pct C steels containing 1.2 Pct Si-1.5 Pct Mn and 4 Pct Ni: Part II. effect of testing temperature on stress-strain behavior and deformation-induced austenite transformation. *Metall. Trans. A*, 23(4):1233–1241, 1992. doi:10.1007/BF02665054.

[115] S. Seelecke. Equilibrium thermodynamics of pseudoelasticity and quasiplasticity. *Continuum Mech. Therm.*, 8:309–322, 1996. doi:10.1007/s001610050046.

[116] J. Shaw and S. Kyriakides. Initiation and propagation of localized deformation in elasto-plastic strips under uniaxial tension. *Int. J. Plasticity*, 13(10):837–871, 1997. ISSN 0749-6419. doi:10.1016/S0749-6419(97)00062-4.

[117] A. Shibata, T. Murakami, S. Morito, T. Furuhara, and T. Maki. The origin of midrib in lenticular martensite. *Mater. Trans.*, 49(6):1242–1248, 2008. doi:10.2320/matertrans.MRA2007296.

[118] J. C. Simo and T. J. R. Hughes. *Computational Inelasticity.* Interdisciplinary Applied Mathematics. Springer, 1998.

[119] P. Šittner, M. Landa, P. Lukáš, and V. Novák. R-phase transformation phenomena in thermomechanically loaded NiTi polycrystals. *Mech. Mater.*, 38(5-6):475–492, 2006. ISSN 0167-6636. doi:10.1016/j.mechmat.2005.05.025.

[120] P. Šittner, L. Heller, J. Pilch, C. Curfs, T. Alonso, and D. Favier. Young's modulus of austenite and martensite phases in superelastic NiTi wires. *J. Mater. Eng. Perform.*, 23(7):2303–2314, 2014. ISSN 1059-9495. doi:10.1007/s11665-014-0976-x.

[121] L. Skálová, R. Divišová, and D. Jandová. Thermo-mechanical processing of low-alloy TRIP-steel. *J. Mater. Process. Tech.*, 175(1-3):387–392, 2006. ISSN 0924-0136. doi:10.1016/j.jmatprotec.2005.04.067.

[122] V. Smyshlyaev and J. Willis. On the relaxation of a three-well energy. *Proc. R. Soc. London A*, 455:779–814, 1998. doi:10.1098/rspa.1999.0335.

[123] E. Stein and O. Zwickert. Theory and finite element computations of a unified cyclic phase transformation model for monocrystalline materials at small strains. *Comput. Mech.*, 40(3):429–445, 2007. doi:10.1007/s00466-006-0118-x.

[124] S. Stupkiewicz and H. Petryk. Modelling of laminated microstructures in stress-induced martensitic transformations. *J. Mech. Phys. Solids*, 50:2303–2331, 2002. doi:10.1016/S0022-5096(02)00029-7.

[125] K. Sugimoto, J. Sakaguchi, T. Iida, and T. Kashima. Stretch-flangeability of a high-strength TRIP type bainitic sheet steel. *ISIJ International*, 40(9):920–926, 2000. doi:10.2355/isijinternational.40.920.

[126] K. Sugimoto, M. Murata, and S. Song. Formability of Al-Nb bearing ultra high-strength TRIP-aided sheet steels with bainitic ferrite and/or martensite matrix. *ISIJ International*, 50(1):162–168, 2010. doi:10.2355/isijinternational.50.162.

[127] A. S. J. Suiker and B. Thijsse. Nucleation, kinetics and morphology of displacive phase transformations in iron. *J. Mech. Phys. Solids*, 61(11):2273–2301, 2013. ISSN 0022-5096. doi:10.1016/j.jmps.2013.06.002.

[128] A. S. J. Suiker and S. Turteltaub. Computational modelling of plasticity induced by martensitic phase transformations. *Int. J. Numer. Meth. Eng.*, 63(12):1655–1693, 2005. ISSN 1097-0207. doi:10.1002/nme.1327.

[129] A. S. J. Suiker and S. Turteltaub. Numerical modelling of transformation-induced damage and plasticity in metals. *Model. Simul. Mater. Sc.*, 15:147–166, 2007. doi:10.1088/0965-0393/15/1/S13.

[130] Q. Sun and K. Hwang. Micromechanics modelling for the constitutive behavior of polycrystalline shape memory alloys-i. derivation of general relations. *J. Mech. Phys. Solids*, 41:1–17, 1993. doi:10.1016/0022-5096(93)90060-S.

[131] Q. Sun, K. Hwang, and S. Yu. A micromechanics constitutive model of transformation plasticity with shear and dilatation effect. *J. Mech. Phys. Solids*, 39: 507–524, 1991. doi:10.1016/0022-5096(91)90038-P.

[132] K. Tanaka. A thermomechanical sketch of shape memory effect: one-dimensional tensile behavior. *Res. Mech*, 18:251–263, 1986.

[133] S. Thylander, A. Menzel, and M. Ristinmaa. An electromechanically coupled micro-sphere framework: application to the finite element analysis of electrostrictive polymers. *Smart Mater. Struct.*, 21(094008):1–10, 2012. doi:10.1088/0964-1726/21/9/094008.

[134] D. D. Tjahjanto, S. Turteltaub, and A. S. J. Suiker. Crystallographically based model for transformation-induced plasticity in multiphase carbon steels. *Continuum Mech. Therm.*, 19(7):399–422, 2008. ISSN 0935-1175. doi:10.1007/s00161-007-0061-x.

[135] D. D. Tjahjanto, A. S. J. Suiker, S. Turteltaub, and S. van der Zwaag. Parametric study of multiphase TRIP steels undergoing cyclic loading. *Comp. Mater. Sci.*, 50 (4):1490–1498, 2011. ISSN 0927-0256. doi:10.1016/j.commatsci.2010.12.004.

[136] Y. Tomita and T. Iwamoto. Computational prediction of deformation behavior of TRIP steels under cyclic loading. *Int. J. Mech. Sci.*, 43(9):2017–2034, 2001. doi:10.1016/S0020-7403(01)00026-1.

[137] C. Truesdell and R. Toupin. The classical field theories. In S. Flügge, editor, *Handbuch der Physik*, volume 3. Springer, Berlin, 1960.

[138] S. Turteltaub and A. S. J. Suiker. Transformation-induced plasticity in ferrous alloys. *J. Mech. Phys. Solids*, 53(8):1747–1788, 2005. ISSN 0022-5096. doi:10.1016/j.jmps.2005.03.004.

[139] S. Turteltaub and A. S. J. Suiker. Grain size effects in multiphase steels assisted by transformation-induced plasticity. *Int. J. Sol. Struct.*, 43(24):7322–7336, 2006.

ISSN 0020-7683. doi:10.1016/j.ijsolstr.2006.06.017.

[140] S. Turteltaub and A. S. J. Suiker. A multiscale thermomechanical model for cubic to tetragonal martensitic phase transformations. *Int. J. Sol. Struct.*, 43(14-15): 4509–4545, 2006. ISSN 0020-7683. doi:10.1016/j.ijsolstr.2005.06.065.

[141] M. Šilhavý. *The Mechanics and Thermodynamics of Continuous Media.* Springer, 1997. ISBN 9783540583783.

[142] T. Waffenschmidt, A. Menzel, and E. Kuhl. Anisotropic density growth of bone – a computational micro-sphere approach. *Int. J. Sol. Struct.*, 49:1928–1946, 2012. doi:10.1016/j.ijsolstr.2012.03.035.

[143] X. Wang, B. Huang, Y. Rong, and L. Wang. Microstructures and stability of retained austenite in TRIP steels. *Mat. Sci. Eng. A: Struct.*, 438-440(0):300–305, 2006. ISSN 0921-5093. doi:10.1016/j.msea.2006.02.149.

[144] Z. Xie, Y. Liu, and J. V. Humbeeck. Microstructure of NiTi shape memory alloy due to tension-compression cyclic deformation. *Acta Mater.*, 46(6):1989–2000, 1998. ISSN 1359-6454. doi:10.1016/S1359-6454(97)00379-0.

[145] S. Yadegari, S. Turteltaub, and A. S. J. Suiker. Coupled thermomechanical analysis of transformation-induced plasticity in multiphase steels. *Mech. Mater.*, 53(0):1–14, 2012. ISSN 0167-6636. doi:10.1016/j.mechmat.2012.05.002.

[146] S. Yadegari, S. Turteltaub, A. S. J. Suiker, and P. J. J. Kok. Analysis of banded microstructures in multiphase steels assisted by transformation-induced plasticity. *Comp. Mater. Sci.*, 84(0):339–349, 2014. ISSN 0927-0256. doi:10.1016/j.commatsci.2013.12.002.

[147] S. Zaefferer, J. Ohlert, and W. Bleck. A study of microstructure, transformation mechanisms and correlation between microstructure and mechanical properties of a low alloyed TRIP steel. *Acta Metall. Mater.*, 52(9):2765–2778, 2004. ISSN 1359-6454. doi:10.1016/j.actamat.2004.02.044.

[148] M. Zhang, L. Li, R. Fu, D. Krizan, and B. D. Cooman. Continuous cooling transformation diagrams and properties of micro-alloyed TRIP steels. *Mat. Sci. Eng. A: Struct.*, 438-440:296–299, 2006. ISSN 0921-5093. doi:10.1016/j.msea.2006.01.128. Proceedings of the International Conference on Martensitic Transformations.

[149] J.-L. Zhao, Y. Xi, W. Shi, and L. Li. Microstructure and mechanical properties of high manganese TRIP steel. *J. Iron Steel Res. Int.*, 19(4):57–62, 2012. ISSN 1006-706X. doi:10.1016/S1006-706X(12)60088-0.

[150] R. Zhu, S. Li, I. Karaman, R. Arroyave, T. Niendorf, and H. J. Maier. Multiphase microstructure design of a low-alloy TRIP-assisted steel through a combined computational and experimental methodology. *Acta Mater.*, 60(6-7):3022–3033, 2012. ISSN 1359-6454. doi:10.1016/j.actamat.2012.02.007.

Curriculum Vitae

Personal Data

Name	Richard Ostwald
Date of Birth	April 28, 1986
Place of Birth	Recklinghausen, Germany
Nationality	German

Professional Occupation

07/2009 – onwards	Scientific Assistant, Institute of Mechanics, TU Dortmund University
10/2008 – 06/2009	Intern, Siemens AG, Mülheim/Ruhr, Germany, Turbines and Generators Factory, Mechanical Calculations Department
01/2006 – 06/2008	Student Representative in the Mechanical Engineering Faculty Council, TU Dortmund University
02/2005 – 09/2008	Student Assistant, Institute of Mechanics, TU Dortmund University

University Education

06/2009	Academic Degree: Diploma (Dipl.-Ing.)
10/2004 – 09/2008	Studies of Mechanical Engineering, TU Dortmund University

School Education

06/2004	University-entrance Diploma, Hittorf Secondary School, Recklinghausen